UNIVERSITÉ SORBONNE PARIS CITÉ

Thèse préparée
à l'INSTITUT DE PHYSIQUE DU GLOBE DE PARIS
École doctorale STEP'UP – ED N°560
IPGP - Équipe de Tectonique et Mécanique de la Lithosphère

Dynamic earthquake ruptures on multiscale fault and fracture networks

par

Kurama OKUBO

présentée et soutenue publiquement le
09 Novembre 2018

Thèse de doctorat de Sciences de la Terre et de l'environnement

dirigée par Yann Klinger & Harsha S. Bhat

devant un jury composé de:

Marine Denolle Assistant Professor (Harvard University, USA)	Rapporteur
Isabelle Manighetti Physicienne (UMR Géoazur)	Rapporteur
Alexandre Schubnel Directeur de recherche (ENS Paris)	Examinateur
Ioannis Stefanou Chargé de recherche - IFSTTAR (Ecole des Ponts ParisTech)	Examinateur
Esteban Rougier Research Scientist (Los Alamos National Laboratory, USA)	Invité
Harsha S. Bhat Chargé de recherche (ENS Paris)	Co-directeur de thèse
Yann Klinger Directeur de recherche (IPGP)	Directeur de thèse

Remerciements

Tout d'abord, Je tiens à exprimer mes plus vifs remerciements à Harsha S. Bhat pour vos multiples encouragements répétés et ses conseils avisés malgré ses nombreuses charges. Il a toujours souligné l'importance de la perception de la nature pour recherche, et ainsi ça m'a motivé d'analyser la profondeur des résultats.

J'exprime tous mes remerciements à Yann Klinger pour me donner l'opportunité de faire le premier d'une collaboration de recherche. Il m'a appris la complexité de la nature et aussi une approche scientifique pour faire face au problème.

J'aimerais remercier Esteban Rougier pour son soutien continu et son aide pendant mon stage à Los Alamos.

Je tiens à remercier Alexandre Schubnel et Raúl Madariaga pour sa participation à la comité de thèse et toutes remarques intéressantes. Je remercie Marion Thomas pour ses nombreux conseils depuis la deuxième année de master à l'IPGP. Je remercie Dmitry Garagash pour les suggestions constructives dans l'analyse. Un tout grand merci Aochi-san pour son soutien et les discussions sur la modélisation de la rupture. Merci Nobu-san pour m'apprendre à vivre en France.

Une partie de mon évaluation et mon analyse a été accomplie pendant mon stage à Los Alamos National Laboratory. La vie était totalement différente. Je l'ai adoré quand-même, et ils ont progressé à très grande vitesse grâce à tous les soutiens de Zhou Lei, Earl E. Knight, Paul A. Johnson et mes ami(e)s dans l'équipe géophysique à LANL.

J'adresse toute ma gratitude à tous mes ami(e)s à l'IPGP et à l'ENS pour les supports et pour partager une soirée dans un bar. Pour finir, un grand merci à mes parents et mon chien.

Contents

List of Figures

List of Tables

List of symbols and abbreviations

Variables	Units	Description
E	Pa	Young's modulus
μ	Pa	Shear modulus
ν	-	Poisson's ratio
ρ	kg m^{-3}	Density
c_p	m s^{-1}	Dilatational wave velocity
c_s	m s^{-1}	Shear wave velocity
p^p	Pa	Penalty (eq. 2.2)
p^c, p^f	Pa	Stiffness of elastic loading for cohesion and friction (eq. 2.20 and 2.23)
$\delta_{I/II}$	m	Normal (mode I) and tangential (mode II) displacement
$\delta^{c,e}_{I/II}$	m	Critical displacement for elastic loading of tensile and shear cohesion (eq. 2.21)
$\delta^{c,c}_{I/II}$	m	Maximum displacement for softening of tensile and shear cohesion (eq. 2.22)
$\delta^{f,e}_{II}$	m	Critical slip for elastic loading of shear friction (eq. 2.40)
$\delta^{f,c}_{II}$	m	Critical slip distance of slip-weakening law, conventionally denoted by D_c (eq. 2.14)
$\delta^{f,s}_{II}$	m	Critical slip distance for slip-strengthening of shear friction (eq. 2.40)
$C_{I/II}(\delta_{I/II})$	Pa	Cohesion for tensile (mode I) crack and shear (mode II) crack
$C^p_{I/II}$	Pa	Cohesive strength for tensile and shear cohesion
f_s	-	Static friction coefficient
f_d	-	Dynamic friction coefficient
$f^n_I(\delta_{II})$	N	Normal force
$f^f_{II}(\delta_{II})$	N	Shear friction force
$\tau(\delta_{II})$	Pa	Friction
τ_p	Pa	Peak strength for friction (eq. 2.15)
τ_r	Pa	Residual strength for friction (eq. 2.16)
G^c_{IC}	J m^{-2}	Tensile fracture energy for cohesion (eq. 2.13)
G^c_{IIC}	J m^{-2}	Shear fracture energy for cohesion (eq. 2.13)

Variables	Units	Description
G^f_{IIC}	J m^{-2}	Shear fracture energy for friction (eq. 2.14)
D_I	-	Tensile damage component (eq. 2.10)
D_{II}	-	Shear damage component (eq. 2.10)
D	-	Damage (eq. 2.11)
D^T	-	Damage type (eq. 2.12)
A^p	m^2	Area of point (see Figure 2.7)
h	m	Length of edge (see Figure 2.7)
Following notations are used only in chapter 2.4		
$\mu(\delta_{II})$	-	Slip-dependent friction coefficient
μ_s	-	Static friction coefficient
μ_d	-	Dynamic friction coefficient
E^c_i	J	Dissipated energy by cohesion
E^f_{II}	J	Dissipated energy by friction
$f^f_{II}(\delta_{II})$	N	Shear friction force
τ_{II}	Pa	Shear traction
f_n	N	Normal force
σ_n	Pa	Normal stress
	Note: * denotes the initial value. *e.g.* $\delta_I^{*c,e} = \delta_I^{c,e}(0)$	

Abbreviation	description
FDEM	Combined Finite-Discrete Element Method
HOSSedu	Hybrid Optimization Software Suite - educational version developed by Los Alamos National Laboratory (*Knight et al.*, 2015)
BIEM	Boundary Integral Equation Method
FEM	Finite Element Method
SEM	Spectral Element Method
FDM	Finite Difference Method
DEM	Discrete Element Method
ADER-DG	Arbitrary high-order accurate DERivative Discontinuous Galerkin method
STF	Source Time Function

Foreword

This thesis is based on the work conducted during my PhD at the laboratory of lithosphere tectonics and mechanics, Institut de Physique du Globe de Paris, and at the geology laboratory, École Normale Supérieure in Paris, under the supervision by Yann Klinger, Harsha S Bhat and Esteban Rougier. Part of the work was conducted during my research internship at EES-17 - Earth and Environmental Sciences Division, Los Alamos National Laboratory, New Mexico, USA.

Sections of Chapter 4 will appear in the following paper: Klinger, Y., Okubo, K., Vallage, A., Champenois, J., Delorme, A., Rougier, E., Lei, Z., Knight, E. E., Munjiza, A., Satriano, C., Baize, S., Langridge, R., and Bhat, H. S. (2018), Earthquake damage patterns resolve complex rupture processes, *Geophys. Res. Lett.*, accepted.

Sections of Chapter 2, 3 are in preparation as: Okubo, K., Bhat, H. S., Rougier, E., Marty, S., Schubnel, A., Lei, Z., Knight, E. E., and Klinger, Y., Dynamics, radiation and overall energy budget of earthquake rupture with coseismic off-fault damage, *J. Geophys. Res.* to be subm.

Sections of Chapter 5 are in preparation as: Okubo, K., Bhat, H. S., Rougier, E., Lei, Z., Knight, E. E., and Klinger, Y., Coseismic off-fault damage on simple fault structures, *Comput. Geosci.* to be subm.

Résumé

Les zones de faille naturelles présentent une complexité structurelle à différentes échelles. Elles sont composées d'un réseau de failles majeures où le glissement principal s'effectue, lui-même entouré d'un réseau méso- et microscopique de fractures. Cette complexité géométrique impacte la dynamique de la rupture, la propagation des ondes sismiques ainsi que le bilan énergétique lors des tremblements de terre. Les observations géologiques et géophysiques des systèmes de faille montrent une corrélation entre la distribution spatiale de la densité de microfractures et la distance au plan principal de rupture. De leur étude de terrain, *Faulkner et al*. (2011) ont déduit que cette structure particulière des zones de failles s'explique par les irrégularitiés géométriques et l'endommagement cosismique. Les expériences en laboratoire sur la rupture dynamique montrent également un contenu haute-fréquence enrichi, comme il est observé pour les séismes naturels. Ceci est considéré comme la contribution de l'endommagement cosismique. Les outils de modélisation numérique, qui prennent en compte l'endommagement cosismique, ont permis d'explorer l'évolution des microfractures dans les zones de failles durant les séismes, et leur impact en retour sur la rupture dynamique. En revanche, les modèles existants ne permettaient pas la génération, dynamique, de fractures secondaires dans le milieu qui entourent les failles majeures. Dans cette étude, afin de pouvoir modéliser des ruptures sismiques le long de failles à géométrie réaliste, associées à la création de fractures secondaires, nous proposons une approche qui allie la modélisation des milieux continus et discontinus, en utilisant la méthode combinée des éléments finis et discrets (FDEM). Nous présentons d'abord les résultats des modélisations de rupture dynamique avec génération de fractures secondaires. Ces simulations illustrent les mécanismes de l'endommagement, une diminution de la vitesse de rupture, et les radiations hautes fréquences en champ proche. Le budget énergétique est également modifié en raison des radiations et de la dissipation de l'énergie de fracture lié à l'endommagement. Nous avons par la suite réalisé des expériences numériques afin de reproduire la rupture dynamique lors du séisme de Kaikōura (magnitude 7.8), qui s'est produit en 2016, sur le système de failles de l'île sud de la Nouvelle-Zélande. Nous avons pu démontrer qu'en comparant les observations de terrain avec la nature de l'endommagement et les profils de déplacement générés par nos modèles, il est possible de discriminer parmi les différents scénarios potentiels de rupture cosismique. En conclusion, les travaux réalisés au cours de cette thèse proposent une nouvelle génération de modèles qui, grâce à l'approche combinée des milieux continus et des milieux discrets, permet l'activation et la génération de systèmes de fractures secondaires en lien avec les séismes sur les failles majeures. Ils démontrent les effets significatifs que peut jouer l'endommagement généré lors des séismes.

Abstract

Multiscale fault structures consist of macroscopic major fault networks surrounded by mesoscopic and microscopic fracture networks, considered as off-fault damage. Such geometrical complexity of natural fault structure modifies the rupture dynamics, the seismic wave radiation and the overall energy budget associated with earthquakes. Field observations have recorded a correlation of fracture density to the distance from the fault cores, and also a strong link with the quantity of fault slip. In their geological study, *Faulkner et al*. (2011) concluded that the observed scaling inside the fault zone is better explained by the geometric irregularities and/or the coseismic damage. An enhanced high-frequency content, expected to be caused by the coseismic damage, is also observed during laboratory experiments of dynamic ruptures. Past work has explored the evolution of secondary coseismic off-fault damage caused by the dynamic earthquake ruptures within the context of effective constitutive laws. However, the current existing models cannot allow for the activation of individual secondary off-fault cracks due to limitations of model formulations. Here we propose a continuum-discontinuum approach framework with combined finite-discrete element method (FDEM) to model dynamic earthquake rupture with the coseismic off-fault damage along natural fault networks. We firstly modeled the dynamic earthquake rupture with the coseismic off-fault damage on a single planar fault. We showed the mechanism of dynamically generated off-fault fracture networks, the decrease in rupture velocity and the enhancement of high-frequency radiation in near-field ground motion. The overall energy budget is modified due to the additional radiation, and dissipation of the energy, associated with the secondary off-fault cracks. We then conducted a dynamic earthquake rupture modeling on the 2016 Kaikōura earthquake, which shows a great potential to narrow down a subset of hypothetical rupture scenarios by comparing the displacement field perturbed by the coseismic off-fault damage with the observations. Overall, this work has opened an avenue to model the dynamic earthquake ruptures with the continuum-discontinuum approach framework, which elucidates the effect of coseismic off-fault damage on the earthquake rupture dynamics and has shown the potential of further applications to natural fault systems.

1. Introduction

Earthquakes are explained as sudden release of energy along faults, which is accumulated in the Earth's crust over the years (*Scholz*, 1998). A part of the released energy is consumed to break the material on and off the fault, while the other part is converted to kinetic energy, which is radiated as seismic waves, and heat (*Sibson*, 1977). The dynamic slip, or opening, of discontinuities causes the destructive earthquakes with perceptible seismic waves. Slow or quasi-static deformation, with imperceptible radiation, is classified as slow earthquakes (e.g. *Obara*, 2002; *Ide et al.*, 2007) or the creep (e.g. *Rogers and Nason*, 1971). In the following discussions, the term "earthquake" indicates the dynamic earthquake events with significant radiation.

At the present day, slip on fault is recognized as a common mechanism of earthquakes. However, it has a long history before it was widely accepted. The initial motion of P wave has been of interest to explain the earthquake source mechanics since the early 20th century (*Omori*, 1912). *Ishimoto* (1932) showed the distribution of initial motion of P wave, which can be now explained by the double couple earthquake focal mechanism (Figure 1.1). There was also a great debate over whether the force equivalent problem associated with dislocations on the discontinuity could be explained by single couple or double couple model. Historically, *Steketee* (1958) first derived the static displacement field caused by the dislocations, which leads to the double couple model. *Maruyama* (1963) and *Burridge and Knopoff* (1964) then pointed out that the double couple is an exact equivalent body force, which was subsequently reformulated with seismic moment tensor (*Kostrov*, 1974; *Backus and Mulcahy*, 1976a,b).

Field observations of fault outcrop has brought us the representative fault model, where the localized shear band that consists of cataclasite is surrounded by damaged host rock (Figure 1.2). It is thus assumed that the fault zone is well-localized (*Rattez et al.*, 2018), even in depth, and slip occurs on the pre-existing faults (*Scholz*, 1998). From the discussion above, we deduce that the earthquake is caused by the localized slip on the pre-existing faults, i.e., dynamic earthquake ruptures, which converts a part of the strain energy accumulated in the medium to the seismic wave and the other energy components.

We then need to discuss the transition from stable (during interseismic period) to unstable (earthquakes) state of earthquake rupture processes, where the energy is stably accumulated during the stable loading and is released at critical point due to the dynamic slip on the fault (*Ohnaka*, 2003). The time scale is usually years for stable loading, and seconds to minutes for unstable release. *Brace and Byerlee* (1966) demonstrated the cycle of this stable-to-unstable state, called stick-slip, in laboratory experiments as an analogy with natural earthquakes. Then this stick-slip behavior of the fault was modeled by spe-

cific friction laws applied on the fault surfaces. The major friction laws are generally classified into the slip-dependent and the rate-dependent friction laws. Slip-weakening law was proposed by *Ida* (1972) and *Palmer and Rice* (1973), who model the weakening of frictional resistance due to the lubrication, and thus the slip is unstably accelerated when the friction reaches its peak strength. This slip-weakening friction law has been widely used for the dynamic earthquake rupture modeling because of the simplicity of its formulation (e.g. *Andrews*, 1976, 1985; *Dalguer et al.*, 2003; *Aochi et al.*, 2000). It can model a single stick-slip event by artificially nucleating rupture, which spontaneously propagates on pre-existing faults.

Rate and state friction law was proposed by *Dieterich* (1978, 1979a,b) based on a series of experiments. This law represents the frictional change as a function of slip velocity, and a history dependent valuable. *Rice and Ruina* (1983) and *Ruina* (1983) demonstrated the potential of the rate and state friction law to model the periodic stick-slip instability, which subsequently has a great potential of modeling the periodic sequence of earthquake events (e.g. *Tse and Rice*, 1986; *Rice*, 1993; *Rice and Ben-Zion*, 1996; *Lapusta et al.*, 2000; *Lapusta and Rice*, 2003; *Kaneko et al.*, 2011; *Thomas et al.*, 2014; *Romanet et al.*, 2018). Therefore, the mechanism of triggering dynamic earthquake ruptures on the fault can be explained by the frictional instability, modeled by these friction laws.

As mentioned above, the dynamic earthquake rupture is triggered when the shear traction on the fault reaches the peak strength of friction. Thus the stress state in the medium plays an important role to analyze the nucleation of ruptures. *Okada* (1985) and *Okada* (1992) derived a set of formulations, which gives the theoretical solutions of surface and internal deformations in half-space from the slip distribution on the pre-existing faults. It has been used to estimate the stress change after main earthquake events, and to analyze the sequence of aftershocks (e.g. *King et al.*, 1994; *Stein*, 1999; *Cocco and Rice*, 2002).

Mohr-Coulomb yield criterion is a common failure criterion, proposed by *Coulomb* (1773), where the peak strength of shear traction, τ^p, is given by

$$\tau^p = c + f_s(\sigma_n - p), \tag{1.1}$$

where c is the cohesion, f_s is the static friction coefficient, σ_n is the normal stress on the fault and p is the pore fluid pressure in the fault zone (see also *Beeler et al.* (2000)). Then the Coulomb failure stress change, $\Delta\sigma_f$, is defined as following

$$\Delta\sigma_f = \Delta\tau + f_s(\Delta\sigma_n + \Delta p), \tag{1.2}$$

where $\Delta\tau$ is the shear traction change on the fault, $\Delta\sigma_n$ is the normal stress change and Δp is the pore pressure change (*Stein*, 1999). Thus the increase in $\Delta\sigma_f$ simply indicates that the failure is more likely to occur.

Figure 1.3 shows an example of a distribution of Coulomb failure stress change associated with the 1992 Landers, Big Bear, and Joshua Tree earthquakes. The location of aftershocks after Landers main shock occurred is superimposed on the Coulomb failure stress change. It shows a significant correlation between stress changes and aftershocks, which implies that the earthquake ruptures are fairly characterized by the Mohr-Coulomb yield criterion. It also highlights that the geometrical complexity of the faults plays a crucial role in the stress changes, and the subsequent aftershocks.

While the static analysis of the rupture nucleation using Coulomb failure stress change has been attempted, the dynamics of earthquake ruptures has been also studied by theoretical and numerical approaches. *Kostrov* (1974), *Rice* (1980) and *Freund* (1990) systematically documented the dynamic fracture mechanics of earthquakes, which are the basis of the other analysis of dynamic ruptures. *Madariaga* (1976) proposed the circular fault model, which developed theoretical solutions of dynamic circular crack and the associated radiation. The numerical modeling of spontaneous dynamic earthquake rupture was pioneered by *Andrews* (1976), which demonstrated the evolution of accumulated slip and slip velocity associated with the dynamic rupture propagation with finite difference method (FDM). Subsequently, many studies have been conducted in the FDM framework to better understand the dynamic processes of spontaneous earthquake ruptures (e.g. *Day*, 1982; *Okubo*, 1989; *Harris et al*., 1991; *Andrews*, 1999; *Yamashita*, 2000; *Andrews*, 2005). The dynamic photoelasticity in laboratory experiments has also elucidated the stress field during the dynamic rupture propagation. (e.g. *Rosakis et al*., 1999, 2006).

As the research on the earthquake ruptures has been progressed, the importance of geometrical complexity has come to the light. Many studies have pointed out the role of geometrical complexity in the rupture dynamics (e.g. *Segall and Pollard*, 1980; *King and Nábělek*, 1985; *Sibson*, 1985; *Bhat*, 2007; *Wei et al*., 2011; *Kobayashi et al*., 2017; *Hamling et al*., 2017). Here, let us extend the terminology of the "geometrical complexity" for the coseismic off-fault damage as it is formed by an aggregation of smaller scale fracture network. Based on this interpretation, we illustrate a schematic of hierarchical structure of a fault system in a wide range of length scales (Figure 1.4), where the fault network consists of macroscopic (in kilometric scale), mesoscopic (in metric) and microscopic (in micrometric) geometrical complexities. As all these geometrical complexities should be taken into account for the dynamic earthquake rupture modeling, it is no doubt important to investigate the effect of coseismic off-fault damage.

The effect of coseismic off-fault damage has been widely studied by theoretical analysis (e.g. *Poliakov et al*., 2002; *Rice et al*., 2005; *Ngo et al*., 2012), field observations (e.g. *Manighetti et al*., 2001, 2004; *Mitchell and Faulkner*, 2009, 2012; *Rempe et al*., 2013; *Perrin et al*., 2016a), and numerical approaches (e.g. *Andrews*, 2005; *Ben-Zion and Shi*, 2005; *Dunham et al*., 2011a,b; *Xu et al*., 2012a,b; *Bhat et al*., 2012; *Ma and Hirakawa*, 2013; *Cappa et al*., 2014; *Xu et al*., 2015; *Thomas and Bhat*, 2018). Theoretical analysis illustrated the potential failure area and the orientation of secondary tensile and shear cracks caused by the stress concentration around the tip of crack based on dynamic fracture mechanics (*Poliakov et al*., 2002; *Rice et al*., 2005; *Ngo et al*., 2012). The field observations have demonstrated the existence of off-fault damage, and its implications for the elastic modulus, permeability and the accumulated slip (e.g. *Manighetti et al*., 2001; *Mitchell and Faulkner*, 2012; *Rempe et al*., 2013; *Cappa et al*., 2014). *Mitchell and Faulkner* (2009) showed the distribution of microfracture density in the damage zone around a fault core from field observations, which exponentially decreases with distance from the fault. *Thomas and Bhat* (2018) then reproduced this characteristic damage pattern by dynamic earthquake rupture modeling with coseismic off-fault damage using homogenized constitutive laws. They also demonstrated the oscillation of slip velocity and enhanced high-frequency radiation due to damage. The experimental results have also addressed the

implications of coseismic off-fault damage for rupture dynamics and radiation (e.g. *Passelègue et al.*, 2016).

However, an important, and intuitive, physical phenomenon remains to be incorporated into the model formulations: the dynamic activation of secondary off-fault cracks. The previous models involve only prescribed faults in the medium due to limitations of model formulations, and thereby the effect of coseismic off-fault damage is homogenized by constitutive formulations. Thus, the dynamic generation/activation of such secondary off-fault fracture network, and its implications for rupture dynamics, is poorly understood. This problem brings us to the motivation of the present thesis.

Let us list questions to be addressed in this thesis:

1. How is the secondary off-fault fracture network, where the length scale is much smaller than the main faults, activated by the dynamic earthquake ruptures on prescribed faults?

2. What is the effect of the feedback from secondary off-fault fracture network on the main rupture?

3. Is the overall energy budget modified by the activation of secondary off-fault fracture network, as a part of energy is dissipated by the secondary cracks?

4. How does the coseismic off-fault damage evolve in the natural fault system?

5. Is the modeled coseismic off-fault damage comparable to the observations?

To address these questions, we developed a continuum-discontinnuum approach framework with the combined finite-discrete element method (FDEM) (*Munjiza*, 2004; *Munjiza et al.*, 2011, 2015), which allows for dynamic earthquake rupture modeling on the prescribed faults with spontaneous activation of secondary off-fault fracture network. The aim of Chapter 2 and 3 is to address the questions 1, 2, and 3 listed above. We firstly describe systematic model formulations of a continuum-discontinnuum approach framework. We then model dynamic earthquake ruptures with coseismic off-fault fracture network, and its implications for the rupture dynamics, the radiations and the overall energy budget.

Then the aim of Chapter 4 is to address the rest of questions. To demonstrate the application for the natural fault system, we conducted the dynamic earthquake rupture modeling associated with the 2016 Kaikōura earthquake. We traced the main fault geometry around the Jordan-Kekerengu-Papatea triple junction from the surface rupture map. We then examined hypothetical earthquake rupture scenarios to investigate the rupture dynamics and the coseismic damage pattern associated with each scenario. We compared the displacement profiles across the faults to the observational results obtained by the optical image correlations. It clearly shows a correlation with certain scenario, and thus demonstrates a great potential to narrow dawn a subset of possible rupture scenarios.

In Chapter 5, we discuss the preliminary results from modeling first-order geometrical complexities, such as kinks, roughness and stepovers, as well as thrust earthquakes. These results show the potential for fundamental analyses of these geometrical complexities though a limited number of simulations have been conducted so far.

Overall, in this thesis, we attempt to elucidate the effect of dynamically activated secondary fracture network around the faults as the multiscale geometrical complexity must play an important role in the earthquake rupture dynamics. The continuum-discontinuum approach framework with the FDEM allows for modeling the dynamic earthquake ruptures with the dynamic activation of the coseismic off-fault fracture network, which provides better understanding of the proposed questions.

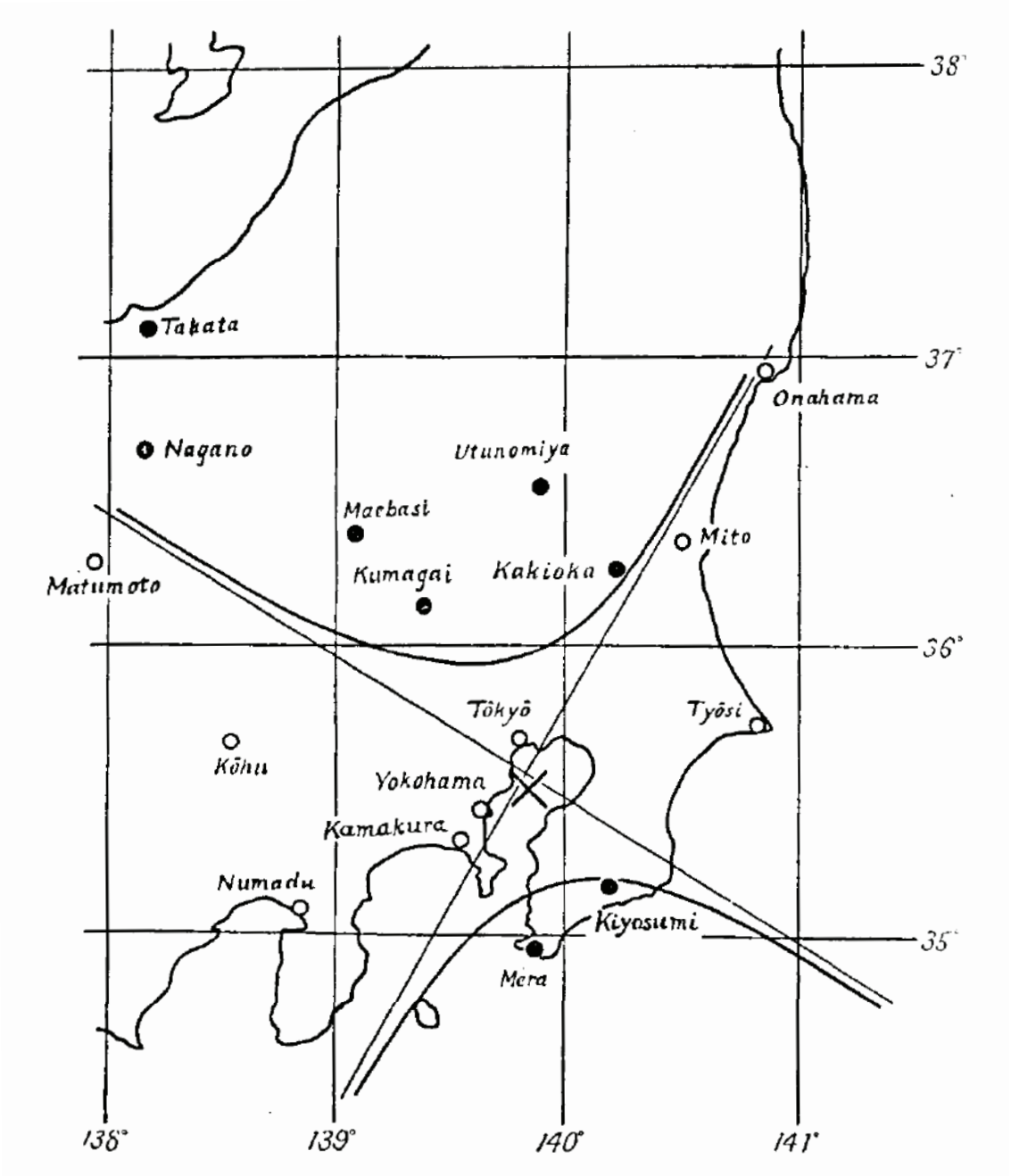

Figure 1.1: Distribution of the initial motion of P wave for an earthquake event on August 3rd, 1926 in the Kanto region, Japan. Filled circles indicate compressive motion, while unfilled circles indicate extensional motion. The cross mark indicates epicenter. Reprinted from *Ishimoto* (1932).

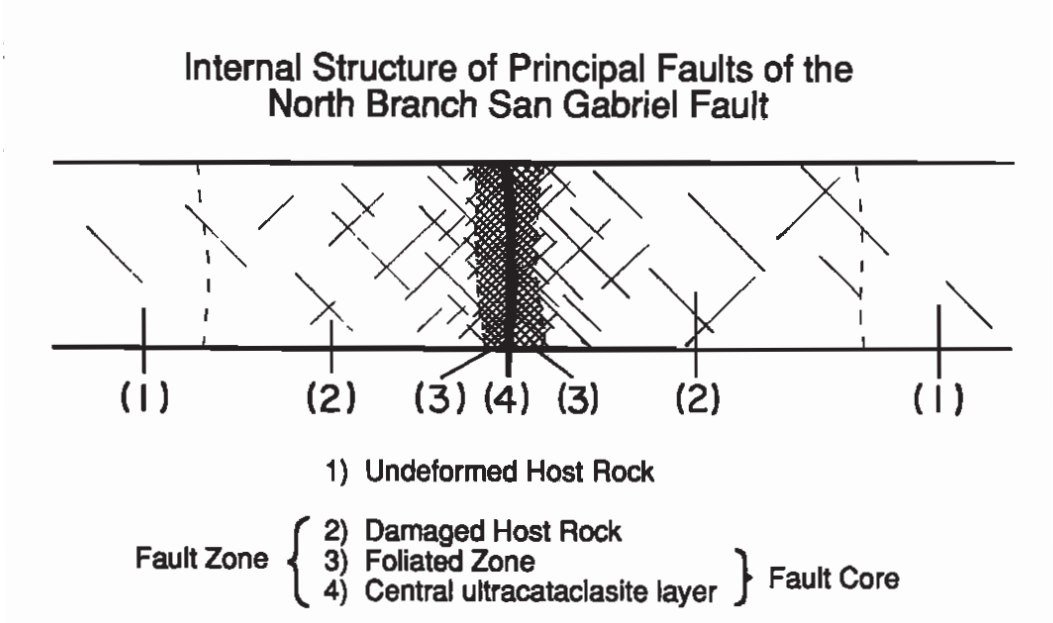

Figure 1.2: Schematic of the internal structure of a simple fault zone. Reprinted from *Chester et al*. (1993).

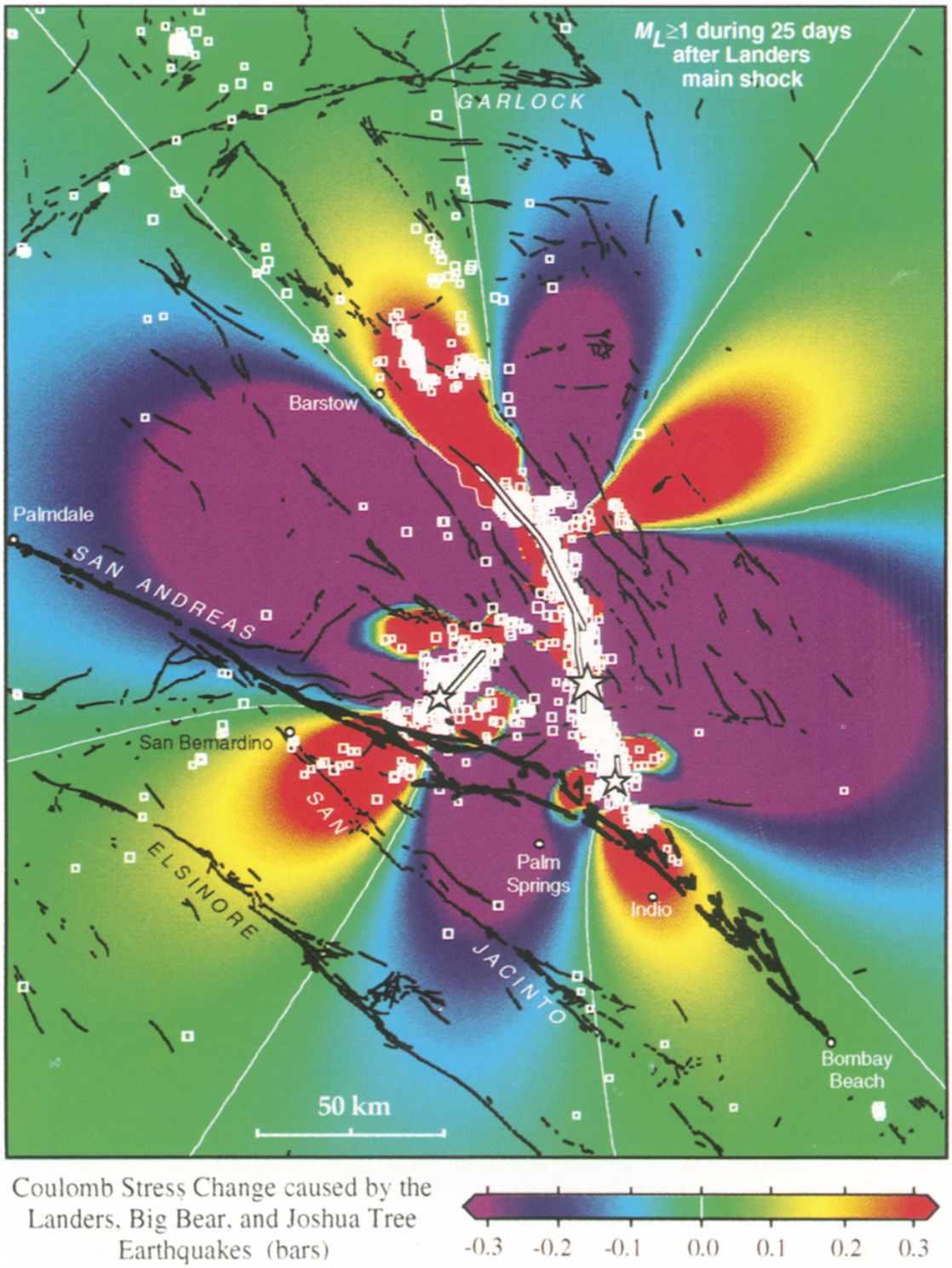

Figure 1.3: Coulomb failure stress change at a depth of 6.25 km caused by the 1992 Landers, Big Bear, and Joshua Tree earthquakes, and the location of aftershocks. Reprinted from *King et al.* (1994)

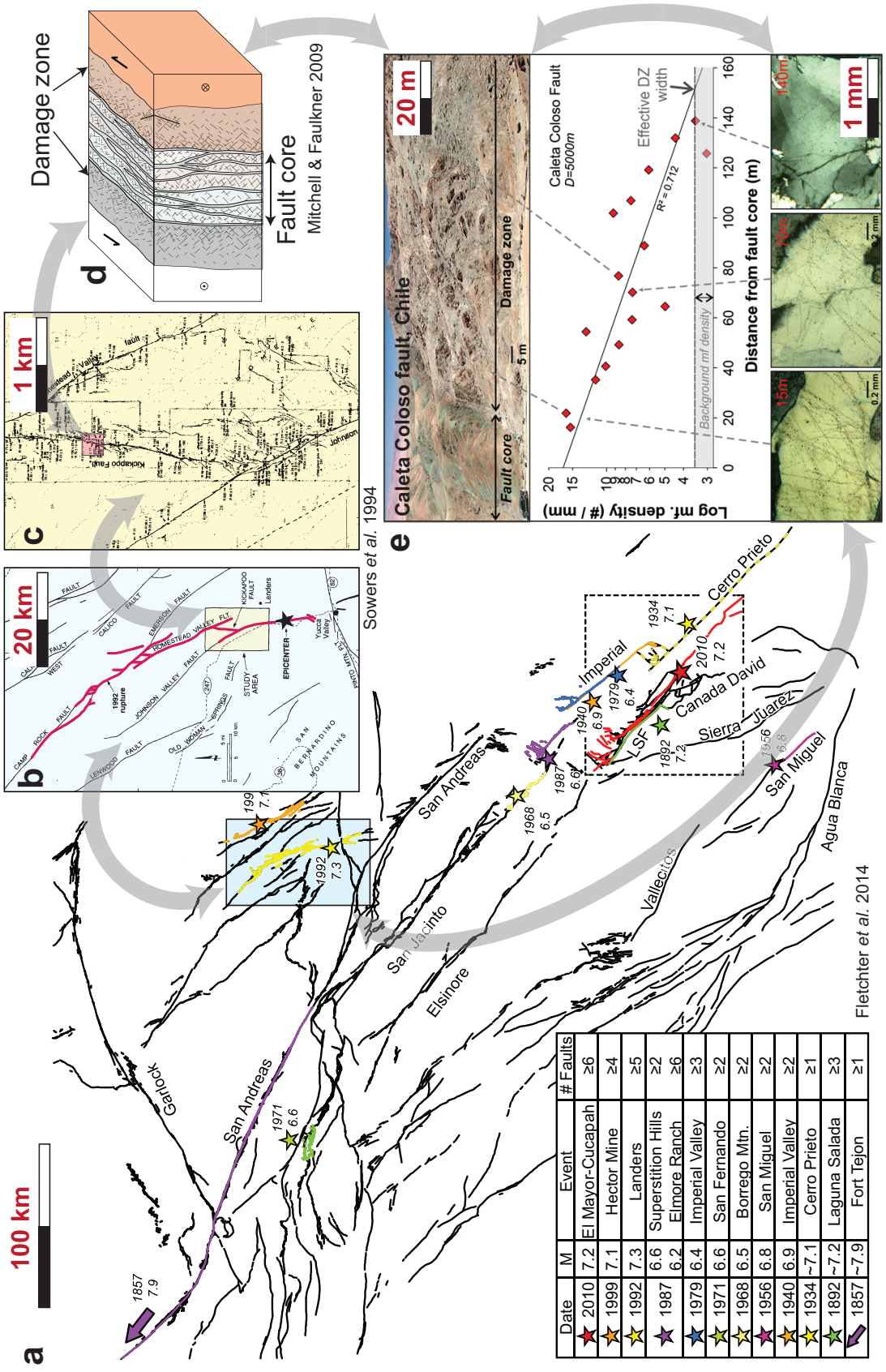

Date	M	Event	# Faults
2010	7.2	El Mayor-Cucapah	≥6
1999	7.1	Hector Mine	≥4
1992	7.3	Landers	≥5
1987	6.6	Superstition Hills	≥2
	6.2	Elmore Ranch	≥6
1979	6.4	Imperial Valley	≥3
1971	6.6	San Fernando	≥2
1968	6.5	Borrego Mtn.	≥2
1956	6.8	San Miguel	≥2
1940	6.9	Imperial Valley	≥2
1934	~7.1	Cerro Prieto	≥1
1892	~7.2	Laguna Salada	≥3
1857	~7.9	Fort Tejon	≥1

Figure 1.4: (Continued on the following page.)

Figure 1.4: Hierarchical structure of fault systems in a wide range of length scales. Each inset shows a part of a fault system at different length scales. (a) Fault map of the Big Bend domain or the central domain of the Pacific-North American Plate Boundary (*Fletcher et al*., 2014). Black and color lines indicate the fault trace and historic ruptures, respectively. (b) Fault traces (in black) and the rupture trace (in red) of the 1992 Landers earthquake (*Sowers et al*., 1994). (c) Fault trace around the Kickapoo fault (*Sowers et al*., 1994). (d) Schematic of strike-slip fault zone structure, showing multiple fault cores surrounded by damage zones (*Mitchell and Faulkner*, 2009). (e) The variation in microfracture density within a fault damage zone as a function of distance from fault core (*Mitchell and Faulkner*, 2012).

2. Continuum-discontinuum approach framework for modeling dynamic earthquake ruptures

Avant-propos

Il ait aujourd'hui notoirement reconnu que l'endommagement cosismique, autour des failles majeures, est un facteur clé dans la compréhension des mécanismes de rupture dynamique et dans le calcul du bilan énergétique lié aux tremblements de terre (e.g. *Faulkner et al.*, 2011; *Thomas and Bhat*, 2018). En effet, les séismes altèrent la réponse mécanique du milieu en générant ou réactivant des fractures secondaires autour des failles (e.g. *Manighetti et al.*, 2004; *Mitchell and Faulkner*, 2009). L'endommagement modifie les propriétés élastiques (e.g. *Faulkner et al.*, 2006), ce qui impacte en retour la rupture, le rayonnement sismique et le mouvement du sol proche de la faille. *Sibson* (1977) a proposé un model conceptuel pour le calcul du bilan énergétique lors des tremblements de terre. Dans ce modèle, l'hypothèse est fait qu'une partie de l'énergie, accumulée au cours de la période intersismique, est convertie en ondes sismiques, alors que le reste est dissipé par fracturation dans la zone de la faille. Les contributions de l'endommagement cosismique au bilan énergétique est donc primordiale pour l'étude des ondes sismiques émises pendant les tremblements de terre. Cependant, les techniques numériques existantes ne permettaient pas de modéliser la génération dynamique de fractures secondaires en tension et/ou de cisaillement (Mode I and Mode II) ; essentiellement en raison des limites numériques et de formulation du problème. Ainsi, dans ce chapitre, nous présentons le modèle développé qui permet la création et l'activation d'un système de fractures secondaire pendant la rupture sismique. Le modèle allie la modélisation des milieux continus et discontinus, en utilisant la méthode combinée des éléments finis et discrets (FDEM). Dans ces chapitres 2 et 3 sont développés : les mécanismes de génération d'un réseau de fractures secondaires, le changement de vitesse de rupture associé, et les radiations haute fréquences générées par l'endommagement cosismique. Nous détaillons ensuite le bilan énergétique lié à la rupture dynamique. Ce dernier suggère une diminution de l'efficacité sismique si on considère l'équilibre énergétique entre les radiations additionnelles et la dissipation de l'énergie de fracture dans le réseau de fractures secondaires. Les résultats numériques tels que l'optimisation du temps de calcul, l'impact de la résolution et l'implémentation du model sont résumés en annexes.

2.1 Introduction

Coseismic off-fault damage has been recognized as a key factor towards understanding dynamic earthquake rupture mechanisms and the associated overall energy budget. *Sibson* (1977) conceptually proposed a formulation for the overall energy budget of dynamic earthquake ruptures; a part of the energy released from accumulated strain energy by interseismic deformation is converted to seismic wave radiation, whereas the rest is expended in inelastic deformation processes within fault zone. His study is recognized as the first attempt to describe the partition of energy associated with localized active fault ruptures. *Wallace and Morris* (1986) characterized the structure of fault zones from the observation of deep mines in North America, in which fault cores are surrounded by fractured rock. Based on field observations of San Gabriel and Punchbowl faults in southern California, *Chester et al*. (1993) also proposed similar fault zone structures, where the fault core is surrounded by a much thicker zone of damaged host rock. Field measurements of microfracture density as a function of distance in fault-normal direction at various scales have also been conducted in order to understand the spatial distribution and geometric characteristics of off-fault damage zones (*Shipton and Cowie*, 2001; *Mitchell and Faulkner*, 2009; *Faulkner et al*., 2011; *Savage and Brodsky*, 2011). These analyses showed that microfracture density is significantly higher close to the fault and exponentially decreases with distance from the fault core (*Mitchell and Faulkner*, 2009), evidencing the presence of the off-fault damage.

Indeed, off-fault damage does not comprise only microscopic fractures concentrated within fault cores, but also mesoscopic geometrical complexities of fault systems (*Ando and Yamashita*, 2007; *Perrin et al*., 2016a), such as fault branches and step-overs. In this sense, fault zones involve features ranging from well-localized fault cores filled by cataclasites to mesoscopic secondary fractures, all of which should be taken into account for the overall energy budget of earthquake ruptures. Mesoscopic off-fault damage also results in the change of the characteristics of deformation on the main fault (*Manighetti et al*., 2004; *Cappa et al*., 2014).

In summary, Figure 1.4 illustrates the schematic of a hierarchical fault structure in multi length scales ranging from microfractures to the global fault system. All these geometrical complexities of fractures play a role in the energy balance during the earthquakes. Thus, the modeling of off-fault damage dynamically induced by earthquake ruptures is crucial to understand realistic faulting processes, radiation and the energy balance of earthquakes.

To investigate the mechanisms of secondary cracks dynamically induced by rupture propagation, numerous studies have been performed via theoretical approaches, experimental investigations and numerical modeling. *Poliakov et al*. (2002) and *Rice et al*. (2005) showed the potential failure area around rupture front with steady-state cracks based on a theoretical formulation. The numerical modeling for spontaneous ruptures with off-fault damage has been also conducted to demonstrate the evolution of coseismic off-fault damage induced by dynamic ruptures and its implication for rupture dynamics (*Yamashita*, 2000; *Dalguer et al*., 2003; *Andrews*, 2005; *Ben-Zion and Shi*, 2005; *Ando and Yamashita*, 2007; *Templeton and Rice*, 2008; *Viesca et al*., 2008; *Ma and Andrews*, 2010;

Dunham et al., 2011a; *Bhat et al.*, 2012; *Gabriel et al.*, 2013; *Thomas and Bhat*, 2018). They revealed that the complicated feedback from the off-fault damage has a significant effect on the dynamic rupture itself and its consequent radiation patterns. Furthermore, what is of interest here is the enhanced high-frequency radiation in the near-fault ground motion (*Hanks*, 1982; *Castro and Ben-Zion*, 2013; *Passelègue et al.*, 2016; *Thomas and Bhat*, 2018), which is of practical importance for earthquake engineering (*Aki*, 1987).

Although previous studies have addressed the effect of coseismic off-fault damage on earthquake dynamics, up to now state-of-the-art numerical techniques used for earthquake rupture modeling were not able to describe off-fault fracture processes as actual tensile and shear (Mode I and Mode II) cracks mainly due to limitations of computation and model formulation. Hence the role of secondary off-fault fracture networks formed by the coalescence of secondary cracks in the rupture dynamics, the radiation and the overall energy budget remains to be fully understood. Therefore, our aim in this paper is to model the activation of secondary off-fault fracture networks dynamically activated by earthquake ruptures using a novel numerical tool based on the combined finite-discrete element method (FDEM) that allows us to quantify its contribution to rupture dynamics, radiations and energetics of earthquakes.

We demonstrate that FDEM performs well in modeling dynamic earthquake ruptures with dynamically activated secondary fracture networks in the off-fault medium. The strength of the off-fault medium is governed by prescribed cohesion and friction laws, which allow for both tensile and shear cracks to be formed. In this paper, we firstly present a cross-validation analysis of FDEM, for its application to earthquake rupture modeling. We then highlight the secondary fracturing mechanisms activated in the off-fault medium which are induced by earthquake ruptures and the consequent high-frequency radiation generated by the secondary off-fault cracks. We finally investigate the evolution of the damage zone size with depth by a systematic case study and discuss the energy contributions of off-fault damage to the overall energy budget. This analysis clearly demonstrates the non-negligible contribution of off-fault damage to the earthquake rupture dynamics.

2.2 Continuum-discontinuum approach for dynamic earthquake rupture modeling

Geological faults can be defined as discontinuities in a continuum medium, where the deformation can be described by appropriate constitutive law. From this perspective, we consider both the faults and the off-fault damage in the same framework as an aggregation of fractures at different length scales. The activation of new fractures in the medium is represented as the loss of cohesive resistance. Frictional processes then take place at the boundary of the fracture surfaces, and they have a significant contribution in the overall energy budget of earthquakes. Therefore, we need a modeling scheme able to handle both continuum (deformation) as well as discontinuum processes (fractures) within the same framework. This model requires an efficient contact algorithm to compute contact, cohesive and frictional forces, operating on every fracture surface and potential failure planes. In this study, we use the combined Finite-Discrete Element Method (FDEM) (*Munjiza*

et al., 1995) as the first-of-its-kind application to dynamic earthquake rupture modeling. Here, we firstly describe the fundamentals of FDEM and then show the model description of the dynamic earthquake rupture simulations with coseismic off-fault damage.

2.2.1 Formulation of FDEM

The application of FDEM, pioneered by *Munjiza et al*. (1995), has been expanded in the last couple of decades to solve broad scientific problems associated with fracturing and failure of solid media such as block caving, rock blasting, dam stability, rock slope stability and hydraulic fracturing (e.g. *Mahabadi et al*., 2014; *Lisjak et al*., 2014; *Lei et al*., 2014; *Zhao et al*., 2014; *Lei and Ke*, 2018). In the FDEM framework, a solid medium is firstly discretized into finite elements, in which the deformation is governed by stress-strain constitutive laws as in the conventional finite element method (FEM). The interaction among individual elements is then computed based of prescribed cohesion and friction laws. The governing equation follows the dynamic equilibrium given by

$$\mathbf{Kx} + \mathbf{M}\ddot{\mathbf{x}} + \mathbf{C}\dot{\mathbf{x}} = \mathbf{b}, \tag{2.1}$$

where $\mathbf{x}$ is the vector of nodal displacements, $\dot{\mathbf{x}}$ and $\ddot{\mathbf{x}}$ are the first and second time derivatives of displacements, indicating the vector of velocity and acceleration respectively, $\mathbf{K}$ is the stiffness matrix, $\mathbf{M}$ is a diagonal mass matrix, $\mathbf{C}$ is a damping matrix and $\mathbf{b}$ is an external static loading (*Munjiza et al*., 2015, eq. 3.41). $\mathbf{Kx}$ represents the equivalent internal forces in the system. The external loading is caused by prescribed boundary conditions or by contact interactions between discretized finite elements. In the FDEM framework, the interaction is evaluated between any couple of elements, called contactor and target, illustrated in Figure 2.1 (*Lei et al*., 2014). To enhance the computational efficiency, the contact detection algorithm plays a key role to efficiently determine the location of intersections between contactor and target, and compute the cohesion and the friction applied on the interface. We thus employed MRCK (Munjiza-Rougier-Carney-Knight) contact detection algorithm (*Lei et al*., 2014). In essence, it makes use of the concept of temporal coherence that the position of elements does not change so much at two consecutive time intervals that the initial mapping of elements to detect contacts can be used without large modification during simulations, especially suitable for our problem with small strain assumption.

The penalty function method is widely used in FDEM framework (e.g. *Munjiza et al*., 1999; *Rougier et al*., 2011; *Lisjak et al*., 2013; *Mahabadi et al*., 2014; *Lei et al*., 2014) to derive the magnitude and the orientation of contact force vector f_N when the target and contactor collide into each other. The schematic of the opening and slip displacements, $\delta_{I/II}$, and the contact force between contactor and target are also illustrated in Figure 2.1. The contactor is allowed a small penetration into target to evaluate the contact force. f_N is then determined by

$$f_N \propto p^p P_G, \tag{2.2}$$

where P_G is the potential accounting for the penetration of contactor into target, p^p is a penalty term, which decides the local error in displacements (*Munjiza*, 2004; *Munjiza et al*., 2011). The number of integral points per edge (e.g. two points per edge for the case

in Figure 2.1) is chosen a priori, which also has an effect of integration error of f_N. Note that the cohesion and friction are added to the external loading separately from the contact force f_N derived from the penalty function.

Viscous damping is often applied to suppress artificial numerical errors. One of the terms is called Munjiza Viscosity developed by *Munjiza et al*. (2015), which is essentially strain rate-dependent viscous damping. The relationship between Munjiza viscosity and the canonical dynamic viscosity, η (Pa $\cdot$ s), is derived as

$$\eta = \frac{1}{2}\check{M}_\alpha = \frac{1}{2}\check{M}_\beta = \check{M}_\psi, \tag{2.3}$$

where $\check{M}_\alpha$, $\check{M}_\beta$ and $\check{M}_\psi$ are Munjiza viscosity (Pa $\cdot$ s) defined by *Munjiza et al*. (2015, eq. 17.133). In this study, we utilized the FDEM-based software tool, HOSSedu (Hybrid Optimization Software Suite - Educational Version), developed by Los Alamos National Laboratory (LANL) (*Knight et al*., 2015). More details of main algorithmic solutions used within HOSSedu can be found in a series of monographs (*Munjiza*, 2004; *Munjiza et al*., 2011, 2015). The computational efficiency for earthquake rupture modeling with the FDEM is discussed in Appendix A.

2.3 Model description

In this section we describe the prestress condition and failure criteria used for dynamic earthquake rupture modeling with coseismic off-fault damage. The sign convention used in this work considers that tensile stresses and clockwise rotations are positive as shown in Figure 2.2. The symbols used in the following sections are summarized in the list of symbols.

2.3.1 Initial stress state in depth

We follow a similar process to that proposed by *Templeton and Rice* (2008) and *Xu et al*. (2012a) to make an assumption of initial stress state as a function of depth. For the sake of simplicity, we assume the prestress state linearly increases in depth based on the lithostatic and the hydrostatic conditions without any consideration of actual prestress state, which is generally nonlinear in depth (e.g. *Zoback and Healy*, 1992). A main fault plane is set parallel to the depth direction z while the xy - plane is perpendicular to z. The x-axis is aligned with the main fault and the origin of the x-y coordinate system is located in the middle of the main fault. The initial stress state is set for triggering a right-lateral strike-slip on the main fault. We solve this problem assuming plane strain conditions. The initial stress state is initially uniform in the homogeneous and isotropic elastic medium, and is given by

$$\sigma_{ij}^0 = \begin{bmatrix} \sigma_{xx}^0 & \sigma_{yx}^0 \\ \sigma_{yx}^0 & \sigma_{yy}^0 \end{bmatrix}. \tag{2.4}$$

Let normal stress σ_{yy}^0 on the main fault be given by linear overburden effective stress gradient such that

$$\sigma_{yy}^0 = -(\rho - \rho_w)gz, \tag{2.5}$$

where ρ is the density of rock, ρ_w is the density of water, g is the gravitational acceleration and z is the depth measured from the ground surface. The initial shear stress σ^0_{yx} is estimated in terms of the seismic S ratio, defined by *Andrews* (1976), on the main fault such as

$$S = \frac{f_s(-\sigma^0_{yy}) - \sigma^0_{yx}}{\sigma^0_{yx} - f_d(-\sigma^0_{yy})}, \tag{2.6}$$

where f_s and f_d are the static and dynamic friction coefficients respectively. The value of the S ratio defines whether the rupture velocity is supershear ($S < 1.77$), or remains sub-Rayleigh ($S > 1.77$) in 2-D. Thus the initial shear stress on the main fault can be written as

$$\sigma^0_{yx} = \frac{f_s + S f_d}{1 + S}(-\sigma^0_{yy}). \tag{2.7}$$

The horizontal compressive stress σ^0_{xx} is then determined by the normal stress σ^0_{yy}, shear stress σ^0_{yx} and the given orientation of the initial compressive principal stress to the main fault ψ (indicated in Figure 2.2b) as follows:

$$\sigma^0_{xx} = \left(1 - \frac{2\sigma^0_{yx}}{\tan(2\psi)\sigma^0_{yy}}\right)\sigma^0_{yy}. \tag{2.8}$$

The relationship of the magnitude of σ^0_{xx} and σ^0_{yy} depends on ψ in the following manner:

$$\begin{cases} (-\sigma^0_{xx}) \geq (-\sigma^0_{yy}), & 0 < \psi \leq \pi/4 \\ (-\sigma^0_{xx}) < (-\sigma^0_{yy}), & \pi/4 < \psi < \pi/2 \end{cases} \tag{2.9}$$

which is consistent with the condition of initial stress state defined by *Poliakov et al.* (2002) and *Rice et al.* (2005).

2.3.2 Failure criteria

In the FDEM framework, cracks are represented as the loss of cohesion at the interfaces of the finite elements in the model. The combined single and smeared discrete crack approach (*Munjiza et al.*, 1999) is generally accepted as a crack model based on fracture energy, where the cohesion and friction are prescribed following actual representations of experimental stress-strain curves (*Lei et al.*, 2014). It is worth noting that the cohesion and the friction against the opening or sliding motion between contactor and target are a function of displacements defined by the aperture δ_I and the slip δ_{II} between the contactor and the target.

The cohesive and frictional resistances are applied on every interface between elements (i.e. at every edge), which is regarded as a potential failure plane. Both cohesion and friction curves are divided into two parts, an elastic loading part and a displacement-weakening part as shown in Figure 2.3. In the elastic loading part, the resistant forces against displacements acting on the interface increase quadratically (for the case of cohesion) or linearly (for the case of friction) with the stiffness of the elastic loading portions being p^c, p^f respectively. Since this elastic loading part ideally should be zero to represent the material continuity, the stiffnesses, p^c and p^f, are chosen to be much higher than

the Young's modulus of the material E in order to minimize the displacements associated with the elastic loading. In this study, we chose $p^c = 1000E$, and p^f is chosen in the same order of p^c as described in the following section. When the applied traction on the interface reaches the peak tensile or shear cohesion strengths $C^p_{I/II}$, the connection starts to be weakened, and eventually it loses the cohesion (Figure 2.3b). When the shear traction reaches to frictional strength τ_p, it decreases down to the residual strength at critical displacements D_c as shown in Figure 2.3c. The friction curve follows the linear slip-weakening law, originally proposed by *Ida* (1972) and *Palmer and Rice* (1973), which has been widely used for dynamic earthquake rupture modeling (e.g. *Andrews*, 1976; *Aochi and Fukuyama*, 2002; *De La Puente et al*., 2009). Eventually, the shear strength is represented by Mohr-Coulomb failure criteria. Note that the friction law is operating both on the main fault and the secondary cracks activated in the off-fault medium.

The mixed mode fracture is evaluated by a damage parameter, D, which is defined as

$$D_i = \frac{\delta_i - \delta_i^{c,e}}{\delta_i^{c,c} - \delta_i^{c,e}} \quad i = I, II \tag{2.10}$$

$$D = \sqrt{D_I^2 + D_{II}^2}\ (0 \leq D \leq 1) \tag{2.11}$$

$$D^T = \frac{D_I}{D} = \left\{ \begin{array}{ll} 1, & \text{for purely tensile crack} \\ 0, & \text{for purely shear crack} \end{array} \right\}, \tag{2.12}$$

where D_i $(i = I, II)$ is the components of damage for tensile and shear crack, δ_i is the normal and the tangential displacement, $\delta_i^{c,e}$ is the initial critical displacement for elastic loading, $\delta_i^{c,c} - \delta_i^{c,e}$ is the maximum displacement during linear-softening where $\delta_i^{c,c}$ is the initial critical displacement for linear-weakening part, D is the degree of damage and D^T indicates the type of damage. Similar expressions can be found in *Rougier et al*. (2011) and *Lisjak et al*. (2014).

Since we employed a linear softening law, the fracture energies related with cohesion for tensile (mode I) and shear (mode II) (i.e., the energy required to completely break the connection of the contact) are evaluated as

$$G^c_{iC} = \frac{1}{2} C^p_i \left(\delta_i^{c,e} - \delta_i^{c,c}\right) \quad i = I, II \tag{2.13}$$

where G^c_{iC} is the tensile and the shear fracture energy and C^p_i is the tensile and the shear cohesive strength. The fracture energy for friction is, following *Palmer and Rice* (1973), described as

$$G^f_{IIC} = \frac{1}{2} D_c \left(\tau_p - \tau_r\right) \tag{2.14}$$

where G^f_{IIC} is the fracture energy for friction, $D_c = \delta^{f,c}_{II}$ is the critical slip distance for friction and τ_p and τ_r are the peak strength and the residual strength for friction, defined as

$$\tau_p = f_s(-\sigma_n) \tag{2.15}$$

$$\tau_r = f_d(-\sigma_n), \tag{2.16}$$

where f_s and f_d are the static and dynamic friction coefficients and σ_n is the normal stress on the contact surface. Note that the elastic loading part $\delta_i^{f,e}$ is much smaller than D_c, so that the representation of fracture energy G^f_{IIC} by equation (2.14) is acceptable even without the consideration of elastic loading part.

2.3.3 Closeness to failure

Here, we describe the parametrization of the failure criteria based on the fracture energy estimated from the experiments and observations (*Viesca and Garagash*, 2015; *Passelègue et al*., 2016), and the closeness to failure, proposed by *Templeton and Rice* (2008) and *Viesca et al*. (2008), which indicates the safety of the initial stress state to the failure of the material represented by the ratio of the radius of the Mohr's circle to the distance to the Mohr-Coulomb criteria. Let σ_1 and σ_2 be the maximum and minimum compressive principal stresses. Assume a Mohr-Coulomb friction criteria with shear peak strength C_{II}^p. Then the closeness to failure, d_{MC}, is derived from geometrical relationships such that

$$\begin{aligned} d_{MC} &= \frac{\sigma_2 - \sigma_1}{2C_{II}^p \cos\phi - (\sigma_1 + \sigma_2)} \\ &= \frac{\left(\frac{\sigma_1}{\sigma_2} - 1\right)}{\left(\frac{\sigma_1}{\sigma_2} + 1\right) - 2\left(\frac{C_{II}^p}{\sigma_2}\cos\phi\right)} \end{aligned} \tag{2.17}$$

where ϕ is the friction angle as $\tan\phi = f_s$ (Figure 2.4). Thus $d_{MC} < 1$ means no failure and $d_{MC} \geq 1$ implies the initiation of failure in shear on the corresponding plane. Note that d_{MC} locally changes due to perturbations of the stress field.

To make the medium equally close to failure, regardless of the stress state, d_{MC} is kept constant with depth. By assuming the constant angle of maximum compressive principal stress Ψ and the seismic ratio S, the ratio of principal stresses σ_1/σ_2 is derived to be constant with depth. Thus from equation (2.17), the ratio C_{II}^p/σ_2 has to be kept constant to obtain an equal closeness to failure with depth, implying that peak cohesion C_{II}^p must increase linearly in depth. Therefore we first calculate σ_{ij}^0 as described in previous section, and then we then derive C_{II}^p as follows

$$C_{II}^p = \frac{\sigma_2 - \sigma_1 + d_{MC}(\sigma_1 + \sigma_2)\sin\phi}{2d_{MC}\cos\phi}, \tag{2.18}$$

where d_{MC} should be chosen carefully to avoid C_{II}^p being negative. C_I^p is chosen from the experiments (*Cho et al*., 2003), and is kept constant with depth.

The dissipated fracture energy related with cohesion, $G_{IC/IIC}^c$, is defined by equations (2.13) and (2.14). An acceptable range for C_I^p is between 1-10 MPa extracted from experimental results, and kept constant with depth. C_{II}^p is calculated using equation (2.18) which varies in depth.

Let p^c be the stiffness of the elastic loading curve for cohesion. Then the tensile and the shear cohesion $C_i(\delta_i)$ $(i = I, II)$ in elastic loading part is described as quadratic function such as

$$C_i(\delta_i) = C_i^p \left[\frac{2\delta_i}{\delta_i^{c,e}} - \left(\frac{\delta_i}{\delta_i^{c,e}}\right)^2\right], \tag{2.19}$$

$$C_i^p = \frac{p_c}{2h}\delta_i^{c,e}, \tag{2.20}$$

where p_c is the penalty term for cohesion and h is the size of a particular finite element (*Munjiza et al.*, 1999, eq. (11)). Thus

$$\delta_i^{c,e} = \frac{2hC_i^p}{p_c}, \tag{2.21}$$

$\delta_i^{c,c}$ is then derived from equation (2.13) as

$$\delta_i^{c,c} = \frac{2G_{iC}^c}{C_i^p} + \delta_i^{c,e}. \tag{2.22}$$

Hence with given initial stress state σ_{ij}^0, closeness to failure d_{MC} and the fracture energy G_{iC}^c, we can determine the rest of parameters relevant to cohesion law in a consistent way.

In this study, the initial stress state is firstly determined as described in section 2.3.1. The closeness to failure is a priori chosen following previous studies (e.g. *Templeton and Rice*, 2008). The shear fracture energy G_{IIC}^c is approximated from observations and experiments (*Viesca and Garagash*, 2015; *Passelègue et al.*, 2016), and the tensile fracture energy is then assumed from the relationship between fracture energy and fracture toughness that is $G_{IC}/G_{IIC} = (K_{IC}/K_{IIC})^2$, where K_{IC}/K_{IIC} is estimated from the experimental results by *Rao et al.* (2003).

2.3.4 Friction law

When the amount of slip exceeds the elastic slip distance for cohesion $\delta_{II}^{c,e}$, the cohesive force starts weakening. We assume that the friction starts weakening at $\delta_{II}^{f,e} = \delta_{II}^{c,e}$ so that the cohesion and the friction start weakening at the same amount of slip. We do this by adjusting the stiffness of elastic loading for friction p^f, as follows

$$p^f = \frac{\tau_{II}^p}{2C_{II}^p} p^c. \tag{2.23}$$

The fracture energy related with friction, G_{IIC}^f, is approximated from the equation (2.14).

One interesting question is, as pointed out by *Rice et al.* (2005), what parameters vary with depth,. In our parametrization, normal stress on the fault lithostatically increases with depth. *Lachenbruch* (1980) proposed a formula of frictional resistance similar with the exponential slip-weakening law, where the slip-weakening distance D_c on the fault is almost independent of depth because it is composed by physical parameters like the width of fault gouge and other coefficients related with pore fluid or rock material, which are assumed to be constant with depth (also referred in *Rice et al.* (2005)). In this case, G_{IIC}^f on the fault derived by equation (2.14) increases with depth as the strength drop linearly increases as $\tau_p - \tau_r = (f_s - f_d)\left\{-\sigma_{yy}^0(z)\right\}$ in our model description, described as

$$G_{IIC}^f(z) = \frac{1}{2} D_c^* \left(\tau_p - \tau_r\right), \tag{2.24}$$

where D_c^* is a given constant critical slip distance with depth. This is the first scenario that we consider. The second scenario is to assume that G_{IIC}^f on the fault is kept constant

with depth. In this case, D_c decreases with depth, as a function of a given constant G_{IIC}^{f*} on the fault, as follows

$$D_c(z) = \frac{2G_{IIC}^{f*}}{(f_s - f_d)\left\{-\sigma_{yy}^0(z)\right\}}. \tag{2.25}$$

For the sake of simplicity, we call the first scenario constant D_c case, and the second scenario constant G_{IIC} case.

In both scenarios, as proposed by *Palmer and Rice* (1973), the process zone size R_0 for the quasi-stationary crack, over which the friction is weakened with ongoing slip to the residual strength, is described as

$$R_0(z) = \frac{9\pi}{32(1-\nu)} \frac{\mu D_c^*}{(f_s - f_d)\left\{-\sigma_{yy}^0(z)\right\}}, \tag{2.26}$$

for the constant D_c case. while

$$R_0(z) = \frac{9\pi}{16(1-\nu)} \frac{\mu G_{IIC,f}^*}{\left[(f_s - f_d)\left\{-\sigma_{yy}^0(z)\right\}\right]^2}, \tag{2.27}$$

for the constant G_{IIC} case. As shown by equations (2.26) and (2.27), R_0 decreases with depth as $\left\{-\sigma_{yy}^0(z)\right\}^{-1}$ for constant D_c case and $\left\{-\sigma_{yy}^0(z)\right\}^{-2}$ for constant G_{IIC} case.

Since the size of potential failure area is of the same order of magnitude as $R_0(z)$ (e.g. *Poliakov et al.*, 2002), the damage zone is expected to decrease with depth, as mentioned by *Rice et al.* (2005). To verify this hypothesis, we explore the two scenarios to understand the evolution of off-fault damage in depth.

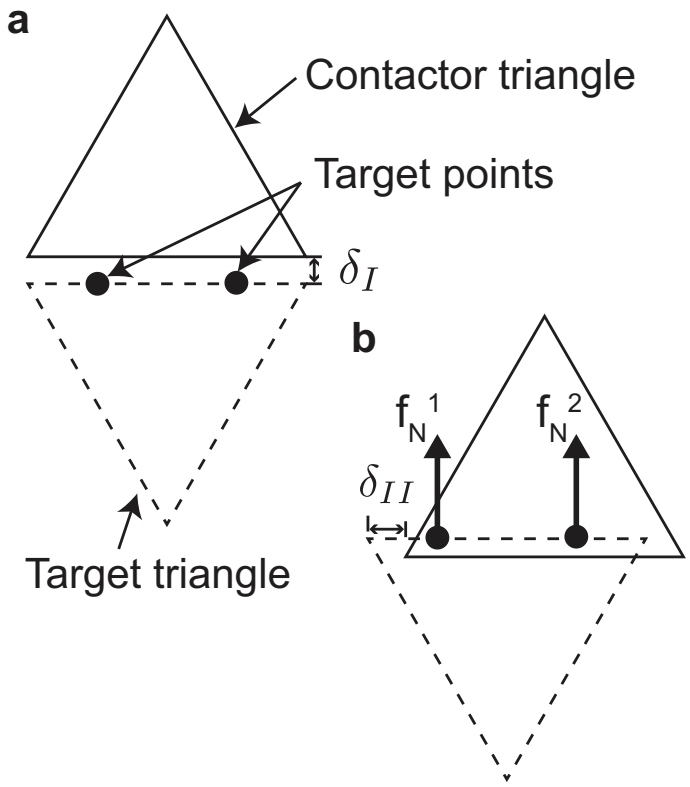

Figure 2.1: Schematic of contactor and target. (a) tensile and (b) shear displacements and contact forces are indicated. The number of target points drawn in black dots is properly chosen for desirable numerical accuracy.

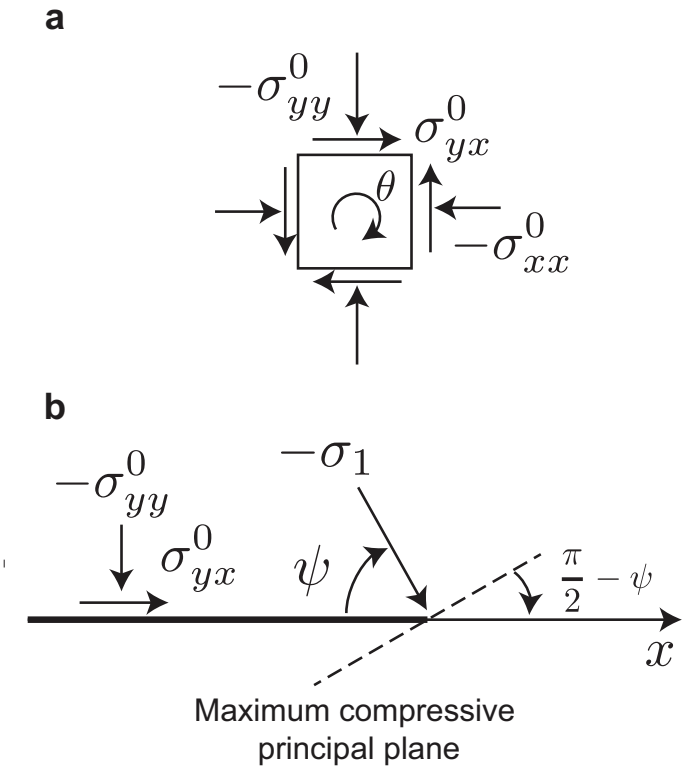

Figure 2.2: Sign convention for stress and orientation. (a) Tensile and clockwise directions are positive for stresses. (b) Sign convention for the stresses on the fault. $-\sigma^0_{yy}$ and σ^0_{yx} are respectively initial normal traction and shear traction applied on the fault along the x axis. $-\sigma_1$ is maximum compressive principal stress with the angle ψ to the fault.

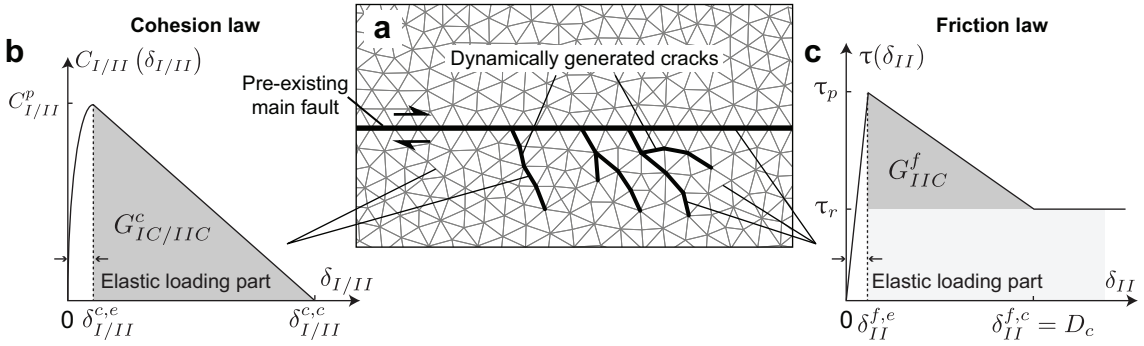

Figure 2.3: Schematic of contact algorithm. (a) Computational domain discretized using an unstructured mesh. Every interface between elements is regarded as a potential failure plane, where cohesion and friction stresses are operating as a function of displacements $\delta_{I/II}$. (b) Linear displacement softening cohesion law. The area highlighted in gray under the softening part of the curve indicates the fracture energy associated with cohesion in tension G^c_{IC} and in shear G^c_{IIC} respectively. (c) Linear slip-weakening law. The energy dissipated by frictional process is divided into the fracture energy associated with friction, G^f_{IIC}, while the rest is considered as heat.

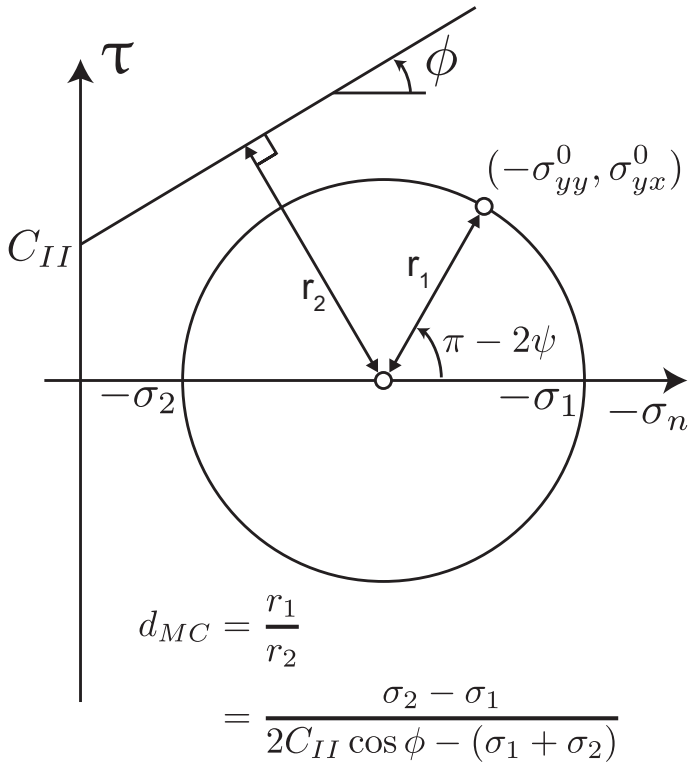

$$d_{MC} = \frac{r_1}{r_2} = \frac{\sigma_2 - \sigma_1}{2C_{II}\cos\phi - (\sigma_1 + \sigma_2)}$$

Figure 2.4: Mohr-Coulomb failure criteria and closeness to failure, d_{MC}.

Table 2.1: Scaling Factors for Nondimensionalization.

Quantity	Scale	Unit
Length	R_0	m
Time	R_0/c_s	s
Velocity	c_s	m/s
Acceleration	c_s^2/R_0	m/s^2
Stress	c_s^2/R_0^3	Pa
Energy	c_s^2	J

2.3.5 Nondimensionalization

Since the size of the off-fault damage zone is assumed to be on the same order of the process zone size, it is comprehensible to scale the in-plane field dimensions by dividing them by the spatial factor R_0 (e.g. *Templeton and Rice*, 2008). In this study, the model parameters are thus nondimensionalized in space and time by scaling factors such as the process zone size R_0 for the length and R_0/c_s for the time. Subsequently, other variables are also nondimensionalized by the combination of those two scaling factors. Since the density of medium does not change during simulations, the nondimensionalization of mass is not necessary in our problem. It is thus assumed to have a physical value through the simulation. All scaling factors are summarized in Table 2.1.

2.4 Theory of Contact Algorithm for HOSS

In this section, we describe the contact algorithm between contactor and target cell. When contactor has an intersection with target cell the cohesion and friction forces are calculated based on the damage state and the normal and tangential displacements. The cohesive and frictional force are then applied to each point on the edge of contactor as an external force in the equation of motion. Both cohesion and friction have initial elastic loading part where the resistive force increases linearly with friction and quadratically with cohesion, as they are well represents the fracturing process in comparison with experiments. When it reaches the given initial peak strength, the cohesion starts to be broken with linear-softening law and friction decreases following the slip-weakening law. Damage value then increases as the cohesion decreases, which makes the peak cohesive strength lower than the initial peak strength as a function of damage. Subsequently the cohesion curve dynamically changes with the increase of damage. In mixed mode failure, the change of cohesion curve interacts with both tensile and shear cohesion, which results in complex cohesive response during the failure even if the movement of point is simple as shown in the validation of mixed mode failure discussed below. Here we show all formulations for deriving the cohesion and friction, characteristic displacements associated with them and damage quantity.

2.4.1 Notation system for contact Algorithm

Since a variety of parameters need to be described, we first define the notation system for the variables. The components of tensile and shear are represented by I and II respectively, denoted by subscript. Attributes of parameters are denoted by superscript. Star in superscript, *, denotes the initial value. The symbols used in this section are summarized in the list of symbols. We assume unit out-of-plane thickness for the following formulations.

2.4.2 Cohesion for tensile and shear crack

The degree of damage on a contact is evaluated by a quantity D defined as

$$D_i = \frac{\delta_i - \delta_i^{*c,e}}{\delta_i^{max}} \quad i = I, II \tag{2.28}$$

where D_i shows components of damage for tensile and shear crack, δ_i is normal and tangential displacement, $\delta_i^{*c,e}$ is the initial critical displacement for elastic loading, $\delta_i^{max} = \delta_i^{*c,c} - \delta_i^{*c,e}$ is the maximum displacement during linear-softening where $\delta_i^{*c,c}$ is the initial critical displacement for linear-softening part. This equation is identical to equation (2.10).

The peak strength is modified by the damage as following

$$C_i^p(D) = (1 - D)C_i^{*p}, \tag{2.29}$$

where C_i^p is the peak strength for tensile and shear cohesion, C_i^{*p} is the initial value of the peak strength written as

$$C_i^{*p} = C_i^p(0). \tag{2.30}$$

Then the tensile and shear cohesion is derived as

$$C_i(\delta_i) = \left\{ \begin{array}{ll} \dfrac{C_i^p \delta_i}{\delta_i^{c,e}} \left(2 - \dfrac{\delta_i}{\delta_i^{c,e}}\right), & \delta_i < \delta_i^{c,e} \\ C_i^{*p} \left[1 - \dfrac{(\delta_i - \delta_i^{*c,e})}{\delta_i^{max}}\right], & \delta_i^{c,e} \leq \delta_i < \delta_i^{c,c} \\ 0 & \delta_i^{c,c} \leq \delta_i \end{array} \right\}, \tag{2.31}$$

where $C_i(\delta_i)$ is the cohesive stress [Pa]. $\delta_I^{c,c}$ does not change during the breaking process of cohesion, thus

$$\delta_I^{c,c} = \delta_I^{*c,c}. \tag{2.32}$$

Then the cohesive force is derived as

$$f_i^c(\delta_i) = A^p C_i(\delta_i) \tag{2.33}$$

where A_p is an area of point k on the edge of contactor. If the displacements of all point are same such that $\delta_i^k = \delta_i$ the cohesive stress in [Pa] is described as following

$$C_i(\delta_i) = \frac{f_i^c}{h}, \tag{2.34}$$

Where h is length of edge of the contactor and $f_i^c = \sum_{k=1}^{N} f_i^{c,k}$, $f_i^{c,k}$ is cohesion force applied at point k on edge and N is the number of points par face. The boundary condition of C_i is set by stiffness for cohesion p^c as

$$\left.\frac{dC_i}{d\delta_i}\right|_{\delta_i=0}^{D=0} = \frac{p^c}{h}. \tag{2.35}$$

Thus

$$\delta_i^{*c,e} = \frac{2hC_i^{*p}}{p^c}. \tag{2.36}$$

Then the $\delta_i^{c,e}$ is derived as the crosspoint of the first and second curve of equation (2.31) written as

$$\delta_i^{c,e} = \left(1 - \frac{C_i^p}{C_i^{*p}}\right)\delta_i^{max} + \delta_i^{*c,e} \tag{2.37}$$

$$= D\delta_i^{max} + \delta_i^{*c,e}. \tag{2.38}$$

For the derivation flow of cohesion we firstly start with the damage in previous step to derive $C_i^p(D)$ in equation (2.29).Then we derive $\delta_i^{c,e}$ by equation (2.38), which gives $C_i(\delta_i)$ by equation (2.31). It is noteworthy that this formulation can deal with unloading by preserving the damage D. It is shown in the following section for the validation of unloading and reloading. The cohesion curve is illustrated in Figure 2.5.

2.4.3 Friction for shear crack

The friction for shear cracks is decomposed into initial elastic loading and slip-dependent law, which is described as

$$f_{II}^f(\delta_{II}) = \left\{ \begin{array}{ll} p^t \dfrac{A^p}{h}\delta_{II}, & \delta_{II} < \delta_{II}^{f,e} \\ \\ \mu(\delta_{II}) f_n, & \delta_{II} \geq \delta_{II}^{f,e} \end{array} \right\}, \tag{2.39}$$

where $f_{II}^f(\delta_{II})$ is shear friction force, $\delta_{II}^{f,e}$ is critical tangential displacement for elastic loading of shear friction, p^f is stiffness for friction, $\mu(\delta_{II})$ is slip-dependent friction coefficient and f_n is normal force. In friction $\delta_{II}^{f,e}$ is constant such that $\delta_{II}^{f,e} = \delta_{II}^{*f,e}$. $\mu(\delta_{II})$ is described depending on the tangential displacement δ_{II} as following

$$\mu(\delta_{II}) = \left\{ \begin{array}{ll} -(\mu_s - \mu_d)\dfrac{\delta_{II}}{\delta_{II}^{f,c}} + \mu_s, & \delta_{II}^{f,e} \leq \delta_{II} < \delta_{II}^{f,c} \\ \\ \mu_d, & \delta_{II}^{f,c} \leq \delta_{II} < \delta_{II}^{f,s} \\ \\ k^\mu(\delta_{II} - \delta_{II}^{s,f}) + \mu_d, & \delta_{II}^{f,s} \leq \delta_{II}^k \end{array} \right\}, \tag{2.40}$$

where μ_s, μ_d and $\delta_{II}^{f,c}$ are static and dynamic friction coefficient and characteristic slip distance in conventional slip-weakening law, $\delta_{II}^{f,s}$ is critical tangential displacement for slip-strengthening of shear friction and k^μ is stiffness for slip-strengthening of shear friction .

$\delta_{II}^{f,c}$ is usually denoted by D_c in the framework. Slip-strengthening part is introduced to avoid too much slip on the prescribed fault due to limitations of the model formulations on the penalty functions. The first formulation of equation (2.40) shows the slip-weakening part, then the second shows residual part and the third shows slip-strengthening part, respectively. The magnitude of rate of change for $\mu(\delta_{II})$ is same with slip-weakening and slip-strengthening is adjusted as same by choosing k^{μ} as

$$k^{\mu} = \frac{(\mu_s - \mu_d)}{\delta_{II}^{f,c}}. \tag{2.41}$$

If we assume the equivalent displacements and normal forces on the all points of the edge, the shear traction τ_{II} can be written as

$$\tau_{II} = \frac{f_{II}^{f}}{h}, \tag{2.42}$$

where $f_{II}^{f} = \sum_{k=1}^{N} f_{II}^{f,k}$. Then

$$\tau_{II} = \mu(\delta_{II})\sigma_n, \tag{2.43}$$

where σ_n is normal stress on the edge. When we assume the initial critical tangential displacement for elastic loading of shear cohesion is same as that of shear friction, i.e., $\delta_i^{*c,e} = \delta_i^{*f,e}$, the stiffness for friction is derived by the stiffness for cohesion and initial peak strength as following

$$p^{f} = \frac{\tau_{II}^{*p}}{2C_{II}^{*p}} p^{c} \tag{2.44}$$

where $\tau_{II}^{*p} = \mu_s f_I^{*n}/h$ shows peak strength for friction. In summary, the friction curve is illustrated in Figure 2.6.

2.4.4 Dissipated energy by cohesion and friction

Dissipated energy by the cohesive and frictional process on an edge, E_i^c and E_{II}^f, are obtained by

$$E_i^c = \sum_{k=1}^{N} \int_0^{\delta_i^k} f_i^{c,k}(\xi) d\xi, \tag{2.45}$$

for the cohesion and

$$E_{II}^f = \sum_{k=1}^{N} \int_0^{\delta_{II}^k} f_{II}^{f,k}(\xi) d\xi, \tag{2.46}$$

for the friction. The integration error at point k is estimated by

$$err \leq \frac{1}{2} ML \tag{2.47}$$

where

$$M = \left\{ \begin{array}{ll} \max \left| \dfrac{df_i^{c,k}}{dt} \right|, & \text{for cohesion} \\ \\ \max \left| \dfrac{df_{II}^{f,k}}{dt} \right|, & \text{for friction} \end{array} \right\} \tag{2.48}$$

$$L = \max |\Delta\delta_i^k| \tag{2.49}$$

where $\Delta\delta_i^k$ is change of displacement during one time step. Since small time step is chosen in our problem ($\Delta\delta_i^k$/particle velocity $\sim 10^{-5}$), the accumulated error is much smaller than the total dissipated energy.

2.4.5 Validation of contact force algorithm

In this section, we show the validation of the response of contact force and associated parameters by two-block test. The schematic of test model is shown in Figure 2.7, where the motion of top block is imposed on the fixed base block to obtain the ideal response of contact force. Firstly we show purely sliding test which provides the slip-weakening and slip-strengthening response as shown in Figure 2.8. The top block is initially overlapped with base block. Then the top block moves in tangential direction. The comparison between theoretical and output results of frictional stress and the dissipated energy by friction $E_{II}^{f,h}$ is shown in Figure 2.9.

We then show the response of mixed mode failure in Figure 2.10 and comparisons to theoretical solutions in Figures 2.11 and 2.12. Here the top block is overlapped with base block in the beginning. The top block then moves in shear direction until the damage reaches to 0.5. Subsequently the top block is immediately pulled up until the cohesion is totally broken. It shows that the responses of cohesion and friction behave in a nonlinear way with mixed mode failure even if the motion of top block is relatively simple such as this case.

Finally, we show the unloading and reloading test with pure tensile failure in Figures 2.13, 2.14, 2.15 and 2.16. Here the top block is pulled up until the damage reaches 0.5. Then we put it back to the initial position and pull it up again until the cohesion is broken. The cohesion is no longer reach to the initial peak strength in the reloading part due to the accumulation of damage. These results verify the response of cohesion and friction, and the output of damage, damage type and the dissipated energy.

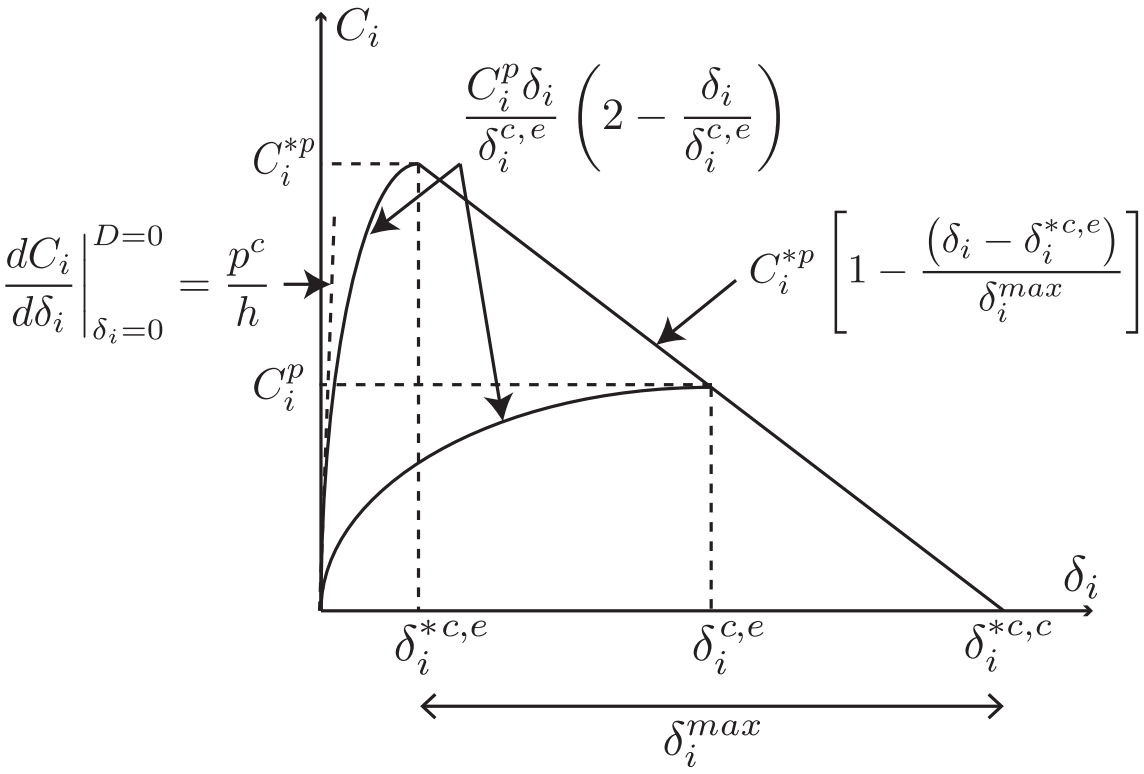

Figure 2.5: Cohesion curve ($i = I, II$).

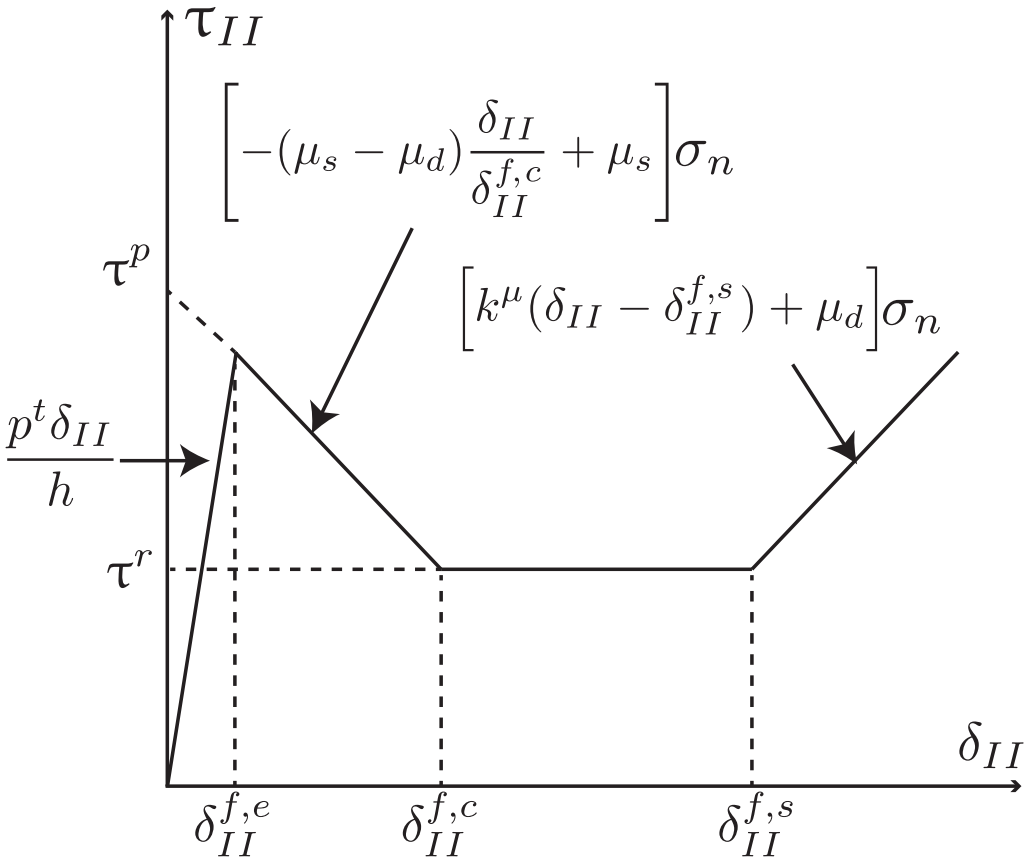

Figure 2.6: Friction curve.

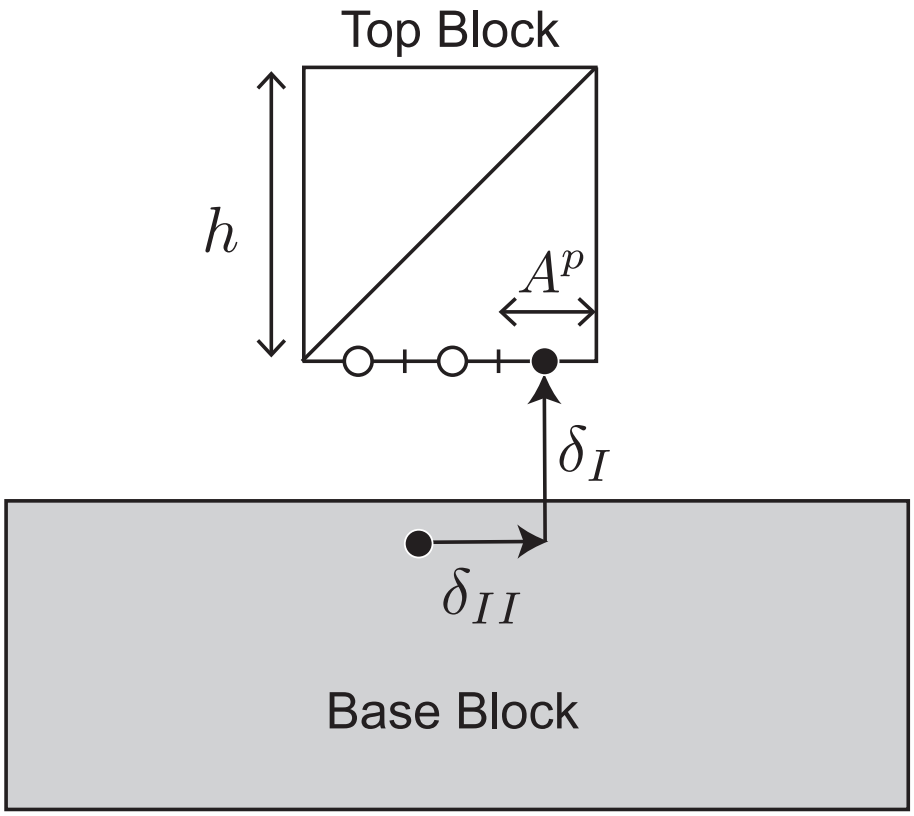

Figure 2.7: Schematic of the geometry of cell and displacement for two block test. Note that $\delta_I = 0$ when a point is on the edge.

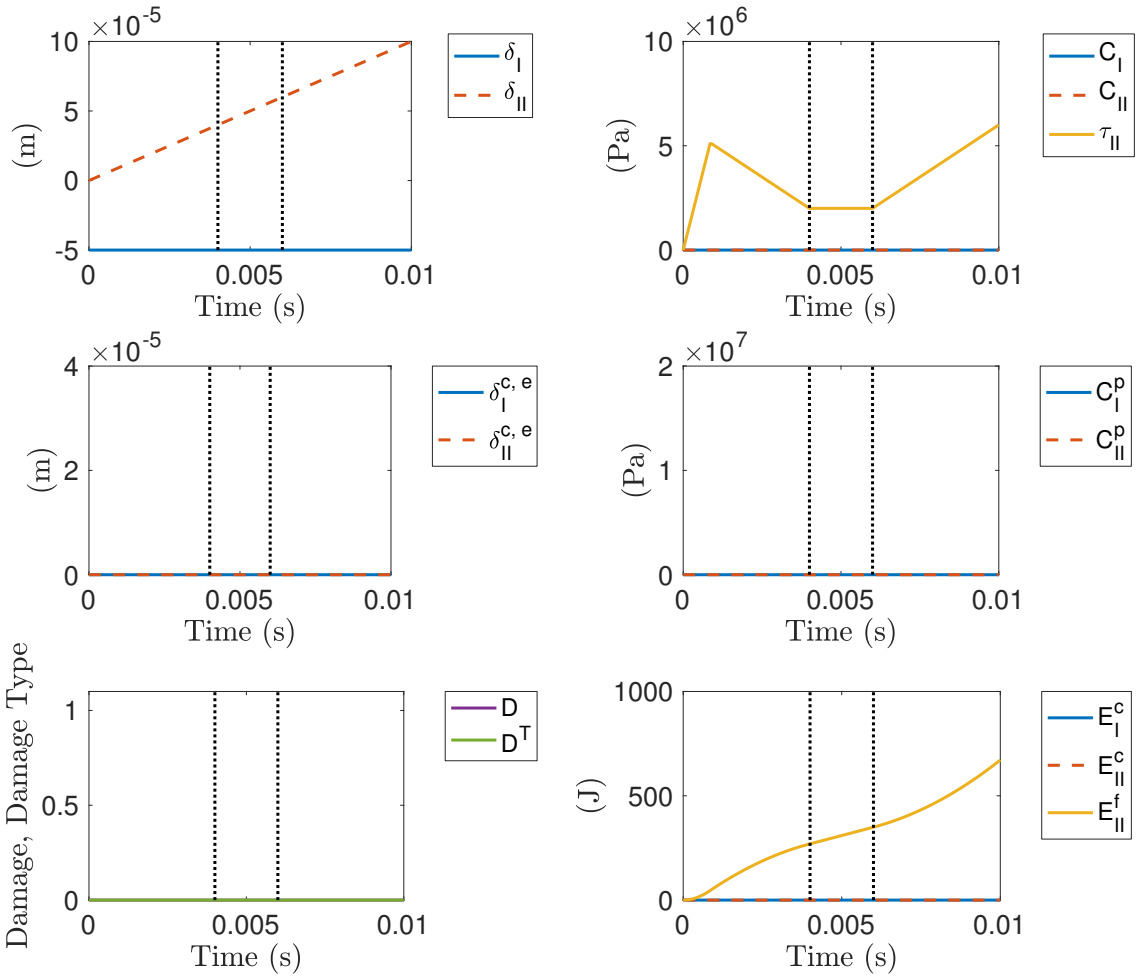

Figure 2.8: Response of friction and associated parameters for the purely sliding test. First vertical line indicates the time when the friction is fully weakening and the second vertical line indicates the initiation of slip-strengthening.

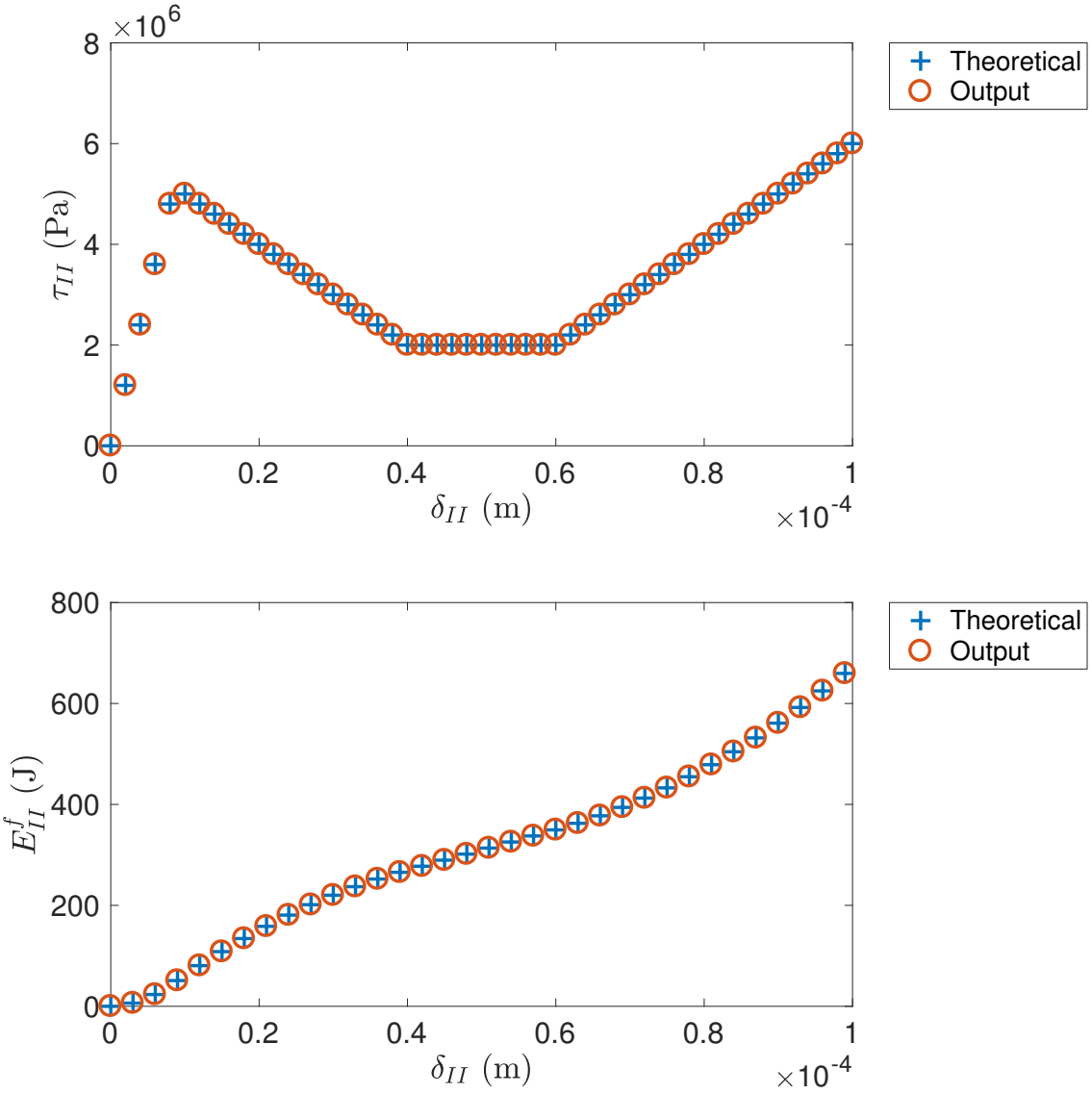

Figure 2.9: Comparison of friction and dissipated energy by frictional process between theoretical results and outputs .

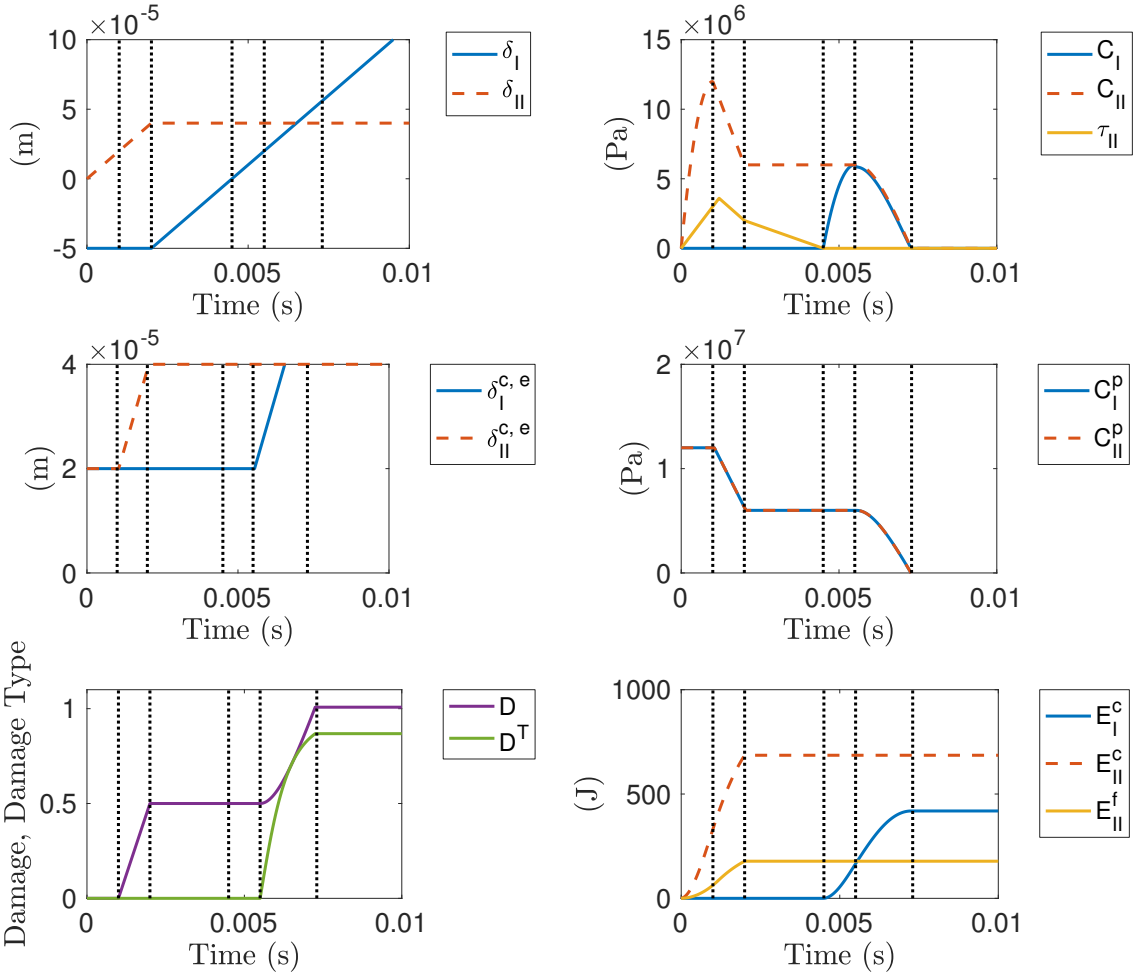

Figure 2.10: Response of tensile cohesion and associated parameters for the mixed mode failure test. The first vertical line indicates the initiation of softening with shear cohesion, the second indicates the change of motion of the top block from tangential direction to tensile, the third indicates the initiation of tensile cohesion ($\delta_I = 0$), the fourth indicates the initiation of softening with tensile cohesion and the fifth indicates the time when the cohesion is completely broken.

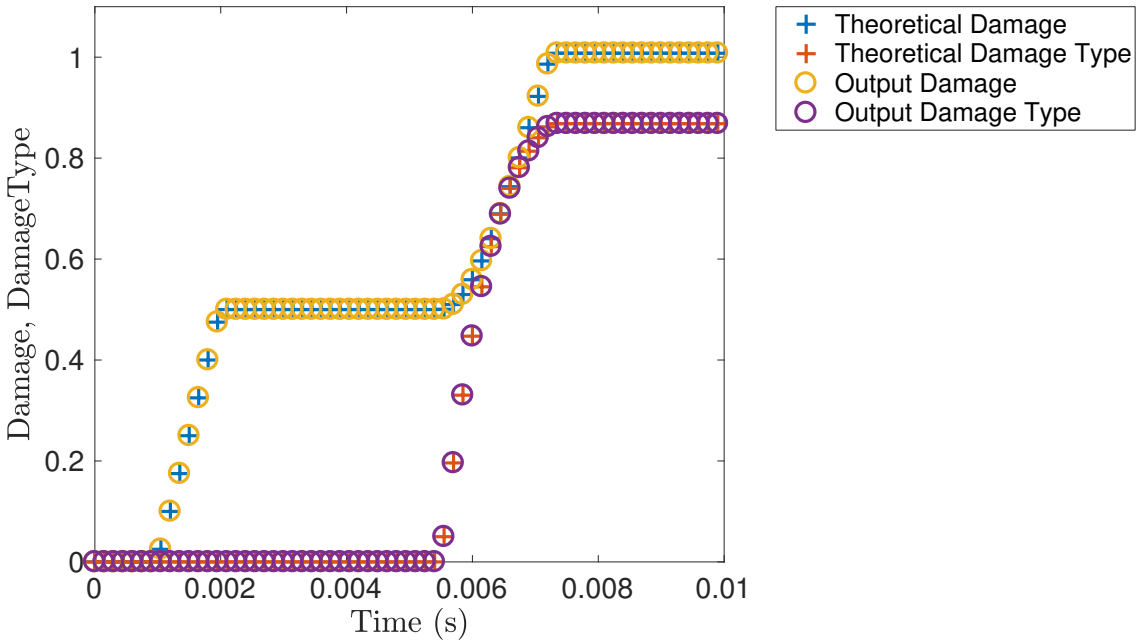

Figure 2.11: Comparison of damage and damage type by cohesive and frictional process between theoretical results and outputs .

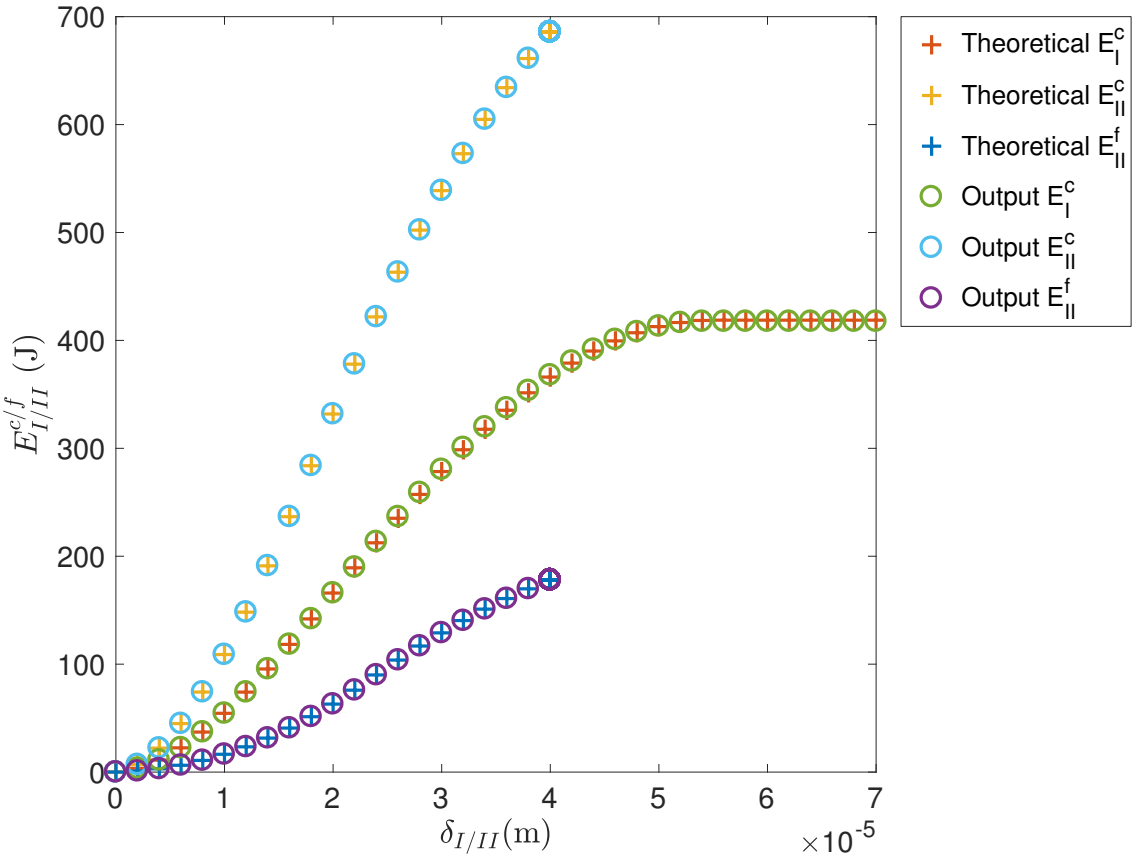

Figure 2.12: Comparison of dissipated energy by cohesive and frictional process between theoretical results and outputs .

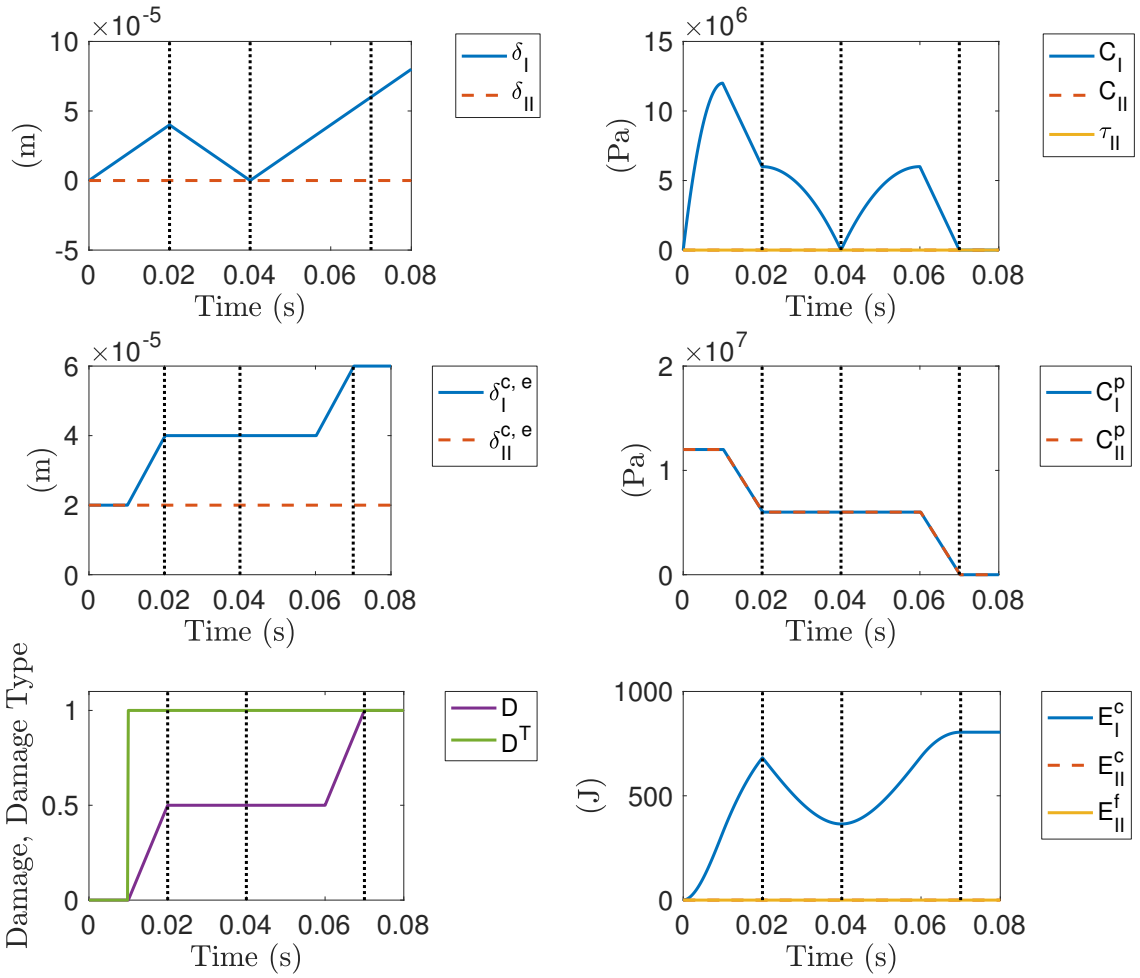

Figure 2.13: Response of tensile cohesion and associated parameters for the unloading and reloading test. The first vertical line indicates the initiation of unloading, the second indicates the initiation of reloading and the third indicates the time when the cohesion is totally broken.

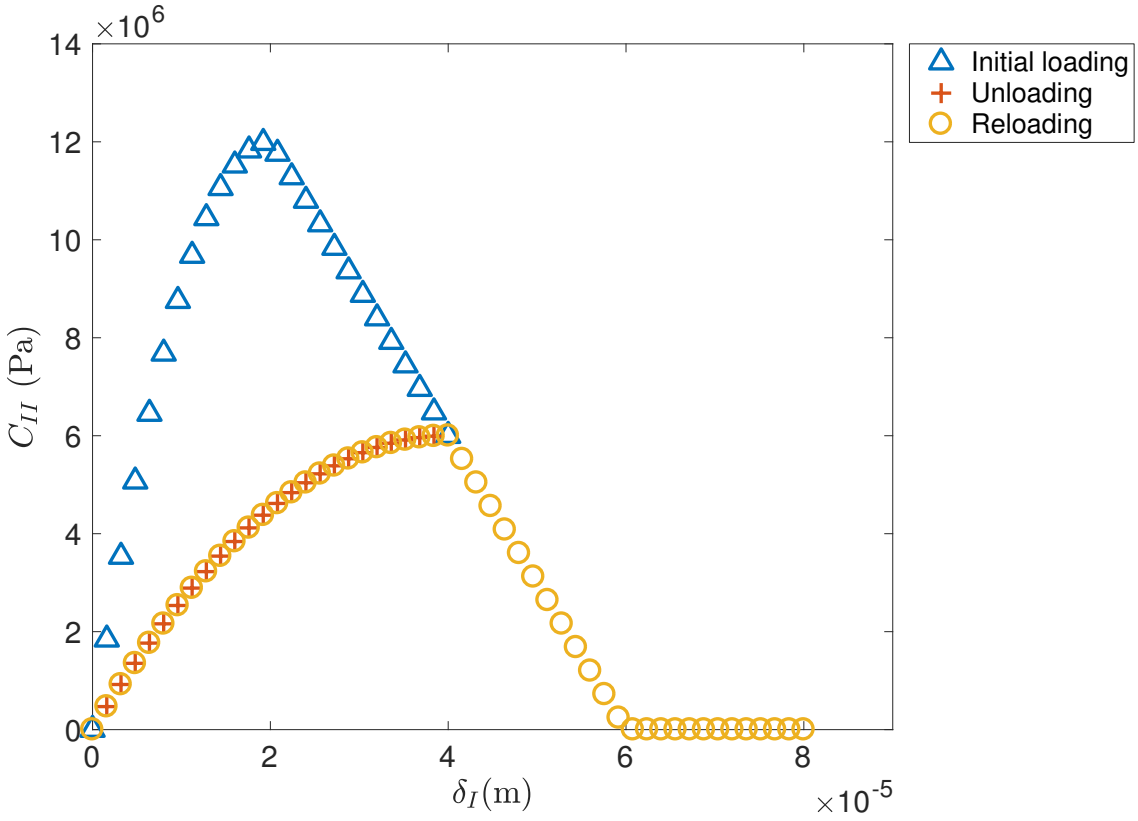

Figure 2.14: Theoretical response of tensile cohesion.

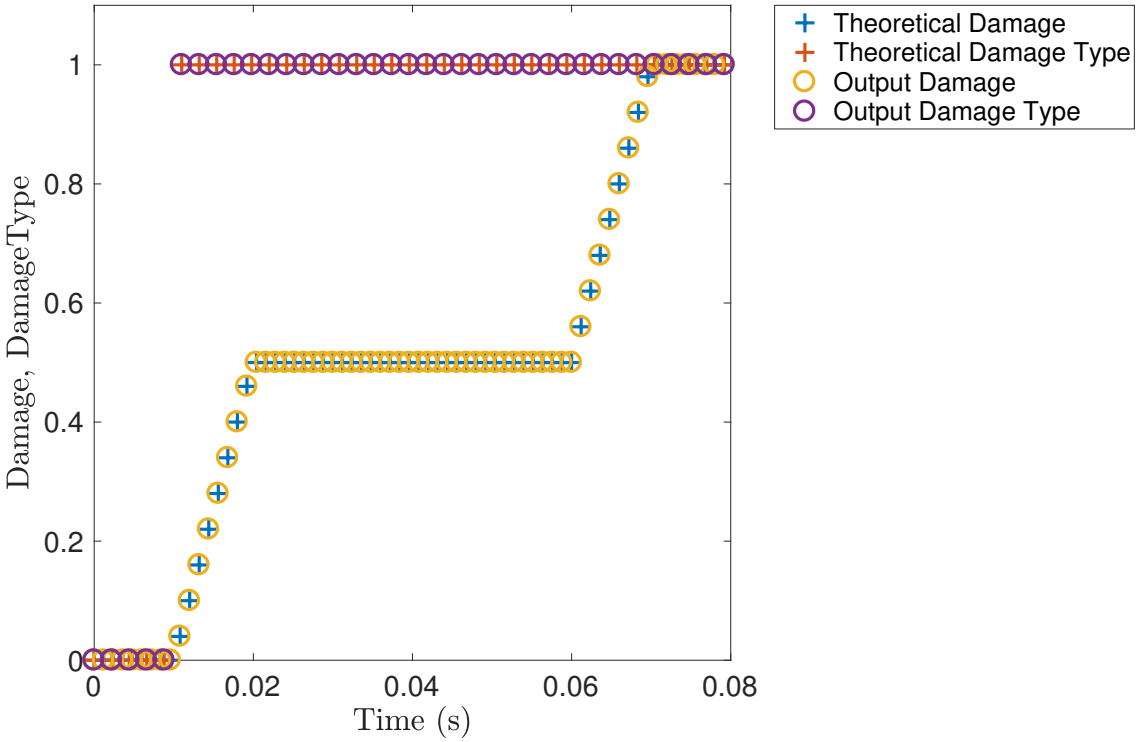

Figure 2.15: Comparison of damage and damage type by tensile cohesion between theoretical results and outputs .

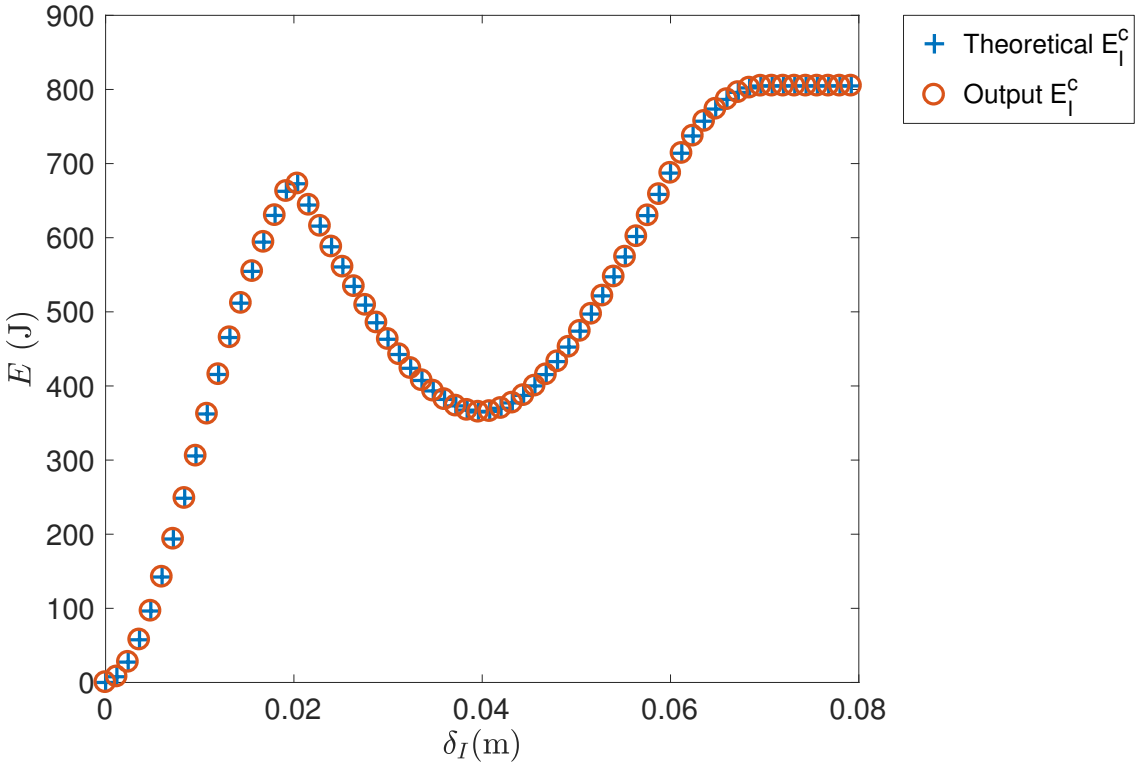

Figure 2.16: Comparison of dissipated energy by tensile cohesion between theoretical results and outputs .

2.5 Cross-validation of 2-D FDEM for earthquake rupture modeling

2.5.1 Validation of 2-D in-plane problem

In this section, we perform cross-validation of the FDEM to assess the achievable accuracy of earthquake rupture modeling by comparing the results against other numerical schemes. In our analysis we chose the finite different method (FDM), the spectral element method (SEM) and the boundary integral equation method (BIEM) as comparison basis, which have been verified in previous studies (e.g. *Koller et al.*, 1992; *Day et al.*, 2005; *Kaneko et al.*, 2008). The cross-validation effort follows a similar process as the one proposed by *Kaneko et al.* (2008). The first arrival time of the rupture is a suitable benchmark to evaluate the numerical precision of the rupture solution (*Day et al.*, 2005), because it characterizes the behavior of earthquake rupture propagation and subsequently the radiated wave field in the surrounding elastic medium. In this study, the rupture arrival time is defined at the time when the shear traction reaches the peak strength τ_p, which corresponds to the slip at the initiation of slip-weakening.

We follow the version 3 of the benchmark problem proposed by the Southern California Earthquake Center/U.S. Geological Survey (SCEC/USGS) dynamic earthquake rupture code verification exercise (*Harris et al.*, 2009), commonly used for cross-validating numerical schemes (*Day et al.*, 2005; *Kaneko et al.*, 2008; *Rojas et al.*, 2008; *De La Puente et al.*, 2009). The model is originally described in 3-D so that the 2-D analog model was used in this study, similar to *Rojas et al.* (2008), *Kaneko et al.* (2008), and *De La Puente et al.* (2009).

Figure 2.17 illustrates the model setup for the cross-validation, which has a single planar fault in the middle of a homogeneous and isotropic elastic medium. The linear slip-weakening law with zero cohesion is operating along the fault. Since the outer boundary edges are fixed, the model domain size is set large enough to avoid the interference from waves originating reflected boundaries. The domain is discretized by spatially adaptive unstructured triangular mesh, where the element size is smallest on and around the fault and increases in proportion to the distance from the main fault. The grid spacing is a priori defined uniformly on the fault itself. For the sake of cross-validation, the off-fault cracking is not allowed so that the off-fault medium behaves as a purely elastic material.

Material constants and frictional properties are listed in Table 2.2. A slippery zone where frictional resistance is lower than outside is set in the middle of the fault to nucleate the earthquake rupture from the patch. The length of the slippery zone is slightly greater than the critical nucleation length at instability, L_c, derived by *Palmer and Rice* (1973) such as

$$L_c = \frac{2\mu D_c(\tau_p - \tau_r)}{\pi(\sigma_{yx}^0 - \tau_r)^2}. \tag{2.50}$$

Since the shear traction and the slip rate vary significantly within the process zone around the rupture front, the resolution of the grid, often defined by the number of grid points within the process zone, is considered as a useful indication of the numerical accuracy in earthquake rupture modeling (*Day et al.*, 2005). The dynamic process zone size,

$R_f(v_r)$, is generally inversely proportional to the rupture velocity v_r, given by *Rice* (1980, eq. (6.16)) and *Freund* (1990, eq. (6.2.35)) such as

$$R_f(v_r) = A_{II}(v_r)^{-1} R_0, \tag{2.51}$$

$$A_{II}(v_r) = \frac{v^2 \alpha_s}{(1-\nu) c_s^2 R}, \tag{2.52}$$

where

$$R = 4\alpha_s \alpha_p - \left(1 + \alpha_s^2\right)^2, \tag{2.53}$$

$$\begin{cases} \alpha_p^2 = 1 - v^2/c_p^2 \\ \\ \alpha_s^2 = 1 - v^2/c_s^2. \end{cases} \tag{2.54}$$

It is notable that the function $A_{II}(v_r)$ has the properties that $A_{II} \to 1$ as $v_r \to 0^+$ and $A_{II} \to \infty$ as $v_r \to c_R$, where c_R is the Rayleigh wave speed as the limiting speed in the context of sub-Rayleigh rupture. Thus the process zone size gradually shrinks and asymptotically converges to zero as the rupture velocity approaches c_R, which is typically known as Lorentz contraction. The process zone resolution is defined with the median value of $R_f(v_r)$ in previous studies (*Day et al.*, 2005; *Kaneko et al.*, 2008), providing the effective grid resolution of the process zone through the simulation. However, for the sake of simplicity, we use the quasi-stationary process zone size R_0 for evaluating the grid resolution. Thus the process zone resolution in this study implies an indication of numerical accuracy related with grid size rather than the actual number of grid points within the actual process zone size during rupture propagation.

Figure 2.18 shows the the comparison of slip velocity history at x = 9 km from the center of the main fault. The results of HOSS are compared with other results by FDM, SEM and BIEM, where the grid spacing on the fault is chosen for the highest resolution as $\Delta x = 8$ m ($\Delta x/R_0 = 116$) for HOSS, FDM and BIEM and $\Delta x = 10$ m ($\Delta x/R_0 = 93$) for SEM. Note that in the framework of SEM, to effectively enhance the numerical accuracy, Lagrange polynomials are chosen as a basis function for the Galerkin method and an element is then discretized by the Gauss-Lobatto-Legendre (GLL) points for the numerical integration, which is not spatially uniform. Thus the grid spacing of SEM is evaluated by average spacing, which implies the minimum grid spacing of SEM is equivalent to $\Delta x = 8$. The oscillation of slip velocity observed in FDM, SEM and the BIEM results is related to artificial viscous damping. There is no viscous damping in the BIEM and the FDM, whereas the SEM utilizes the Kelvin-Voigt viscous damping. The value of viscosity for the SEM is carefully chosen to avoid over damping of rupture propagation. For HOSS, we applied the Munjiza viscosity described in equation (2.3), which is high enough to removes the high-frequency numerical noise. It is notable that the comparison of HOSS results to BIEM is no longer fair due to the artificial viscous damping, so that the evaluation of the effect of viscous damping on the rupture propagation is worthwhile, and is discussed in section 2.5.2. The slip velocity of HOSS is globally in accordance with the other methods except for the peak slip velocity. The peak slip velocity of HOSS is 4.1 percent smaller than that of BIEM and the rupture arrival time is slightly faster than the

others. Both of the small discrepancies are explained by the artificial viscous damping applied on the whole medium by the Munjiza viscosities such that the strain rate-dependent viscosity smooths the rise of slip velocity, which causes the reduction of the peak velocity and accelerates the rupture arrival time.

Figure 2.19 shows the grid convergence of HOSS and other results. The numerical accuracy as a function of grid resolution is evaluated by the root-mean-square (RMS) difference, interpolated with the spacing of 100 m over the right side of the fault region given by 3.0 km $\leq x \leq$ 9.0 km in the same manner proposed by *Kaneko et al.* (2008). The RMS error of the rupture arrival time is defined by the comparison to the benchmark solution provided by the solution of BIEM with highest resolution. The convergence rate of HOSS is similar with the BIEM following the power law with the scaling exponent of 1.6 for HOSS and 1.4 for BIEM though the RMS error is slightly higher than the FDM and SEM due to the viscosity. Thus the numerical accuracy is assured with proper grid size Δs small enough to satisfy the required error range of the earthquake rupture modeling.

2.5.2 Error assessment with various artificial viscous damping

As mentioned above, the high-frequency numerical oscillation is suppressed by the viscous damping, whereas the smoothed velocity field causes the reduction of the peak velocity and the acceleration of rupture arrival time as shown in Figure 2.18. Thus the evaluation of the effect of artificial viscous damping is required to assess the numerical precision of the earthquake rupture modeling. Figure 2.20 shows the RMS error of the rupture arrival time with various viscosity values and grid resolutions with the highest resolution of BIEM as reference. The number of points per edge is defined as that of target points within the edge of elements at which the contact force is evaluated by equation (2.2) (*Lei et al.*, 2014), which plays a significant role on the integration accuracy of the distributed contact forces. We performed the analysis of the RMS error with one point and two points per edge. Grid size is defined by the spacing of the grids on the fault, while the process zone resolution is evaluated by $R_0/\Delta x$, same as Figure 2.19. The viscous damping is controlled by the dynamic viscosity η, input into the FDEM framework in the form of Munjiza viscosity defined by equation (2.3). The dynamic viscosity is then nondimensionalized by the volumetric Munjiza elastic constant, M_v, in plane strain, defined by

$$M_v = \frac{\nu E}{(1+\nu)(1-2\nu)}, \tag{2.55}$$

and the time step Δt in calculation. Note that the time step is constant during the simulation. The derivation of the Munjiza elastic constants is documented in *Munjiza et al.* (2015, Chapter 17). In Figure 2.20, the circles indicate the tested combinations of the viscosity values and the grid resolutions, where the size of circles with monochromatic gradation represents the proportion of the viscous values to the theoretically derived reference viscosity, called the critical viscosity ($M_v^c = 2h_{min}\sqrt{\rho M_v}$, where h_{min} is the length of minimum edge among all elements). The RMS error is desirable with proper combination of the viscous damping and grid resolution. The saddle of the RMS error along $\eta/M_v\Delta t \approx 10^2$ is explained by the competition between the numerical oscillation and the

Table 2.2: Stress and Frictional Parameters used for 2-D Cross-validation.

Valuables (units)	**Nucleation Area**	**Outside Nucleation**
σ^0_{yx} (MPa)	70.0	70.0
$-\sigma^0_{yy}$ (MPa)	120.0	120.0
f_s	0.554	0.677
f_d	0.430	0.525
D_c (m)	0.4	0.4
c_p (m/s)	6000.0	6000.0
c_s (m/s)	3464.0	3464.0
E (GPa)	85.4	85.4
μ (GPa)	32.0	32.0
ν	0.33	0.33
τ_p (MPa)	66.5	81.2
τ_r (MPa)	51.6	63.0
$\Delta\sigma = \tau_0 - \tau_r$ (MPa)	18.4	7.0

Note: $\Delta\sigma$ is the stress drop, where τ_0 is initial shear traction on the fault.

overdamped system. In addition, it is clearly shown that the convergence of the RMS error is better with the two integral points per edge. Hence the grid resolution, viscosity values and the number of points per face should be carefully chosen for the required numerical accuracy. Since the number of points per edge should be more than two to allow for the secondary cracks in off-fault medium due to numerical reasons, we chose the proper grid size and viscosity based on Figure 2.20b in the following section.

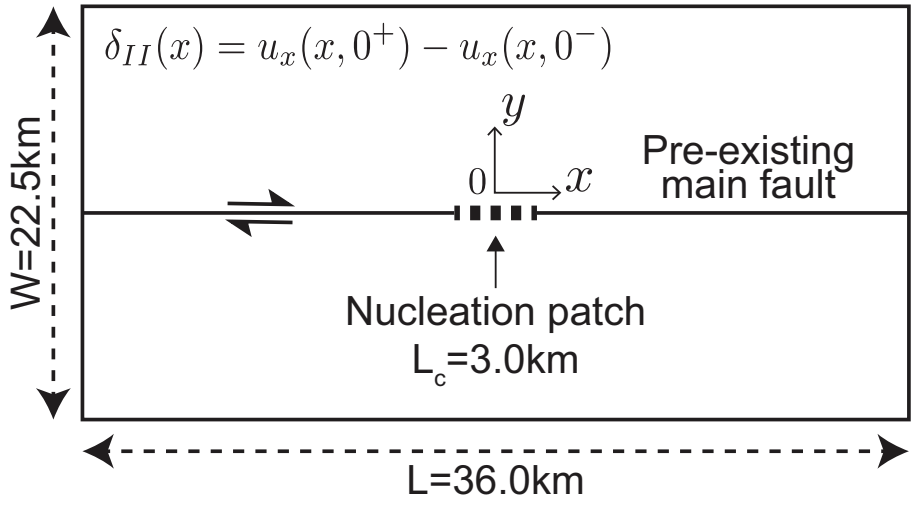

Figure 2.17: Schematic model for 2-D cross-validation. $\delta_{II}(x)$ is slip on the fault defined as $\delta_{II}(x) = u_x(x, 0^+) - u_x(x, 0^-)$.

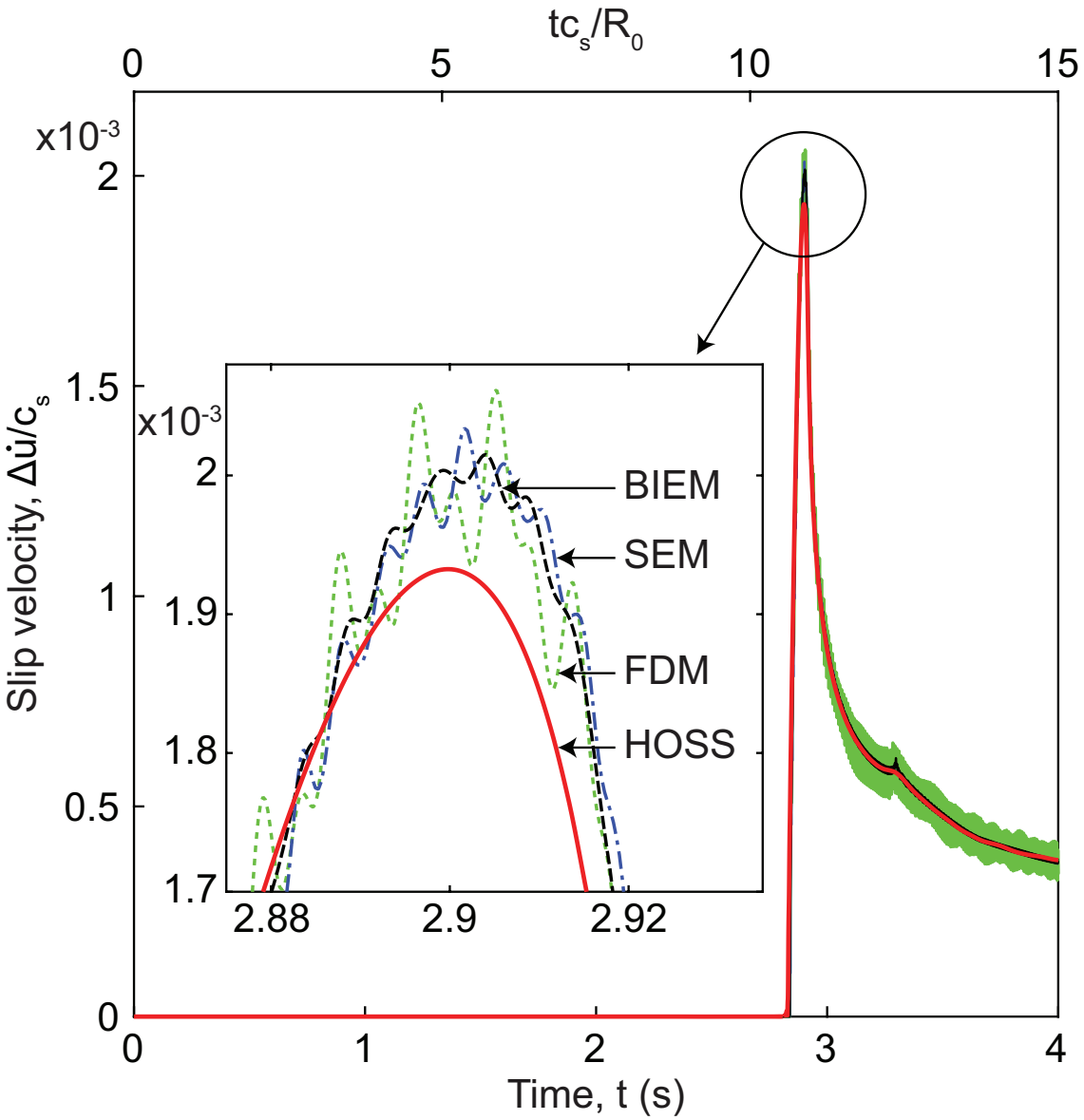

Figure 2.18: Slip velocity histories at $x = 9.0$ km ($x/R_0 = 9.7$). The grid size on the fault is 8 m ($\Delta x/R_0 = 116$) for HOSS, FDM and BIEM and 10 m ($\Delta x/R_0 = 93$) for SEM. The HOSS simulation is performed with one point per edge. The inset shows the focused window around the peak velocity at $t = 2.9$s.

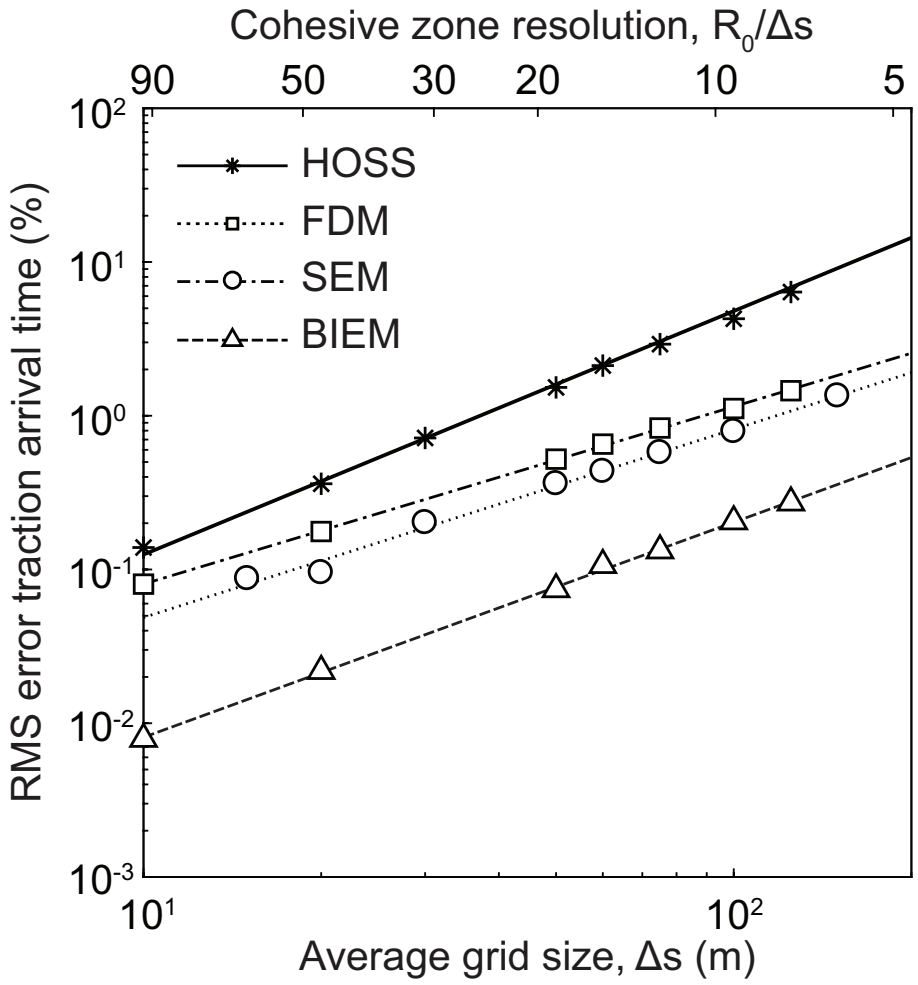

Figure 2.19: Grid convergence as a function of process zone resolution. The RMS error is calculated by the comparison of rupture arrival time to the benchmark result provided by the highest-resolution solution of BIEM at linear interpolated points with the spacing of 100 m over the fault region given by 3.0 km $\leq x \leq$ 9.0 km. The HOSS simulations are performed with two points per edge.

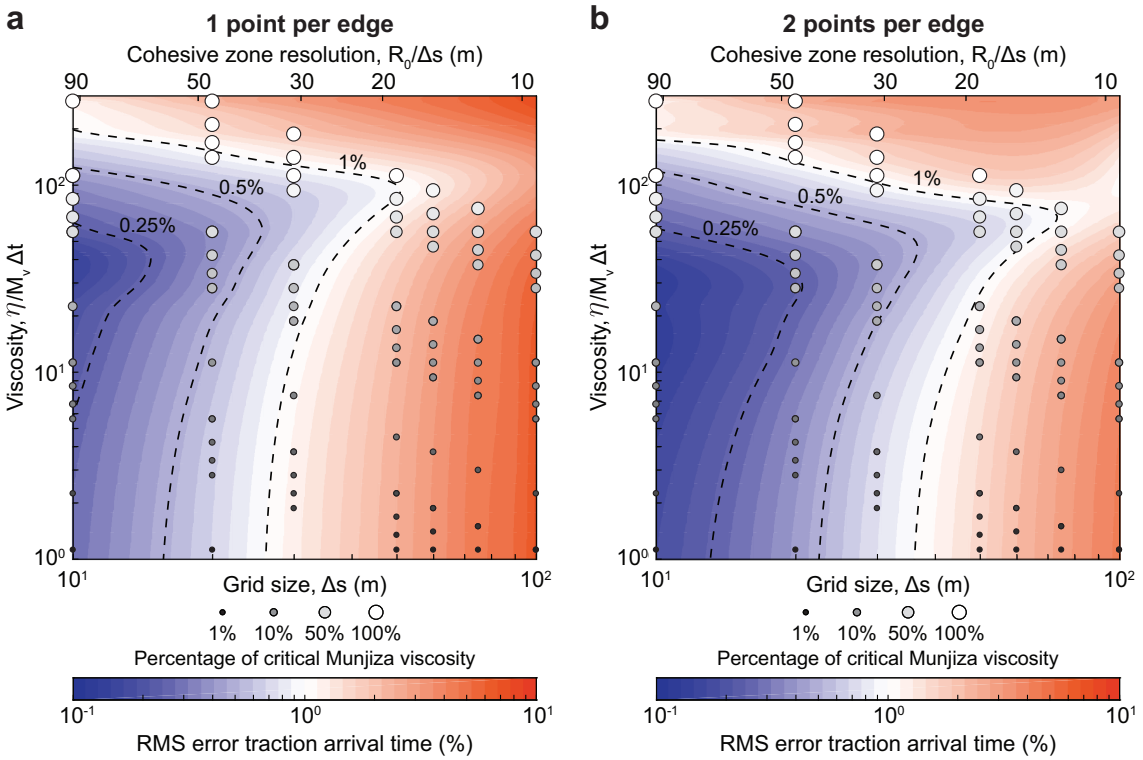

Figure 2.20: RMS error of the rupture arrival time with viscous values and grid resolutions. (a) shows the error with one point per edge of element, while (b) with two points per edge. The circles show the tested combinations of the viscous values and grid resolutions, where the size of circles with monochromatic gradation represents the proportion of viscous values to the critical viscosity (the viscosity is higher with white and large circles). The color contour is interpolated with the tested combinations. Viscosity is nondimensionalized by the Munjiza constant M_v and the time step Δt.

3. Dynamics, radiation and overall energy budget of earthquake rupture with coseismic off-fault damage

3.1 Dynamic earthquake rupture modeling with coseismic off-fault damage

3.1.1 Model description

We next perform the dynamic earthquake rupture modeling allowing for the activation of secondary cracks in the off-fault medium. As described in section 2.3.1, the initial stress state is uniformly set as a function of depth z. We conducted a set of 2-D simulations; two different S ratios, S = 1.0 and 0.7, with two different assumptions of frictional property on the main fault, in which D_c or G^f_{IIC} is kept constant in depth, each of which was performed at depth between 2km and 10km with 1km interval. In the following section, we define the term "constant D_c case" as keeping $D_c(z) = D^*_c$, and "constant G_{IIC} case" as keeping $G^f_{IIC}(z) = G^{f*}_{IIC}$ in depth. Furthermore, we examined the models with and without coseismic off-fault damage to investigate the effect of the latter on the rupture dynamics. We denote these cases as "with damage" and "no damage" cases. In the no damage case, both tensile and shear cohesion are large in the off-fault medium to prevent the off-fault damage. We conducted 72 simulations in total.

Figure 3.1 shows the case study in depth and the initial stress state in depth. Every simulation is conducted in plane strain. Since the boundaries are fixed, the domain size is set large enough to avoid the effects of reflection from the boundaries. The magnitude of the initial stress linearly increases in depth, whereas the quasi-static process zone size R_0 decreases inversely of the normal stress $-\sigma^0_{yy}(z)$ for constant D_c case, and decreases with the square of $-\sigma^0_{yy}(z)$ for constant G^f_{IIC} case. Figure 3.1b shows $R_0(z)$ for constant G^f_{IIC} case. The properties associated with the contact algorithm, such as $\delta^{c,e}_{I/II}$ and $\delta^{f,e}_{I/II}$, are also chosen following the section 2.3.1. The fracture energy in off-fault medium $G^{f*,\text{off-fault}}_{IIC}$ is kept constant in depth with both constant D_c and constant G^f_{IIC} cases. *Viesca and Garagash* (2015) and *Passelègue et al.* (2016) show the scaling law between the amount of slip and the fracture energy G^f_{IIC}. Since the amount of slip of off-fault cracks is estimated to be much smaller than that of main fault, we chose 0.01 MJ/m^{-2} and 3 MJ/m^{-2} for $G^{f*,\text{off-fault}}_{IIC}$ and G^{f*}_{IIC}, respectively. We also explored various d_{MC} to evaluate the off-fault damage

pattern. The rupture is not successfully nucleated with higher d_{MC}, such as $d_{MC} \geq 0.6$ examined in *Templeton and Rice* (2008), within a framework of FDEM because the wing cracks immediately nucleate at both ends of nucleation patch, causing numerous shear cracks around the wing cracks, which eventually arrest rupture propagation on the main fault. Note that there is initially no damage in the off-fault medium, interpreted as cohesive intact rock at $T = 0$. The parameters used in the case study are summarized in Table 3.1. Procedure of modeling dynamic earthquake rupture modeling with FDEM framework is described in Appendix B.

3.1.2 Snapshots of dynamic earthquake ruptures with coseismic off-fault damage

Figure 3.2 is a snapshot of dynamic rupture with dynamically activated off-fault cracks. We plot the particle velocity field with dynamically activated cracks around the main fault induced by the dynamic earthquake rupture. The off-fault cracks are plotted when the degree of damage D exceeds 0.01, that is, when the stress state on the potential failure plane reaches its cohesive strength and the cohesion starts weakening. We see the initiation of new cracks around the rupture tip and a highly perturbed particle velocity field on the damage side of the main fault. The extensional side of the main fault is damaged, whereas almost no damage is observed in the compressional side, which is supported by the theoretical analysis of potential failure area (*Poliakov et al.*, 2002; *Rice et al.*, 2005) and other simulations (e.g. *Andrews*, 2005). The secondarily activated cracks form an intricate network by means of crack coalescence, and comprise of tensile, shear and mixed mode cracks. We later discuss this secondary fracturing process in the off-fault medium, and its effect on the radiated wave field near the fault and the overall energy budget. Figures 3.3 to 3.6 are a sequence of snapshots for this case, where the rupture propagation, radiation and the evolution of secondary fracture network are illustrated.

Figure 3.7 is a set of snapshots for the supershear case with S = 0.7. The rupture is nucleated and propagates with sub-Rayleigh rupture velocity in the earlier phase. Then a daughter crack is born ahead of the rupture front at T = 4.7 s, which then transitions to a supershear rupture. During the rupture transition from sub-Rayleigh to supershear, a characteristic damage pattern appears; there is a gap of off-fault cracks around the transition phase (around x = 10.2 km in Figure 3.7). This can be explained by the Lorentz contraction of the process zone size. The process zone drastically shrinks at the limiting speed of the rupture, which is c_R in mode II crack. Since the damage zone size is scaled by the process zone size, it is minimized when the rupture velocity reaches the limiting speed. Then it resumes the off-fault cracking with the initiation of supershear rupture. This feature has been also pointed out by *Templeton and Rice* (2008); *Thomas and Bhat* (2018).

3.1.3 Implications for rupture velocity

Although the existence of coseismic off-fault damage has been widely studied, the effect of such dynamically activated fracture networks on the rupture dynamics still remains to

be fully elucidated because of the complex internal feedback of the activation and growth of secondary cracks, which changes the characteristics of the rupture and the subsequent radiation. To quantitatively evaluate it, we firstly focus on the slip velocity on the fault. Figure 3.8 shows the evolution of slip velocity on the main fault with four cases; S = 1.0 or 0.7, each of which with or without damage. Here we plot the contour of slip velocity in space and time. In Figure 3.8a, there is a clear transition from sub-Rayleigh to supershear around $x/R_0 = 20$, which is also shown in the inset. However, when the dynamically activated off-fault fracture network is taken into account, the supershear transition is not observed during the simulation as shown in Figure 3.8b. Hence, the secondary cracks can arrest supershear transition in a certain stress conditions. A more detailed parametric study is needed for future work. In this case, the rupture propagates at sub-Rayleigh speed with the oscillation of slip velocity due to the dynamically fracturing processes occurring in the vicinity of the rupture front. The inset in Figure 3.8b shows the snapshot of oscillating slip velocity on the main fault. The sharp peak of slip velocity is totally destroyed and the entire slip velocity fluctuates due to the off-fault cracking. Figures 3.8c and 3.8d show the cases with $S = 0.7$, where the rupture transitions to supershear because of the large ratio of the initial shear traction to the normal traction on the main fault. In this case, both with and without off-fault damage cases show supershear transition. The time of supershear transition is longer with off-fault damage due to the decrease of rupture velocity, whereas the difference of transition length is still obscure with these results. The two insets in the figures show the clear difference in the peak of slip velocity and the fluctuation with off-fault damage. In addition, the rupture arrival is delayed by off-fault damage, implying the decrease of rupture seed due to off-fault damage.

The rupture velocity is calculated from the set of first arrival times along the main fault. Figure 3.9 shows the evolution of rupture velocity in time. We take the time derivatives of first arrival time in discretized space along the main fault to calculate the representative rupture velocity at a certain position. Since it is difficult to capture the exact time when rupture velocity jumps to supershear, i.e. where the curve of first arrival time has a kink and is non-differentiable, the error caused by the smoothing of the rupture velocity is taken into account as shown by the error bars in Figure 3.9. Therefore the markers in the forbidden zone $c_R < v_R < c_s$ do not conclusively indicate that the rupture velocity is between them due to the uncertainty. In addition, there is also an error caused by the limited number of discretization in time and space with large rupture velocity, which is also included in the error bar.

Regardless of the uncertainty, the comparison between the no damage and with damage cases highlights the effect of the off-fault damage on the rupture velocity and the supershear transition. For S = 0.7, the rupture transitions to supershear in both cases though the rate of increase in rupture velocity is lower for the case with damage. For S = 1.0, however, the supershear transition is suppressed by coseismic off-fault damage. Thus, dynamic off-fault cracking around the rupture front can suppress the supershear transition because a part of strain energy accumulated in the vicinity of the rupture front, which is spent for the supershear transition in the case without damage, is dissipated by the secondary off-fault cracking.

Table 3.1: Parameters used for Case Study in Depth.

Variables	**Values**	**Unit**
E [a]	75	GPa
μ^a	30	GPa
ν [a]	0.25	-
ρ [a]	2700	kg m^{-3}
ρ_w	1000	kg m^{-3}
ψ	60	degree
S	0.7, 1.0	-
d_{MC}	0.4	-
f_s	0.6	-
f_d	0.2	-
p^p	75E3	GPa
p^c	75E3	GPa
G_{IIC}^{f*} [b]	3	MJ m^{-2}
$G_{IIC}^{f*,\text{off-fault}}$ [b]	0.01	MJ m^{-2}
D_c^* [b]	0.3	m
C_I^p [c]	8	MPa
C_{II}^p	Determined by equation (2.18)	
K_{IC}/K_{IIC} [d]	0.385	-

Note. [a] Assuming representative values of granite from *Nur and Simmons* (1969). [b] *Viesca and Garagash* (2015); *Passelègue et al*. (2016). [c] *Cho et al*. (2003). [d] *Rao et al*. (2003).

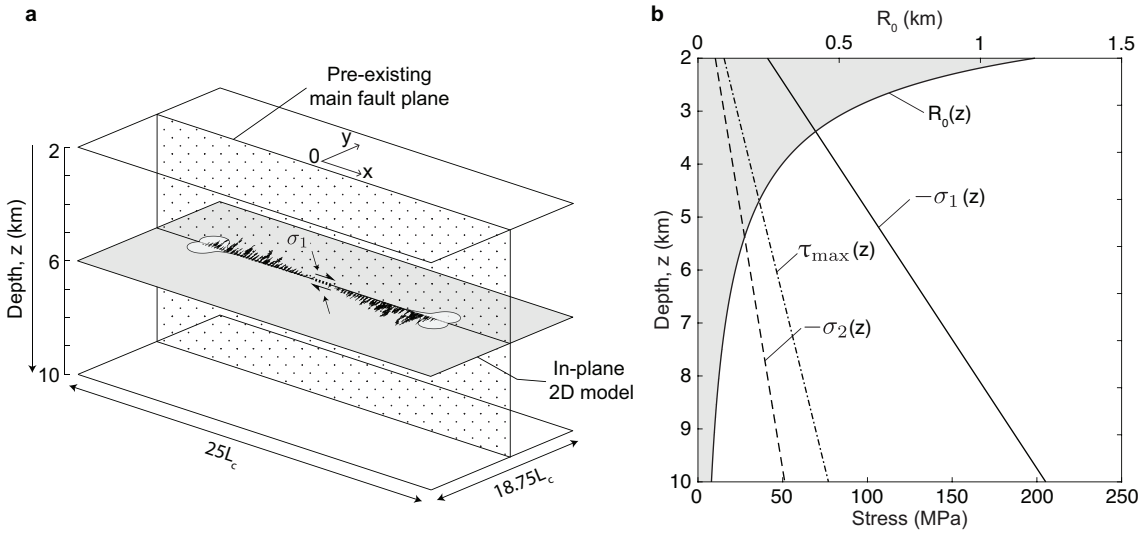

Figure 3.1: Schematic model for case study in depth. (a) In plane 2-D slices in depth for the earthquake rupture modeling with coseismic off-fault damage. Dotted plane indicates the pre-existing main fault plane on which only friction is operating. Nucleation patch is in the middle of the main fault. The tensile and shear cohesion are assigned in the off-fault medium so that it behaves as a brittle material. Simulations are performed every 1 km from z = 2 to 10km in depth. (b) The evolution of initial stress state and quasi-static process zone size in depth. Three lines indicate the maximum and minimum compressive principal stress $[-\sigma_1(z), -\sigma_2(z)]$, and the maximum shear traction $\tau_{max}(z)$. The line with shaded area indicates the quasi-static process zone size R_0 with constant G_{IIC} case in depth.

3.1.4 Mechanism of the activation of secondary off-fault fracture network

We next investigate the fracturing process in off-fault medium induced by the dynamic rupture propagation. Since the FDEM allows for both tensile and shear cracks, an intricate secondary fracture network is formed in the off-fault medium as dynamic rupture propagates on the main fault. In this section we aim to illustrate how the off-fault fracture network evolves, which also explains the damage pattern around the main fault. Figure 3.10 shows the tensile cracks, determined by the damage type $D_t \geq 0.9$, and shear cracks, $D_t \leq 0.1$, in the same condition with Figure 3.2. The three snapshots highlight the evolution of secondary cracks with time. To understand the stress state around dominantly tensile and shear cracks, the normalized first stress invariant

$$\frac{I_1(t)}{I_1^{init}} = \frac{\sigma_{kk}(t)}{\sigma_{kk}^0}, \tag{3.1}$$

for tensile cracks, and the normalized closeness to failure d_{MC}, defined by equation (2.17), for shear cracks are superimposed on the trace of secondary cracks. The first stress invariant I_1 implies the change of invariant volumetric and the closeness to failure d_{MC} indicates the distance of the current stress state to the failure in shear.

We plot the region where $I_1/I_1^{init} \leq 0.6$, which infers the stress state is less compressive than the initial stress state or extensional, for tensile cracks in Figure 3.10a. Similarly, the region where $d_{MC}/d_{MC}^{init} \geq 1.0$, which indicates the stress state is closer to Coulomb

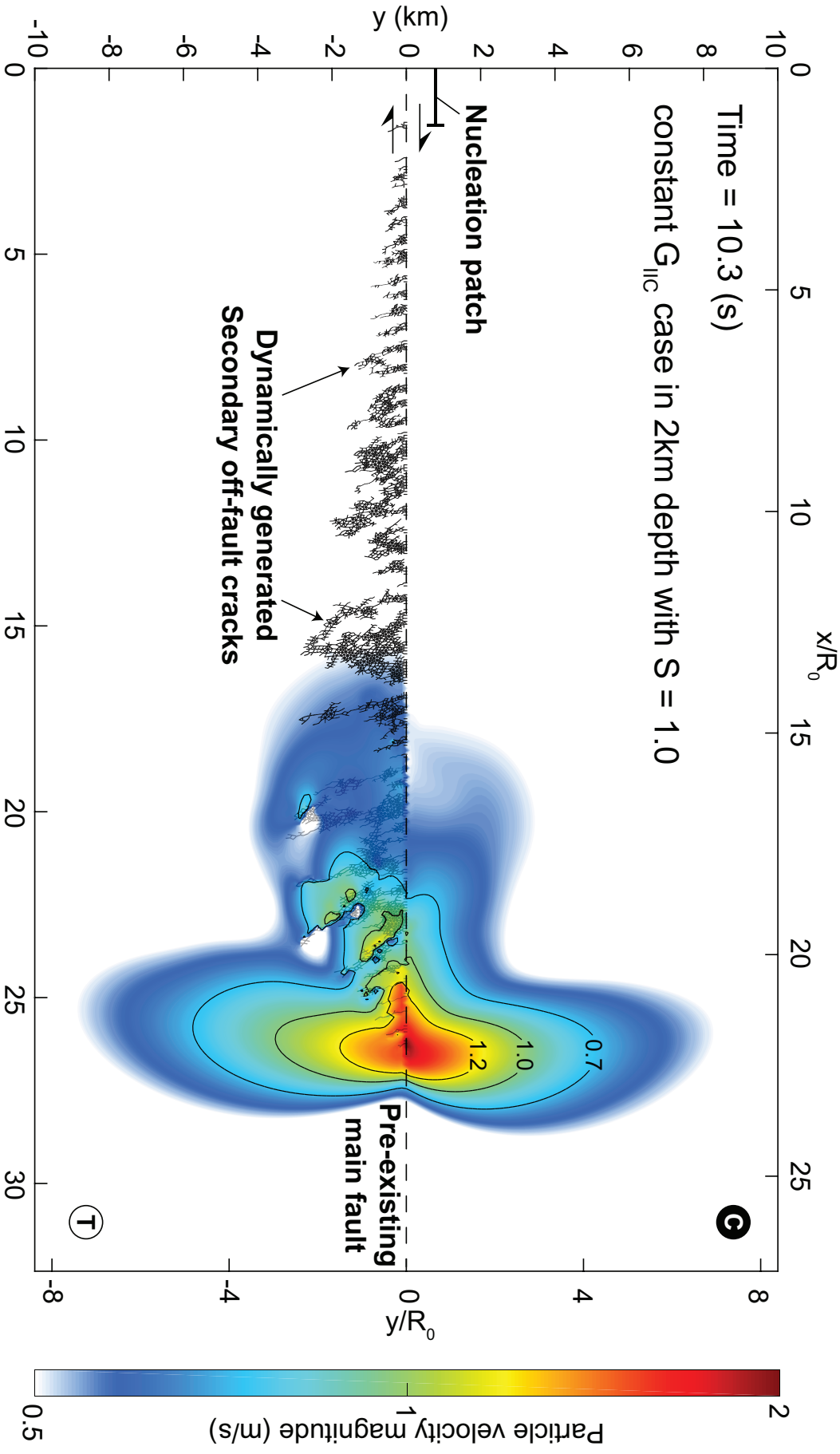

Figure 3.2: (Continued on the following page.)

Figure 3.2: Snapshot of a dynamic rupture with secondarily activated fracture network at 2 km depth. Color contour indicates the particle velocity magnitude, dotted line indicates the main fault and the solid lines show the secondary fracture network dynamically induced by the stress perturbation around rupture front. The bottom and left axis show the actual length scale, while the top and right axis show the nondimensionalized length scaled by R_0. S ratio is 1.0 and the frictional parameters are chosen with the condition of constant G_{IIC} with depth.

failure criteria for shear crack, is plotted in Figure 3.10b. Note that the both regions do not assure that the stress state reaches to the peak cohesion so that the region is not necessarily broken.

The three snapshots in Figure 3.10a illustrate that the tensile cracks are always initiated just behind the rupture front with a certain dominant orientation. This dominant angle is experimentally and theoretically studied by *Ngo et al.* (2012), and has a reasonable correspondence with the angle obtained from our analysis. It is remarkable that the position of tensile crack initiation is always behind the rupture tip and at the end of the dynamic process zone, $R_f(v_r)$ (*Viesca et al.*, 2009). Then it continues to propagate even after rupture front passes because the stress concentration still remains around the tip of secondary growing tensile cracks (see the dotted reference circle). Additional tensile cracks are also formed due to the intricate coalescence of cracks, including all crack types. On the other hand, shear cracks are activated after the initiation of the tensile cracks in the region located just behind of rupture front (Figure 3.10b). As the secondary fracture network matures, the number of shear cracks increases behind the rupture front. The intact region is first exposed to the stress concentration induced by the dynamic rupture propagation and then the internal feedback as shown in the reference circle in Figures 3.10b (i) and (ii). Once it generates new shear cracks in the off-fault medium, the concentrated stress is relaxed as shown in Figure 3.10b (iii). Figure 3.11 shows the rose diagram of the crack orientations. As expected, it has a dominant orientation around 60 degrees for tensile cracks, the direction of the maximum compressive principal stress. The shear cracks also have two dominant orientations, which correspond to conjugate failure planes (*Poliakov et al.*, 2002; *Rice et al.*, 2005). There is no dominant orientation for mixed mode cracks.

In this way, we can understand the elaborate fracturing process of off-fault medium induced by the dynamic earthquake rupture. This intricate process to form the secondary fracture network changes the rupture dynamics and causes additional radiation, which enhances high-frequency components in near-field ground motion discussed in the following section. In addition, we examined the mesh dependency of the fracturing process because the potential failure planes are restricted to the element boundary. This analysis can be found in Appendix C.

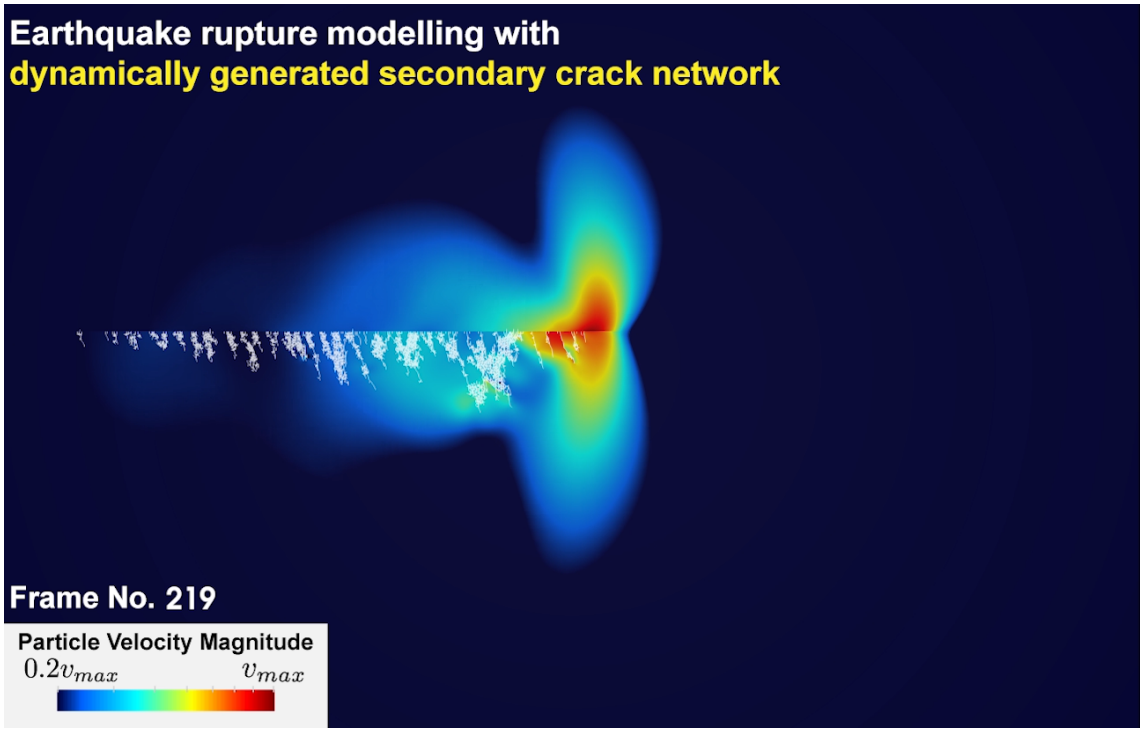

Figure 3.3: A series of Snapshots of dynamic earthquake rupture with coseismic off-fault damage. Color contour indicates particle velocity magnitude. White lines indicate the coseismic off-fault fracture network. Since all parameters are nondimensionalized in the simulation, time is represented by frame number.

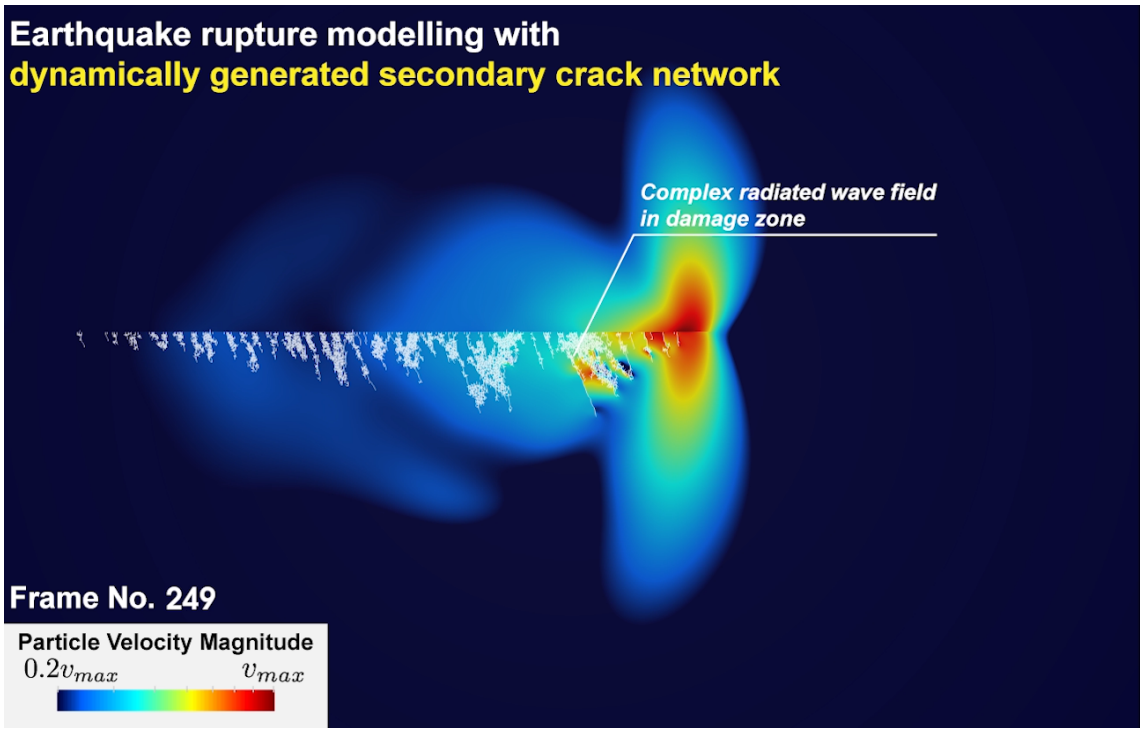

Figure 3.4: Snapshot at frame number 249.

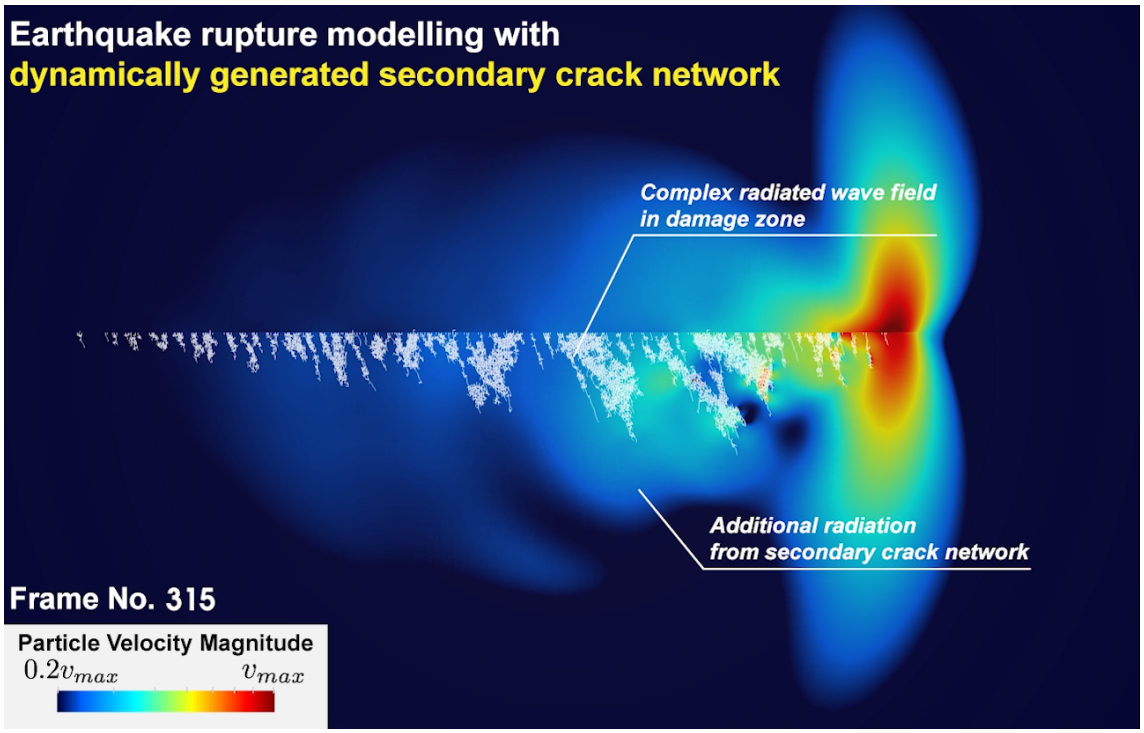

Figure 3.5: Snapshot at frame number 315.

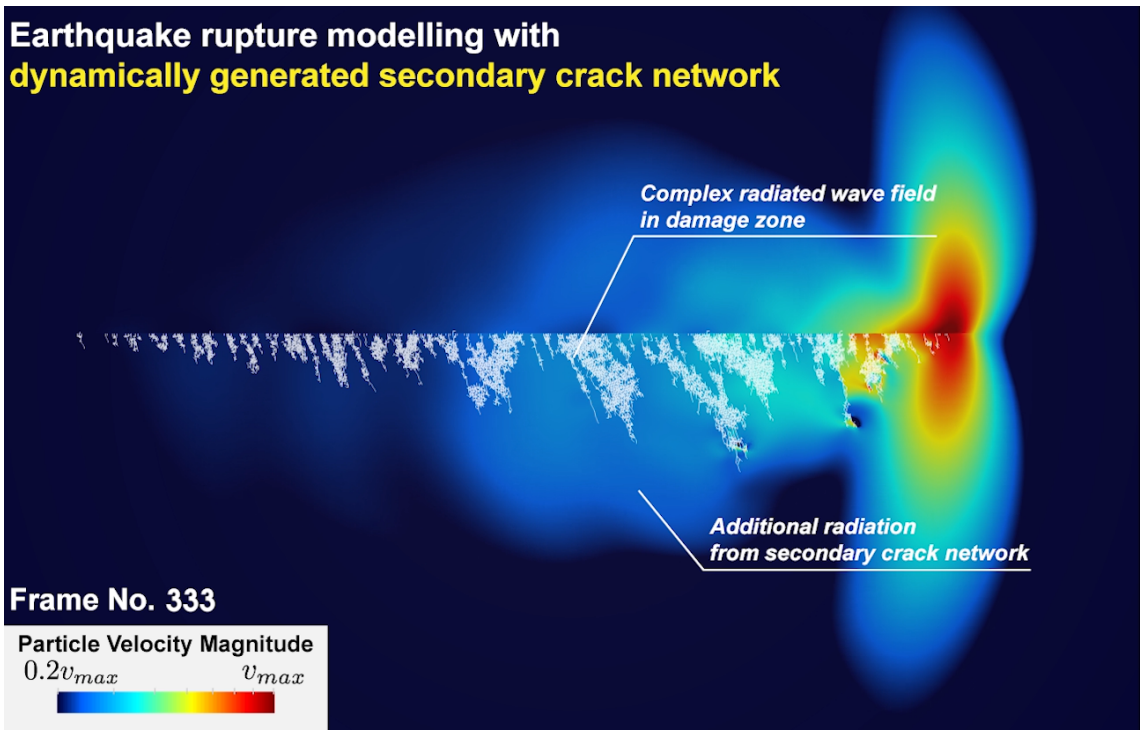

Figure 3.6: Snapshot at frame number 333.

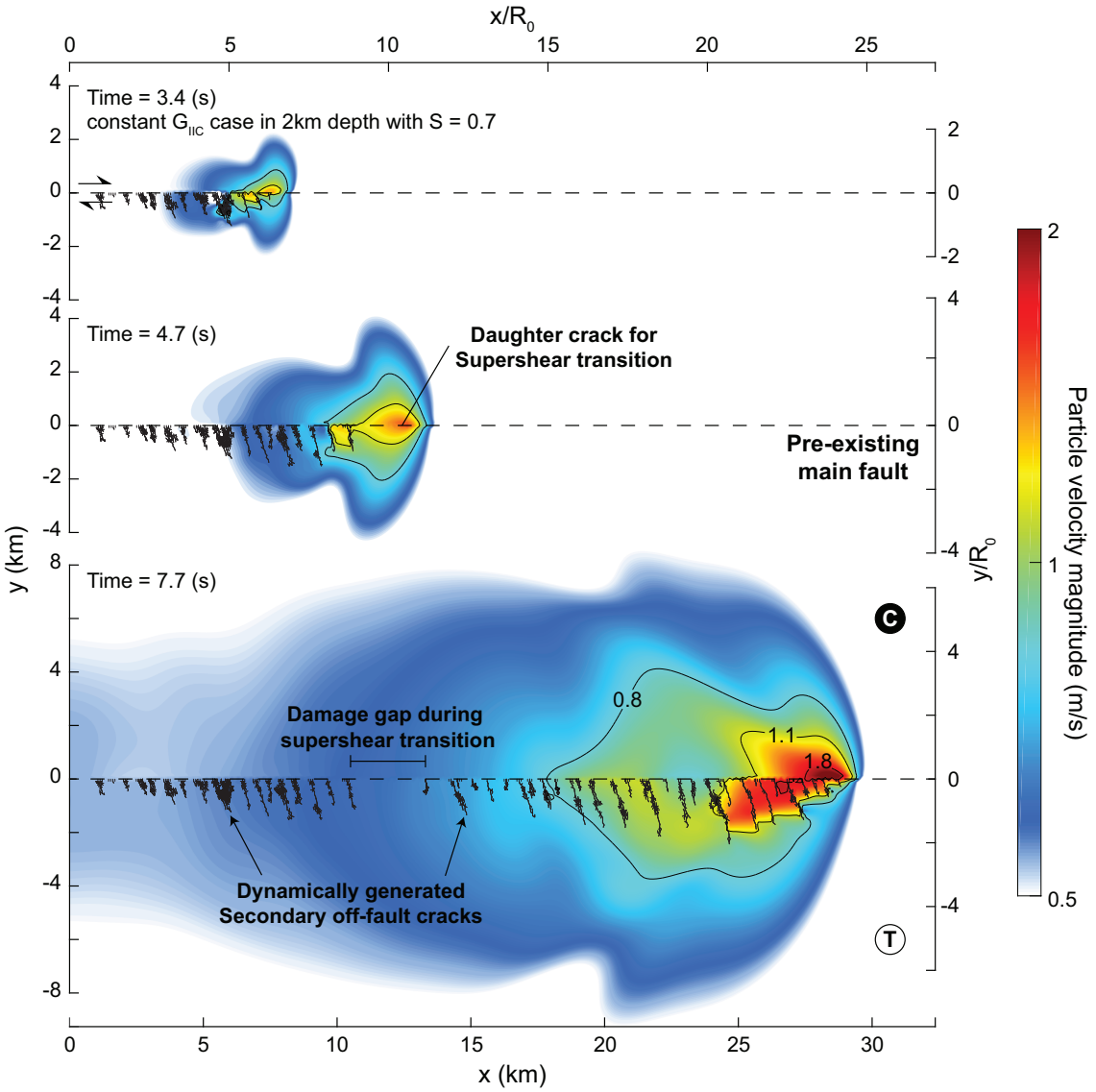

Figure 3.7: Snapshots of supershear rupture. The color contour and the lines follow the same format as Figure 3.2. S ratio is 0.7 and the frictional parameters are chosen with the condition of constant G_{IIC} case at 2 km depth. The rupture velocity is sub-Rayleigh until T=3.4s (top), then a daughter crack is born ahead of the sub-Rayleigh rupture front at T=4.7s (middle), which transitions to the supershear followed by the sub-Rayleigh rupture (bottom).

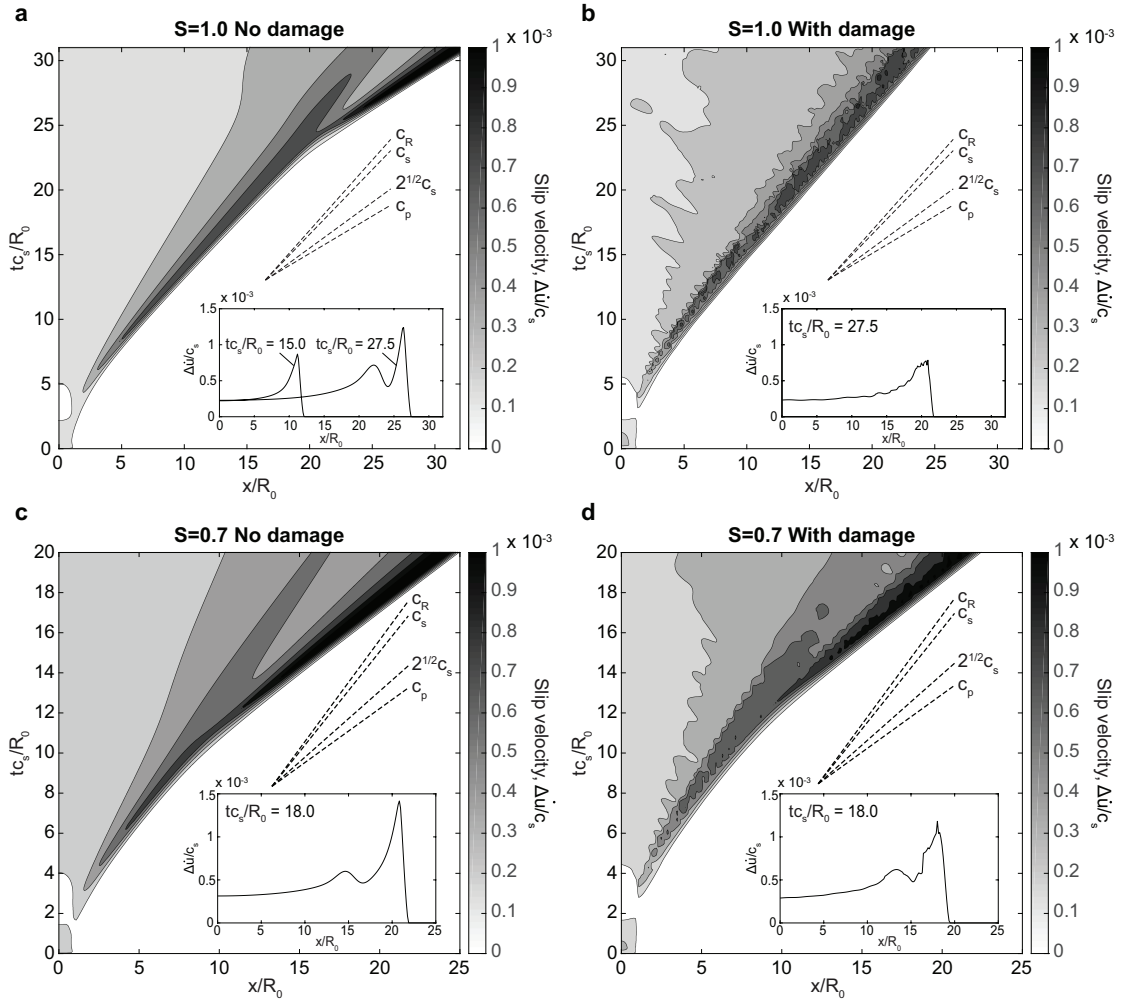

Figure 3.8: The evolution of slip velocity in time and space. There are four cases:(a) S = 1.0 with no damage in the off-fault medium (b) S = 1.0 with damage (c) S = 0.7 with no damage (d) S = 0.7 with damage. For the cases without damage, we set extremely high cohesion for both tensile and shear so that the off-fault medium is not broken; thus the medium behaves as purely elastic. The color contour indicates the slip velocity scaled by c_s. Dotted lines are the reference of the slope corresponding to each wave velocity. Insets show the distribution of slip velocity on the main fault at certain time.

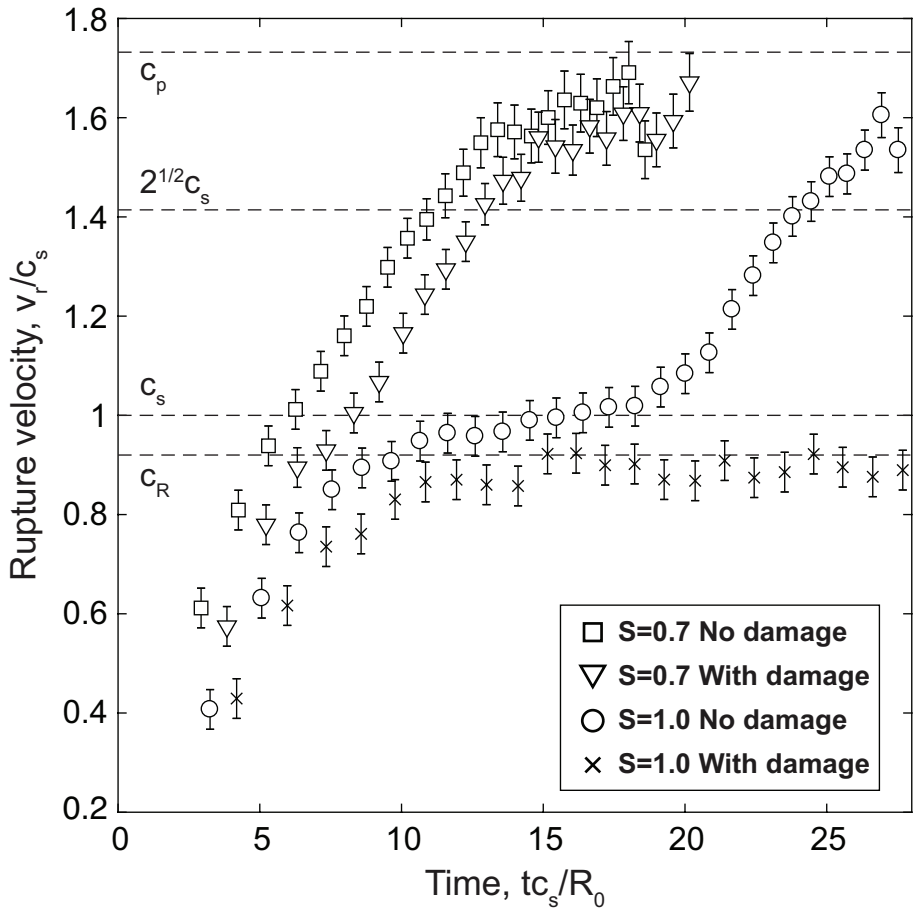

Figure 3.9: Rupture velocity inferred from Figure 3.8. Due to inherent discretization errors, it is difficult to precisely capture the jump of rupture velocity from sub-Rayleigh to supershear. The error is estimated from the difference between the slope of c_R and c_s, the grid spacing and the time step.

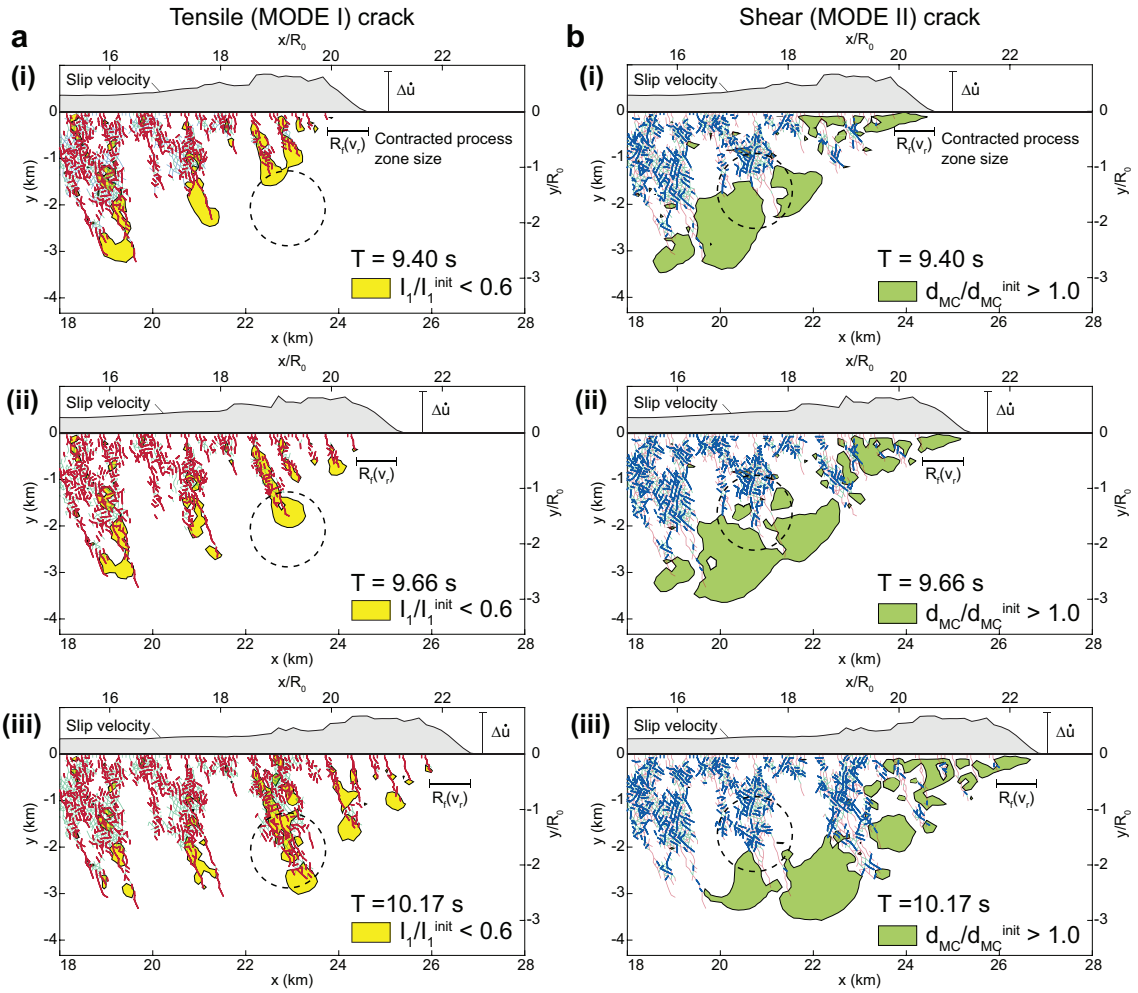

Figure 3.10: Fracturing process around the vicinity of the rupture front. (a) Activation and evolution of tensile cracks. Red heavy lines indicate the tensile crack with damage type $D_T \geq 0.9$ (see equation 2.12) and damage $D \geq 0.01$. There are three snapshots at (i) T=9.40s (ii) T=9.66s (iii) T=10.17s. Solid line on the top of the main fault indicates the slip velocity on the main fault. Dotted circle is plotted at the same position in the domain as a reference for comparison among the snapshots. The filled area in yellow shows where the ratio of the first stress invariant to its initial value $I_1(t)/I_1^{init}$ is less than 0.6. The lighter lines in the fracture network indicate shear and mixed mode cracks. $R_f(v_r)$ shows the process zone size. (b) Similar plot for shear cracks. Blue heavy lines indicate the shear crack with damage type $D_T \leq 0.1$ and damage $D \geq 0.01$. The filled area in green shows where the ratio of closeness to failure to its initial value $d_{MC}/d_{MC}^{init} > 1.0$, where d_{MC}^{init} is 0.4 everywhere in the domain.

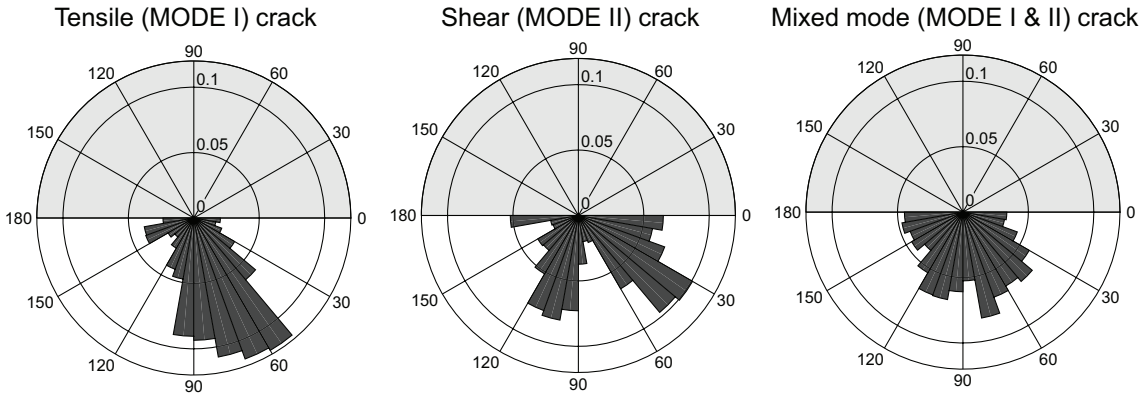

Figure 3.11: Rose diagram depicting the orientation of secondarily activated cracks at T= 10.17 s. The cracks in the right side of nucleation patch are evaluated ($x \geq 0$ in Figure 3.2) . The top half corresponds to the compressive side, whereas the bottom half corresponds to the extensional side.

3.2 High-frequency radiation

3.2.1 Enhanced high-frequency radiation by the secondary off-fault cracks

Since the enhanced high-frequency radiation is of interest to earthquake engineering, the origin of high-frequency radiation has been studied over decades (e.g. *Madariaga*, 1977; *Hanks and McGuire*, 1981; *Hanks*, 1982; *Dunham et al.*, 2011b; *Castro and Ben-Zion*, 2013; *Passelègue et al.*, 2016). There are multiple factors that enhance the high-frequency radiation, such as sudden nucleation and arrest of rupture, complex fault geometry, roughness of the fault surface and the nonlinear response in subsurface sedimentary rock. In this study, we propose that the coseismic off-fault damage is also a candidate which contributes to the enhancement of high-frequency radiation. Since the intricate fracture network is dynamically formed during the rupture propagation, the radiated wave field from the main rupture is significantly perturbed by the additional radiation from the secondary fracture network as well as the oscillation of the slip velocity on the main fault. It is noteworthy that the off-fault cracks also dissipate the stored strain energy by the breakdown of cohesion and the friction, which is crucial for the overall energy budget associated with dynamic earthquake rupture.

To quantitatively evaluate the enhancement of high-frequency radiation, we employ the maximum cutoff frequency in the amplitude spectrum of fault-normal acceleration, which is also called f_{max} in seismology (*Hanks*, 1982). In this paper, however, we do not use the latter to avoid the confusion.

Figure 3.12 shows an example of the comparison in amplitude spectrum with and without off-fault damage. Fault-normal acceleration is used in this analysis. The signal time window starts from the first arrival time at the location of each sensor and ends at the end of the simulation. We then apply a band-pass filter of 0.1 Hz and 99 Hz, and a Tukey window to the acceleration in time domain. We compare the values of the maximum cutoff frequency, which indicate the enhancement of high-frequency components in ground acceleration.

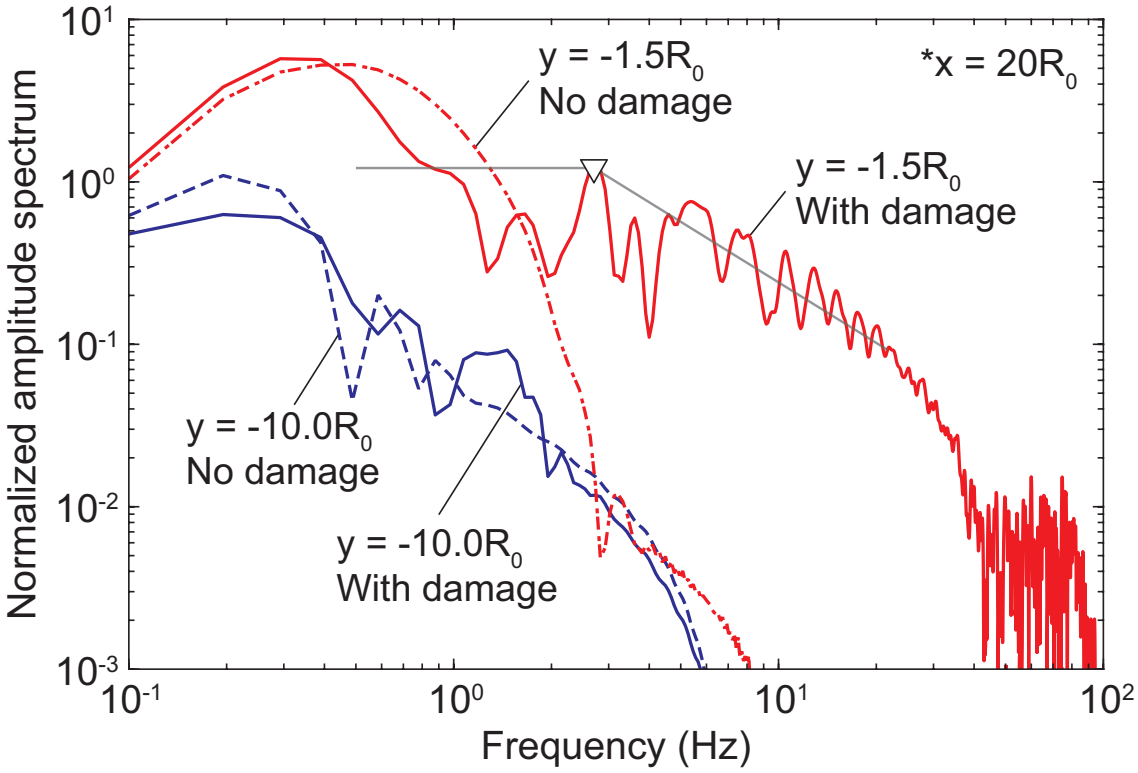

Figure 3.12: Comparison of amplitude spectrum with and without off-fault damage. Solid line indicates the fault-normal amplitude spectrum with off-fault damage at $x = 20R_0, y = -1.5R_0$ (in red) and $-10.0R_0$ (in blue). Dotted line indicates the same quantities with no damage cases. Inverted triangle indicates the inferred maximum cutoff frequency. Amplitude spectrum is normalized by the amplitude at lowest frequency for the cases without damage with $y = -1.5R_0$.

Figure 3.13 shows the spatial distribution of maximum cutoff frequency, its profile across the fault, the waveforms and the spectrogram of a sensor near the main fault. Figure 3.13a highlights the region where the high-frequency radiation is enhanced, which mostly overlaps with the secondary fracture network. To demonstrate it, we infer the damage zone W_{damage} from the envelope of the secondary fracture network and plot the profiles of maximum cutoff frequency across the main fault normalized by W_{damage} (Figure 3.13b). The stack of profiles for different positions along the main fault suggests that the high-frequency components are enhanced within $-1 \leq y/W_{damage} \leq 0$, i.e. only in the damage zone. The high frequency radiation is then attenuated by the geometric dispersion outside of the damage zone. Thus the high-frequency radiation caused by the off-fault damage can be observed only in near-field ground motion. Figure 3.13c shows the waveform of the fault-normal acceleration corresponding to the location indicated in Figure 3.13a. The spike is observed close to the fault in the extensional side after the P and SV waves arrive, which is caused by the secondary cracking. This sequence is consistent with the mechanism of secondary off-fault cracking discussed above; the secondary fracture network evolves after the rupture passes on the main fault. The spectrogram in Figure 3.13d illustrates that the spike primarily contributes to the high-frequency radiation.

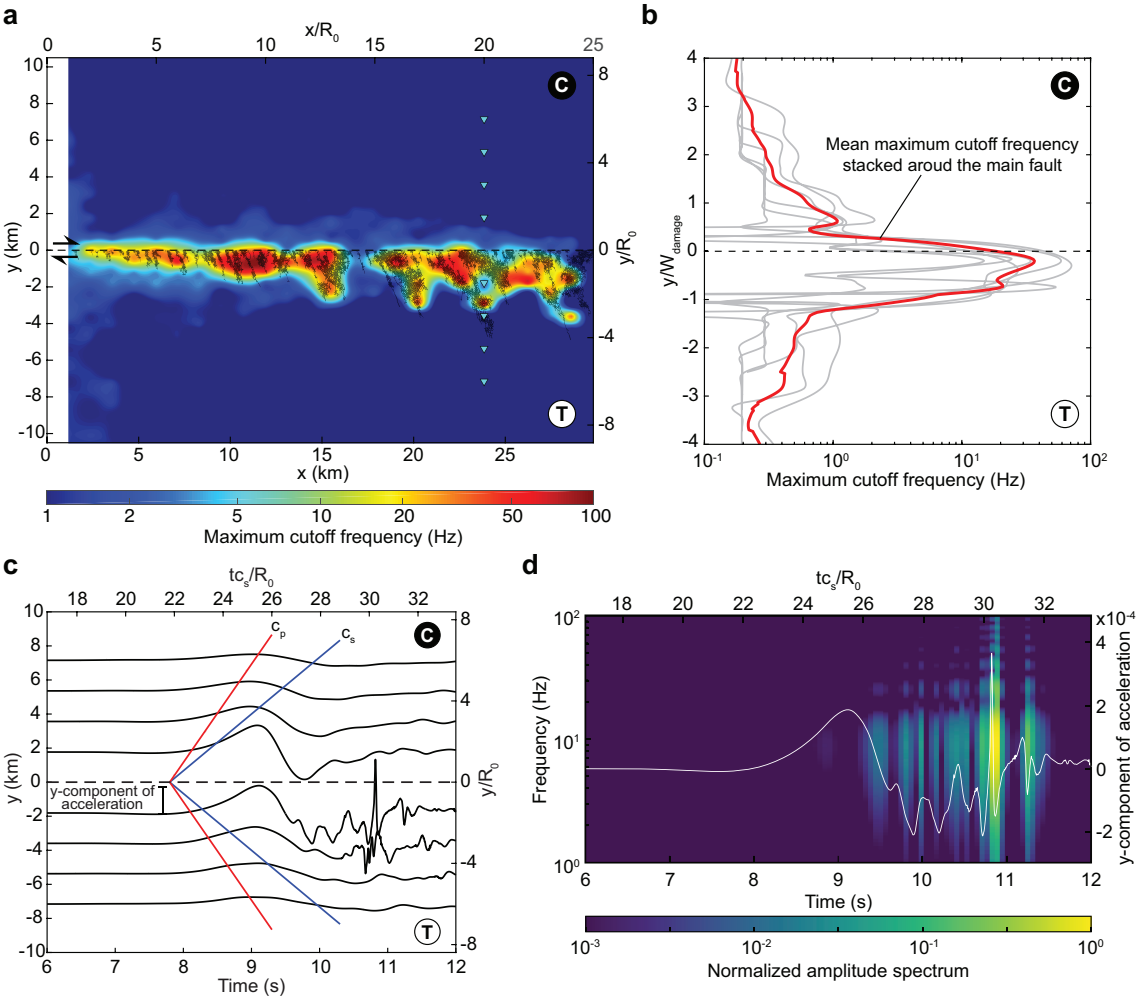

Figure 3.13: Enhanced high-frequency radiation in near-field ground motion. (a) Spatial distribution of maximum cutoff frequency. Color contour shows the maximum cutoff frequency. the "C" and "T" indicate the compressive and extensional side respectively. The off-fault cracks are superimposed with the black lines. This result corresponds to S=1.0, constant G_{IIC} case at 2 km depth. Inverted triangles (in cyan) correspond to the sensor locations for (c). (b) Maximum cutoff frequency profiles across the main fault. The distance y is normalized by the width of the damage zone. Lighter gray lines indicate the profiles at every $2.5R_0$ from $x/R_0 = 2.5$ to $x/R_0 = 25$. The thick red line indicates the mean value of all the profiles. (c) Fault-normal acceleration at the locations indicated in (a). Solid color lines indicates the P and S wave arrival times respectively. (d) Fault-normal acceleration spectrogram at $x/R_0 = 20$ and $y/R_0 = -1.5$. The associated waveform is superimposed in white.

3.2.2 Experimental results of high-frequency radiation

The enhanced high-frequency radiation from the dynamic ruptures is also studied by experimental analyses (e.g. *Passelègue et al*., 2016). They conducted systematic stick-slip experiments with saw-cut Westerly granites under servo-controlled triaxial loading, i.e., the axial stress, σ_1, and the confining pressure, σ_3, ranging from 10 to 90 MPa, to show the enhanced high-frequency radiation in acoustic recordings of the stick-slip events. The acoustic sensors are externally located on the surface of specimen as shown in Figure 3.14a, which record the motion of the normal component to the surface. The array of acoustic sensors is shown in Figure 3.14b. The representative Fourier spectra are obtained by taking an average of 13 acoustic sensors indicated in the Figure 3.14b in order to get rid of directivity effects.

Figure 3.14c shows the Fourier spectra with different confining pressures. For the sake of comparison, each spectral amplitude is normalized by its maximum value. The enhanced high-frequency components are clearly observed under higher confining pressures. The theoretical corner frequencies, f_c, for v_r=2000m/s (for sub-Rayleigh) and v_r=5000m/s (for supershear) are indicated, which implies that the rupture transitions to supershear with $\sigma_3 > 20$MPa. Certainly, one of the possible reasons for the enhanced high-frequency components is the supershear transition. However, there is also a characteristic enhanced frequency band from 400kHz to 800kHz, which can be caused by the coseismic off-fault damage. Thus they conducted back-projection analysis to investigate the spatiotemporal evolution of seismic energy release in this frequency band. Figure 3.14d shows a snapshot of back-projection results for a certain stick-slip event with $\sigma_3 = 90$ MPa. The rupture is spontaneously nucleated at the edge of the saw-cut surface, and propagates downward. The color contour shows the normalized coherency function, which indicates the most likely location of the origin of the signal within this frequency band. The theoretical rupture front is also superimposed on the fault surface. It shows that the high-frequency signals within this band originate just behind the rupture front, which can be caused by the secondary off-fault fracture networks as compared to the inferred fracture mechanism discussed in subsection 3.1.4. In summary, the experimental results demonstrate the first-order analysis of the mechanism of enhanced high - frequency radiations, which is in good agreement with the secondary fracturing mechanism inferred by the dynamic earthquake rupture modeling with coseismic off-fault damage. Further information of these experiments can be found in *Marty et al*. (2018).

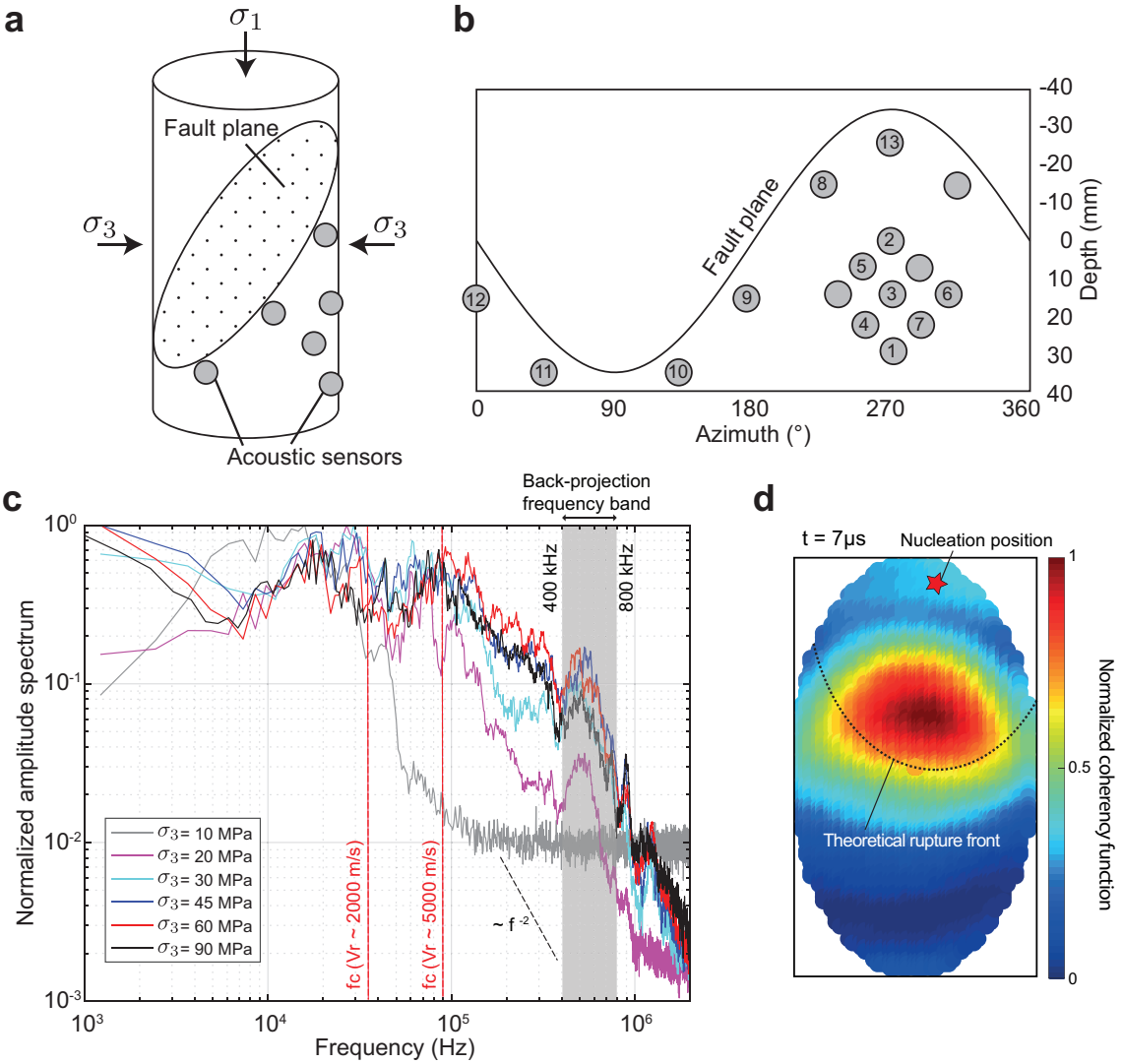

Figure 3.14: Enhanced high-frequency radiation and back-projection analysis in laboratory experiments. (a) Experimental setup of stick-slip experiments with saw-cut Westerly granite. The specimen is pre-cut, and stick slip events spontaneously occur under servo-controlled triaxial loading. Acoustic sensors are externally located on the surface of the specimen. (b) Array of acoustic sensors. The sensors assigned numbers are used to calculate the averaged Fourier spectra. (c) Fourier spectra under different confining pressures. Red dashed lines indicate the theoretical corner frequency at $v_r = 2000$m/s and $v_r = 5000$m/s. Highlighted box indicates the frequency band used for the back-projection analysis. (d) Snapshot of back-projection results with $\sigma_3 = 90$MPa at $t = 7\mu$s from the rupture nucleation. Red star indicates the nucleation position. Dashed line indicates the theoretical rupture front. Color contour shows the normalized coherency function, which indicates the most likely location of the origin of signals with the frequency band.

3.3 Case study at different depths

We next investigate the evolution of off-fault fracture network with depth. In general, the flower-like structure of the damage zone with depth has been widely accepted, which assumes the damage zone width becomes narrower with depth and extends towards the surface of earth's crust (*Ben-Zion et al.*, 2003; *Ma and Andrews*, 2010; *Perrin et al.*, 2016b). We examined a set of cases as described in section 3.1.1 to explore the change of damage pattern and the damage zone width with depth. Figure 3.15 show the pattern of secondary fracture network and the rose diagram of orientation of off-fault cracks for the three cases with constant G_{IIC} in depth. The isolated fracture network, in which all cracks coalesce with each other, is separately plotted with different colors. The dimensions are scaled by R_0 so that the size of the fracture network are comparable by visual inspection of the figure. The number of isolated fracture network is higher for the shallower case than the deeper case, implying that the off-fault fracture network becomes more intricate and denser with depth. The orientation of tensile and shear cracks is slightly more distributed with depth though it still has preferable orientations.

Figure 3.16 shows the distribution of fracture density around the fault at 2km and 10km depths, and the profiles of fracture density as a function of the fault. To evaluate the distribution of fracture density, we firstly impose representative square grids around the fault, and calculate the normalized fracture density, $\hat{P}_{21}$, in the each grid defined as

$$\hat{P}_{21} = \frac{\text{length of fracture trace in a grid}}{\text{area of grid}} R_0. \tag{3.2}$$

We carefully chose the grid size, which involves a reasonable number of potential failure planes. In this analysis, the grid size is set as $0.2R_0$, which is, on average, three times larger than the size of potential failure planes. As discussed above, the fracture density is globally higher at 10 km depth when comparing Figures 3.16a to 3.16b, whereas the distribution of fracture density is sparse for the both cases.

We then show the profiles of fracture density as a function of distance from the fault (Figure 3.16c). To reduce the dependence of the fracture density on evaluating locations, we take an average of fracture density in the rectangular boxes of the evaluation area indicated in Figures 3.16a and 3.16b. The profiles show exponential decrease in fracture density with distance from the fault at both 2km and 10km depths, as pointed out by field observations (e.g. *Mitchell and Faulkner*, 2012). Note that the resolution of the fracture density close to the main fault is not enough to check for pulverized rocks because of limitations in the size of the potential failure planes. It will be resolved by incorporating the FDEM-based continuum-discontinuum analysis with constitutive damage models. It is also noteworthy that the magnitude of $\hat{P}_{21}$ does not monotonically increase with depth because of the dependency of the evaluation locations and the complicated feedback inside the off-fault fracture network.

Figure 3.17 shows the evolution of the damage zone width with depth for the constant G_{IIC} and constant D_c cases. The damage zone is inferred from the envelope of secondary fracture network at $x = 5R_0$, $10R_0$ and $20R_0$. Since there are few cracks being activated in the compressional side, we only plot the extensional side. In both cases, the damage

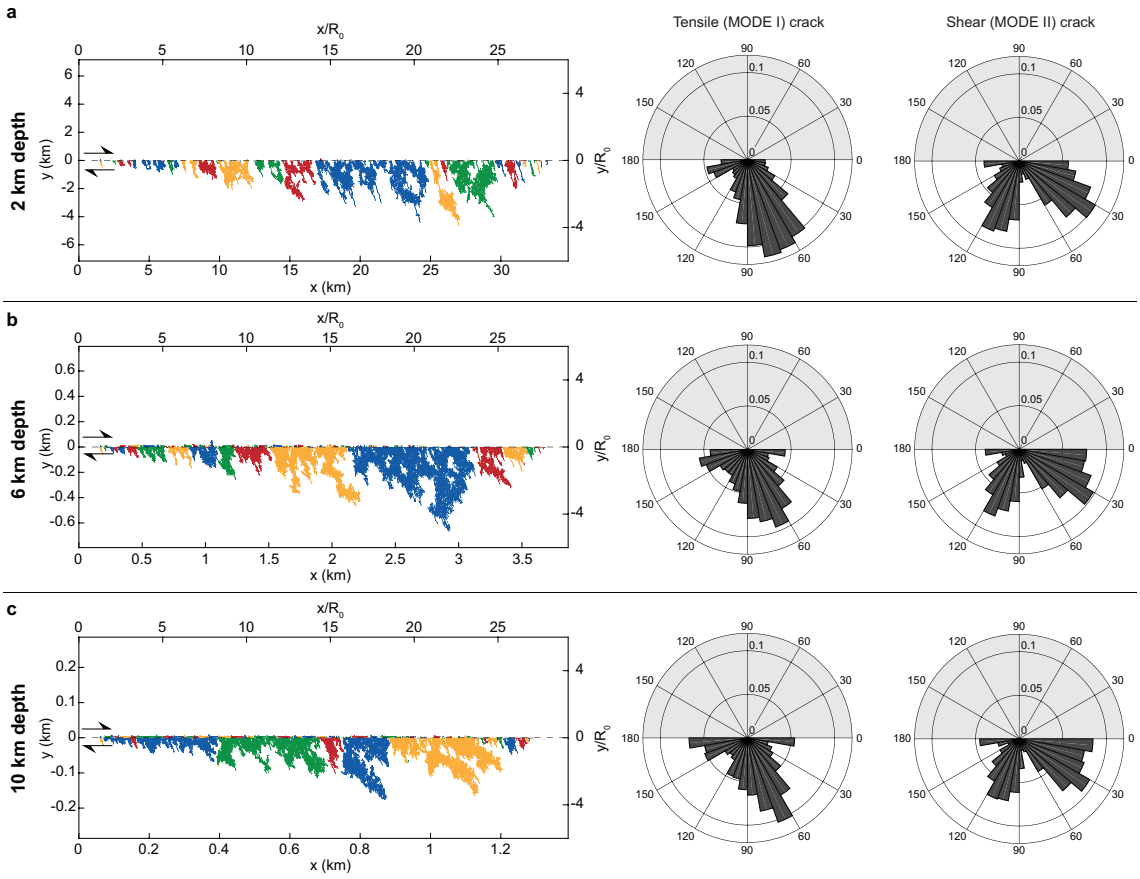

Figure 3.15: Comparison of secondary fracture network and rose diagram at (a) 2km (b) 6 km (c) 10 km depths with constant G_{IIC} case. S ratio is equal to 1.0. An isolated fracture network, in which all small cracks connect with each other, is indicated by different colors. Rose diagrams are plotted at T=12.75 s.

zone width follows, up to a constant factor, the process zone size. Hence the damage zone width decreases with depth, forming the flower-like structure, with fracture connectivity increasing with depth.

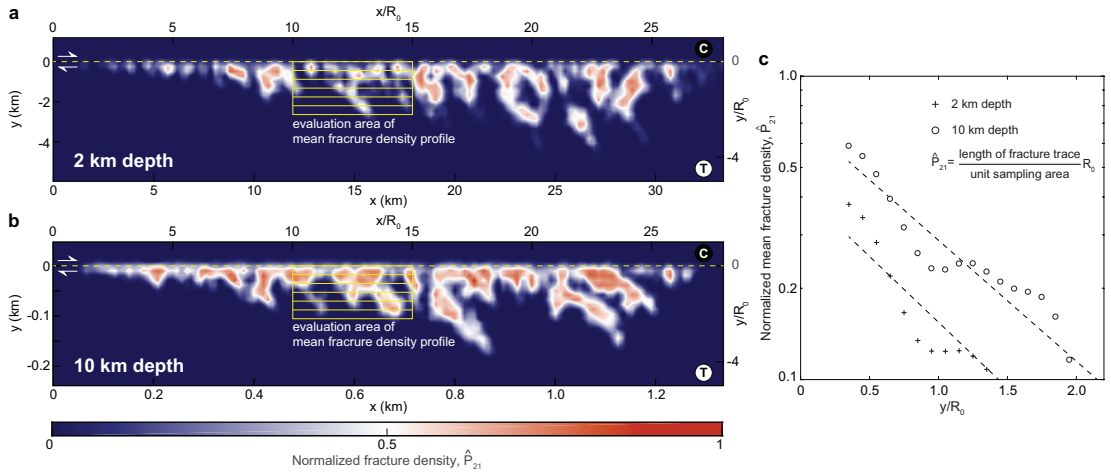

Figure 3.16: Fracture density in off-fault medium at (a) 2km and (b) 10km depths for the cases of constant G_{IIC}. Color contour indicates the normalized fracture density. Boxes indicate the evaluation area of the mean fracture density profiles. The size of inner boxes is exaggerated. (c) Profiles of the mean fracture density as a function of distance from the fault. Markers indicate the mean fracture density in the inner boxes of the evaluation area. Dashed lines indicate fitting curves of each depth. Note that the y-axis is in log scale.

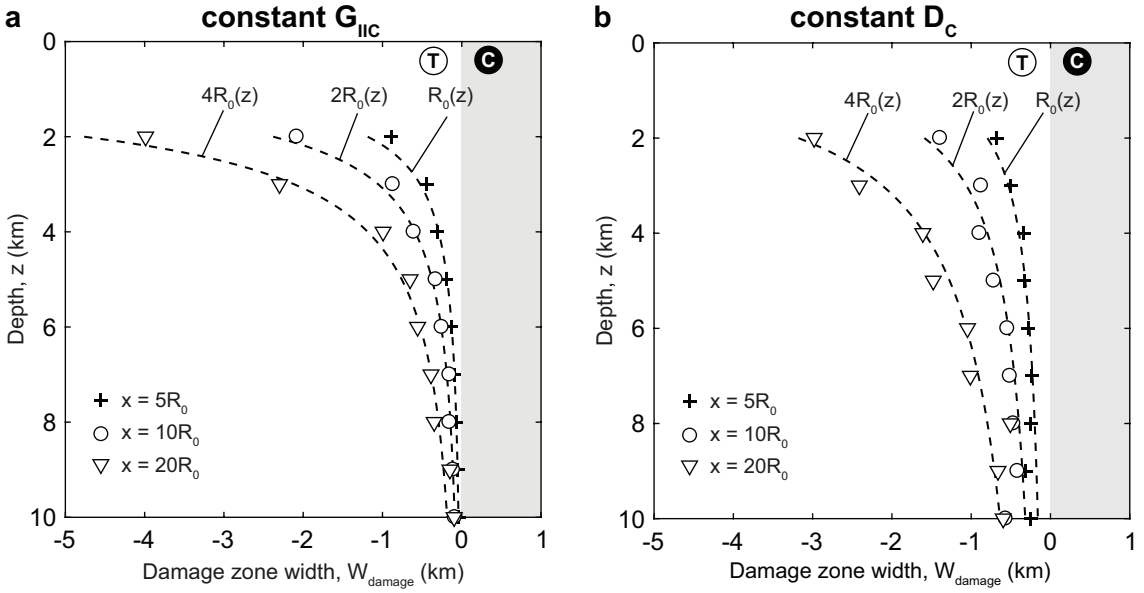

Figure 3.17: Evolution of damage zone width with depth for the cases of (a) constant G_{IIC} and (b) constant D_c. S ratio is equal to 1.0. Type of markers indicates the position on the main fault at which the damage zone width is evaluated. The dotted lines indicate the quasi-static process zone size scaled by constant factors.

3.4 Overall energy budget of earthquake rupture with coseismic off-fault damage

The overall energy budget of an earthquake event plays a key role in understanding the characteristics of the earthquake source, change of potential energy and its associated radiation. The schematic of energy budget was proposed by *Sibson* (1977), which describes the energy flow from a change of potential energy to dissipated energy by frictional processes and energy radiated as seismic waves. Here we first derive the formulation of energy balance, which can be utilized to estimate overall energy budget for dynamic earthquake rupture with coseismic off-fault damage. Although there are various approaches to derive the energy conservation law of earthquake ruptures (e.g. *Rivera and Kanamori*, 2005; *Fukuyama*, 2005; *Shi et al.*, 2008; *Xu et al.*, 2012a), we revisit the derivation of it to identify the energy components in a suitable form for the analysis of the overall energy budget.

3.4.1 Energy balance of earthquake rupture

Consider a volume V, whose surface is S_0, that encompasses faults represented by Γ. Now assume that this volume is linear elastic and only undergoes small deformations. It is notable that this volume is not the entire earth though the formulation below can be simplified to consider the entire earth in which case the surface S_0 is traction free. Let n_i be the outward pointing unit normal to the surface and $T_i = \sigma_{ij} n_j$ be the traction distribution on the surface. u_i, $\dot{u}_i$ and $\ddot{u}_i$ are the particle motion, particle velocity and particle acceleration on the surface, respectively. The linear momentum balance is written as

$$\rho \ddot{u}_i = \frac{\partial \sigma_{ij}}{\partial x_j}, \tag{3.3}$$

where ρ is density. The kinetic energy per unit volume is defined as

$$K = \frac{1}{2} \rho \dot{u}_i \dot{u}_i. \tag{3.4}$$

Consider the integral of the time derivative of K over the volume V,

$$\int_V \frac{dK}{dt} dV = \int_V \rho \ddot{u}_i \dot{u}_i dV = \int_V \frac{\partial \sigma_{ij}}{\partial x_j} \dot{u}_i dV = \int_V \left[\frac{\partial (\sigma_{ij} \dot{u}_i)}{\partial x_j} - \sigma_{ij} \frac{\partial \dot{u}_i}{\partial x_j} \right] dV \tag{3.5}$$

We then apply the divergence theorem to equation (3.5). Since we have a discontinuity in the volume V, the divergence theorem is written as

$$\int_V \frac{\partial F_i}{\partial x_i} dV = \int_{S_0} F_i n_i dS + \int_{\Gamma^+ + \Gamma^-} F_i \eta_i dS, \tag{3.6}$$

where η_i is the normal to the fault surface Γ and $\mathbf{F}$ is an arbitrary vector field, which is continuously differentiable in the volume V. Γ is divided into upper and lower surfaces, which are denoted as Γ^+ and Γ^-. The traction vectors associated with each surface are denoted as T_i^+ and T_i^-, which are equal in magnitude but opposite in direction. Thus $T_i^+ = -T_i^-$. On the surface Γ, we define the relative particle velocity $\Delta \dot{u}_i = \dot{u}_i^+ - \dot{u}_i^-$.

Considering the orientation of surface integral, the instantaneous rate of work being done on the faults is written as

$$\int_{\Gamma^+} T_i^+ \dot{u}_i^+ dS + \int_{\Gamma^-} T_i^- \dot{u}_i^- dS = \int_{\Gamma} T_i \Delta \dot{u}_i. \tag{3.7}$$

where Γ is now a single crack interface of fault. Then the right side of equation (3.5) is transformed with the redefined divergence theorem as

$$\begin{aligned}\int_V \frac{dK}{dt} dV &= \int_V \left[\frac{\partial(\sigma_{ij}\dot{u}_i)}{\partial x_j} - \sigma_{ij}\frac{\partial \dot{u}_i}{\partial x_j} \right] dV \\ &= \int_{S_0} T_i \dot{u}_i dS + \int_{\Gamma^+} T_i^+ \dot{u}_i^+ dS + \int_{\Gamma^-} T_i^- \dot{u}_i^- dS - \int_V \sigma_{ij}\frac{\partial \dot{u}_i}{\partial x_j} dV \\ &= \int_{S_0} T_i \dot{u}_i dS + \int_{\Gamma} T_i \Delta \dot{u}_i dS - \int_V \sigma_{ij}\frac{\partial \dot{u}_i}{\partial x_j} dV\end{aligned} \tag{3.8}$$

Equation (3.8) represents the work balance in the volume V including the faults. By integrating Equation (3.8) over time, it is rewritten as

$$E_{S_0} + E_F + E_K = -\Delta W, \tag{3.9}$$

where

$$E_{S_0} = -\int_0^t dt \int_{S_0} T_i \dot{u}_i dS, \tag{3.10}$$

$$E_F = -\int_0^t dt \int_{\Gamma} T_i \Delta \dot{u}_i dS, \tag{3.11}$$

$$E_K = \int_V K dV, \tag{3.12}$$

$$\Delta W = \int_0^t dt \int_V \sigma_{ij}\frac{\partial \dot{u}_i}{\partial x_j} dV = \int_V \left[\int_0^{\varepsilon_{ij}} \sigma_{ij} d\varepsilon_{ij} \right] dV. \tag{3.13}$$

ε_{ij} is the strain tensor

$$\varepsilon_{ij} = \frac{1}{2}\left[\frac{\partial u_i}{\partial x_j} + \frac{\partial u_j}{\partial x_i} \right]. \tag{3.14}$$

ΔW is the elastic strain energy, which is independent of the integration path (*Palmer and Rice*, 1973). Note that the initial strain is defined to be zero, whereas the initial stress is large. This configuration is commonly used in seismology, as discussed in *Aki and Richards* (2002, BOX 8.5).

It is notable that the energy balance in equation (3.9) is identically conserved during an earthquake rupture even with coseismic off-fault damage. In general, we prescribe the faults Γ in the volume and do not allow for nucleating new fracture surfaces in the medium. However, by supposing all interfaces of elements in the volume as potential failure planes, whose relative displacement Δu is zero until the cohesion starts to weaken, and adequately evaluating the dissipated energy E_F after fracturing, we can estimate the dynamic change of each energy component during an earthquake. In fact, the relative displacement Δu on the potential failure plane is not exactly zero due to the penalty function method in FDEM

framework. Thus, we chose a penalty term p^p large enough so that the accumulated error caused by potential energy of penalty function method is negligible compared with the other energy components.

E_F represents the consumed energy on the fault Γ. It is decomposed into the tensile and shear components as following (*Shi et al.*, 2008)

$$E_F = -\left[\int_0^t dt \int_\Gamma T_n \Delta\dot{u}_I dS + \int_0^t dt \int_\Gamma T_t \Delta\dot{u}_{II} dS\right] \tag{3.15}$$

where T_n and T_t are normal and shear traction respectively, $\Delta\dot{u}_I$ is opening displacement and $\Delta\dot{u}_{II}$ is the amount of slip on the cracks. For mode I tensile crack only cohesion is applied as contact force, which is prescribed by the elastic loading and the softening parts in the linearly weakening cohesion model as described in section 2.3.2. Thus

$$\begin{aligned} -\int_0^t dt \int_\Gamma T_n \Delta\dot{u}_I dS &= -\int_\Gamma \left[\int_0^{\delta_I^{c,e}} C(\delta_I) d\delta + \int_{\delta_I^{c,e}}^{\delta_I^{c,c}} C(\delta_I) d\delta\right] dS \\ &= E_I^e + E_I^c, \end{aligned} \tag{3.16}$$

where E_I^e is the energy consumed in elastic loading part and E_I^c is the energy dissipated for the weakening of cohesion. The consumed energy of mode II shear crack is decomposed into cohesion and friction, which follow the prescribed cohesion and friction law, written as

$$\begin{aligned} &-\int_0^t dt \int_\Gamma T_t \Delta\dot{u}_{II} dS = \\ &-\int_\Gamma \left[\int_0^{\delta_{II}^{c,e}} C(\delta_{II}) d\delta + \int_{\delta_{II}^{c,e}}^{\delta_{II}^{c,c}} C(\delta_{II}) d\delta + \int_0^{\delta_{II}^{f,e}} T_t(\delta_{II}) d\delta + \int_{\delta_{II}^{f,e}}^{\delta_{II}^{*}} T_t(\delta_{II}) d\delta\right] dS \\ &= E_{II}^{c,e} + E_{II}^c + E_{II}^{f,e} + E_{II}^f, \end{aligned} \tag{3.17}$$

where $E_{II}^{c,e}$ and $E_{II}^{f,e}$ are the energy associated with elastic loading,E_{II}^c and E_{II}^f are the energy dissipated by the weakening of cohesion and friction, respectively. δ_{II}^* is a final slip on the crack. The dissipated energy by friction E_{II}^f is often decomposed into the fracture energy and heat (e.g. *Venkataraman and Kanamori*, 2004), which is described in the case of slip-weakening friction law as

$$\begin{aligned} E_{II}^f &= -\int_\Gamma \left[\int_{\delta_{II}^{f,e}}^{\delta_{II}^{*}} T_t(\delta_{II}) d\delta\right] dS \\ &= -\int_\Gamma \left[\int_{\delta_{II}^{f,e}}^{\min\{D_c,\delta^*\}} T_t(\delta_{II}) - \tau_r d\delta + \int_{\delta_{II}^{f,e}}^{\delta^*} \tau_r d\delta\right] dS \\ &= E_G + E_H, \end{aligned} \tag{3.18}$$

where E_G is fracture energy dissipated on activate fracture surfaces and E_H is heat energy. The consumed energies by elastic loading E_I^e, $E_{II}^{c,e}$ and $E_{II}^{f,e}$ are negligible with large p^c and p_f. For the sake of simplicity, we merge $E_{I/II}^c$ with E_G by definition that E_G is the energy spent for reactivating a fracture surface.

Then the energy conservation law represented by the energy components associated with the earthquake rupture is given by

$$E_{S_0} + E_G + E_H + E_K = -\Delta W, \tag{3.19}$$

If we classify the fracture energy E_G in equation (3.19) into the terms related with main faults E_G^{on} and off-fault damage E_G^{off}, equation (3.19) is rewritten as

$$E_{S_0} + E_G^{on} + E_G^{off} + E_H + E_K = -\Delta W, \tag{3.20}$$

where E_G^{on} is the fracture energy dissipated on the main fault and E_G^{off} is the sum of dissipated fracture energy on the off-fault cracks dynamically activated during earthquake rupture. We address the question about the dynamic change of energy components in equation (3.20) to investigate the contribution of coseismic off-fault damage to the overall energy budget during earthquake rupture.

3.4.2 Radiated energy

The radiated energy E_R, defined as the work done by the stress perturbation over a surface S, is an important measurement for earthquakes. Since we canonically work with theory for small incremental stresses from the initial stress state in seismology, where the initial stress is large but the strain is defined to be zero (*Aki and Richards*, 2002, BOX 8.5), we follow the definition of radiated energy proposed by *Kostrov* (1974), given by

$$E_R^* \equiv -\int_0^{t_m} dt \int_{S_0} \left(\sigma_{ij} - \sigma_{ij}^0\right) \dot{u}_i n_j dS, \tag{3.21}$$

where t_m is a duration of an earthquake when the kinetic energy inside the volume turns to be zero after an event, $\sigma_{ij} = \sigma_{ij}(\mathbf{x}, t)$ is the stress in the volume and $\sigma_{ij}^0 = \sigma_{ij}^0(\mathbf{x})$ is the initial stress, $\dot{u}_i$ is the particle velocity and n_j is the outward unit normal vector to S_0. In this study, however, we assume an infinite length of the fault with crack-like ruptures which does not cease during simulation. Therefore, E_R cannot be derived in our model description. We thus alternately employ a quantity similar to E_R^*,

$$E_R(t) \equiv -\int_0^{t} dt \int_{S_0} \left(\sigma_{ij} - \sigma_{ij}^0\right) \dot{u}_i n_j dS. \tag{3.22}$$

Note that the radiated energy defined by equation (3.22) is a function of time during an earthquake, whereas the canonical radiated energy defined as equation (3.21) is determined at the end of earthquake events. The relationship with E_R is then given by

$$\int_0^{t_m} \frac{dE_R(t)}{dt} dt = E_R^*. \tag{3.23}$$

E_R can be evaluated with our model description by setting proper closed surface S_0, indicating the time evolution of radiated energy outward from S_0.

Then equation (3.20) is rewritten with E_R as

$$E_R + E_G^{on} + E_G^{off} + E_H + E_K = -(\Delta W + E_{S_0}^0). \tag{3.24}$$

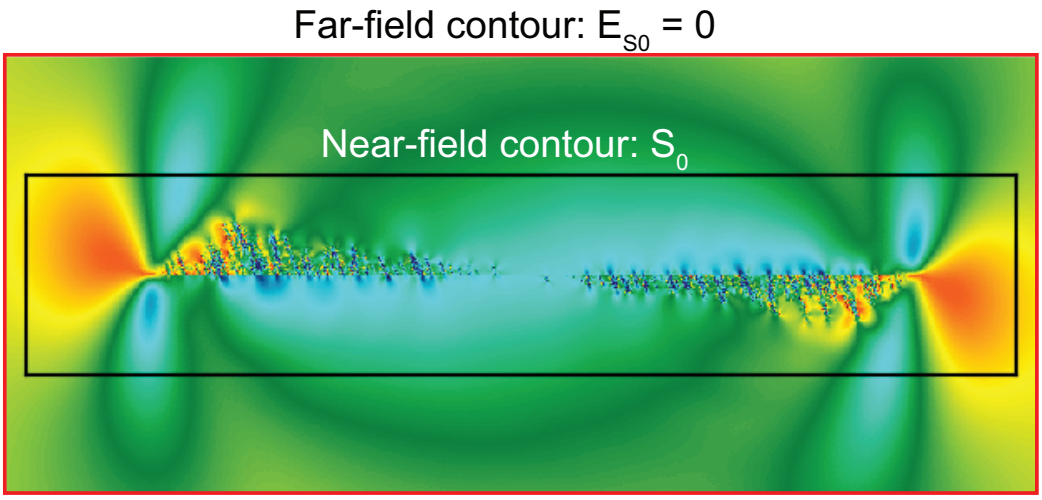

Figure 3.18: Snapshot of dynamic rupture with coseismic off-fault damage. Color contour indicates the second invariant of deviatoric stress tensor, J_2. Solid rectangles indicate near- and far-field contours for the validation of E_{S_0}.

where

$$E^0_{S_0} = -\int_0^t dt \int_{S_0} \sigma^0_{ij} \dot{u}_i n_j dS. \tag{3.25}$$

This term originates from the definition of radiated energy in equation (3.21), which does not appear in the conventional energy conservation law on earthquake (e.g. *Rivera and Kanamori*, 2005) because of reasonable approximation processes used to estimate the radiated energy. In this study, however, we define the energy conservation law with $E^0_{S_0}$ to rigorously estimate the contribution of each energy components to overall energy budget.

3.4.3 Validation of overall energy budget

Figure 3.18 shows a snapshot of dynamic rupture with coseismic off-fault damage, where the closed surface, S_0, is superimposed on the second invariant of deviatoric stress tensor, J_2. Firstly, to validate the calculation of the energy flux across the closed surface, E_{S_0}, we compared the energy dissipated by the cohesion and friction, $E_G^{on/off} + E_H$ inferred by $-(\Delta W + E_{S_0} + E_k) = -(\Delta W + E^0_{S_0} + E_R + E_K)$ from equations (3.20) and (3.24) evaluated on the near-field contour, S_0, to the far-field contour, which encompasses entire medium, and thereby $E_{S_0} = 0$. The comparison should be identical to verify the calculation of E_{S_0} across the S_0. Figure 3.19 shows the evolution of the all energy components during the rupture. Figure 3.20 shows the energy balance and the comparison of the two contours, where the comparison is identical. Therefore, the calculation of E_{S_0} across the S_0 is verified even when we consider the coseismic off-fault damage.

3.4.4 Energy dissipated by viscous damping

The dissipated energy by viscous damping, E_{visco}, should be also taken into account for the overall energy budget in the system. In this section, we calibrate the contribution of

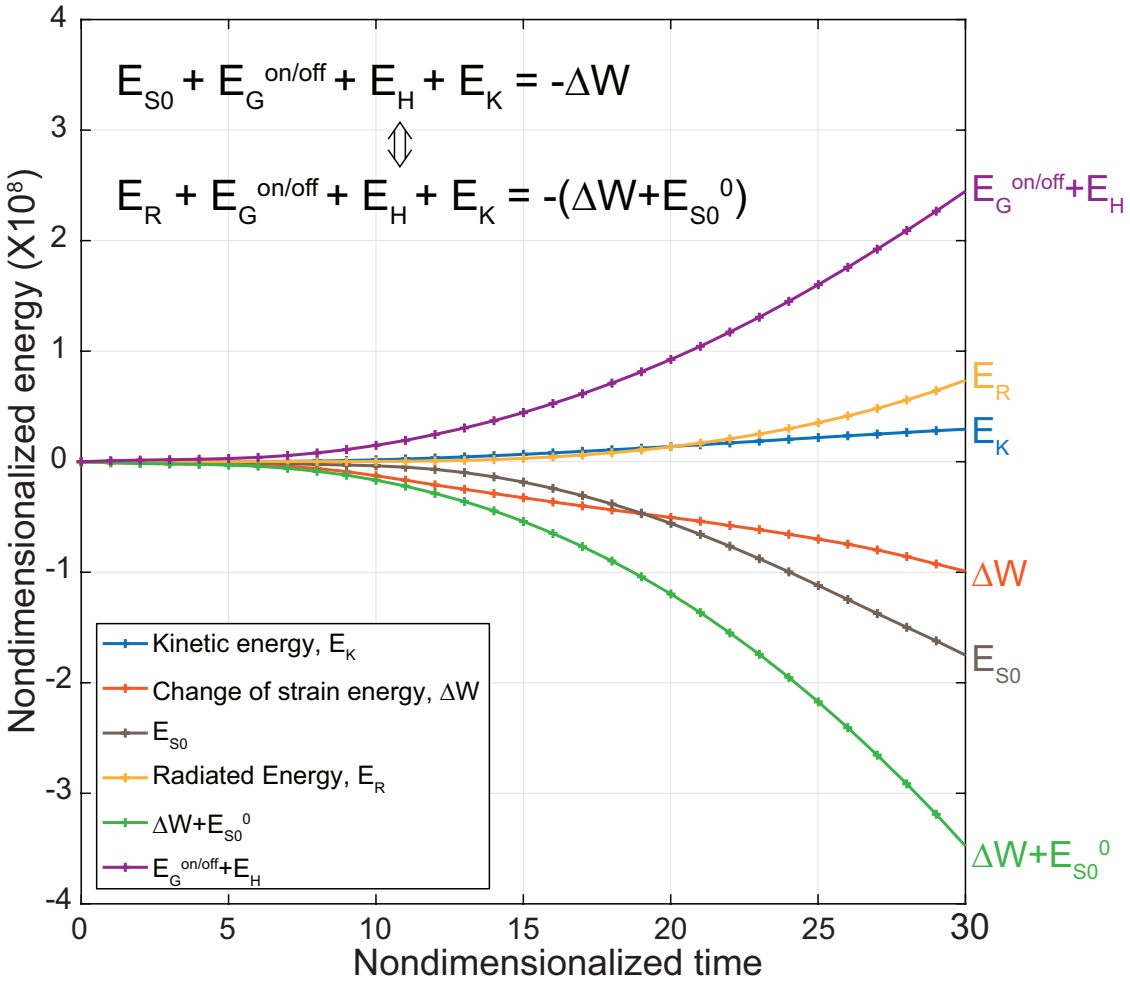

Figure 3.19: The evolution of energy components associated with near-field contour.

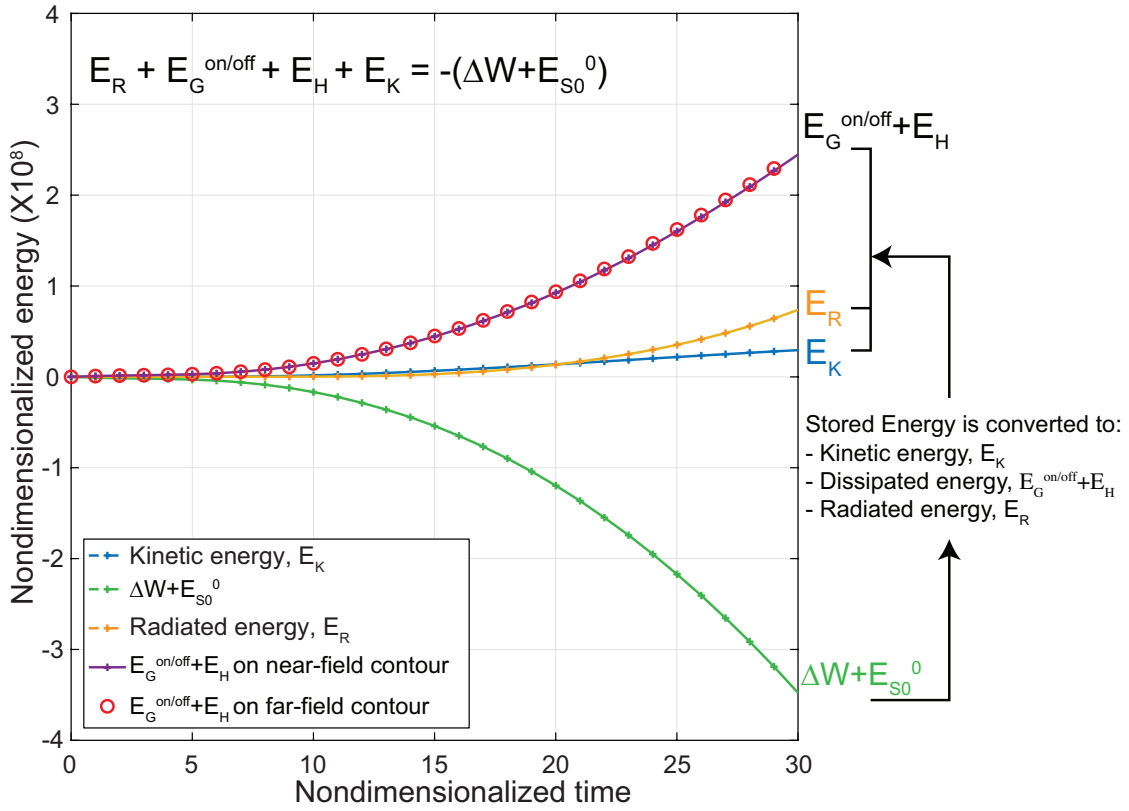

Figure 3.20: Comparison between near- and far-field contour for validation of the E_{S_0} across the S_0. Solid lines indicate the result with near-field contour, whereas the red circles indicate the result with far-field contour.

E_{visco} to the overall energy budget.

The conservation law including E_{visco} is rewritten from equation (3.24) as

$$E_G^{on} + E_H + E_{visco} = -(\Delta W + E_{S_0}^0 + E_R + E_K), \tag{3.26}$$

where E_G^{off} is not considered in this validation because the secondary off-fault cracks are not allowed. To evaluate the E_{visco}, we computed the energy components with purely elastic medium on the far-field contour (Figure 3.18), where E_R and $E_{S_0}^0$ are zero. Since the frictional energy is dissipated only on the main fault for the case with purely elastic medium, the $E_G^{on} + E_H$ can be directly calculated with the virtual sensors along the main fault as benchmark. Thus we compare this result to the indirectly derived dissipated energy by equation (3.26) to extract the E_{visco} from the other energy components.

Figure 3.21 shows the comparison of $E_G^{on} + E_H$ and estimated value of E_{visco}, which provides the ratio of E_{visco} to $E_G^{on} + E_H$. The ratio is around 8.7% at a maximum, which is not negligible in some cases. Therefore, in the following section, we remove the E_{visco} from the overall energy budget, for both cases, with and without coseismic off-fault damage, by calibrating the contribution of E_{visco} with purely elastic cases.

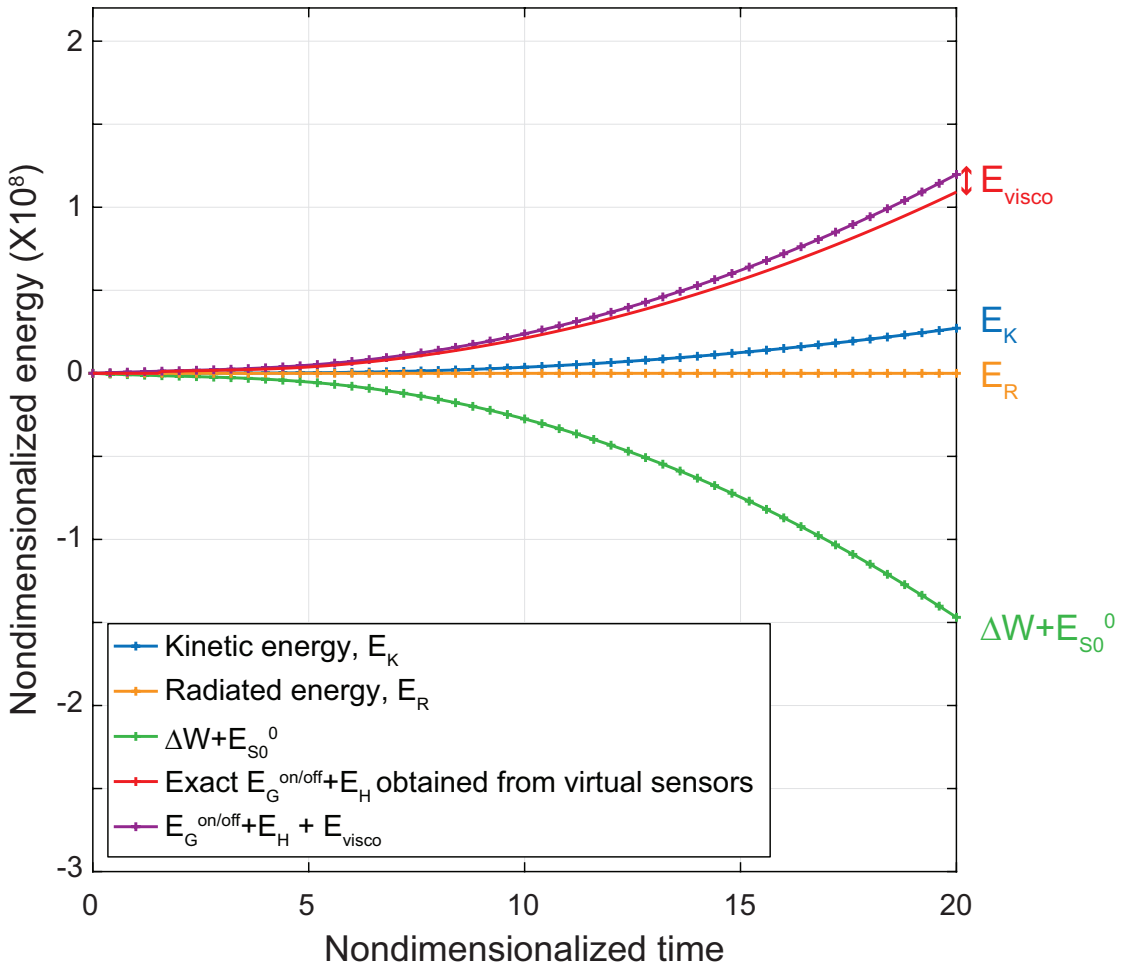

Figure 3.21: Calibration of E_{visco} with purely elastic medium with far-field contour. In this case, E_R and $E^0_{S_0}$ are zero. We evaluate the contribution of E_{visco} by taking difference between the exact $E^{on}_G + E_H$ obtained from virtual sensors and the inferred dissipated energy, $-(\Delta W + E_K)$.

3.4.5 Contribution of coseismic off-fault damage to the overall energy budget

We computed all energy components in equation (3.24) to investigate the contribution of coseismic off-fault cracks to the energy balance. Figure 3.22a shows the schematic of the target volume V and dynamic earthquake rupture with coseismic off-fault damage, in which the energy balance is evaluated. The size of volume is arbitrarily chosen to involve the main rupture and the coseismic off-fault damage zones. The energy conservation is evaluated until the rupture reaches surface S_0. Figures 3.22b and 3.22c show the proportion of each energy component to the sum of change of strain energy ΔW and $E^0_{S_0}$, which is interpreted as an available energy converted to the respective energies in left side of equation (3.24). We evaluated the energy balance when the rupture length reaches $45R_0$ with constant G_{IIC} cases at 2 km and 10 km depths. Figure 3.22b shows the proportion without off-fault damage, where $E_G^{off} = 0$. Figure 3.22c shows the same quantities with coseismic off-fault damage. E_G^{off} clearly has a non-negligible contribution in comparison to the fracture energy on the main fault E_G^{on}, and implies that up to half the amount of E_G^{on} is dissipated on the secondary off-fault cracks as fracture energy. The sum of consumed energy as E_G^{on}, E_G^{off} and E_H is around 70%, which is in agreement with the approximation that it can be more than 50% inferred from the observation of fault gouge (*Wilson et al.*, 2005). To evaluate the effect of secondary off-fault cracks on the fracture energy, we calculate an effective fracture energy G_C^{eff} defined as

$$G_{IIC}^{eff} = G_{IIC}^{f} + \frac{E_G^{off}}{L} \tag{3.27}$$

where L is the rupture length. Note that we assume unit thickness. The second term in the right side is interpreted as the total fracture energy dissipated on the off-fault cracks per unit fracture surface on the main fault, which varies with the rupture propagation.

Figure 3.23 shows the evolution of effective fracture energy as a function of rupture length at 2 , 6 and 10 km with constant G_{IIC} cases. It illustrates the monotonic increase of G_{IIC}^{eff}, which implies the effective fracture energy significantly increases because of the additional energy dissipation on the off-fault cracks as the rupture propagates on the main fault. On the right axis in Figure 3.23, we also denote the effective D_c defined as

$$D_c^{eff} = \frac{2G_{IIC}^{eff}}{(\tau_p - \tau_r)}. \tag{3.28}$$

Note that D_c^{eff}/D_c is thus identically equal to $G_{IIC}^{eff}/G_{IIC}^{f}$ by definition. The D_c^{eff} implies the effective critical slip distance for the rupture on the main fault with coseismic off-fault damage, which also increases with the rupture propagation because of the additional energy dissipation in the off-fault medium.

3.4.6 Source time function

We investigated the effect of the coseismic off-fault damage on the evolution of source time functions (STF), $\dot{M}_0(t)$. The STF on the main fault is defined as follows

$$\dot{M}_0(t) = \mu \int_{S^{\text{main fault}}} \Delta \dot{u}_1(\xi, t) dS, \tag{3.29}$$

where μ is shear modulus, $S^{\text{main fault}}$ is the area of the surface on the main fault, and $\Delta\dot{u}_1(\xi,t)$ is the slip velocity at ξ on the fault. We assume unit thickness in this analysis. Since we assume an infinite planar fault, the STF increases monotonically with time and does not return to zero. Thus we do not compare the shape of STF to the observations, but evaluate the change of STF due to the coseismic off-fault damage.

We demonstrate the STF at 2km and 10km depths as shown in Figure 3.24 and 3.25, respectively, where the cases with coseismic off-fault damage is compared to the cases without off-fault damage. Since the rupture is abruptly nucleated, the initial rise of STF is caused by the nucleation phase. As soon as the rupture starts to propagate and causes the coseismic off-fault damage, the rate of increase in the $\dot{M}_0(t)$ for the case with the coseismic off-fault damage decreases at both 2km and 10km depths. We also show the ratio of $\dot{M}_0(t)$ with the coseismic off-fault damage, $\dot{M}_0^D(t)$, to the case without off-fault damage, $\dot{M}_0^E(t)$, on the right axis of Figure 3.24 and 3.25, which implies that the $\dot{M}_0(t)$ decreases significantly regardless of depth. Therefore, although these results are preliminary due to the assumption of infinite planar fault, the coseismic off-fault damage is expected to change the shape of the STF in natural earthquakes.

3.4.7 Seismic efficiency

The seismic efficiency η_r is an important parameter to quantify the proportion of radiated energy to the sum of radiated energy and fracture energy, which evaluates the balance between the radiated energy as seismic waves and dissipated energy by fracturing of both main faults and off-fault medium (*Kanamori and Brodsky*, 2004); small η_r infers large dissipation by inelastic deformation on the main faults and the off-fault media (*Kaneko et al.*, 2017). The η_r is canonically defined by the radiated energy E_R^* over the sum of E_R^* and the fracture energy on the fault E_G^{on} (*Venkataraman and Kanamori*, 2004; *Passelègue et al.*, 2016). However, since we can only evaluate the temporal radiated energy in equation (3.22) because of the infinite fault length in our model description, we define a modified seismic efficiency for this study, given by

$$\eta_r = \frac{E_R + E_K}{E_R + E_K + E_G^{on} + E_G^{off}}. \tag{3.30}$$

The physical interpretation of this quantity is same with the standard seismic efficiency. We include the kinetic energy E_K remaining in the volume V, most of which is eventually converted into the radiated energy. We evaluated η_r as a function of rupture length with constant G_{IIC} cases at 2 and 10 km depths and compared between with and without off-fault damage to investigate the effect of off-fault damage on the seismic efficiency. Figures 3.26 and 3.27 show the η_r with sub-Rayleigh (S=1.0) and supershear (S=0.7) cases. The relative difference between with and without off-fault damage cases is plotted in the insets, defined as

$$\Delta\eta_r = 1 - \frac{\eta_r^D}{\eta_r^C}, \tag{3.31}$$

where η_r^D and η_r^C indicate the η_r with and without off-fault damage cases, respectively. There is a significant decrease in η_r due to the off-fault damage, particularly in the deeper

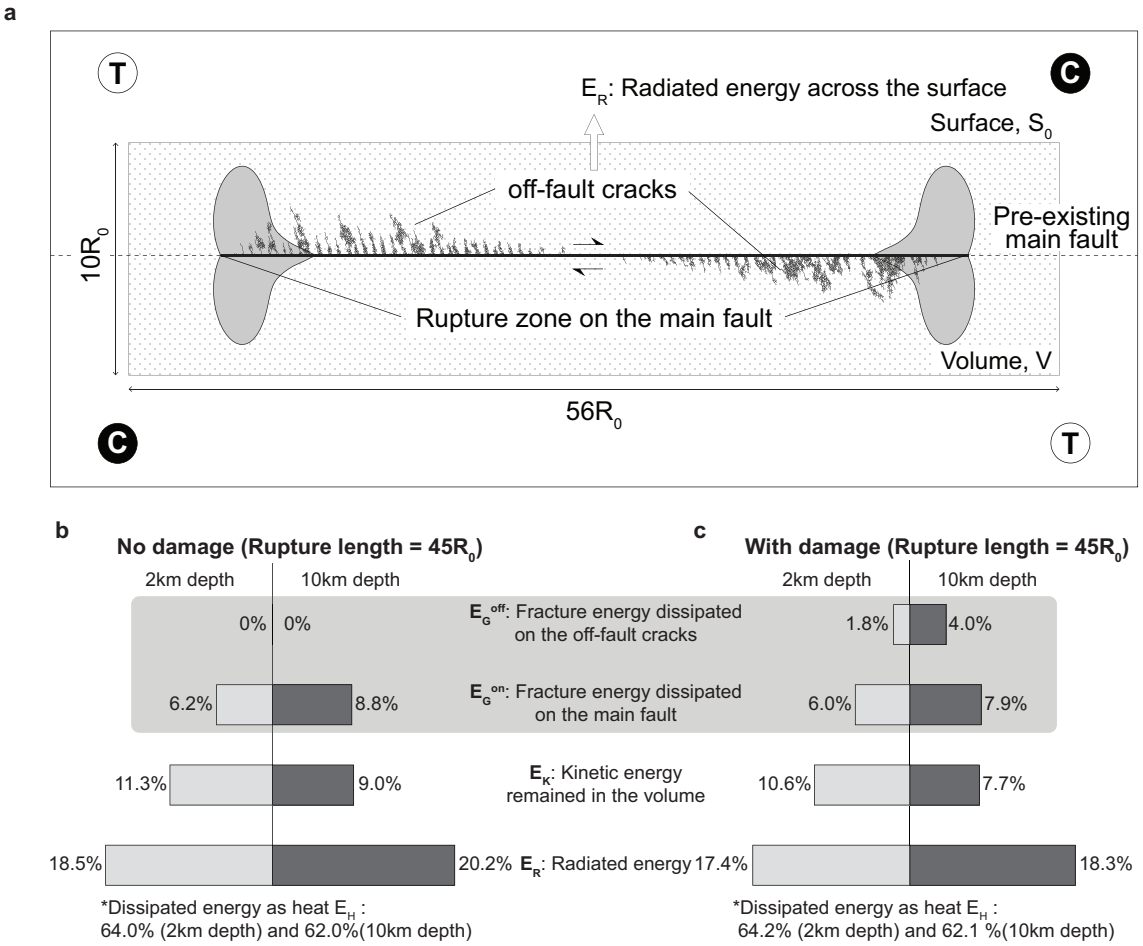

Figure 3.22: Schematic of overall energy budget and the ratio of each energy component. (a)Schematic of overall energy budget. The dotted area shows the target volume V with surface S_0, where the energy balance is evaluated. We assume the target volume is rectangular with unit thickness. The size of the target area is arbitrary chosen as 10 R_0 X 56 R_0. (b) Ratio of energy components without damage at 2 km and 10 km depths with constant G_{IIC} condition. We evaluated this balance when the rupture length reached to $45R_0$. (c) Same plot with coseismic off-fault damage.

case with sub-Rayleigh rupture. This can be explained by the denser and more intricate off-fault fracture network formed in deeper cases. Although the secondary off-fault cracks induce additional radiation, which contributes to the enhanced high-frequency components in the near-field ground motion, the seismic efficiency decreases due to the coseismic off-fault damage. In this sense, we maintain that the coseismic off-fault damage absorbs some of available energy, which is converted to the radiated energy with no off-fault damage assumption. However, since the effective G_{IIC}^{eff} in supershear does not increases as much as the sub-Rayleigh, the decrease in η_r due to the coseismic off-fault damage with supershear cases is smaller than that of sub-Rayleigh cases.

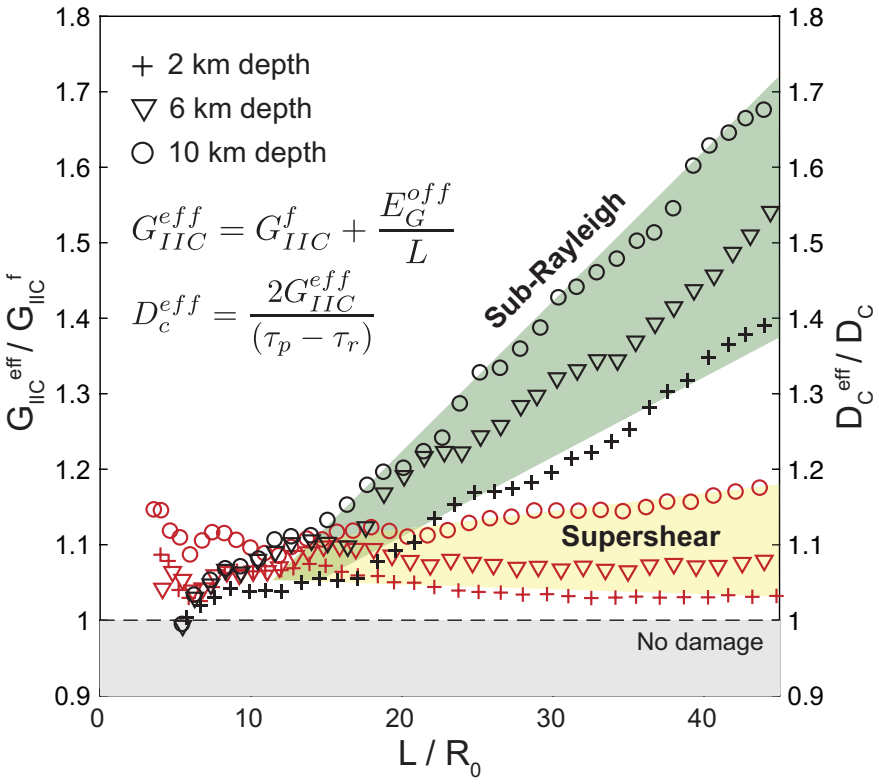

Figure 3.23: Effective fracture energy on the main fault G_{IIC}^{eff} scaled by G_{IIC}^{f} and the D_c^{eff} scaled by the D_c prescribed on the main fault. We evaluate these quantities at 2 km, 6 km and 10 km depths with constant G_{IIC} cases. The sub-Rayleigh cases (black markers highlighted in green) and supershear cases (red markers highlighted in yellow) are plotted as a function of rupture length. Dotted line indicates a reference with no damage cases, where $G_{IIC}^{off} = 0$.

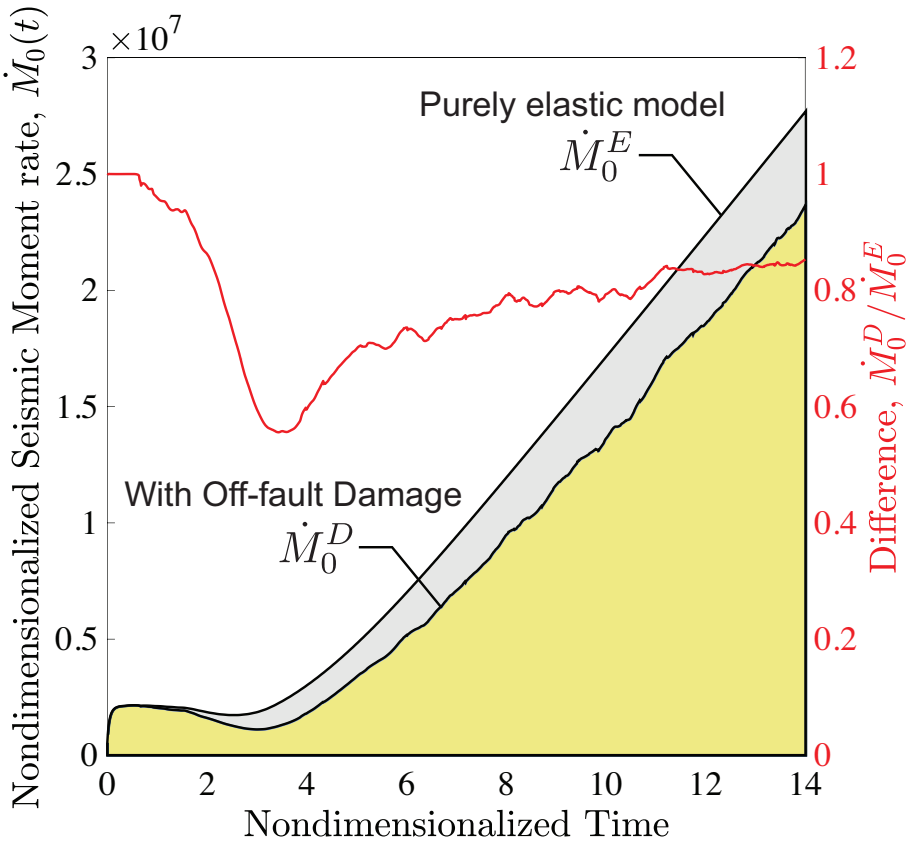

Figure 3.24: Source time function for the case at 2km depth. Both time and the seismic moment rate, $\dot{M}_0^D(t)$, are nondimensionalized by the scaling factors listed in Table 2.1. The ratio of $\dot{M}_0(t)$ with the coseismic off-fault damage, $\dot{M}_0^D(t)$, to the case without off-fault damage, $\dot{M}_0^E(t)$, is shown on the right axis.

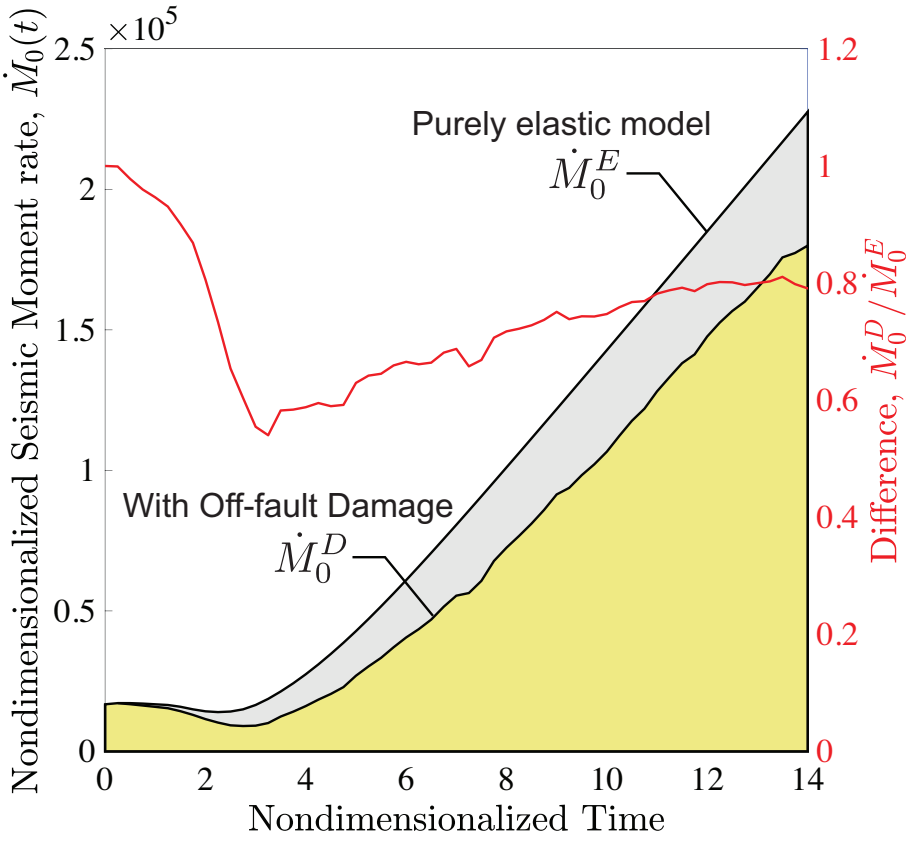

Figure 3.25: Source time function for the case at 10km depth.

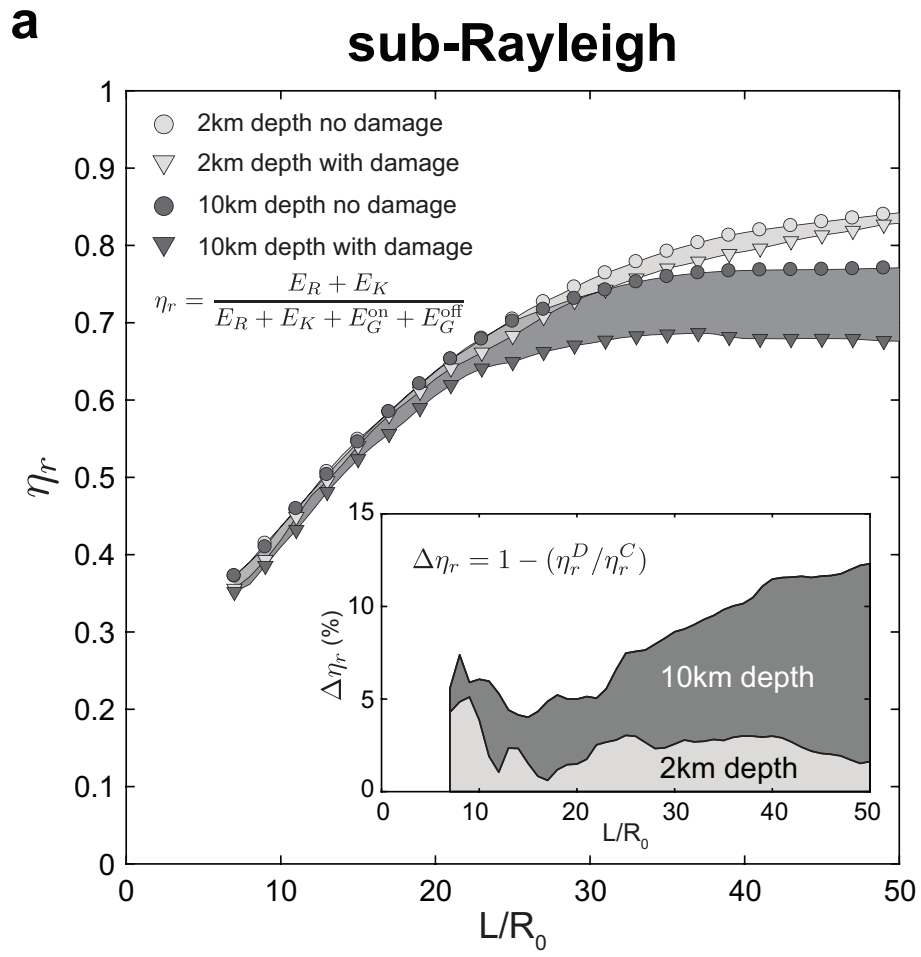

Figure 3.26: Seismic efficiency with and without off-fault damage at 2 km and 10 km depths as a function of rupture length (S=1.0). The circles indicate to the cases without damage, whereas the inverted triangles indicate the cases with off-fault damage. The inset shows the percentage of the decrease in seismic efficiency due to the off-fault damage. Note that the rupture transitions to supershear around $L/R_0 = 40$ for the case without off-fault damage, while it remains sub-Rayleigh with damage.

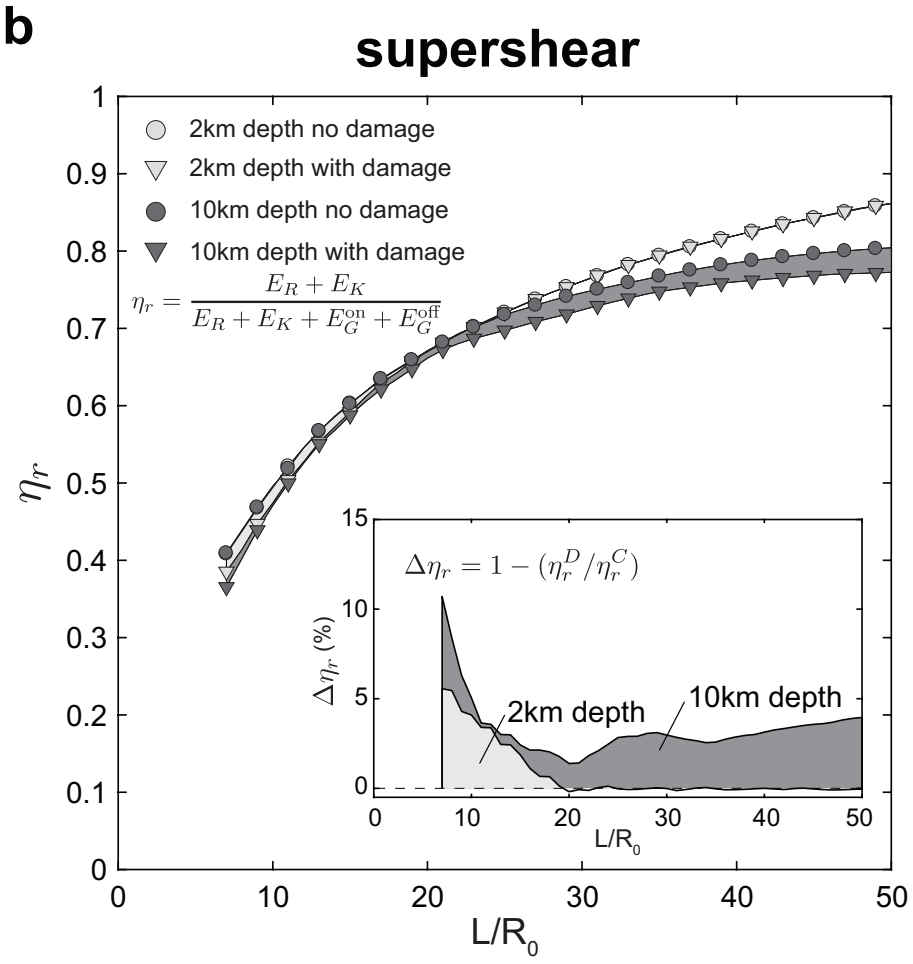

Figure 3.27: Seismic efficiency with and without off-fault damage at 2 km and 10 km depths as a function of rupture length (S=0.7). The rupture transitions to supershear for the cases both with and without off-fault damage.

3.5 Conclusions

Previous studies have documented the existence of coseismic off-fault damage and its effects on the rupture dynamics and associated radiation. However, the mechanism of dynamically generated fracture networks around the main fault induced by the earthquake rupture and the radiated wave field consequently perturbed by the coseismic off-fault damage needed to be elucidated. In this study, we modeled dynamic rupture with coseismic off-fault fracture networks to investigate its effect on the rupture dynamics, radiation and overall energy budget.

We firstly demonstrated a continuum-discontinuum approach framework for dynamic earthquake rupture modeling with FDEM. We conducted a set of cross-validation examples to show the numerical accuracy of FDEM for the dynamic rupture problem for various mesh discretization and viscous damping cases. It was verified that FDEM is one of the optimized schemes for dynamic rupture modeling, which can be applied for the continuum-discontinuum analysis with coseismic off-fault damage. The analysis also provides a reasonable combination of grid size and viscosity, which can be utilized for dynamic earthquake rupture modeling with FDEM. Then we showed the fracturing mechanisms dynamically induced by earthquake ruptures on the main fault and the high-frequency radiation enhanced by the secondary fracture network formed in the off-fault medium. We showed the process of secondary crack activation and the evolution of secondary fracture networks with complicated feedback inside it. Indeed, the rupture velocity decreases due to the coseismic off-fault damage and the supershear transition is delayed, or even stopped. The tensile and shear cracks have preferable orientations in spite of the complicated evolution of the secondary fracture network. The analysis of maximum cutoff frequency of the ground acceleration highlights the enhanced high-frequency radiation in the damage zone. It shows a spike-like particle motion caused by the secondary cracking, which enhances the high-frequency components in the spectrum of ground acceleration. The high-frequency radiation abruptly attenuates due to the geometric dispersion. It is thus very difficult to directly observe the additional radiation induced by coseismic off-fault cracks in far-field seismological observation.

We then compared the evolution of off-fault fracture network with different depth, simulated by the 2-D slices in plane strain with lithostatic assumption. It shows the damage patterns and the distribution of the fracture density with depth, which implies that more intricate off-fault fracture network is generally formed with higher confining pressure (i.e., at deeper cases). Regardless of the off-fault damage patterns, the off-fault cracks maintain their preferable orientation though the distribution of crack angle changes with depth. The damage zone width inferred by the envelope of secondary fracture network becomes narrower with depth, forming a flower-like structure as pointed out by previous studies even considering such intricate off-fault fracture network. The damage zone width can be also scaled by the quasi-static process zone size, which is expected by the theoretical analysis done by *Poliakov et al*. (2002); *Rice et al*. (2005).

Finally, we investigated the overall energy budget during earthquakes, including the contribution of coseismic off-fault damage. We described the energy conservation law which is represented by the energy components associated with dynamic earthquake rup-

ture with coseismic off-fault damage. We then quantified the energy components during an earthquake, and showed a non-negligible effect of secondary off-fault cracks on the overall energy budget. The fracture energy dissipated on the off-fault cracks is more than half of the fracture energy on the main fault at maximum, which causes a significant increase of effective fracture energy. The monotonically increasing effective fracture energy as a function of rupture length implies the scale dependency of the energy contribution of secondary off-fault cracks. We then evaluated the seismic efficiency to elucidate the effect of secondary off-fault cracks on the radiated energy. Indeed, it decreases due to the coseismic off-fault damage even if it contains the additional radiation from the secondary off-fault cracks. The difference is larger with sub-Rayleigh cases at depth, whereas it is small, or even negligible, with supershear cases.

Overall, Figure 3.28 shows the summary of the evolution of the damage zone width, the fracture density and the ratio of dissipated fracture energy on the main fault and the off-fault medium with depth. Here, the fracture density is evaluated as an average of the entire evaluation area indicated in Figure 3.16 with depth. The damage zone width decreases with depth, whereas the contribution of the dissipated fracture energy in the off-fault medium compared to the fracture energy on the main fault becomes larger with depth, and is significant when considering the overall energy budget. **This can be explained by the increase in the fracture density with depth and the complex feedback of the off-fault fracture network. Thus we conclude that the effect of coseismic off-fault damage on the rupture dynamics, radiation and overall energy budget is non-negligible, even where the damage zone width becomes narrower in depth.**

In this study, we conducted simulations with intact rock, and with the fixed orientation of principal stress. Therefore, we observed the coseismic off-fault damage only in the extensional side of the fault. However, in nature, the off-fault damage is often observed in the both sides of the fault. We now assume that the pre-damage of the off-fault medium, initial cohesion on the main fault, which is assumed to be zero in this study, and the orientation of the principal stress play a role in the symmetric off-fault damage across the fault. This needs to be investigated by extensive parametric studies.

Further work should include the investigation of the effect of the orientation of principal stress, or heterogeneity of the toughness of the medium, on the damage pattern and rupture dynamics. Earthquake cycles on the same fault will clarify the saturation of off-fault damage. The fault roughness, which comprises kinks to cause secondary cracks by stress concentration, would change the damage patterns significantly. The full kinematic analysis of earthquake ruptures is not done yet, which will clarify the effect of coseismic off-fault damage on the seismic moment release rate and seismic observations in intermediate- or far-field, though we already showed the additional radiation from secondary off-fault cracks is likely to be observed only within the near-field ground motion.

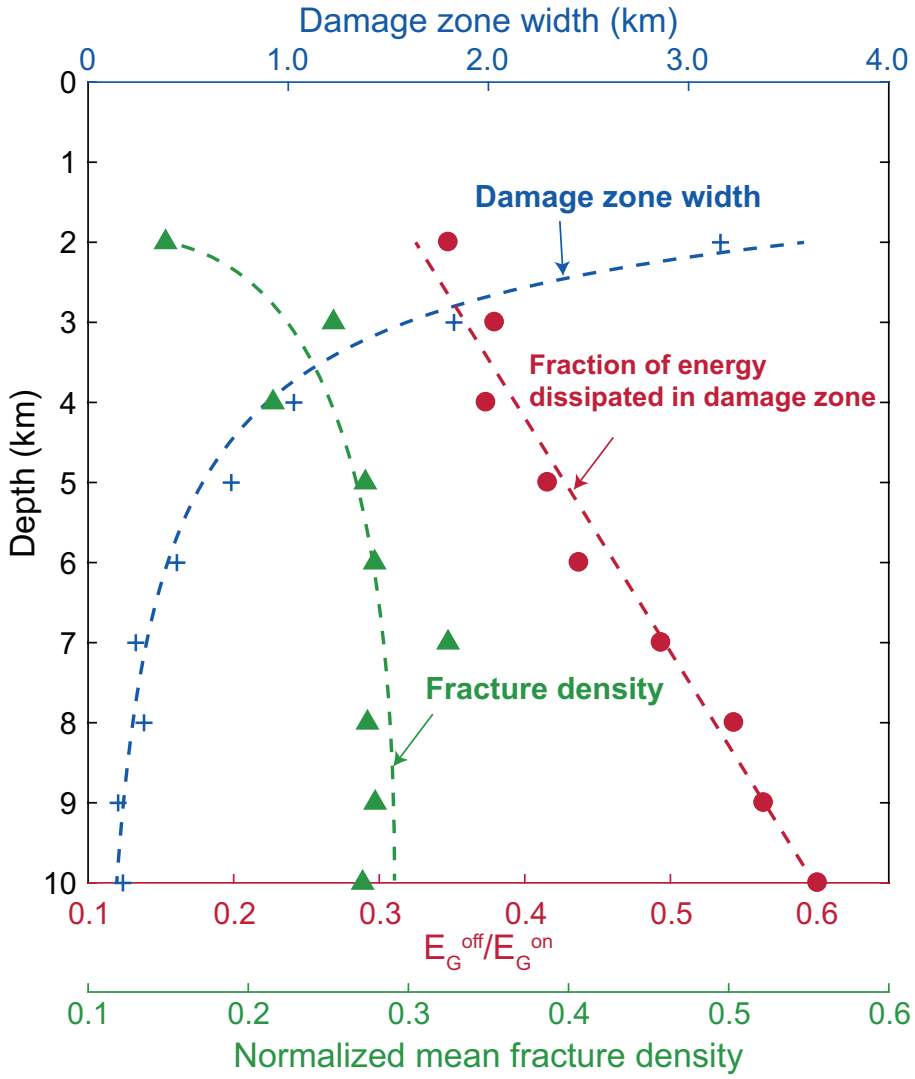

Figure 3.28: Evolution of the damage zone width, fracture density and the ratio of dissipated fracture energy on the fault and off-fault medium with depth. The markers indicate the values at the modeled depths. In this study, the damage zone width is evaluated only on the extensional side of the fault. Solid lines indicate expected trends of the discrete data. Since we conducted simulations in plane strain, we did not discuss the damage pattern and energy budget close to the ground surface.

4. Application to natural fault system: Earthquake damage patterns resolve complex rupture processes on the 2016 Mw 7.8 Kaikōura earthquake in New Zealand

Avant-propos

Une des attentes pour les modélisations numériques de la rupture dynamique est l'application pour la structure faille naturelle afin d'estimer le scénario de rupture et les ondes sismiques conséquentes. La modélisation de rupture dynamique sur les failles naturelles a été réalésé, en utilisant les méthodes conventionnelles telles que BIEM (e.g *Aochi and Fukuyama*, 2002; *Ando and Yamashita*, 2007), et alors ADER-DG (*Ulrich et al.*, 2018). Ces techniques numériques peuvent modéliser la rupture dynamique sur les failles prescrits, même si en trois dimensions avec un nombre suffisant des ressources de calcul. Cependant, une technique de pointe ne peut pas modéliser la génération dynamique des fissures secondaires en raison des limitées de formulations du modèle, qui peut modifier le scénario de rupture lors des séismes sur les failles naturelles. Alors que nous avons discuté un rôle de l'endommagement cosismique, des observations sur le séisme de Kaikōura de magnitude 7.8 ont indiqué que la structure de l'endommagement secondaire peut être une signature du processus de rupture, permettant de réduire un sous-ensemble de scénarios de la rupture prospectives. Ainsi, le séisme de Kaikōura est un des meilleurs exemples pour démontrer un fort potentiel de modéliser la rupture dynamique sur la structure faille naturelle, et alors pour vérifier cette hypothèse en incorporant des observations et des modélisations de l'endommagement cosismique. Dans ce chapitre, nous décrirons le contexte du séisme de Kaikōura, et alors la méthode de la rupture dynamique sur la structure faille naturelle. Nous démontrons les résultats de la modélisation numérique sur les scénarios de rupture hypothétiques pour explorer le processus de rupture et la structure de l'endommagement secondaire. Ces résultats évoquent la possibilité de préciser la hypothèse du processus de rupture en comparant la structure de l'endommagement secondaire et des profils de déplacement obtenus par les observations.

4.1 Introduction

One of the goals of numerical modeling of dynamic earthquake ruptures with coseismic off-fault damage is to apply for natural fault system to evaluate various rupture scenarios, and the resulting ground motion. Dynamic earthquake rupture modeling on natural complex fault networks has been studied with conventional numerical schemes, such as BIEM (e.g *Aochi and Fukuyama*, 2002; *Bhat et al*., 2004; *Ando and Yamashita*, 2007), and recently with Arbitrary high-order accurate DERivative Discontinuous Galerkin method (ADER-DG) (*Ulrich et al*., 2018). These numerical techniques are capable of modeling dynamic earthquake ruptures on prescribed faults, even in 3-D with a decent amount of computer resources. However, these state-of-the-art techniques cannot model the spontaneous activation of the secondary coseismic off-fault cracks due to limitations of model formulation, which may modify the rupture scenario of the natural earthquakes.

While we have discussed the role of coseismic off-fault damage in dynamic earthquake ruptures, it has been pointed out from the observations of the 2016 Mw 7.8 Kaikōura earthquake in New Zealand that the coseismic off-fault damage pattern can be a signature of the rupture process, which potentially could be used to narrow down a subset of possible earthquake rupture scenarios. Therefore, the Kaikōura earthquake is one of the best examples to demonstrate the potential of continuum-discontinuum approach framework to elucidate the rupture scenario on natural earthquakes by the coseismic off-fault damage.

In this chapter, we first describe the background of the Kaikōura earthquake, and the methodology of the dynamic earthquake rupture modeling on natural fault system. We then show the results with hypothetical rupture scenarios to investigate the rupture paths and the relevant coseismic off-fault damage pattern, and compare the profiles of displacement field between the model and the observations to estimate the most likely rupture scenario on this fault system.

4.1.1 The 2016 Mw 7.8 Kaikōura earthquake in New Zealand

Large crustal earthquakes result from ruptures that dynamically propagate through a complex network of faults, whose temporal sequence of failure is not always clear (*Hamling et al*., 2017; *Wei et al*., 2011; *Yue et al*., 2012). Associated secondary faulting and coseismic off-fault damage suggest that a significant part of on- and off-fault deformation patterns are due to state of traction, fault geometry and directivity of the rupture (*Kame et al*., 2003; *Fliss et al*., 2005; *Vallage et al*., 2015; *Thomas et al*., 2017), in addition to some geological structural inheritance (*Choi et al*., 2018). At ground surface, this off-fault damage zone can be hundreds of meter wide (*Mitchell and Faulkner*, 2009; *Vallage et al*., 2015), while it becomes narrower at depth (*Di Toro et al*., 2005). The combined length of surface ruptures associated with the 13th November 2016 Mw 7.8 Kaikōura earthquake in New Zealand (Figure 4.1) reaches 180 km, distributed over more than 15 distinct fault segments (*Hamling et al*., 2017; *Litchfield et al*., 2018), which has been reported as one of the most complex earthquakes ever documented. Although a blind low-angle thrust might have been activated (*Hollingsworth et al*., 2017), the right-lateral strike-slip faults oriented NE-SW, such as the Jordan and the Kekerengu faults, dominate surface ruptures

(*Kääb et al.*, 2017; *Litchfield et al.*, 2018; *Xu et al.*, 2018). The 15 km-long NNW-SSE Papatea fault segment, however, is characterized by left-lateral motion of up to ∼6 m and by vertical throw reaching 10 m (*Langridge et al.*, 2018). Field observations show that the northern tip of the Papatea fault does not connect to the Jordan - Kekerengu fault system (*Langridge et al.*, 2018). All geophysical studies agree that overall the rupture propagated northward from the epicenter (*Duputel and Rivera*, 2017; *Hamling et al.*, 2017; *Wang et al.*, 2018; *Zhang et al.*, 2017). However, because of the rupture complexity, partly at sea, and the possibility of a blind thrust (*Hollingsworth et al.*, 2017), the exact rupture-propagation path remains elusive; in particular the way the rupture propagated through the Papatea - Jordan - Kekerengu triple junction remains debated.

Therefore, we conducted the dynamic earthquake rupture modeling on the triple junction to investigate the rupture paths and off-fault damage pattern. We then compare the model to the coseismic horizontal displacements in the triple junction area using optical satellite image correlation, which shows a better correlation with particular scenario, where the the Papatea fault ruptures first, independently of any assumption about rupture path during earlier part of the rupture.

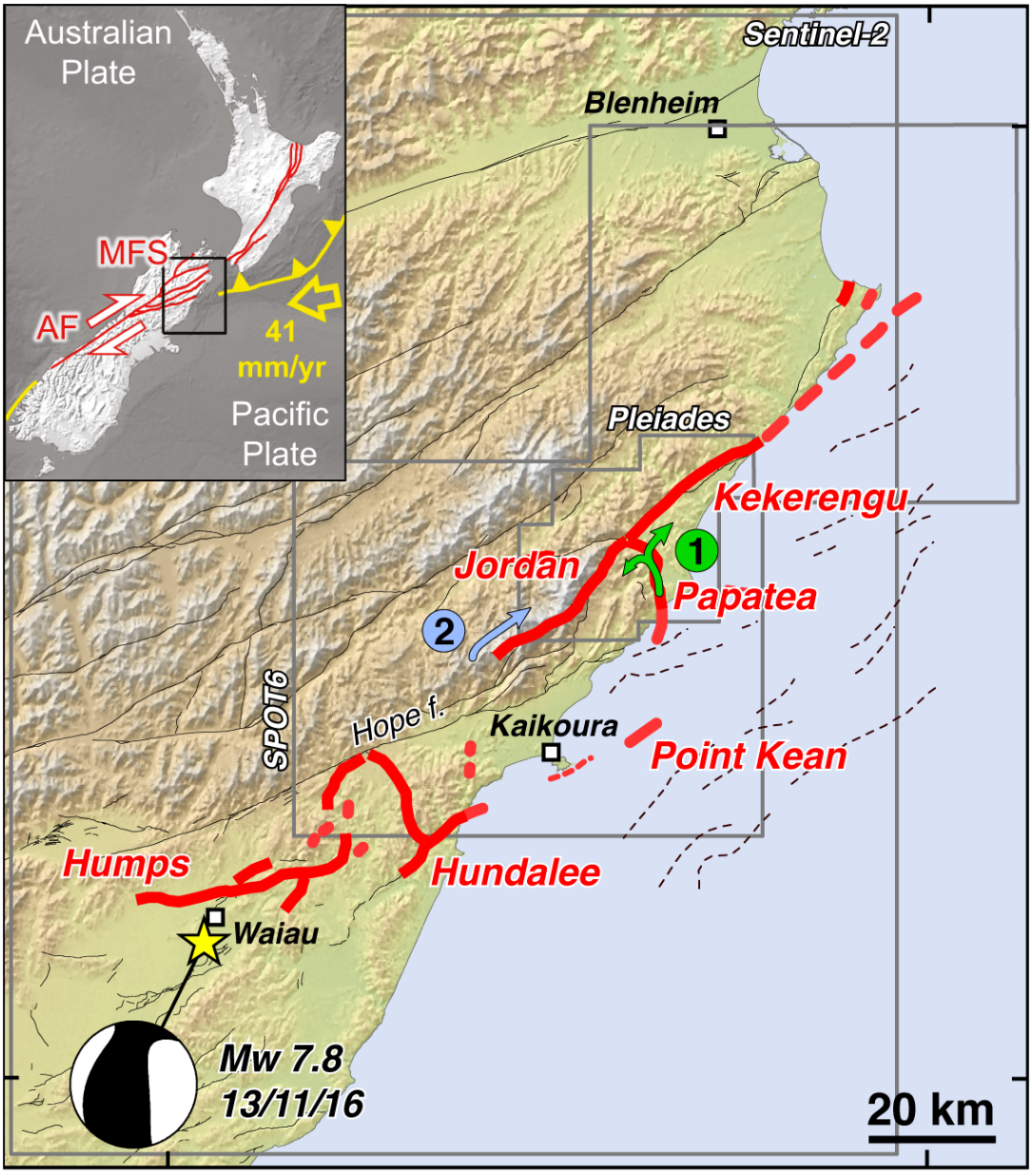

Figure 4.1: Map of the Kaikōura surface ruptures after *Litchfield et al*. (2018). Footprints for the different satellite datasets are indicated. Labels 1 and 2 refer to alternative rupture scenarios. Red solid lines indicate identified surface rupture. The Kaikōura Peninsula fault is indicated in red dashed. Other Quaternary faults in black. AF stands for Alpine Fault and MFS for Marlborough fault system.

4.2 Methodology: Application to natural fault networks

We used a 2-D continuum-discontinuum based scheme, FDEM, to model the spontaneous activation of coseismic off-fault cracks. Although vertical motion is a part of the deformation (*Stirling et al.*, 2017; *Langridge et al.*, 2018), at this stage we limited our study to horizontal deformation. Based on satellite imagery and field observations, we first defined the fault geometry around the Jordan – Kekerengu – Papatea triple junction area and discretized the domain by using unstructured triangular meshes (Figure 4.2a). The mesh size is adaptively controlled to be finer close to the fault to optimize trade-off between the numerical accuracy and computational cost. We then defined the initial stress state σ_{ij} uniformly in the medium. The orientation of the maximum principal compressive stress, φ, was set to N107°. This orientation is chosen to be both compatible with the sense of slip on the different faults activated during the earthquake (Figure 4.3) and with regional focal mechanisms *Townend et al.* (2012). The world stress map is also utilized to estimate the regional stress around the triple junction as shown in Figure 4.4 (*Heidbach et al.*, 2016).

We assumed that the material around the faults has been previously damaged (i.e. weakened) and therefore is less competent than the rest of the material in the model. This low cohesion zone is indicated in Figure 4.2a. The introduction of this weakened material area restricted unrealistic crack propagation at the edge of faults. The orientations of the potential failure planes are kept isotropic (Figure 4.2b). The values of parameters used in our modeling are listed in Table 4.1. As the material is initially intact everywhere in the medium, the CF is uniformly set as 0.45 in the low cohesion zone. We then force a nucleation of the rupture by imposing a low peak strength patch in the nucleation area. The length of this patch is greater than the nucleation length, L_c. Figure 4.5b shows the distribution of the initial shear traction on the prescribed fault normalized by the peak strength, τ_0/τ_p. The grid size, ds, along the prescribed fault is set at 50m. In this way, the number of finite elements per the quasi-static process zone size, R_0, is assured to be between 8 and 14, which is commonly used for the grid resolution of dynamic earthquake rupture modeling. It is usual,ly more than 5 elements per process zone size.

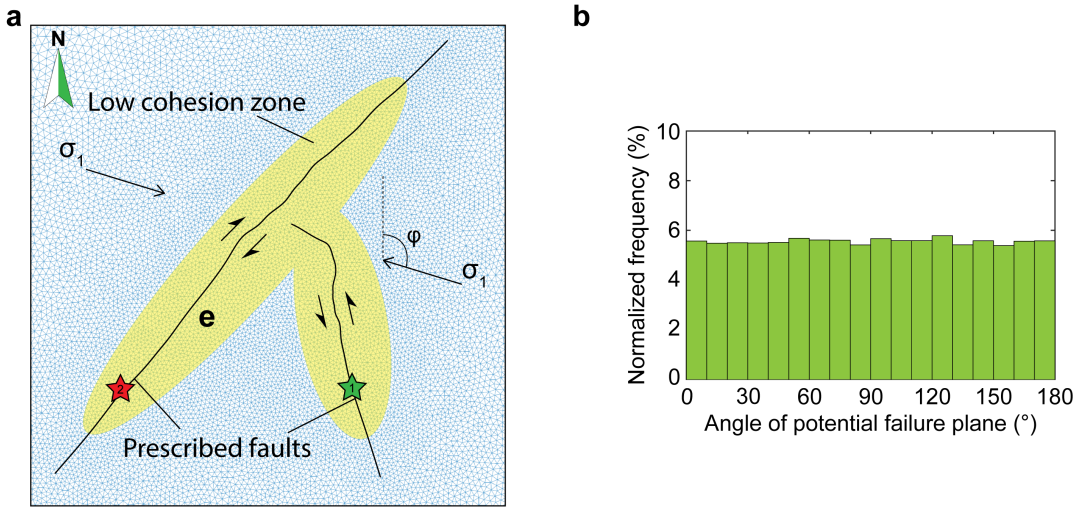

Figure 4.2: Model description of the Jordan - Kekerengu - Papatea triple junction. (a) Schematics of mesh discretization on the prescribed fault system. The Jordan fault, the Kekerengu fault and the Papatea fault are traced as shown in solid black line, according to satellite and field observation. Blue lines show the discrete finite elements. The mesh size is exaggerated for clarity purposes. The overall domain size is 90km x 90km, while the prescribed faults are in 30km x 30km in the middle of the domain to avoid the effects of wave reflections from the domain boundaries. The total number of finite elements is 514,000. σ_1 is the maximum compressional principal stress and φ is the orientation of σ_1 to the north. Arrows show the sense of slip. The areas of weakened material are highlighted in yellow. Green and red stars indicate the position of the rupture nucleation for the first and second scenarios respectively. (b) Histogram of the orientations of potential failure planes.

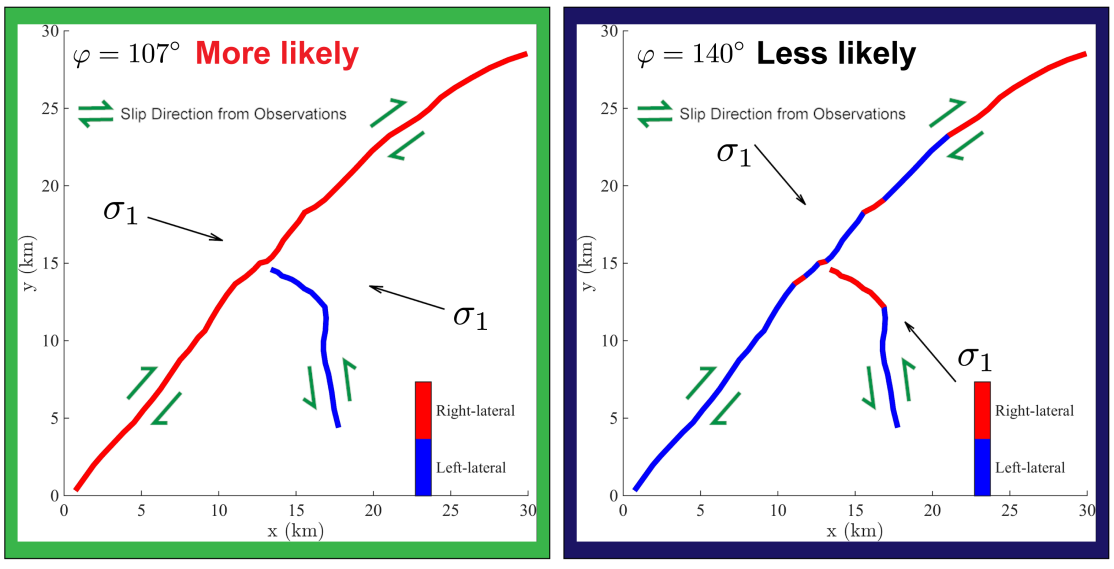

Figure 4.3: Constraints of the orientation of σ_1 in terms of sense of slip on the Jordan-Kekerengu-Papatea fault system. Green arrows indicate the sense of slip observed from the deformation map. Red and blue indicate the potential sense of slip with respect orientation of σ_1. Since the potential sense of slip is harmonized with the observations, the left case at $\phi = 107°$ is more likely than the right case.

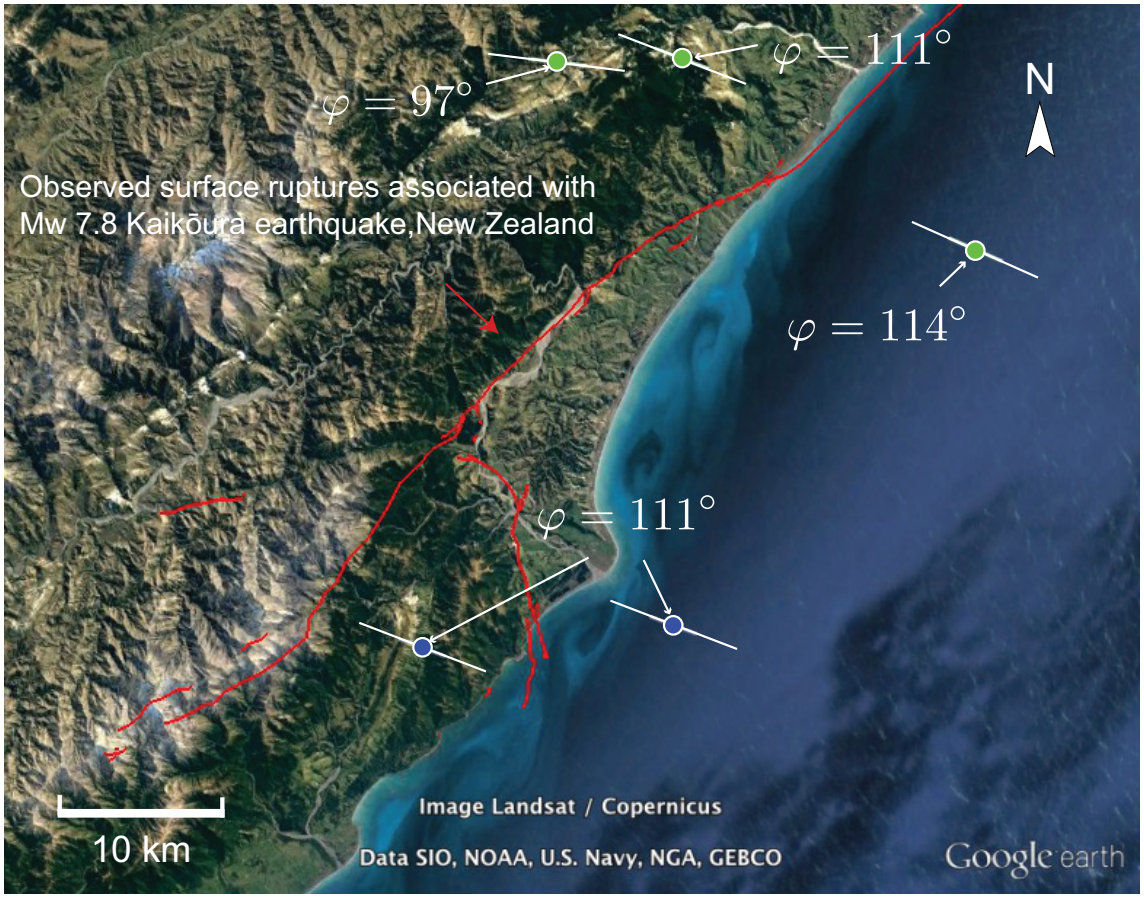

Figure 4.4: Orientation of maximum compressional principal stress estimated by the regional focal mechanisms. Red lines indicate the observed surface ruptures associated with the Kaikōura earthquake. Active fault map is downloaded from the Institute of Geological and Nuclear Sciences Limited (GNS) (*Langridge et al.*, 2016). White lines indicate the orientation of the maximum horizontal compressional stress, φ. This estimated regional stress is downloaded from World Stress Map 2016 (WSM) (*Heidbach et al.*, 2016). Color circles in the middle of white lines indicate the WSM Quality: Green indicates B quality, where the φ is accurate to within $\pm 20°$, while blue indicates C quality to within $\pm 25°$.

Table 4.1: Parameters used in numerical simulations of the Kaikōura earthquake.

Variables	**Values**	**Description**
ρ	2700 kg/m^3	Density
E	75 GPa	Young's modulus
μ	30 GPa	Shear modulus
ν	0.25	Poisson's ratio
σ_1	45.4 MPa	Maximum compressional principal stress
σ_2	19.1 MPa	Minimum compressional principal stress
φ	107°	Orientation of σ_1 to the north
ds	50m	Grid size on prescribed faults
	On prescribed faults	
f_s	0.4	Static friction coefficient
f_d	0.1	Dynamic friction coefficient
$\delta_{II}^f = D_c$	0.17m	Characteristic slip distance
	In off-fault medium	
f_s	0.4	Static friction coefficient
f_d	0.1	Dynamic friction coefficient
$\delta_{II}^f = D_c$	0.017m	Characteristic slip distance
C_I^p	8 MPa / 30 MPa	Peak cohesion for mode I opening crack (Low cohesion zone/the rest of domain)
C_{II}^p	30 MPa / 100 MPa	Peak cohesion for mode II shear crack (Low cohesion zone/the rest of domain)
$\delta_I^{c,c}$	2.7 mm	Critical normal displacement for softening of tensile cohesion
$\delta_{II}^{c,c}$	7.5 mm	Critical tangential displacement for softening of shear cohesion

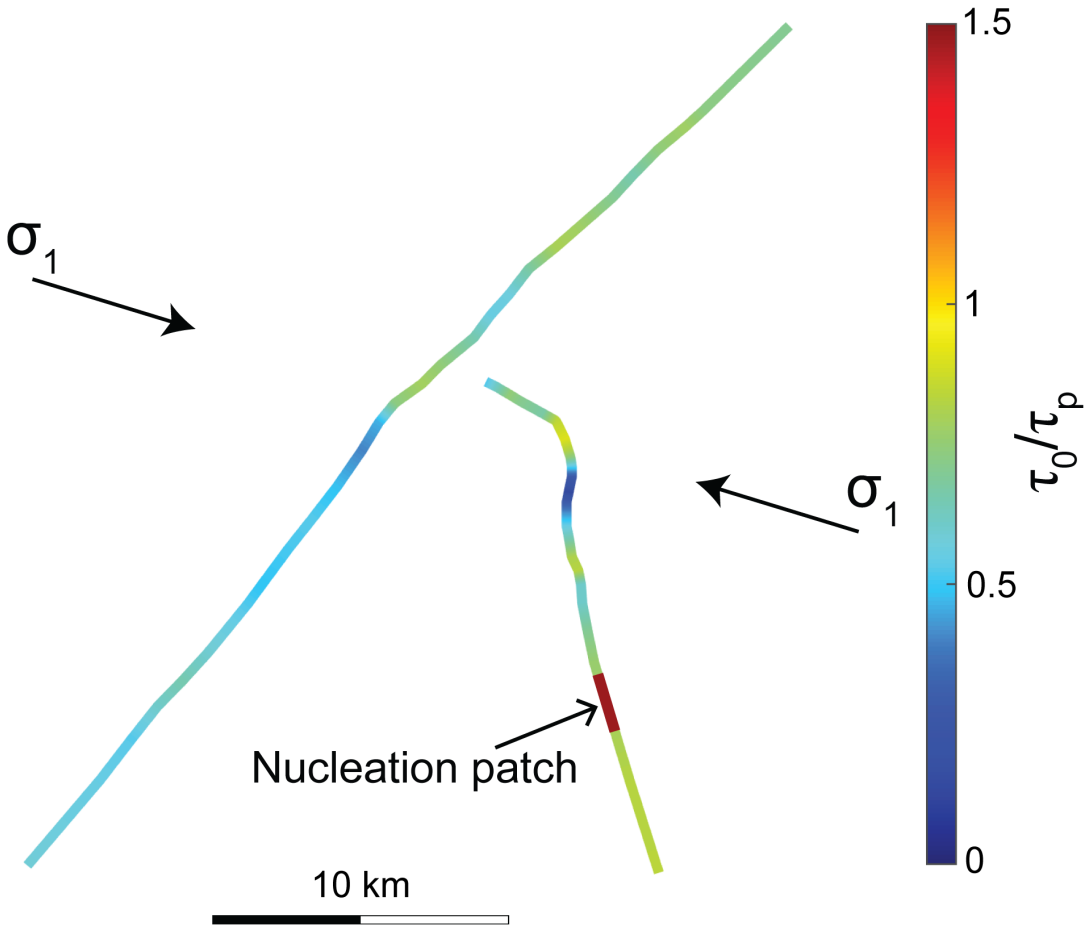

Figure 4.5: Initial shear traction normalized by the frictional strength.

4.3 Displacement measurements derived from optical image correlation

In this section, we describe the optical satellite image correlation technique to obtain the displacement field around the triple junction. This work has been done by Prof. Yann Klinger, Dr. Amaury Vallage, Dr. Johan Champenois and Dr. Arthur Delorme (*Klinger et al.*, 2018). To measure the horizontal displacements associated with the 2016 Kaikōura event, we correlated optical satellite images acquired before and after the earthquake. The correlation processing was conducted by using the open-source software package MicMac (*Rosu et al.*, 2015). The correlation was performed in two steps. In a first step, we correlated 10 m low-resolution Sentinel-2 images embracing the region where the Kaikōura earthquake occurred. In a second step we correlated 1.8 m Spot 6 images with 0.5 m Pleiades images to obtain a high-resolution horizontal displacement field for the Jordan - Kekerengu - Papatea triple junction. The Sentinel-2 images were acquired respectively on April 9th, 2016 and on December 15th, 2016. Although the Sentinel-2 images are multispectral images with pixel resolution varying between 10m and 60m, here we only used the 4 bands with a pixel-resolution of 10m: Red, green, blue and near infrared. These images are orthorectified by the image provider (European Space Agency) and were correlated without any specific pre-processing. For each band, each pair of images (pre- and post-earthquake images) was processed independently. Hence, for each component of the displacement, North-South and East-West components, we obtained 4 displacement maps. To improve the signal-to-noise ratio, these 4 maps were merged for each component of displacement, based on the median value for each quadruplet of pixels. It resulted in 2 horizontal-displacement maps (Figure 4.6), along North-South and East-West directions, which cover almost the entire Kaikōura rupture area with a ground resolution of 10m. The displacement maps were corrected from any low-frequency artifacts by setting the far-field displacement to zero and by crosschecking our results with GPS (https://aria-share.jpl.nasa.gov/events/20161113-NewZealand_EQ/GPS/, last accessed July 2018) and static displacement derived from local strong-motion instruments. Eventually, our Sentinel-2 horizontal displacement maps compare well with previously published horizontal displacement fields computed at similar scale from space geodesy and GPS measurements (*Hamling et al.*, 2017; *Hollingsworth et al.*, 2017; *Kääb et al.*, 2017; *Morishita et al.*, 2017; *Wang et al.*, 2018; *Xu et al.*, 2018)

To image details of the deformation in the close vicinity of the surface rupture, we performed correlation of metric-resolution images. For the images before the Kaikōura earthquake, we used a stereo-pair of images acquired by the satellite SPOT6 on May 18th, 2014. For the images acquired after the earthquake, we used a combination of several tri-stereo images acquired by the satellite Pleiades between December 23rd 2016 and March 18th 2017. The different subsets of Pleiades images were processed separately to ensure the best tuning of the correlation process depending on each subset, and only the final displacement maps were merged. Images needed first to be orthorectified using a Digital Elevation Model (DEM) with a ground resolution similar, at the first order, to the image resolution. Hence, using the Micmac package (*Rosu et al.*, 2015), we computed

pre- and post-earthquake DEMs at the resolution 1.8m from the SPOT6 images, and at the resolution 0.5m from the Pleiades. Because the two sets of images are from different sensors with different native resolution, the Pleiades images had to be downsampled at 1.8m to be consistent with the SPOT6 images, using the open-access GDAL library [Contributors_GDAL/ORG, 2018]. Eventually, a rigid translation ($\sim$10m) was applied to the Pleiades images, based on ground control points (GCP) identified both on SPOT6 and Pleiades images, and located far from major surface ruptures, to accommodate the slight difference in absolute-location estimate between the two sensors.

Then, the pre- and post-earthquake images were correlated to compute the horizontal-displacement field at the resolution of 1.8m. Because the area covered by high-resolution images includes almost everywhere significant coseismic deformation, zero-deformation points cannot be found to remove residual low-frequency correlation artifacts. Therefore, we used the large-scale Sentinel-2 deformation maps as a template to remove any low-frequency signal in the high-resolution displacement maps, which is not associated with tectonic deformation according to the Sentinel-2 measurements. Eventually, using optical satellite images bracketing the date of the Kaikōura earthquake, we measured amplitude and direction of the horizontal displacement field in the triple junction area between the Jordan-Kekerengu fault system and the Papatea fault system (Figures 4.7 and 4.8). The ground resolution of our displacement field is 1.8m, with a displacement detection threshold of about 20 cm (*Rosu et al.*, 2015). Although our measurements might include post-seismic deformation, as post-earthquake images were acquired between December 2016 and March 2017, it should be less than 10% of the coseismic deformation (*Hollingsworth et al.*, 2017) and should not affect significantly our observations.

Figure 4.7 shows the amplitude of the horizontal displacement at the triple junction. Systematic swath profiles every 90 m across different fault segments allow to establish a detailed slip distribution for that part of the Kaikōura rupture. Along the Jordan and the Kekerengu faults, 8 km-long swath profiles, J1, J2, K1 and K2 (Figures 4.7 and 4.8), show the displacement parallel to the fault, where the full strike-slip deformation is highly localized in a band only a few tens of meters wide. Along the Kekerengu fault, we measured a maximum right-lateral coseismic displacement of about 11m, in good agreement with direct field-offset measurements (*Kearse et al.*, 2018). The displacement map reveals that the pattern of deformation along the Papatea fault differs significantly from patterns along Kekerengu and Jordan faults. Along the Papatea fault, swath profiles P1 to P5 show that the gradient of horizontal deformation is not sharp everywhere (Figures 4.7 and 4.8). Instead, at both extremities, the displacement gradient is smoother, which is interpreted as distributed deformation across a damaged fault zone, as confirmed by direct field observations. Thus, the total 6m left-lateral displacement measured along P1 is distributed over a width of 2 kilometers, which is consistent with field (*Langridge et al.*, 2018) and Lidar mapping (*Clark et al.*, 2017) that documented several parallel fault strands at the coast. Actual fault scarps in the deformation zone are indeed also visible on the profile. Along profiles P2 the deformation zone becomes narrower and asymmetric relative to the position of the fault, with most of the distributed deformation located south of Papatea. Profiles P3, P4 and P5, located north of the major bend of the Papatea fault, show that the damage zone becomes wider again, to eventually include the entire triangular zone

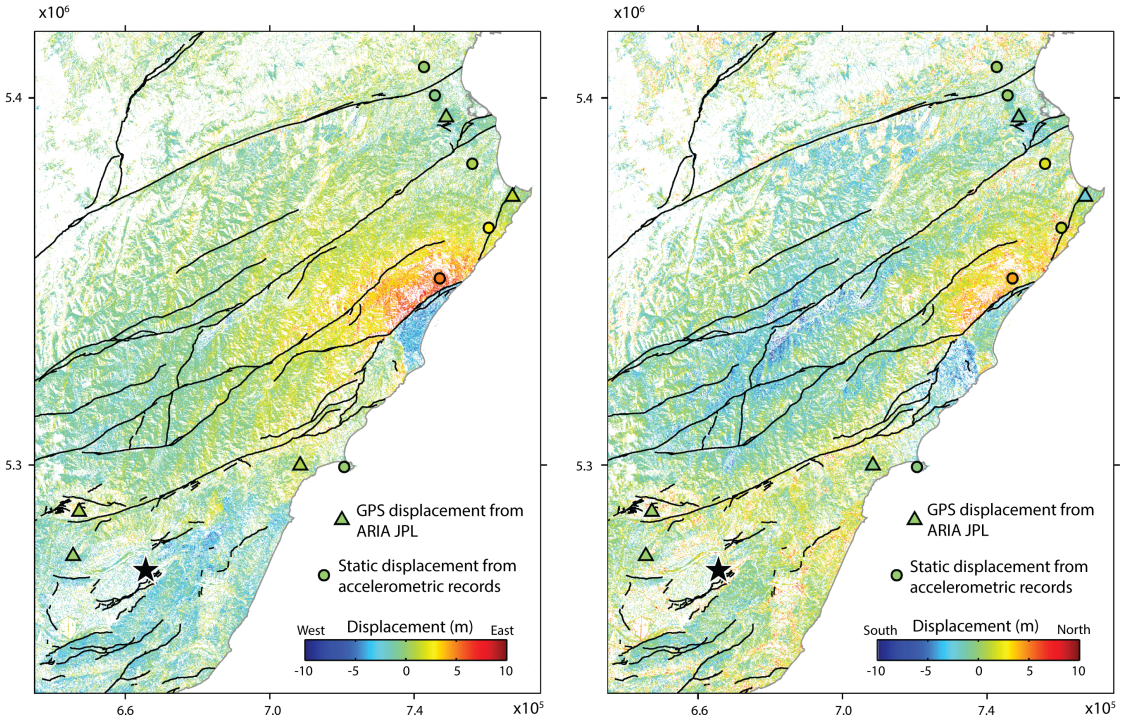

Figure 4.6: East-West and North-South components of displacement computed from the correlation of Sentinel-2 images. Coordinates are in UTM. Consistency of the results is checked by comparison with GPS and static motion derived from local strong-motion instruments, for each component. The far-field displacement is set to be zero. The fault network (black lines) is superimposed from GNS (https://data.gns.cri.nz/af/).

bounded by the Papatea fault, the Kekerengu fault, and to the North-East, by the short Waiautoa fault (Figure 4.7).

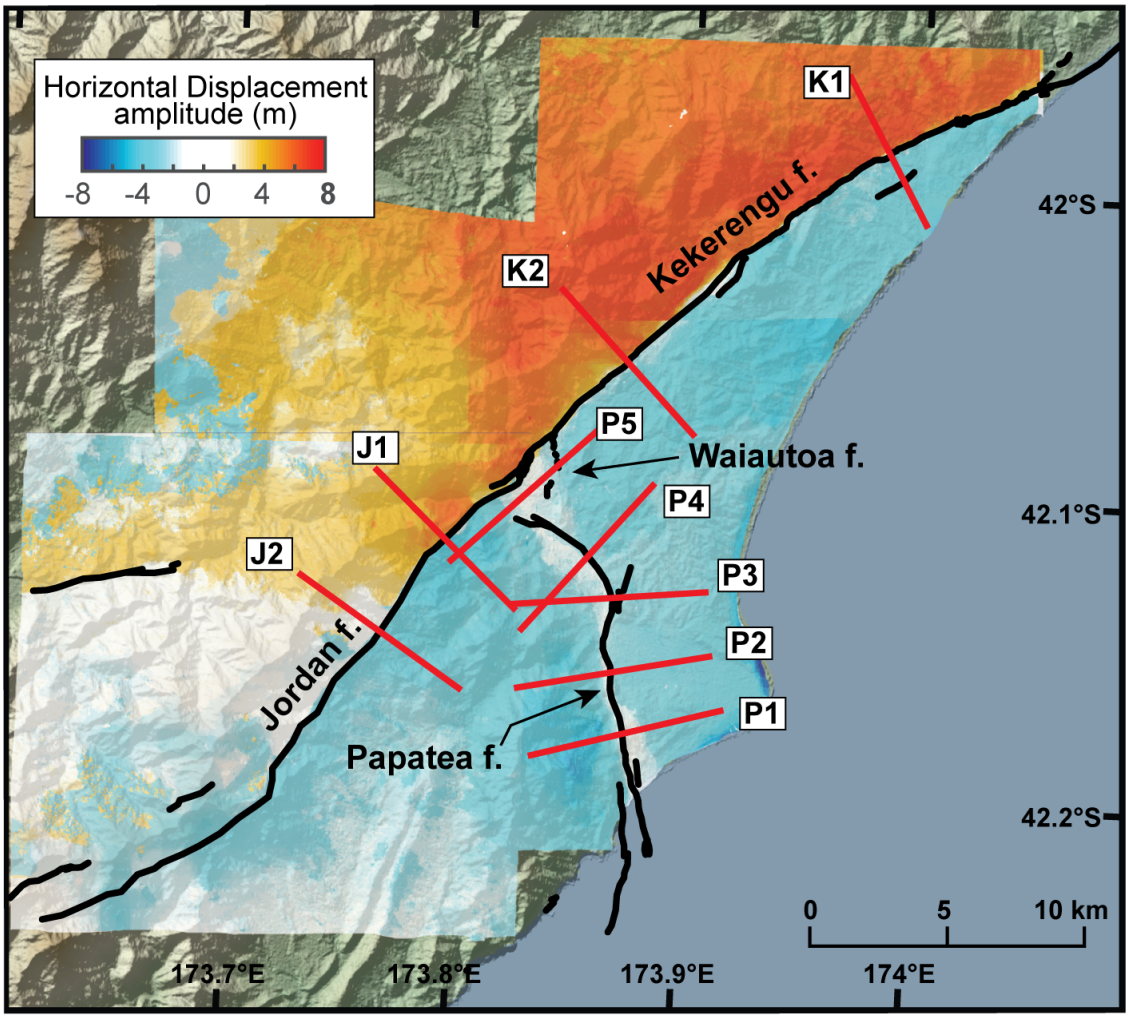

Figure 4.7: Displacement field around the triple junction derived from high-resolution correlation. Earthquake surface ruptures are indicated in black (*Langridge et al.*, 2018). Color corresponds to the amplitude of horizontal displacement (positive towards North east). Low color saturation along the Papatea fault indicates off-fault damage. Red lines show the position of displacement profiles.

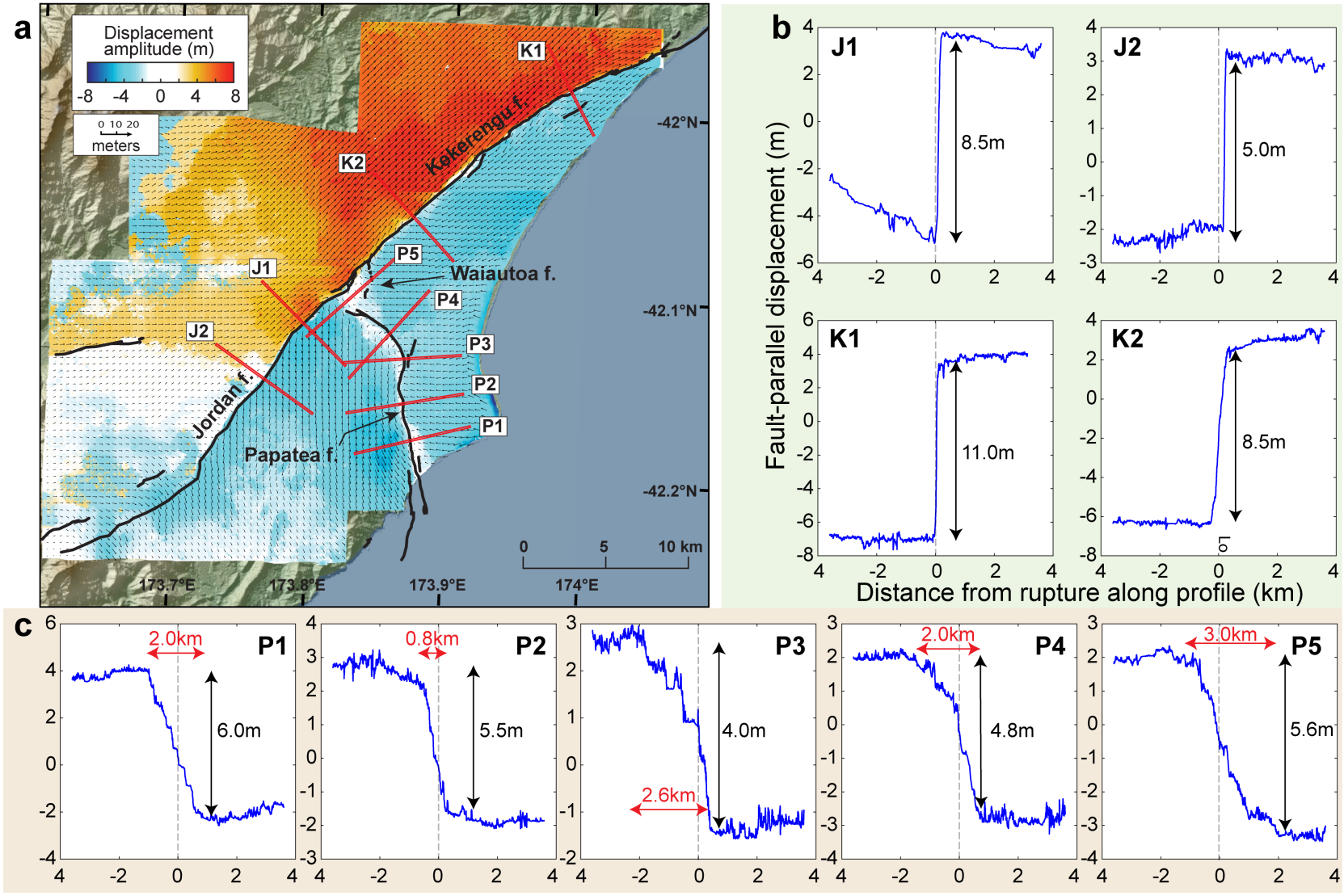

Figure 4.8: (Continued on the following page.)

Figure 4.8: Deformation field and associated displacement profiles. (a) Deformation field around the triple junction with the azimuth of horizontal displacement (arrows). Surface ruptures related to the Kaikōura event are in black (*Langridge et al*., 2018). The size of small arrows scales with the amplitude. (b) Profiles on the Jordan thrust (J1 and J2) and the Kekerengu faults (K1 and K2). (c) Profiles on the Papatea fault (P1 to P5).

4.4 Results: Earthquake rupture scenario and off-fault damage pattern

4.4.1 Hypothetical earthquake rupture scenarios

Although geophysical data clearly indicate that overall the Kaikōura earthquake propagated northward, two key questions remain unsolved about the Kaikōura rupture, which are the rupture scenario of the Jordan-Kekerengu-Papatea triple junction, and the potential activation of a shallow dipping blind thrust, possibly related to the southern end of the Hikurangi subduction (*Hollingsworth et al*., 2017). As for the later, our observations and modeling techniques bring no additional constraints. Thus, in the following we focus only on rupture scenario for the triple junction area. As the rupture globally propagated northward, two classes of scenarios are possible, which are either a rupture first on the Papatea fault that later propagated on the Jordan - Kekerengu fault system, or a rupture first on the Jordan fault that later propagated on the Kekerengu and Papatea fault systems.

In the first scenario, the rupture propagated northward from the epicenter to reach the northern tip of the Hundalee fault and continued northward, offshore, until it would trigger slip on the Papatea fault. This scenario is consistent with observed co-seismic uplift of the Kaikōura peninsula, which implies a shallow thrust fault outcropping offshore the Kaikōura peninsula (*Clark et al*., 2017), and with observation of submarine surface ruptures along the Point Kean Fault (*Litchfield et al*., 2018). This scenario does not rule out additional slip on a deep-seated thrust fault related to the subduction, although its amplitude would have to be limited (*Clark et al*., 2017).

In the second scenario, when the rupture reached the northern tip of the Hundalee fault, instead of continuing off-shore the rupture would jump about 20 km to the NW, to dynamically trigger rupture along the Jordan fault. Limited surface ruptures were documented between the Hundalee and the Jordan faults (*Litchfield et al*., 2018) that might correspond to such rupture jump and potential slip along a deep-seated fault could have play some role in rupture triggering.

Here, we model the two scenarios using the 2-D continuum-discontinuum model allowing for spontaneous activation of secondary off-fault cracks. For the two scenarios, all model parameters are left identical, but for the location of the rupture initiation, which is located either along the southern part of the Papatea fault, or along the southern end of the Jordan fault. Numerical simulation of each scenario led to a distinctive pattern of rupture sequence and off-fault damage. We thus conducted four cases; the first and second scenarios with and without off-fault damage. For the cases without off-fault damage, the peak cohesions in the low cohesion zone is set large enough to avoid the activation of

secondary cracks.

4.4.2 The first scenario: rupture nucleated from the southern part of Papatea fault

Figures 4.9 to 4.17 show the model setup and snapshots of simulation for the first scenario with coseismic off-fault damage, where the rupture is nucleated the southern part of Papatea fault. During the simulation, we recorded the velocity field, the slip velocity on the Jordan thrust - Kekerengu fault and Papatea fault, and the north-south component of ground accelerations close to the triple junction.

The rupture is initiated at the southern end of the fault and propagates northward. When it arrives at the triple junction, it triggers a new rupture on the Jordan-Kekerengu fault system, which propagates bilaterally from the junction (Figures 4.10 to 4.14). While the rupture is propagating along the Papatea fault, significant damage occurs on the western side, around the main kink of the fault (Figures 4.12 to 4.13). A major zone of damage also develops in the triangular zone around the triple junction. No significant damage, however, occurs along the Kekerengu fault and Jordan thrust (Figure 4.17).

The comparison of the displacement profiles between the observations and the model outputs, both nondimensionalized for the sake of comparison by their spatial distribution and amplitude of displacement, shows that qualitatively the model with the coseismic off-fault damage fits well with the observations. For the displacement profiles on Kekerengu fault and Jordan thrust (Figure 4.18g), the slip is well-localized across the fault, which implies less coseismic off-fault damage along these faults. On the other hand, the model outputs with coseismic off-fault damage capture the unique displacement field in the northern part of Papatea fault, which is distributed across the fault due to the secondary fracture network (Figure 4.18h). The model without off-fault damage (dashed black lines in Figure 4.18h) does not represent this distributed deformation because the slip is localized even on the northern part of Papatea fault. Therefore, the coseismic off-fault damage is an indispensable factor to reproduce the distributed deformation field.

At this stage, direct comparison of predicted offset values with observations (Figure 4.19), although they actually are of the same order of magnitude, is not very meaningful due to current limitation imposed by 2-D modeling, while the Papatea fault indeed shows significant vertical motion as well (*Stirling et al.*, 2017; *Langridge et al.*, 2018).

4.4.3 The second scenario: rupture nucleated from the southern part of Jordan thrust

We then show the second scenario, where the rupture is nucleated at the southern part of Jordan thrust. The model parameters used in this simulation is exactly same with the first scenario except for the location of rupture nucleation. Figure 4.20 to 4.24 show the model setup and snapshots for the second scenario with coseismic off-fault damage. In this scenario, the rupture propagates northward after the nucleation and activates off-fault cracks along Jordan thrust. We then found a small nucleation of the rupture at the main kink of the Papatea fault as shown in Figure 4.22, which then propagates bilaterally. This rupture propagating southward is suddenly trapped due to the activation of secondary off-fault cracks around the kink of the northern part of Papatea fault as shown in Figure 4.23. The rupture along the Kekerengu fault is accelerated enough to transition to supershear speeds (Figure 4.23). The pre-stress state is partially preferable for a transition to a supershear rupture due to the fault geometry. Figure 4.24 shows the damage pattern and the displacement field at the end of the simulation. Since the rupture is arrested at the northern part of Papatea fault, slip is not observed on the southern part. The damage is mainly caused along Jordan thrust and Kekerengu fault, whereas there is little damage on Papatea fault.

Figure 4.25 shows the profiles on the Jordan thrust-Kekerengu fault and the Papatea fault, respectively. Since the off-fault damage does not play a role in the profiles on J2 and K2, the model is still compatible with the observations in Figure 4.25g. However, it barely fits with observations even with off-fault damage because there is no significant damage to the west of the Papatea fault as shown in Figure 4.25h. Furthermore, the on-fault slip is not observed with the coseismic off-fault damage on the profile P2 as shown in Figure 4.25h because the rupture is arrested at the northern part of Papatea fault due to the secondary cracks. Therefore, we conclude that this scenario is less likely than the first scenario.

Snapshots for the two scenarios without coseismic off-fault damage are shown in Appendix D.

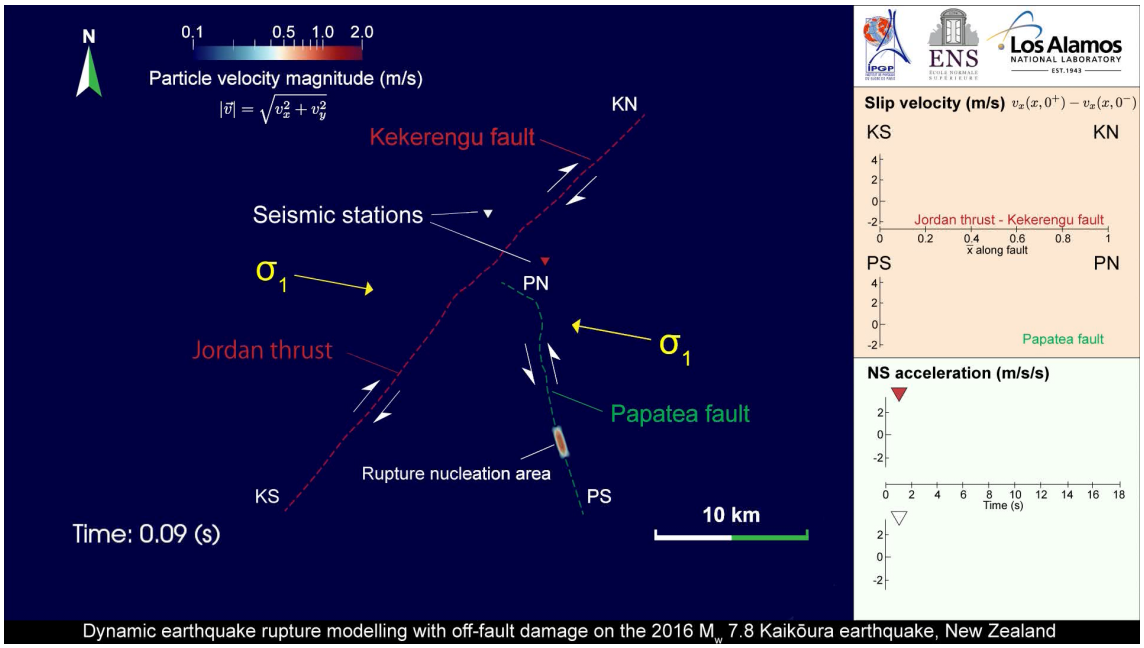

Figure 4.9: Model setup for the first scenario. Dotted lines show the prescribed faults. The top-right window shows slip velocity on the prescribed faults. The position along faults is nondimensionalized by the length of faults. The left-bottom window shows two seismograms associated with the seismic stations indicated by the inverted triangles. Color contour shows the particle velocity magnitude.

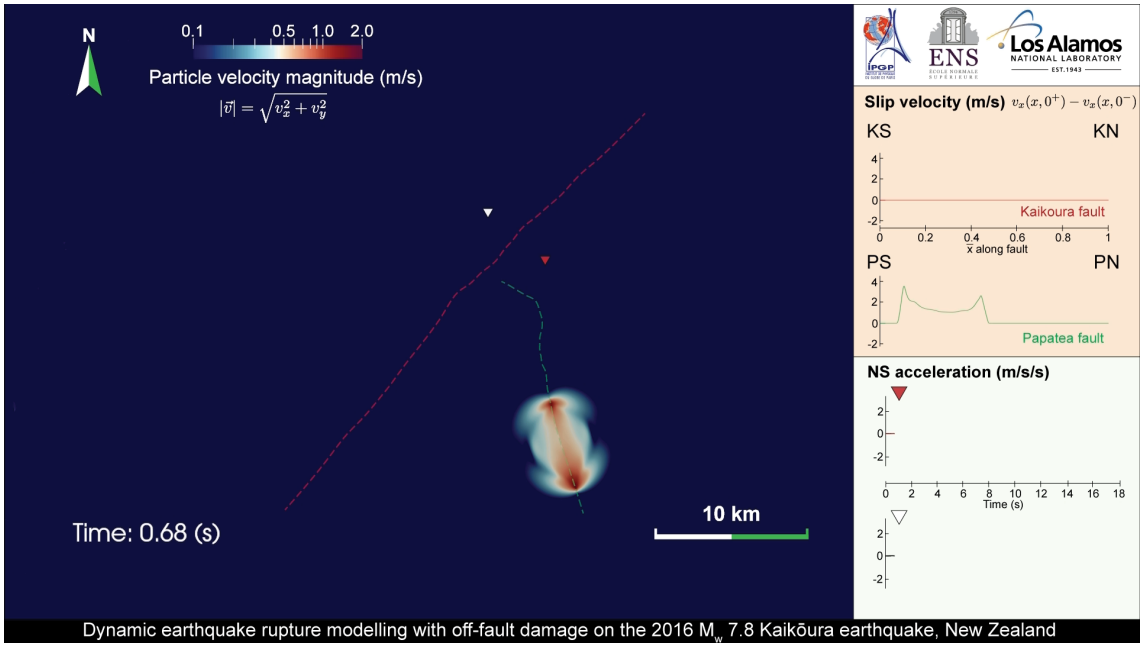

Figure 4.10: Rupture is nucleated bilaterally from the nucleation patch.

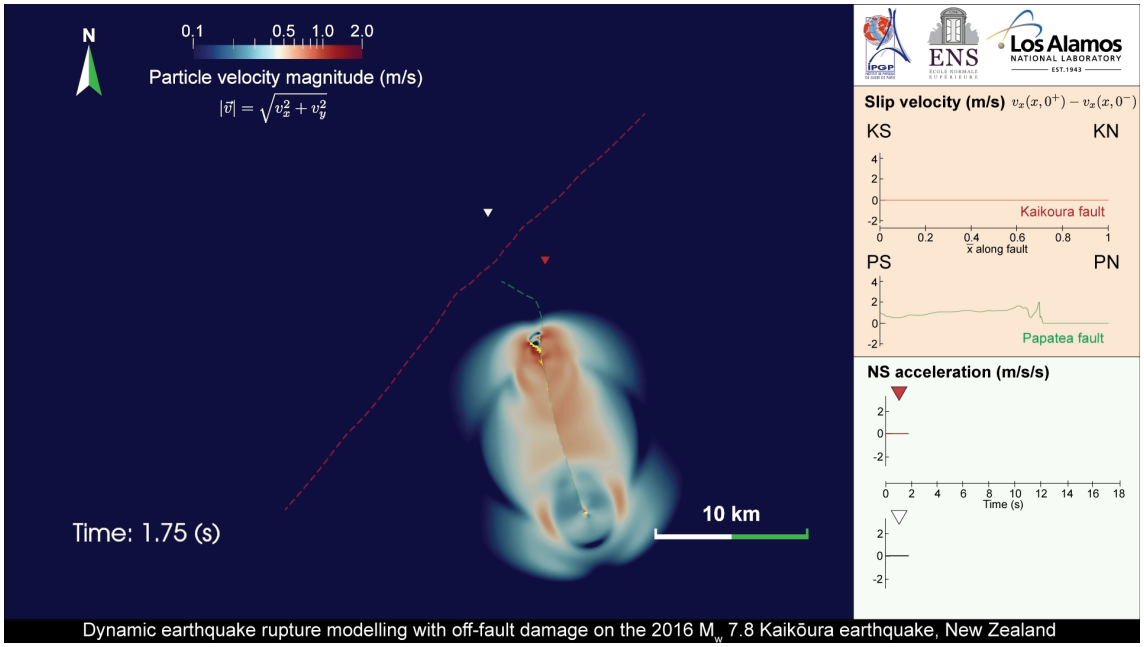

Figure 4.11: The rupture propagates northward generating coseismic off-fault cracks. The yellow lines show the secondarily generated off-fault cracks. The rupture front on the Papatea fault is still ahead of the secondary cracks.

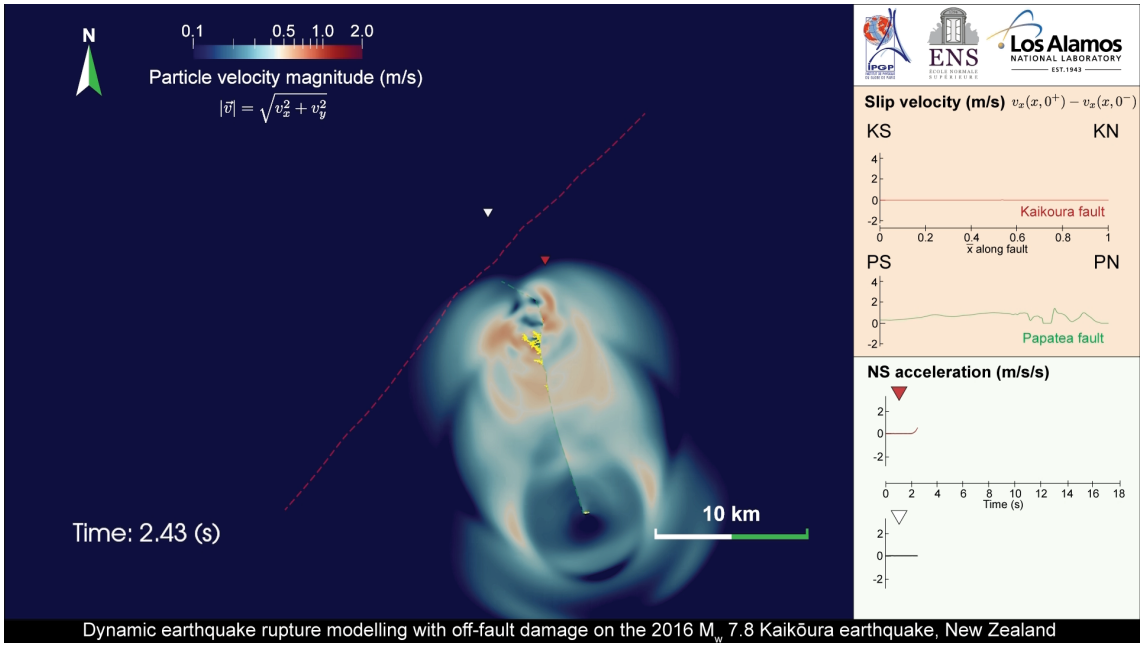

Figure 4.12: The rupture front decelerates due to the pre-stress state, while off-fault cracks propagate to the north-west. The rupture accelerates again around the northern end of Papatea fault, and will eventually jump to Jordan thrust - Kekerengu fault.

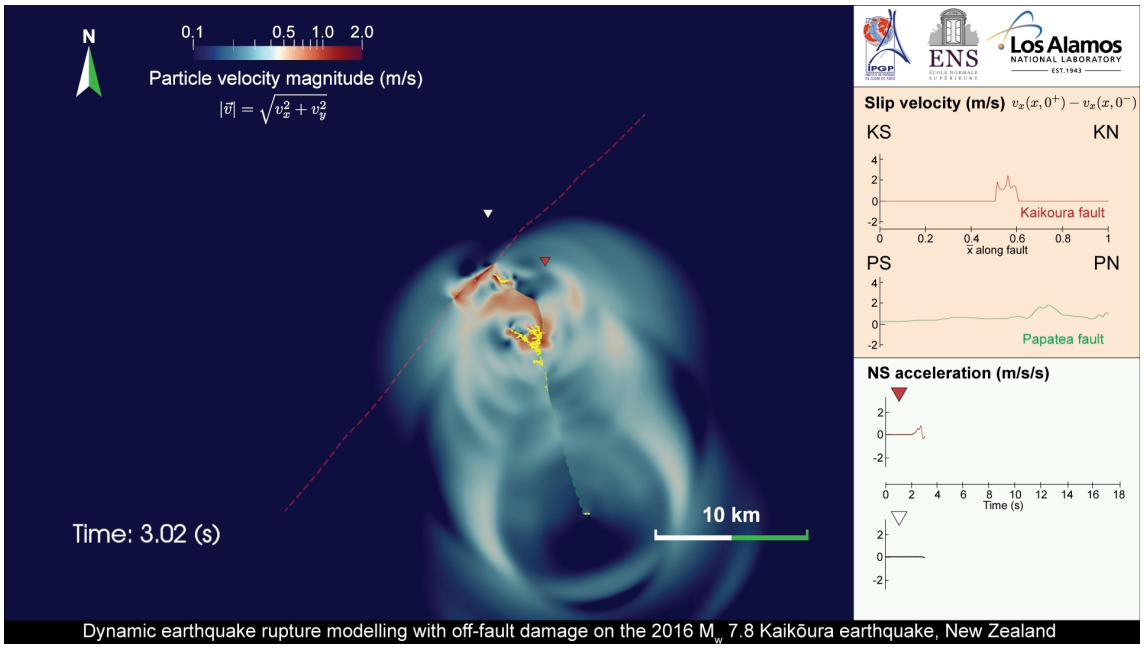

Figure 4.13: The rupture jumps from Papatea fault to Jordan thrust - Kekerengu fault. The northern end of Papatea fault is extended due to the cracking at the tip. The secondary cracks around the kink of Papatea fault becomes more intricate due to the stopping phase arriving from the northern end of Papatea fault.

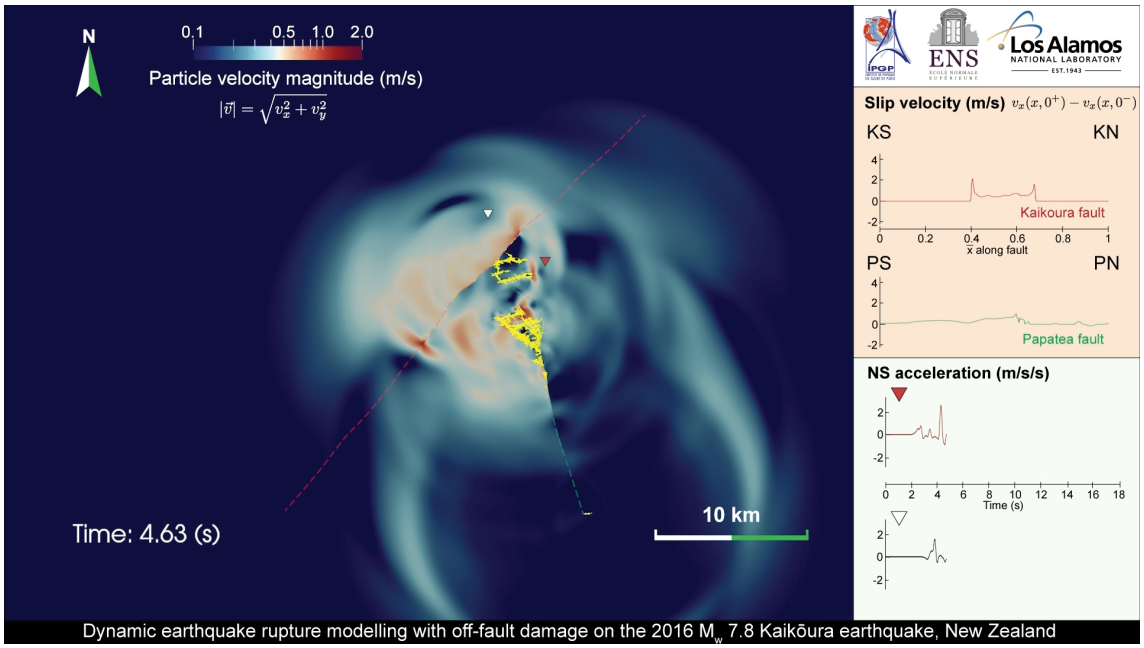

Figure 4.14: The rupture propagates bilaterally on Jordan thrust - Kekerengu fault, while it generates off-fault cracks along the faults. The off-fault medium around the junction is significantly damaged, which in turn emits additional radiation.

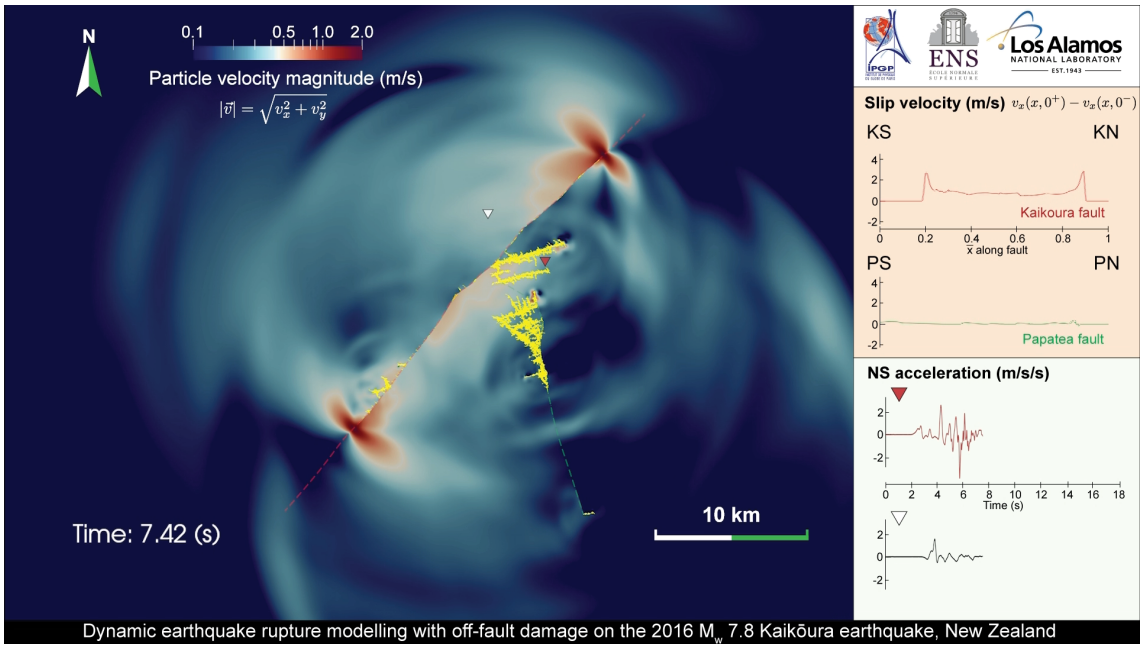

Figure 4.15: The coseismic off-fault damage is observed along Jordan thrust - Kekerengu fault. More damage is caused in the extensional side (north-west on Jordan thrust and south-east on Kekerengu fault). The prominent damage is generated due to small kinks along the faults.

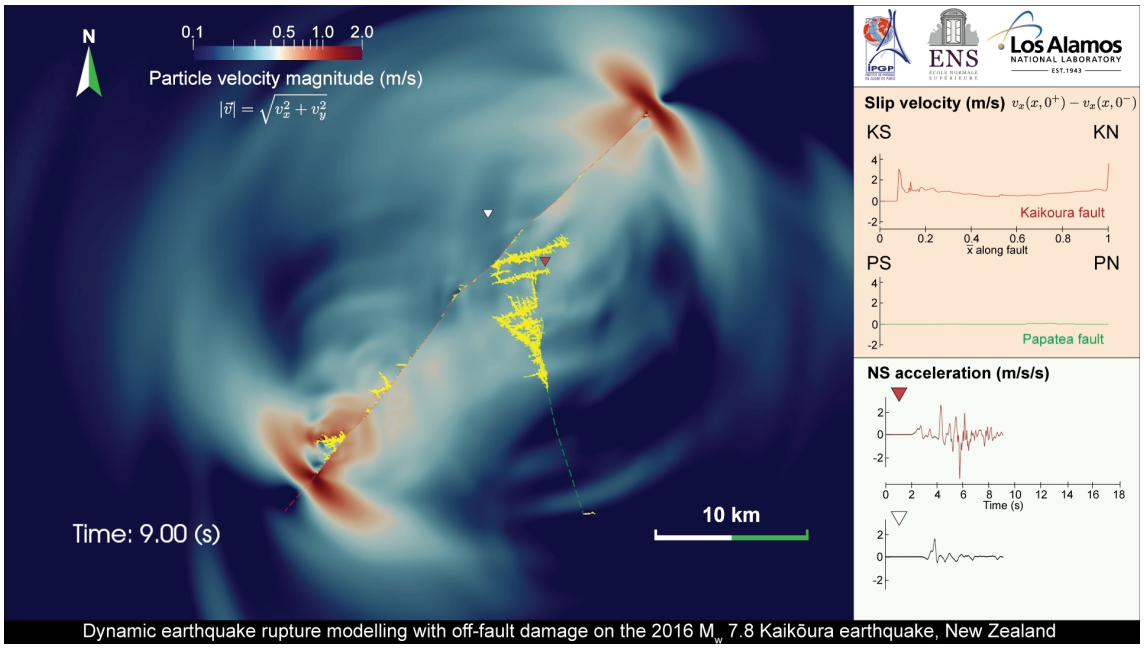

Figure 4.16: The large off-fault cracks near the red station locally enhances the NS acceleration of ground motion.

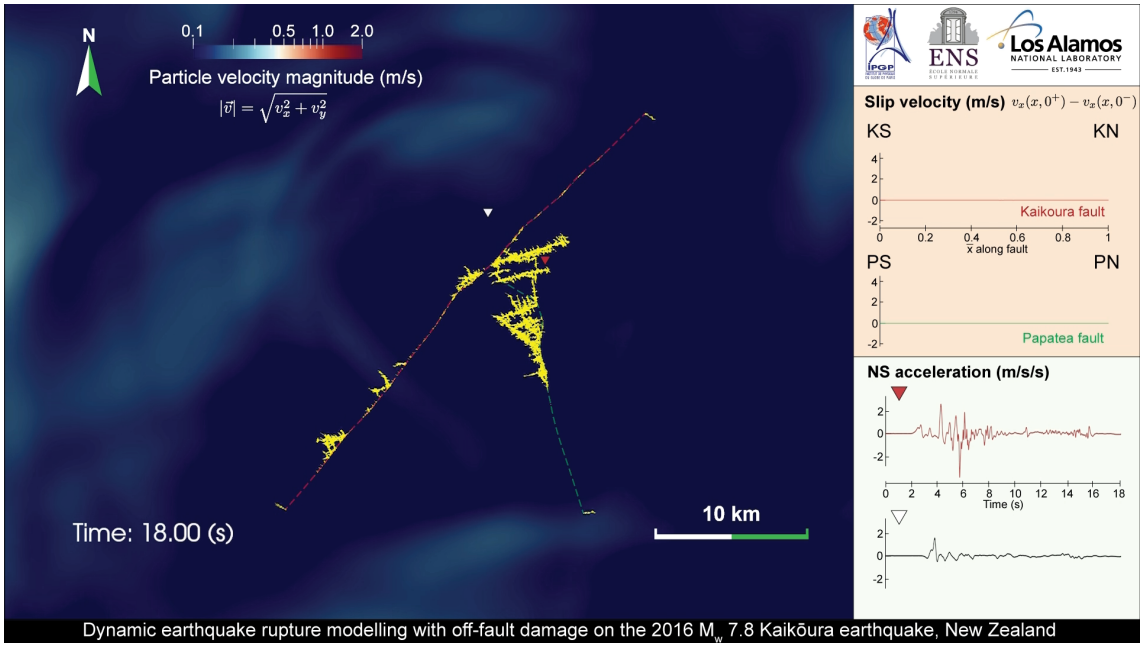

Figure 4.17: The final snapshot of the simulation. Significant off-fault fracture network is formed around the kink of Papatea fault and the junction with Jordan thrust - Kekerengu fault, which produces the distributed deformation field across faults.

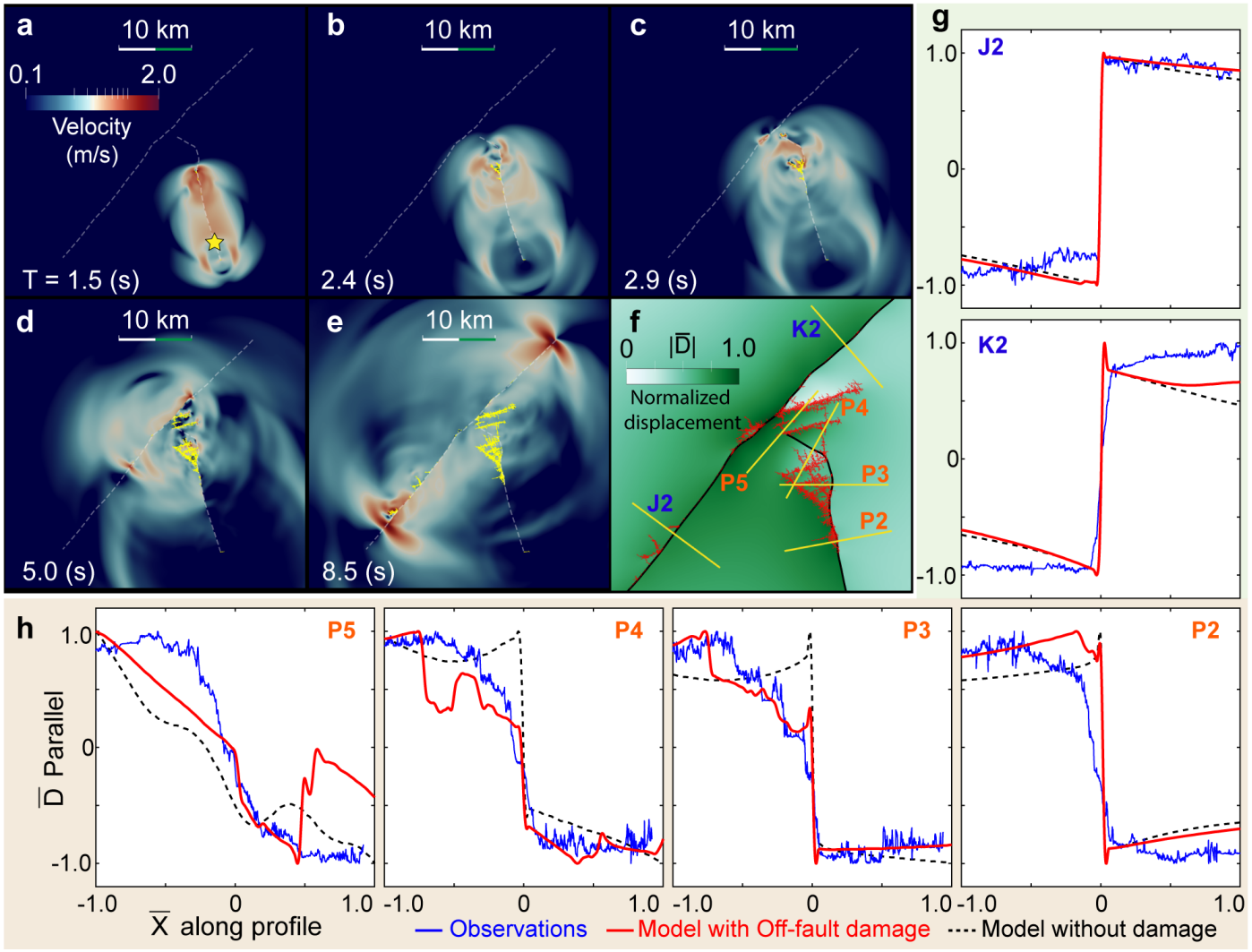

Figure 4.18: (Continued on the following page.)

Figure 4.18: Rupture process, displacement field and profiles of fault-parallel displacement for the first scenario. (a-e) Snapshots of the velocity field associated with rupture nucleated south of Papatea fault (yellow star). Dotted lines show the prescribed faults and yellow lines show the spontaneously activated off-fault fracture network. Secondarily activated off-fault fracture network is highlighted in yellow. (f) Deformation field and fracture network at the end of rupture propagation. (g, h) Measured displacement (blue), modeled displacement including damage (red), and modeled displacement with no damage (black dashed) for the different profiles. For comparison both fault parallel displacements and distance along profiles are scaled by their maximum values.

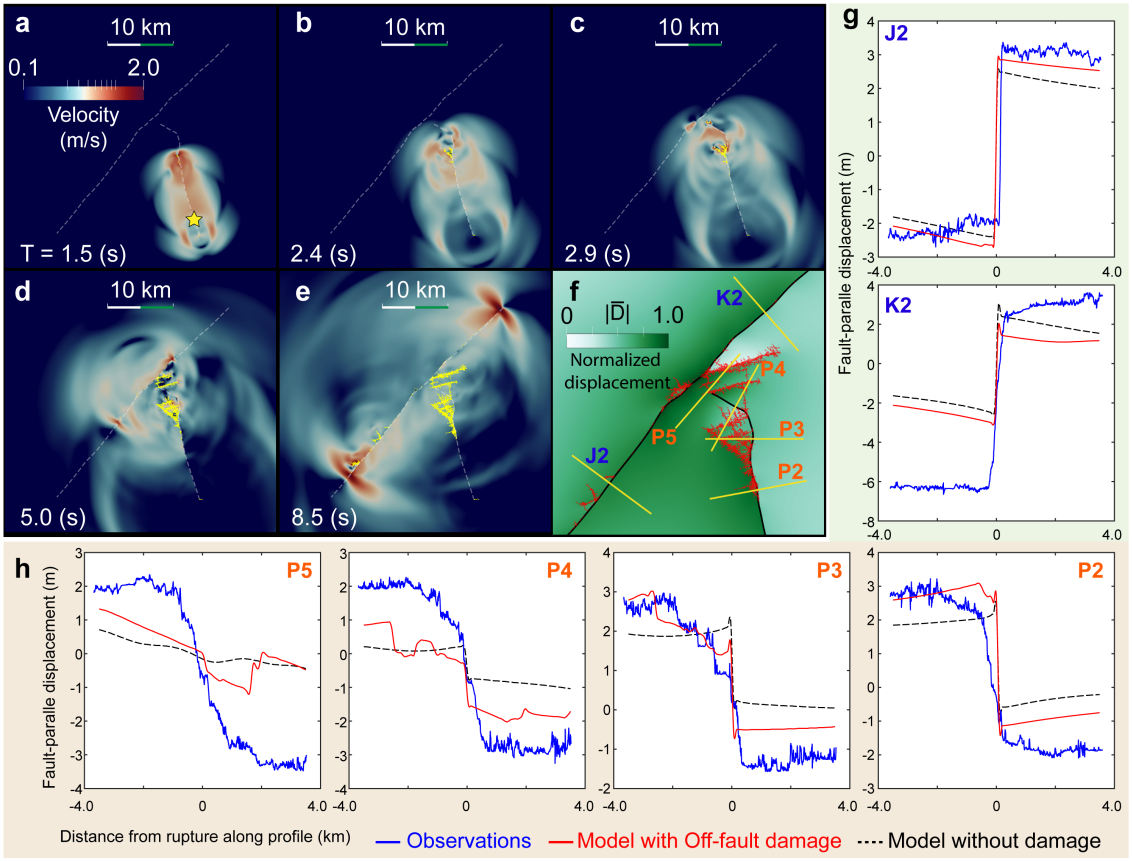

Figure 4.19: Rupture process, displacement field and profiles of fault-parallel displacement for the first scenario in physical length scale. (a-e) Snapshots of the velocity field associated with rupture nucleated south of Papatea fault (yellow star). Dotted lines show the prescribed faults and yellow lines show the spontaneously activated off-fault fracture network. (f) Deformation field and fracture network at the end of rupture propagation. (g, h) Measured displacement (blue), modeled displacement including damage (red), and modeled displacement with no damage (black dashed) for the different profiles. For comparison both fault parallel displacements and distance along profiles are in physical length scale.

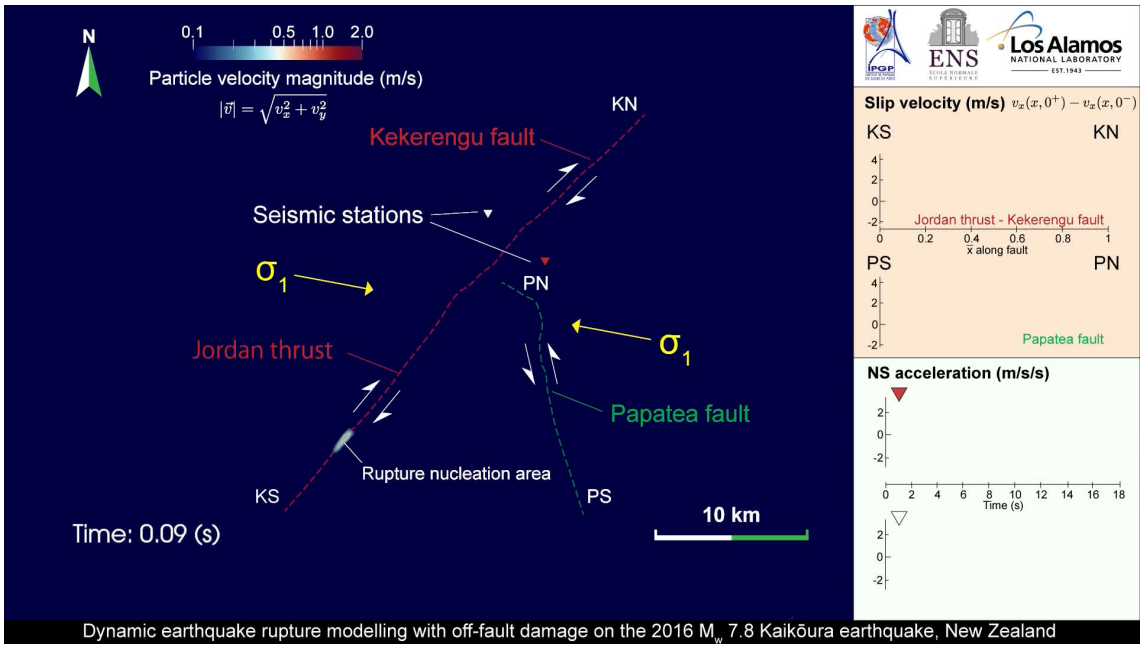

Figure 4.20: Model setup for the second scenario. The rupture is nucleated at the southern end of Jordan thrust.

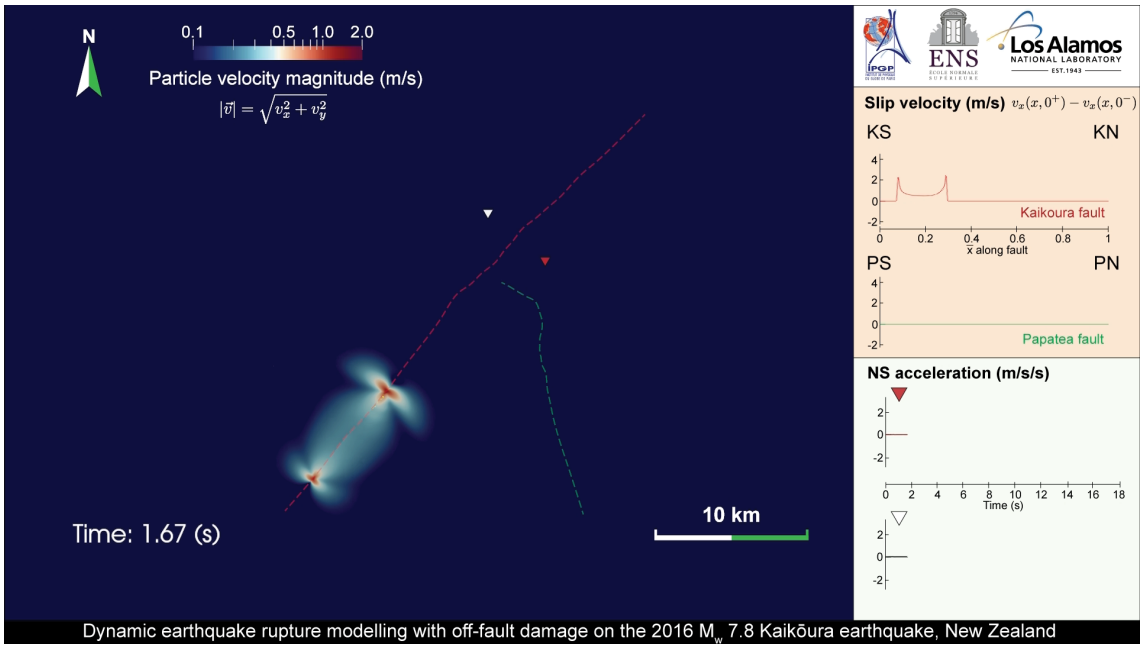

Figure 4.21: The rupture propagates bilaterally on the Jordan thrust. There are few damage in the early part of the rupture propagation.

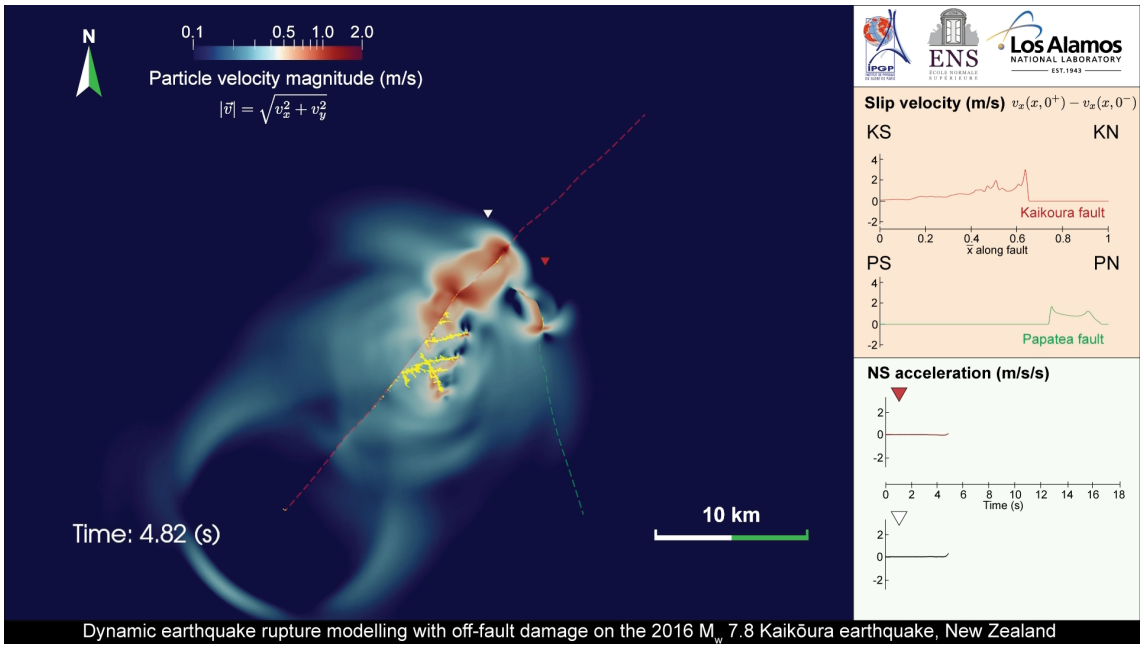

Figure 4.22: The rupture propagates from the southern end of Jordan thrust to northward activating off-fault cracks on the north-east of Jordan thrust. The induced rupture is spontaneously nucleated at the main kink of Papatea fault, which then propagates bilaterally.

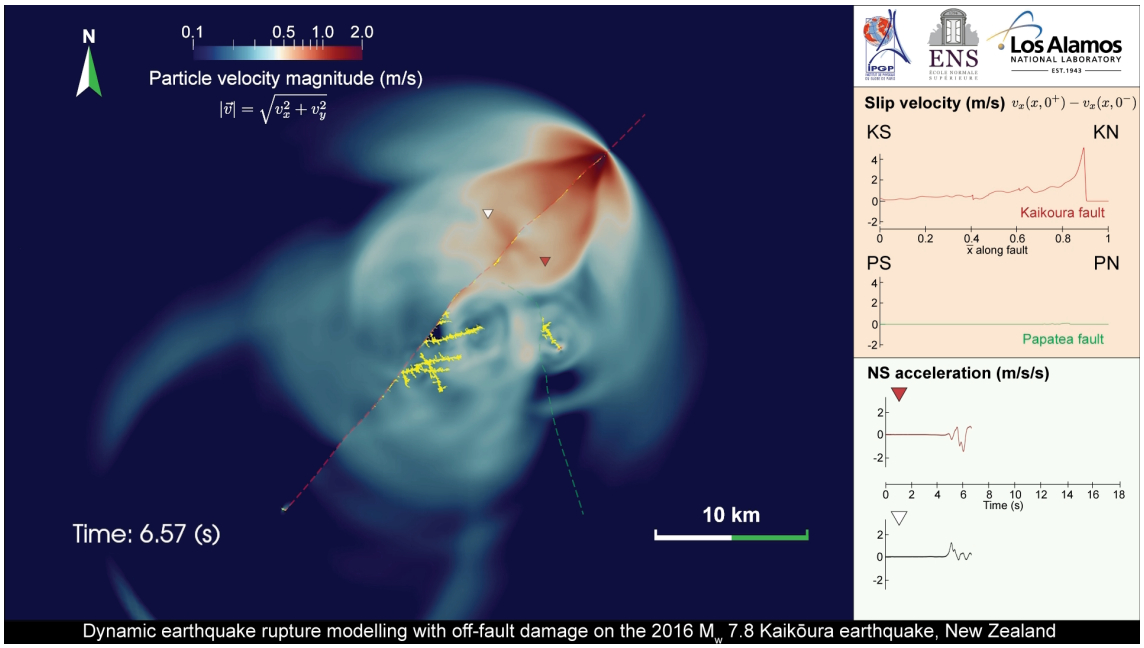

Figure 4.23: The rupture on Kekerengu fault accelerates enough to transition to supershear because the pre-stress condition is partially preferable for transition to supershear due to the change of fault geometry, whereas the rupture on the Papatea fault is arrested due to the secondary off-fault cracks.

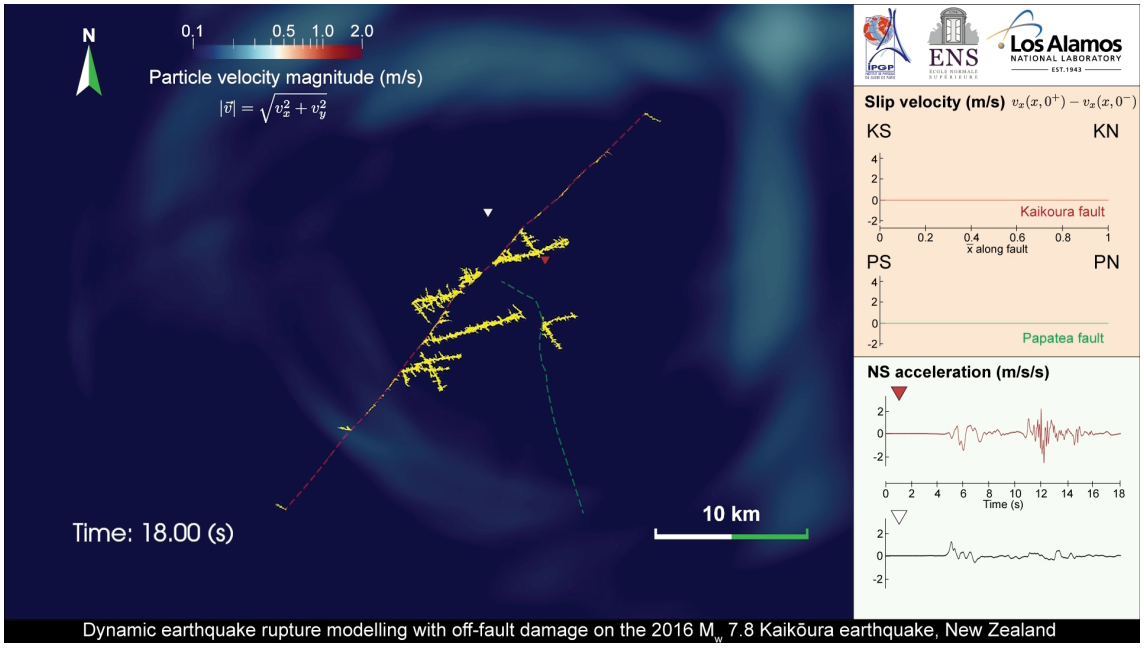

Figure 4.24: The final snapshot for the second scenario. The coseismic off-fault damage is observed on Jordan thrust - Kekerengu fault, whereas there is little damage on Papatea fault because the rupture is arrested on the northern part.

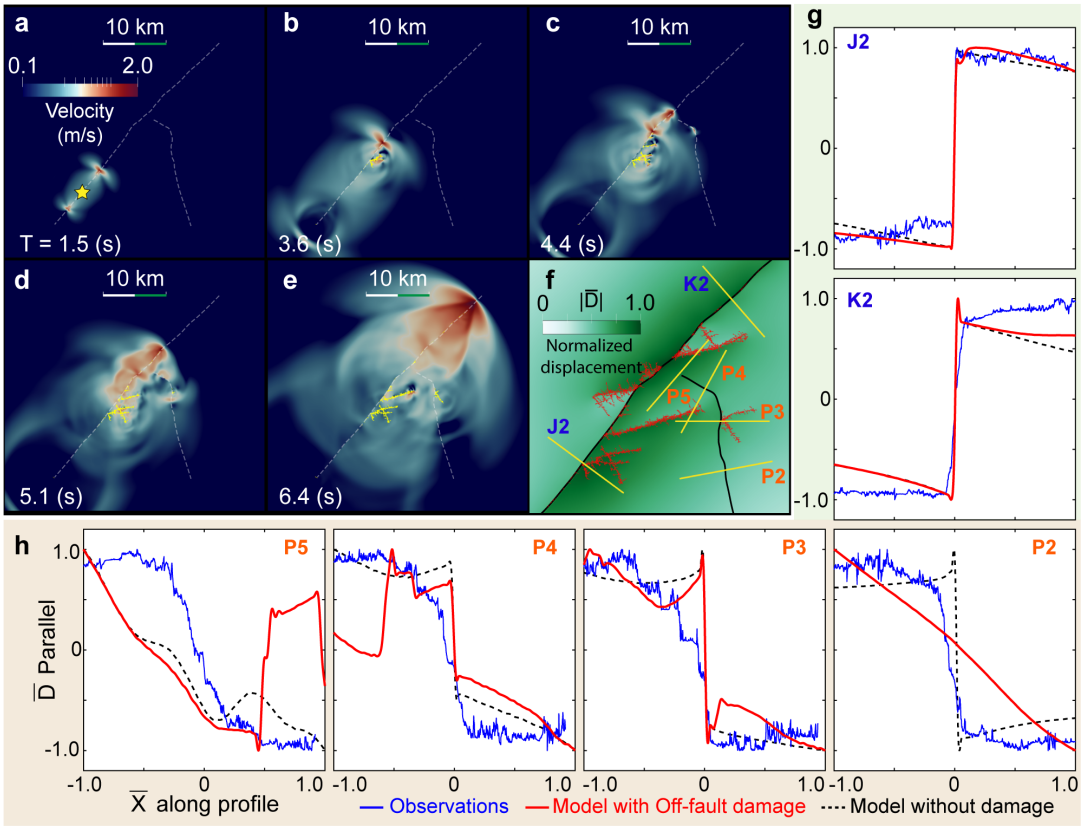

Figure 4.25: Rupture process, displacement field and profiles of displacement parallel to the fault for the second scenario. The rupture is nucleated at the southern end of the Jordan fault (yellow star). (a-e) Snapshots of rupture from south of the Papatea fault to the Kekerengu fault. Dotted line shows pre-existing faults and yellow lines show the secondary fracture network activated by the dynamic earthquake rupture propagation on the main faults. The color contours show the particle velocity magnitude. (f) The displacement field and the fracture network obtained at the end of the earthquake event (at 18s). The yellow lines across the main faults show the position of profiles, i.e., the profile of the displacements parallel to the fault shown in (g) and (h). The blue line shows the observations and the red line shows the model results with off-fault damage. The dotted black line shows the model results when considering a purely elastic medium, which does not allow for off-fault damage. Both the displacement parallel to the fault and the distance from the rupture are normalized with the range of displacement and the length of the profiles respectively.

4.4.4 Stress change, accumulated slip and slip velocity

Change of normal stress, stress drop and accumulated slip are of interest to understand the earthquake rupture processes. Thus we computed the mechanical fields on the prescribed faults. Figure 4.26a shows the trace of the Papatea fault and the dynamically activated off-fault cracks for the first scenario with coseismic off-fault damage. Although it forms an intricate fracture network around the main kink of the fault, we find a large chain of cracks in the direction towards northwest, which plays an important role in the distributed displacement profiles across the fault. As the Papatea fault has relatively large kinks and the initial normal and shear tractions on the fault are therefore heterogeneous, the change of normal stress and stress drop along the fault is significant as shown in Figures 4.26c, d. The comparison between the model with off-fault damage (in red) and the purely elastic model (in blue) of the change of normal stress indicates that the off-fault medium cannot sustain large stress concentrations as shown at x/L = 0.72 in Figure 4.26c. We also find a locally negative stress drop around x/L = 0.72, where the angle of maximum compressional principal stress is fairly orthogonal and thus the initial shear traction is relatively small. Hence, this part can cause negative stress drop after rupture propagation on such a non-planar fault.

Figure 4.26e shows the accumulated slip distribution on the Papatea fault. The accumulated slip is not zero at the ends of prescribed fault with coseismic off-fault damage due to the cracking at the edge of the fault. We found a locally enhanced slip in the case with off-fault damage at x/L = 0.62 on the Papatea fault in Figure 4.26e, which is directly induced by the off-fault cracks in the vicinity of the fault. Figure 4.26f shows slip velocity in time and space, which demonstrates the detailed rupture process on both faults. The rupture is initially nucleated around x/L = 0.3, propagating bilaterally on the Papatea fault. When the rupture reaches x/L = 0.7, it arrests and immediately jumps ahead at x/L = 0.83 due to the distribution of initial traction on the fault. Eventually the whole length of the Papatea fault is ruptured in this scenario. The slip velocity is remarkably perturbed by the spontaneous off-fault cracking. Since the stress distribution is extremely perturbed by the fracture network, negative slip velocity is temporarily induced around x/L = 0.62 at t = 6 s in Figure 4.26f. Figures 4.26g-l shows the same quantities on the Jordan - Kekerengu fault system. As it has less geometrical complexity compared to the Papatea fault, there is little off-fault damage (Figure 4.26g). The change of normal stress and the stress drop are smoothed by the off-fault damage same as the Papatea fault (Figures. 4.26i,j).

4.4.5 Near-field ground motion

As discussed in Chapter 3, the near-field ground motion can be influenced by the coseismic off-fault damage. To investigate the effect of coseismic off-fault damage around natural fault networks on the near-field ground motion, we put 10 stations around the triple junction as shown in Figure 4.27a. Figure 4.27b shows the north-south component of the ground acceleration with and without off-fault damage. The magnitude of acceleration is significantly enhanced at the station 6, where the large secondary cracks are dynamically activated close to the station. The phases are delayed with the coseismic off-fault dam-

age at station 7 and 8 because the rupture remains to be sub-Rayleigh with the off-fault damage, whereas it transitions to supershear without the off-fault damage.

Figure 4.27c shows the amplitude spectra of north-south component of the ground acceleration. The high-frequency components are clearly enhanced at the stations 1, 2, 4 and 6, where the locations of the station are close to the secondary fracture network. Thus they record the additional radiation from the secondary fracture network, which enhance the high-frequency components. There is no comparison to the observations due to the limitation of stations. There is only one available station, KEKS (*Holden et al.*, 2017), which is close to the station 7. However, since this station is far from the triple junction, there is less hope to find the signature of the coseismic off-fault damage in the observed seismograms.

The present analysis demonstrates the preliminary result of the enhanced high-frequency radiation in near-field ground motion by the coseismic off-fault damage with the natural fault network. The earthquake events with the available near-field records, such as the 2016 Kumamoto earthquake (Figure 4.28), is desirable to model the dynamic earthquake rupture to clarify the signature of enhanced high-frequency radiation by the coseismic off-fault damage.

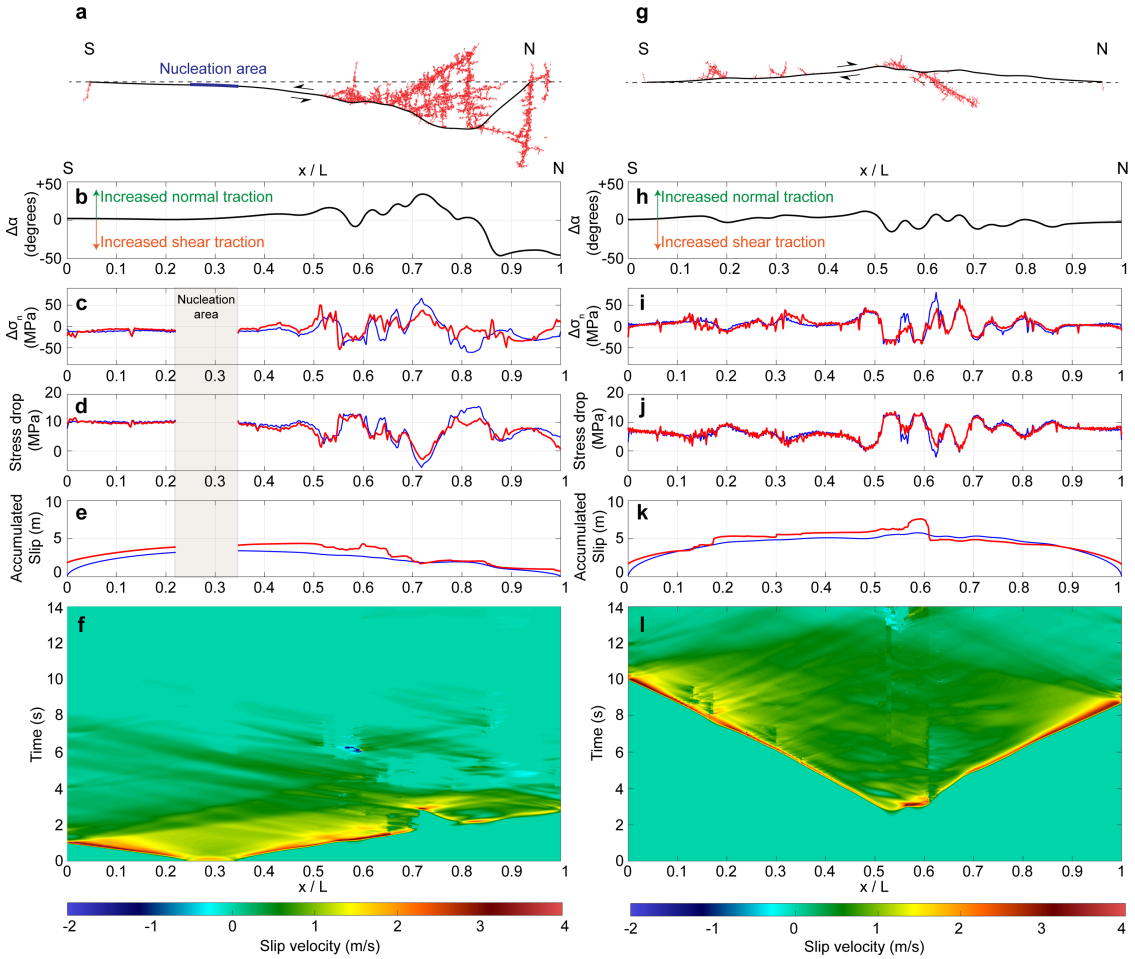

Figure 4.26: Off-fault damage pattern, stress change, slip and slip velocity on the Jordan fault, the Kekerengu fault and the Papatea fault for the first scenario with the coseismic off-fault damage. (a) The trace of secondary fracture network activated by dynamic earthquake rupture (indicated by red) on Papatea fault. The rupture is artificially nucleated at the nucleation segment indicated in blue. Notation S (south) and N (north) indicate the orientation of faults. The dotted auxiliary line shows a reference to measure the angle of the maximum compressional principal stress, $\Delta\alpha$, to the fault shown in (b). (b) orientation of the maximum compressional principal stress. $\Delta\alpha$ indirectly indicates the ratio of normal traction to shear traction. Positive values of $\Delta\alpha$ indicate larger normal traction than the reference traction state on the auxiliary line, whereas negative values show smaller ratio of the normal traction to the shear traction. The angle of maximum compressional principal stress to the reference is 53.6 ° on Papatea fault and 64.8 ° on Kekerengu fault. (c), (d), (e) and (f) the change of normal stress, $\sigma_n^0 - \sigma_n^1$, stress drop, $\tau_n^0 - \tau_n^1$, accumulated slip and slip velocity, respectively. The red line indicates the model with off-fault damage and blue indicates the model without off-fault damage. The color contours in (f) indicates the evolution of the slip velocity on the fault. The horizontal axis shows the position normalized by the length of the fault, and x/L = 0 corresponds to the southern edge of the fault. (g-l) the same quantities on Kekerengu fault.

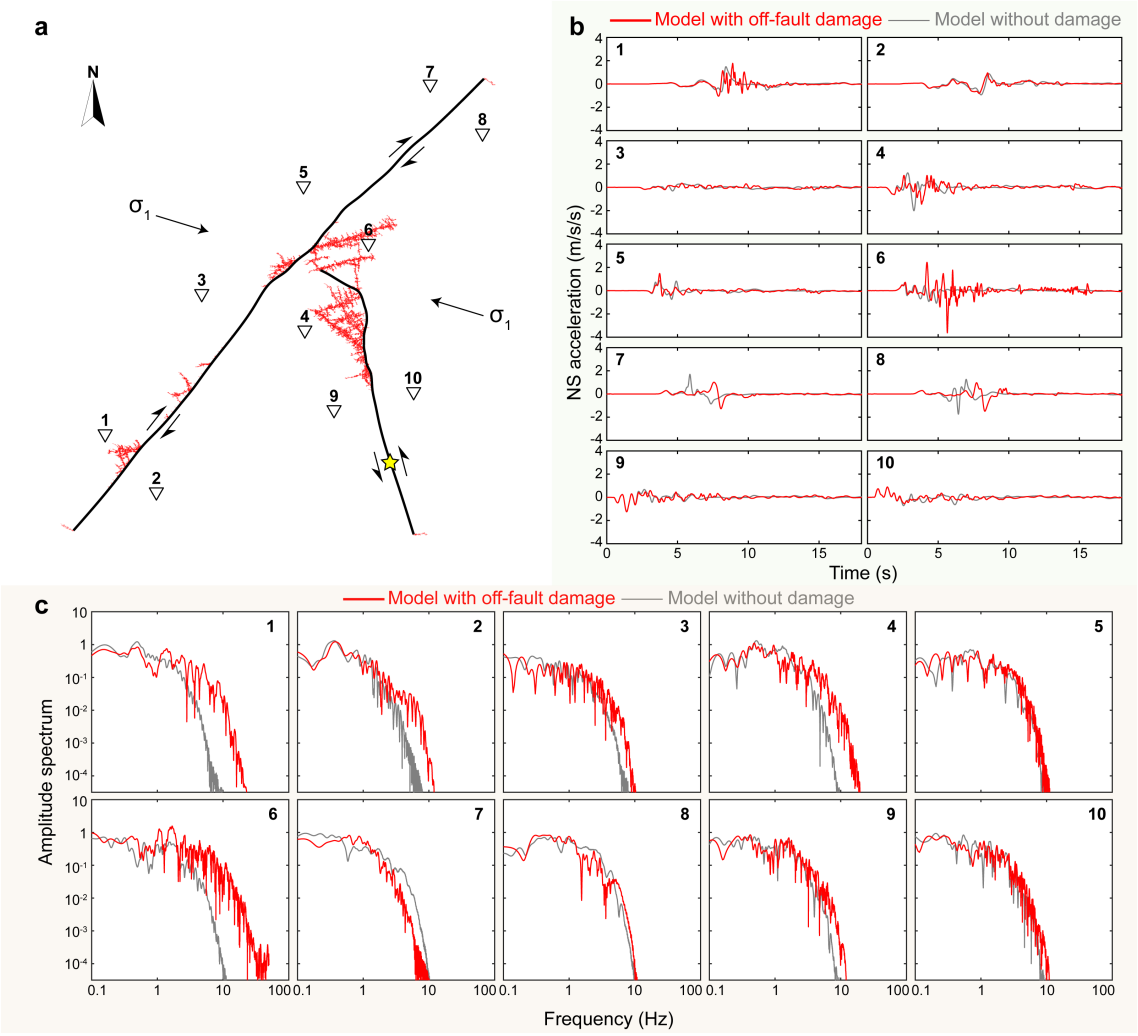

Figure 4.27: Location of the seismic stations and recorded seismograms. (a) Pre-existing fault geometry (indicated by black lines), secondarily activated fracture network (indicated by red lines), and location of the stations indicated by inverted triangles for the first scenario with the coseismic off-fault damage. Rupture is nucleated at the south of Papatea fault indicated by yellow star. (b) North-south component of acceleration. Numbers in the window correspond to the location of the stations in (a). Red line indicates the model with off-fault damage, while gray line indicates the model without off-fault damage. (c) Amplitude spectrum of the NS accelerations obtained with the time window from 0 s to 18 s. The amplitude is not normalized for these spectra.

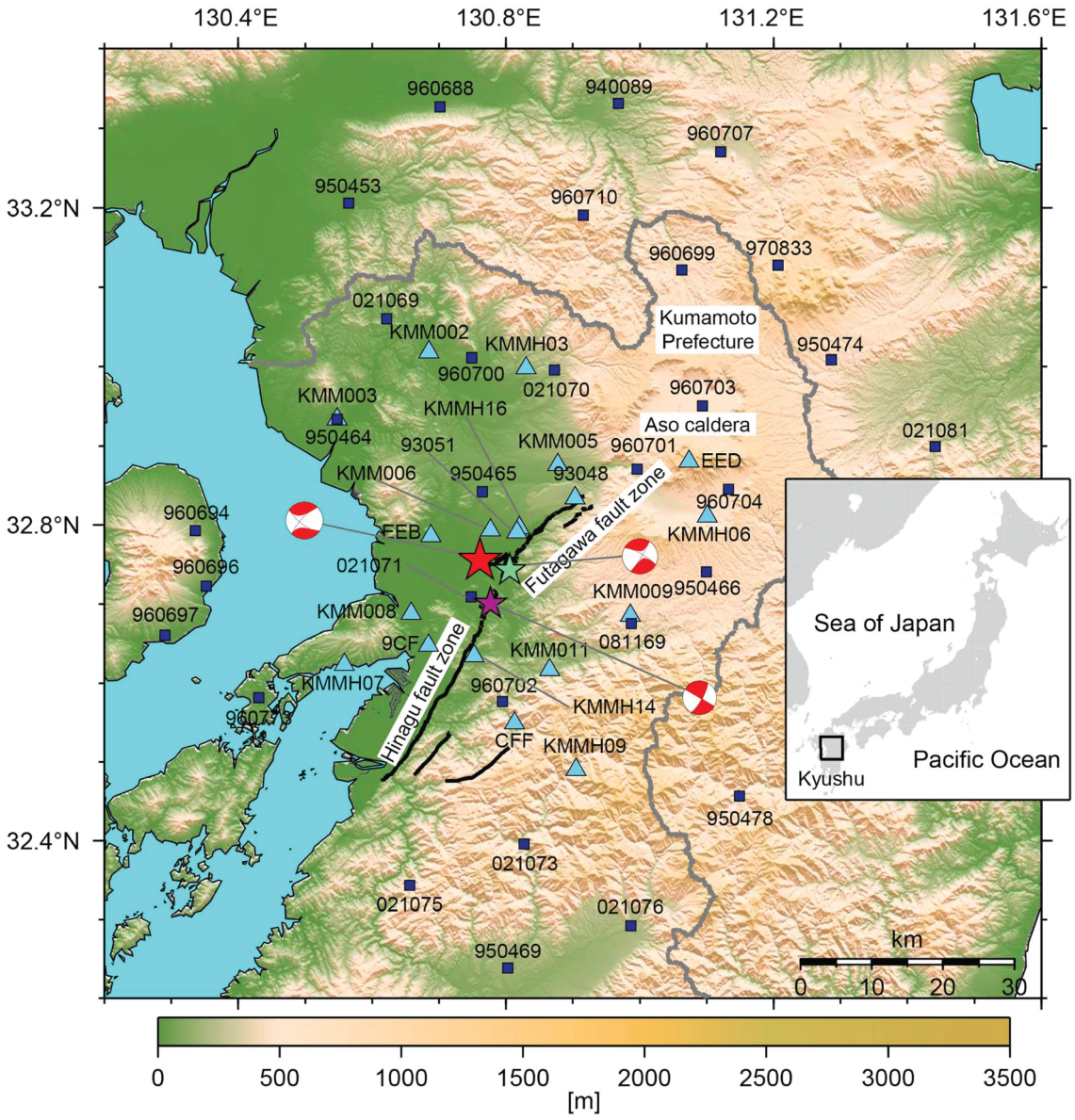

Figure 4.28: Map of the source area associated with the 2016 Kumamoto earthquake sequence. The black square in the inset map shows the studied area. The light green, purple, and red stars denote the epicenters of the first event, the second event, and the largest event, respectively. The sky blue triangles indicate the strong motion stations of K-NET, KiK-net, JMA, and the Kumamoto prefectural government. The dark blue squares indicate the GEONET stations. The thick black lines represent active faults (*Ikeda et al.*, 2001; *Nakata et al.*, 2001). The land topography is indicated by background colors, and the sea areas are colored light blue. The focal mechanisms of the three earthquakes from the Global CMT solutions are shown on the map. The thick gray lines show the boundary of the Kumamoto Prefecture. Reprinted from *Kobayashi et al.* (2017).

4.5 Conclusions

In summary, comparison of the satellite-derived displacement maps and field observation with damage patterns resulting from each modeled scenario (Figures 4.18g, h; 4.25g, h) shows that the Papatea-first scenario is more consistent with the observations: the Papatea fault likely ruptured from the coast towards the triple junction area where it triggered a bi-lateral rupture on the Jordan-Kekerengu fault system (Figure 4.29). Although it is at the current limit of the resolution of seismological data available, the seismic source studies that are focused on the second part of the Kaikōura rupture are compatible with this scenario (*Holden et al.*, 2017; *Xu et al.*, 2018) and this scenario is also fully supported by complex 3D dynamic rupture models (*Ulrich et al.*, 2018). More complexity, however, might still arise from full integration of vertical deformation, which is not included in our model at this stage.

Hence, although the Mw 7.8 Kaikōura earthquake has been deemed one of the most complex continental earthquake ruptures ever documented because of the very large number of fault sections activated, the general rupture mechanism might actually be simple. From the epicenter, the rupture propagated northward, navigating local geometrical complexities, then it extended off-shore along the Hundalee fault and along a Kaikōura peninsula-Point Kean fault. Eventually it dynamically triggered a rupture along the Papatea fault, located at a maximal distance of 12 km, although it might be closer off-shore. The rupture then propagated northward along Papatea and eventually triggered a bi-lateral rupture along the Jordan-Kekerengu fault system. The Papatea block acted as a large-scale compressional jog, which is consistent with the large documented uplift (*Hamling et al.*, 2017; *Morishita et al.*, 2017). If any deep-seated thrust fault was also involved, our work does not bring any additional constraints.

At first glance, surface ruptures might appear very complex during large continental earthquakes, such as the Kaikōura earthquake. This complexity, however, can be resolved and it might be that the rupture follows a rather simple structural path. Comparison between data and model outputs shows unambiguously that off-fault damage should be taken into account to explain that the rupture path and the on- and off- fault displacement fields, which cannot be recovered by utilizing purely elastic models (dashed lines of Figures 4.18g, h). Earthquake simulators used in seismic hazard assessments for complex fault systems, such as for the Southern California fault system (*Field et al.*, 2017), can generate myriads of very large and complex fault ruptures. Providing critical keys, like off-fault damage patterns, to decipher this complexity might help narrow down a subset of most probable scenarios along complex fault networks.

We also demonstrated the evolution of stress state on the prescribed faults and the near-field ground motions. The comparison between the cases with and without off-fault damage shows that the large stress concentration is smoothed by the off-fault fracturing. The amplitude spectra of near-field ground motion highlights the enhanced high-frequency components close to the secondarily activated off-fault fracture network. Although these preliminary results have not been compared with the observations, these results demonstrate the potential to find the signatures of coseismic off-fault damage from the other type of observations, such as the accumulated slip and the near-field ground motion.

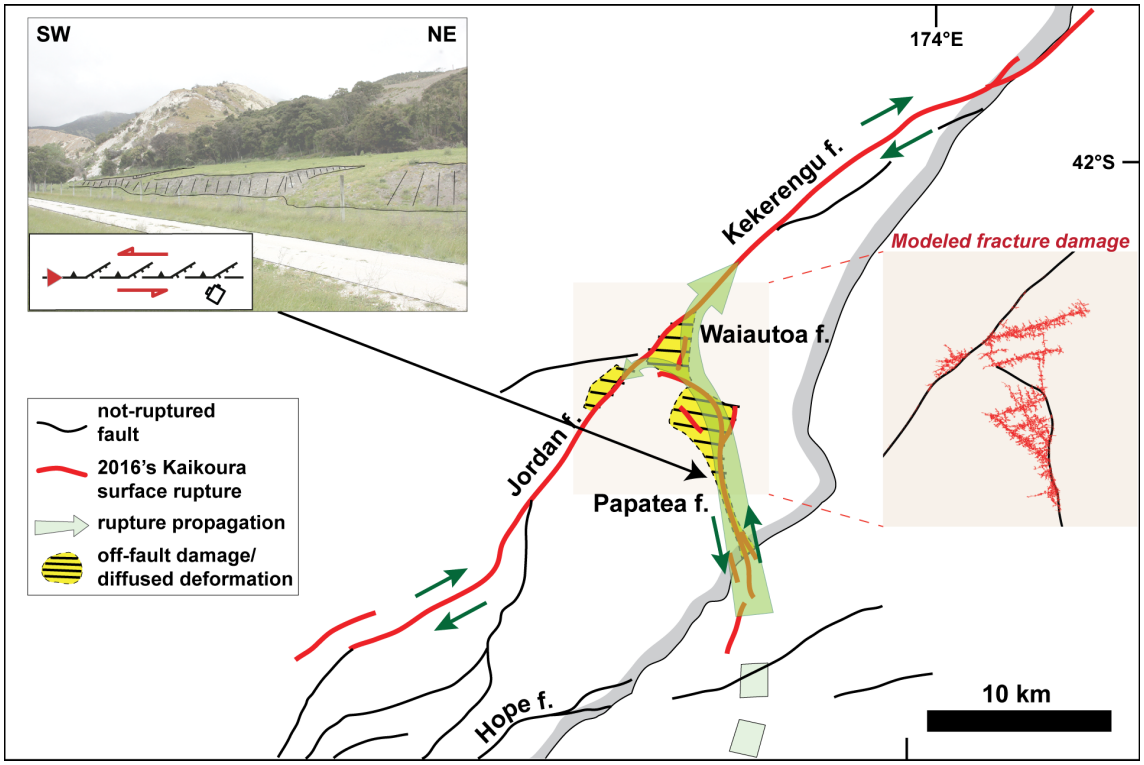

Figure 4.29: Summary of the preferred rupture path and associated fracture damage. Photo inset shows the observed surface damage on the Papatea fault (S42°08'47", E173°52'01"). In addition to the main strike-slip scarp with some thrust, systematic westward branching with normal motion can be seen, which is best explained by left-lateral rupture propagating from the south. Yellow dashed areas correspond to the main areas of damage, from optical correlation and field observation.

5. Perspectives

Avant-propos

Nous avons présenté une approche numérique qui allie la modélisation des milieux continus et discontinus, en utilisant la méthode combinée des éléments finis et discrets (FDEM), afin de modéliser des ruptures dynamiques associées à l'endommagement cosismique. Ce modèle a été utilisé pour reproduire le séisme de Kaikōura. Cependant, il conviendrait d'étudier les complexités géométriques de premier ordre, tels que la rugosité, les failles présentant des « stepovers », plusieurs, ou encore un changement abrupt de direction, afin de mieux comprendre l'effet de l'endommagement sur la mécanique de rupture En effet, les études précédentes ont montré l'importance, en modélisation, d'incorporer ces complexités géométriques (*Harris and Day*, 1993; *Madariaga et al.*, 2006; *Adda-Bedia and Madariaga*, 2008; *Duan and Day*, 2008; *Bhat et al.*, 2007; *Templeton et al.*, 2009; *Dunham et al.*, 2011b; *Romanet et al.*, 2018). La nouveauté consistera ici à considérer l'effet combiné de la structure et l'endommagement sur la mécanique de rupture. Un autre point intéressant serait d'appliquer le modèle pour un chevauchement. Pour ce scénario, la surface libre peut jouer un rôle important dans la mécanique de rupture. *Gabuchian et al.* (2017) a en effet montré la possibilité d'obtenir une « ouverture » temporaire de la faille, à l'approche de la surface libre, pouvant générer une quantité d'endommagement significatif dans les roches sédimentaires En conclusion, ces projets potentiels, qui n'ont pu être adressés, sont extrêmement intéressants et tout à fait réalisables dans le cadre de la FDEM. Bien qu'il faille apporter quelques modifications à l'algorithme, le structure du code ne changerait pas de manière essentielle et ces différents projets pourront être étudier dans un futur proche.

5.1 Introduction

In Chapters 3 and 4, we demonstrated a continuum-discontinuum approach framework for modeling dynamic earthquake ruptures with coseismic off-fault damage. FDEM has a great potential for modeling the deformation and the interactions of solid bodies in multiscale, i.e., fracturing process on- and off-fault, and radiations, because of an efficient contact algorithm. In addition to the mechanical aspects of coseismic off-fault damage and the effect on the high-frequency radiation, we also demonstrated the effect of coseismic off-fault damage on the overall energy budget associated with earthquake ruptures.

However, we have not studied first-order geometrical complexities, such as kinks,

branches, rough faults and stepovers, which needs to be investigated for better understanding of these fundamental effects on rupture dynamics. Therefore, the first perspective is to model dynamic ruptures on the first-order complex fault geometries, which compose the natural fault network. Our preliminary results demonstrate that the coseismic off-fault damage changes rupture dynamics, in accordance with what we observed in the application for the Kaikōura earthquake in Chapter 4.

The second perspective is the application for thrust faults. In this case, we need to consider the free surface, which also plays an important role in rupture dynamics. *Ma and Hirakawa* (2013) shows the effect of coseismic off-fault damage on the deformation of wedge and consequent radiations using inelastic constitutive formulations, which demonstrates the significant absorption of the energy consumed by the inelastic deformation on the wedge. *Gabuchian et al.* (2017) shows the possibility of the fault opening near the free surface, which is also expected to cause a significant damage on the wedge. Our aim of this subject is to reconduct the rupture modeling on thrust faults with spontaneous activation of coseismic off-fault fracture network. Since the feedback from the free surface and the fault opening might cause damage in multiscale, which includes from micro fractures to major branches on the wedge, we need to evaluate the effect of the coseismic damage on the rupture dynamics and radiations, as well as the damage pattern on the wedge. Our preliminary results show the potential of FDEM for the application of thrust faults.

Finally, we list the perspectives, which are not initiated yet, but are profitable and feasible with the FDEM approach framework. Although we need to modify or patch the algorithm, the framework does not change in essence. Therefore, all these perspectives can be studied with the FDEM framework as proposed in this thesis.

5.2 Decomposition of natural fault networks into simple geometrical complexities

5.2.1 Finite faults

We already studied the Kaikōura earthquake as an application for the natural fault network. However, we need to revisit the first-order geometrical complexities to decompose complicated rupture processes on the natural fault network. Our previous work on the fundamental analysis of coseismic off-fault damage (Chapter 3) was conducted on an infinite planar fault. Thus we first study rupture on a finite planar fault. The model setup is shown in Figure 5.1, and the parameters for this simulation is listed in Tables 5.1 and 5.2. These simulations are conducted in the physical dimension.

Figures 5.2 and 5.3 show the snapshots of finite fault modeling without off-fault damage. Thus the off-fault medium behaves as a purely elastic material. In this case, the rupture is bilaterally symmetric and is abruptly arrested at the edges of the main fault. Then Figures 5.4 to 5.7 show the snapshots with coseismic off-fault damage. The rupture first propagates by activating secondary off-fault cracks, same as the results with a infinite planar fault. As discussed in section 3.1.3, the rupture velocity decreases from the comparison at the same time between Figures 5.3 and 5.5. When the rupture reaches to

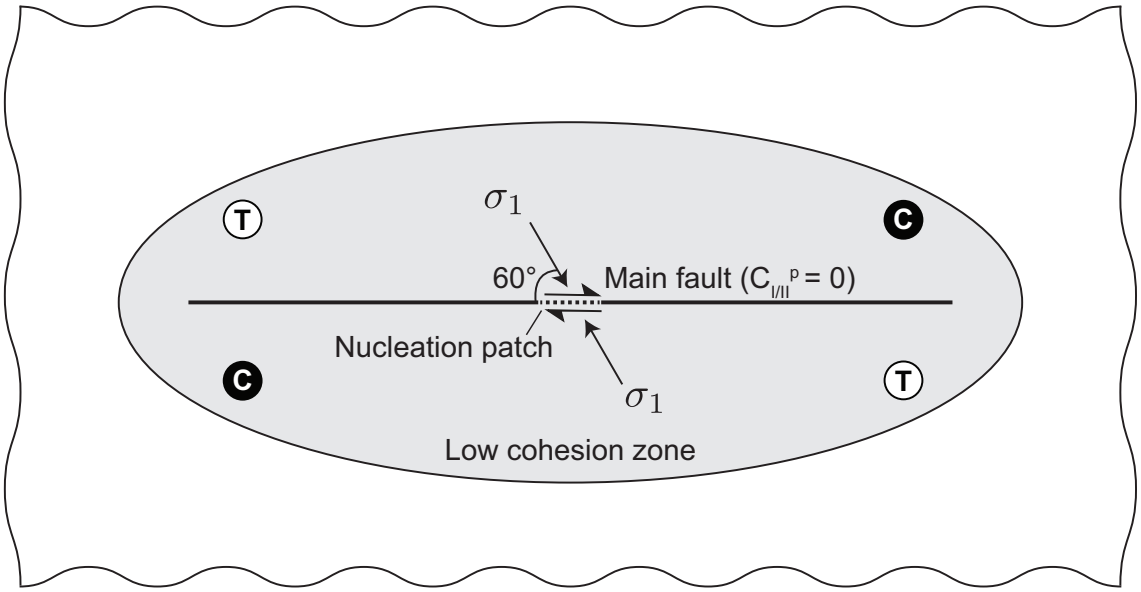

Figure 5.1: Model setup for modeling a planar finite fault. A planar finite fault is prescribed in the middle of the medium. The orientation of the maximum compressive stress, σ_1, is set at 60°. The fault length is 20km. The nucleation patch is set in the middle of the fault, where the static friction coefficient is lower than the rest of the fault. The finite fault is surrounded by low cohesion zone, where the cohesion is lower than the outside region. The cohesion off this outer zone is set large enough to avoid over cracking from the edges of the faults. The grid points per R_0 is set as 10 on the main fault. The medium size is large enough to avoid the reflection from boundaries.

the edges of the main fault, a lot of damage is caused around the edges, and thus the rupture is arrested (Figures 5.6 and 5.7). Since we set the low cohesion zone, the secondary fracture network around the edges eventually stops to evolve, and the earthquake event is terminated.

In conclusion, a lot of damage can be caused at the end of pre-existing faults because of the dynamics of ruptures, which is expected to play a role in the radiation and overall energy budget. Therefore, the future work associated with the finite fault model should include the evaluation of the effect of coseismic off-fault damage on radiation, overall energy budget and the shape of STF.

Table 5.1: Material constants and parameters for modeling a planar finite fault.

Valuables	**Values**	**Descriptions**
E	75 GPa	Young's modulus
μ	30 GPa	Shear modulus
ν	0.25	Poisson's ratio
ρ	2700 kg m^{-3}	Density
σ_n	40 MPa	Normal stress on the main fault
τ	16 MPa	Shear stress on the main fault
σ_1	49 MPa	Maximum compressive principal stress
σ_2	12 MPa	Minimum compressive principal stress
S	1.0	S ratio
d_{MC}	0.45	Closeness to failure
φ	60 $^\circ$	Orientation of σ_1
R_0	552 m	Quasi-static process zone size
L_c	1200 m	Nucleation length
ds	55 m	Grid size on the main fault

Table 5.2: Variables for contact interactions.

On the main fault		
f_s	0.6	Static friction coefficient
f_d	0.2	Dynamic friction coefficient
D_c	0.25 m	Characteristic slip distance
G^f_{IIC}	2 MJ m^{-2}	Fracture energy for friction
In the off-fault medium		
f_s	0.6	Static friction coefficient
f_d	0.2	Dynamic friction coefficient
D_c	12.5 mm	Characteristic slip distance
G^c_{IC}	8 KJ m^{-2}	Fracture energy for tensile cohesion
G^c_{IIC}, G^f_{IIC}	90 KJ m^{-2}	Fracture energy for shear cohesion and friction
C^p_I	8 MPa	Peak cohesion for opening crack in low cohesion zone
C^p_{II}	30 MPa	Peak cohesion for shear crack in low cohesion zone
$\delta^{c,c}_I - \delta^{c,e}_I$	2.0 mm	Critical displacement for softening of tensile cohesion
$\delta^{c,c}_{II} - \delta^{c,e}_{II}$	6.0 mm	Critical displacement for softening of shear cohesion

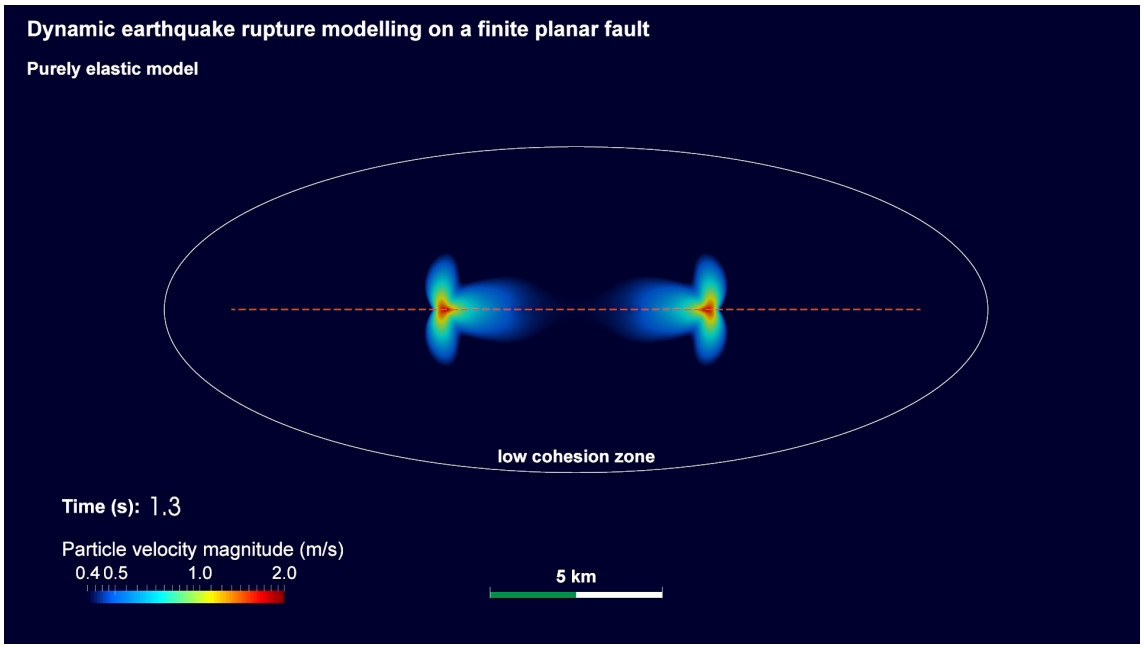

Figure 5.2: Snapshot for finite fault model without coseismic off-fault damage (Purely elastic model). Dashed line indicates the prescribed main fault. Color contour indicates particle velocity magnitude.

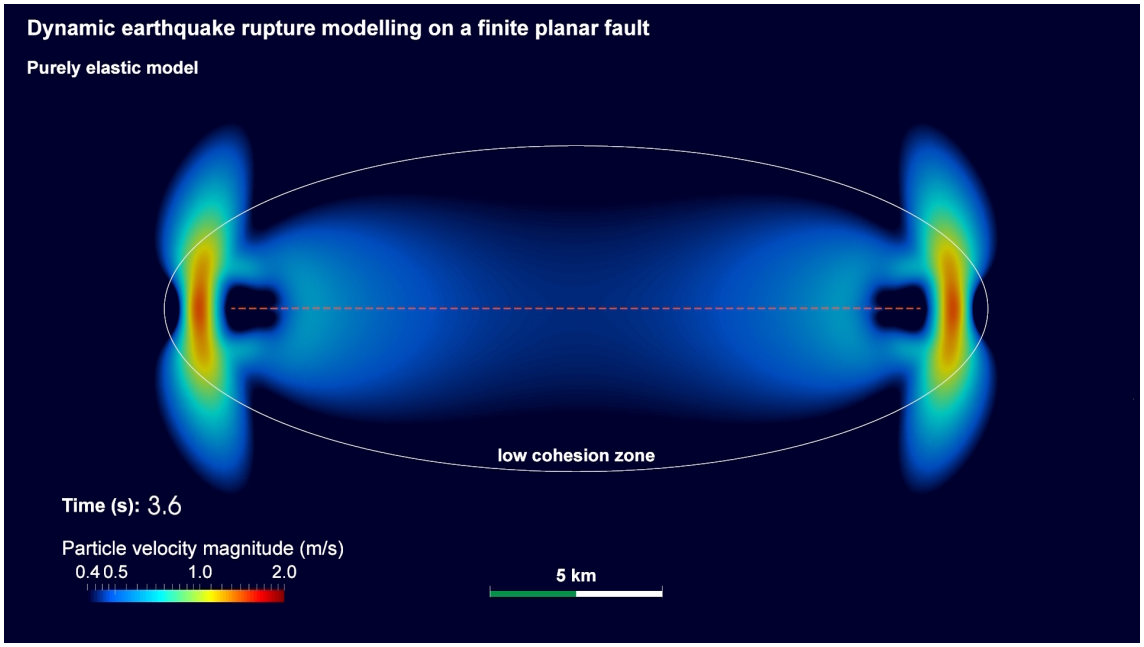

Figure 5.3: Snapshot at T = 3.6s. Rupture is abruptly arrested at the edges of the main fault.

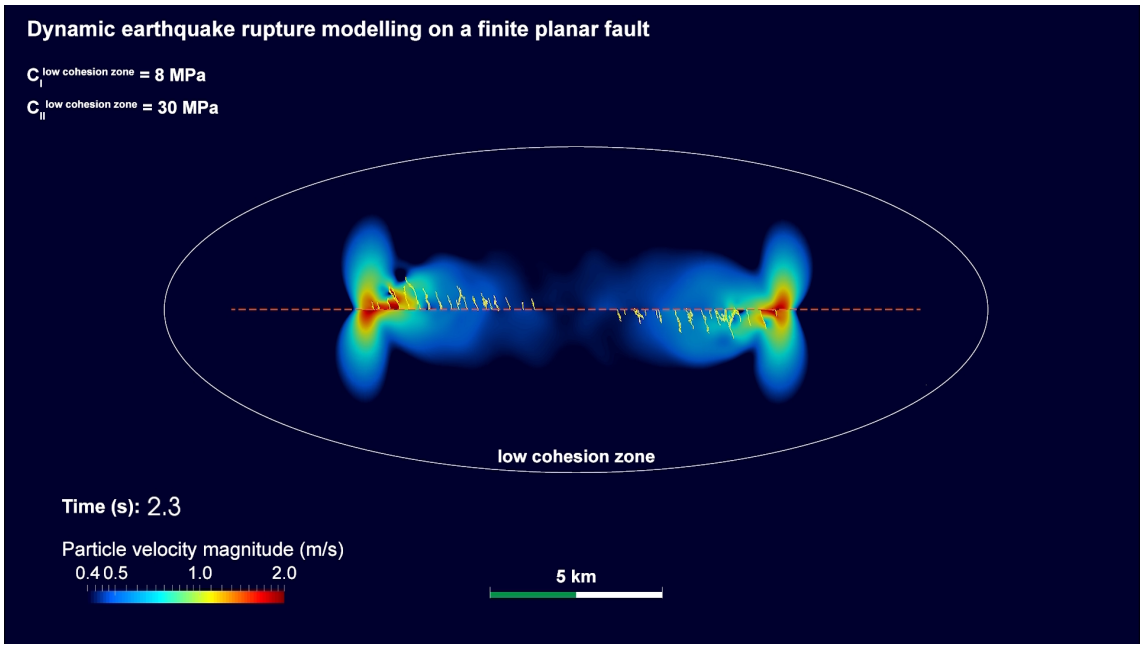

Figure 5.4: Snapshot for finite fault model with coseismic off-fault damage. Dashed line indicates the prescribed main fault. Color contour indicate particle velocity magnitude. Yellow lines indicate the secondarily generate off-fault cracks.

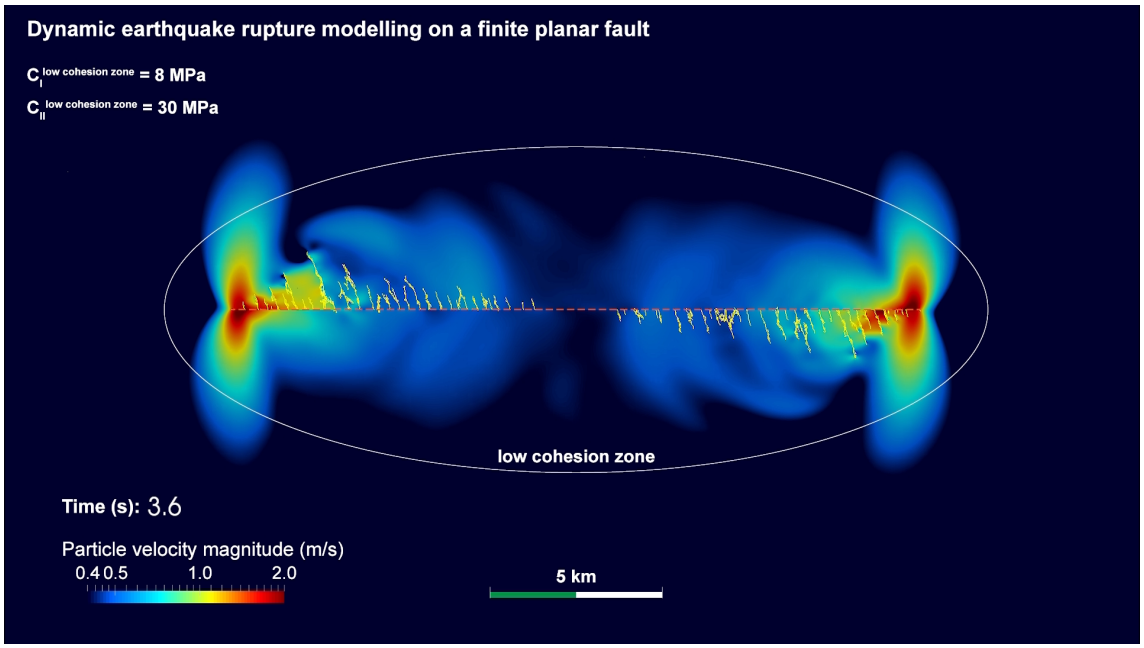

Figure 5.5: Snapshot at T = 3.6s. Compared to (Figure 5.3), the rupture remains to reach the edges of the main fault, which implies that the rupture velocity decreases due to the coseismic off-fault damage.

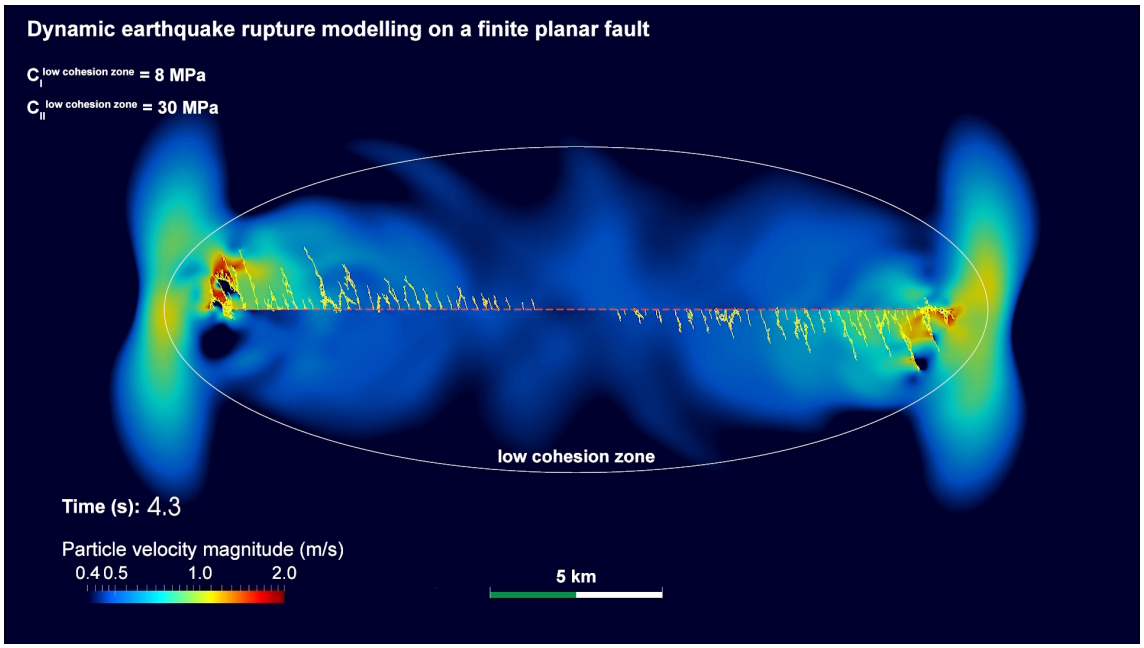

Figure 5.6: Snapshot at T = 4.3s. Rupture reaches the edges of the main fault, and induces the coseismic off-fault damage around the edges.

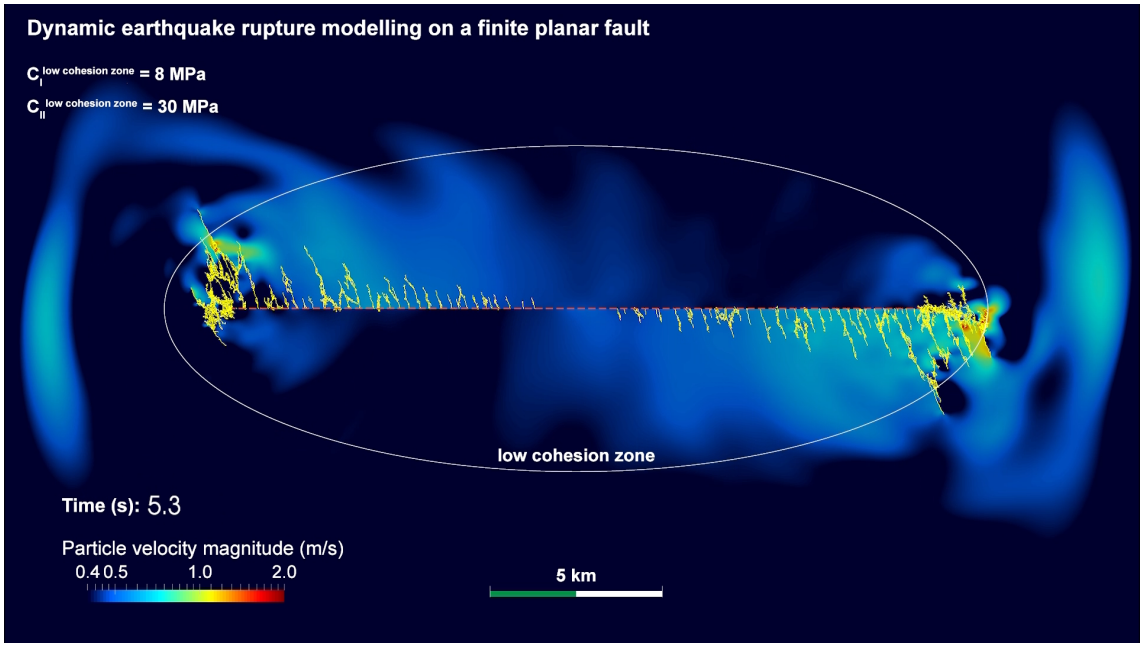

Figure 5.7: Snapshot at T = 5.3s. The coseismic off-fault damage continues to evolve around the edges and perturbs the radiation field. The damage pattern is not bilaterally symmetric because the mesh discretization is not symmetric, which causes the asymmetry of the feedback from the secondary fracture network.

5.2.2 Fault kink

Next, we demonstrate the dynamic earthquake rupture modeling with fault kink. Since the stress is locally concentrated due to the kinks and the roughness, the coseismic off-fault damage could be enhanced by the kinks. We thus conducted simulations with the fault kink, which bends on either compressional or extensional side of the fault.

Figure 5.8 shows the model setup for fault kink. The model parameters are set as same with the finite fault modeling (Tables 5.1 and 5.2). The angle of bend, α, is an important parameter for the rupture propagation on the fault kink. When $\alpha > 0$, the fault bends on the compressional side of the main fault. In this case, the ratio of shear traction to the normal traction, τ/σ_n, decreases as α increases. Thus the rupture is less likely to propagate along a fault bend with large α. On the other hand, when $\alpha < 0$, the fault bends on the extensional side of the main fault, where the τ/σ_n is larger on the fault bend than on the main fault.

In this section, we demonstrate the cases for $\alpha = +10^\circ$ and $\alpha = -10^\circ$ with and without coseismic off-fault damage to investigate the rupture dynamics and the associated damage pattern. Figures 5.9 to 5.12 show results for fault kink bent on the compressional side of the main fault. In this case, the rupture is less likely to propagate along the fault bend due to the decrease in τ/σ_n. Nevertheless, in the case without off-fault damage, the rupture propagates completely on the prescribed fault (Figures 5.10 to 5.12). This result is in accordance with *Templeton et al*. (2009). However, in the case with coseismic off-fault damage, the rupture is arrested at the kink, and significant damage is caused on the extensional side, resulting in the formation of a secondary fault branch (Figure 5.11). Eventually, two major damage paths are generated as shown in Figure 5.12. The orientation of these branches correspond to the conjugate failure planes of the σ_1. Therefore, we expect that secondary fault branches from kinks are naturally generated corresponding to the conjugate failure planes of the regional stress.

Figures 5.13 to 5.16 show for fault kink along the extensional side of the main fault. In this case, the rupture propagates on the prescribed fault for the both cases with and without off-fault damage, without branching from the kink. Supershear transition occurs on the fault bend, and the gap of the coseismic off-fault damage is observed as discussed in the section 3.1.3.

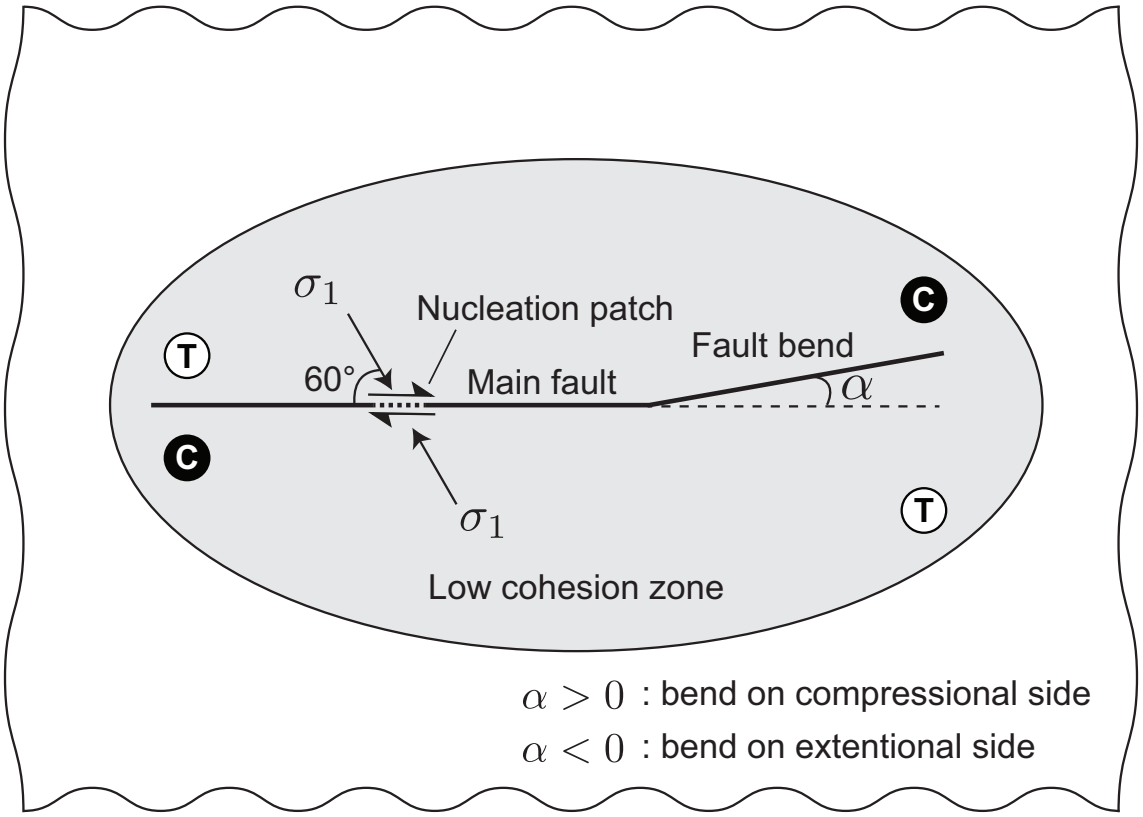

Figure 5.8: Model setup for a fault kink fault. The angle of the fault bend is α. The material constants and relevant model parameters are same with the finite fault modeling (Table 5.1 and 5.2). C and T indicate the compressive and extensional sides, respectively. The length of the main fault is 12.5km, whereas the fault bend is 7.5km.

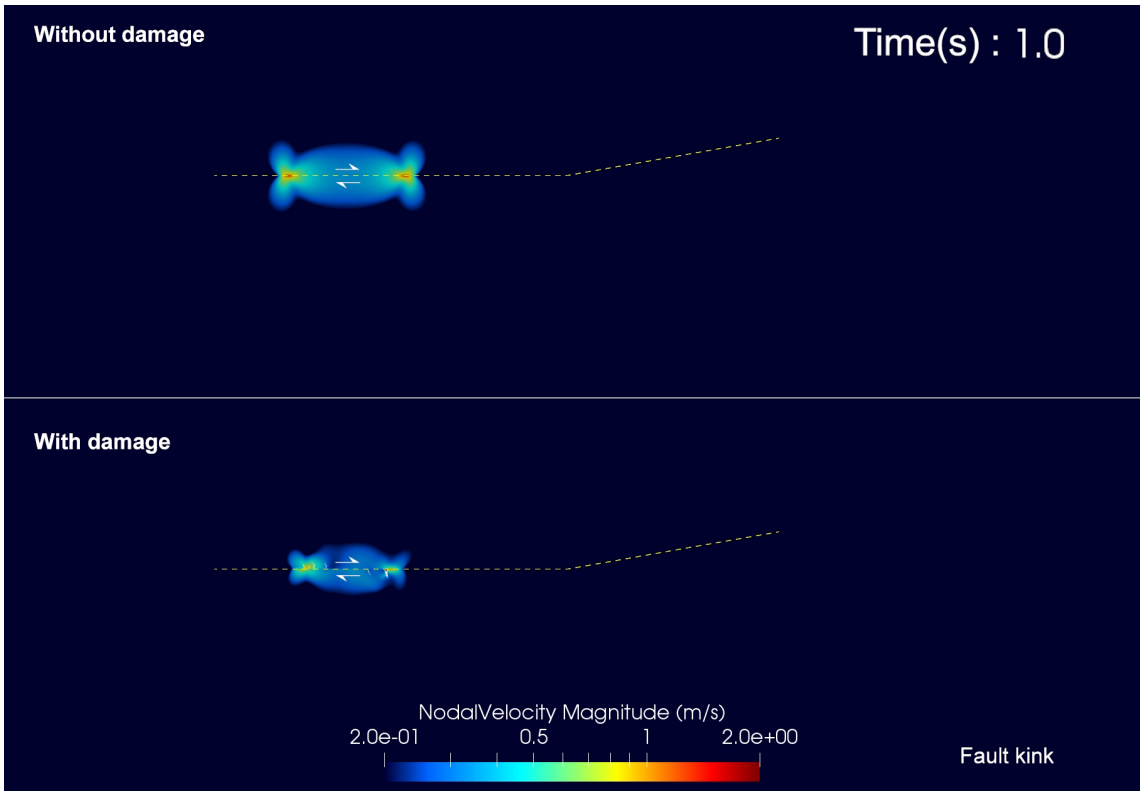

Figure 5.9: Snapshot for fault kink bent on the compressional side of the main fault. The dashed line indicates the prescribed main fault and the bent fault. Top window shows the result without coseismic off-fault damage, while the bottom window shows the result with off-fault damage. The arrows indicate the sense of slip on the main fault. White lines indicate the secondarily activated off-fault cracks

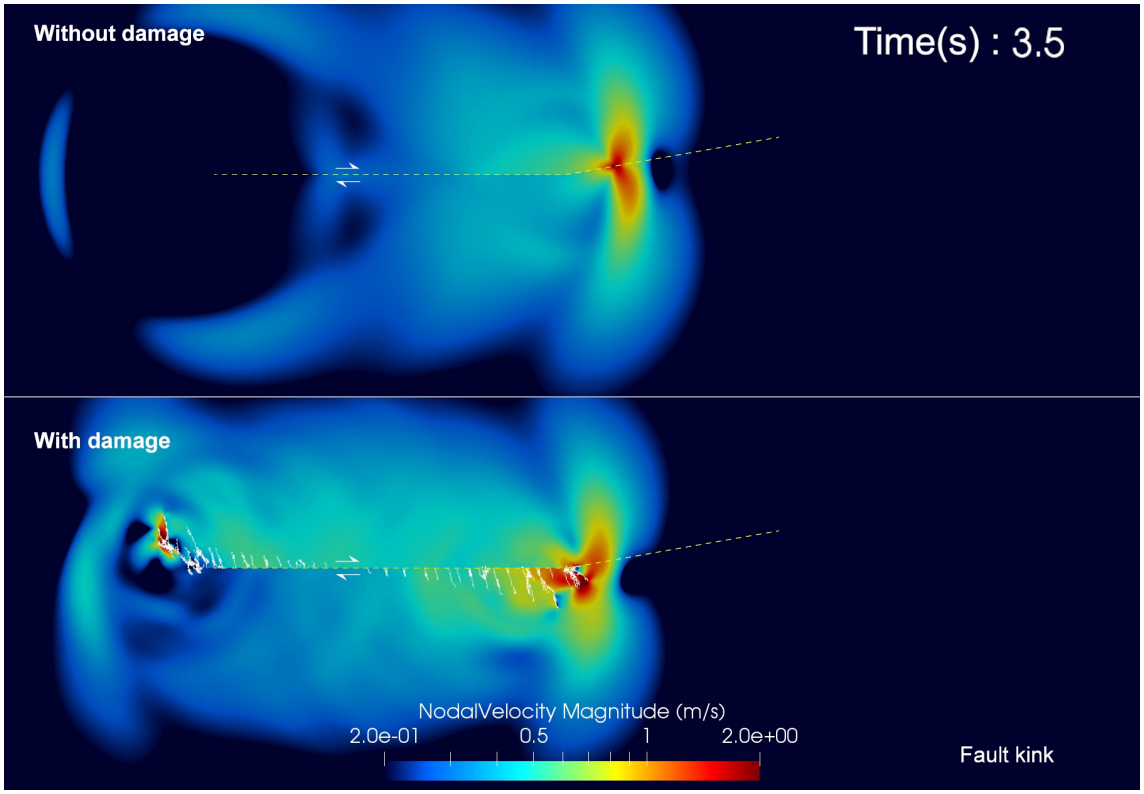

Figure 5.10: Snapshot at T = 3.5s.

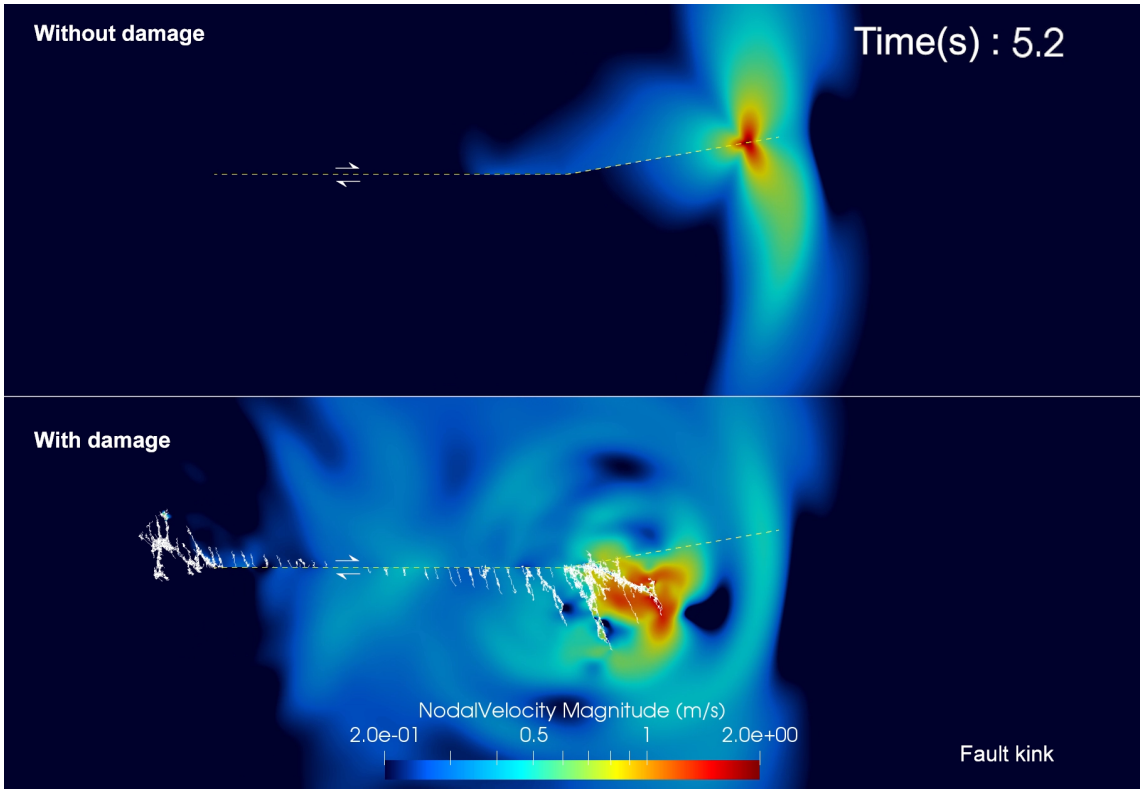

Figure 5.11: Snapshot at T = 5.2s. The rupture propagates on the prescribed bent fault for the case without off-fault damage, whereas the rupture does not propagate the prescribed fault with the coseismic off-fault damage. Instead of the arrest of the rupture at kink, a new fault branch is generated toward the extensional side.

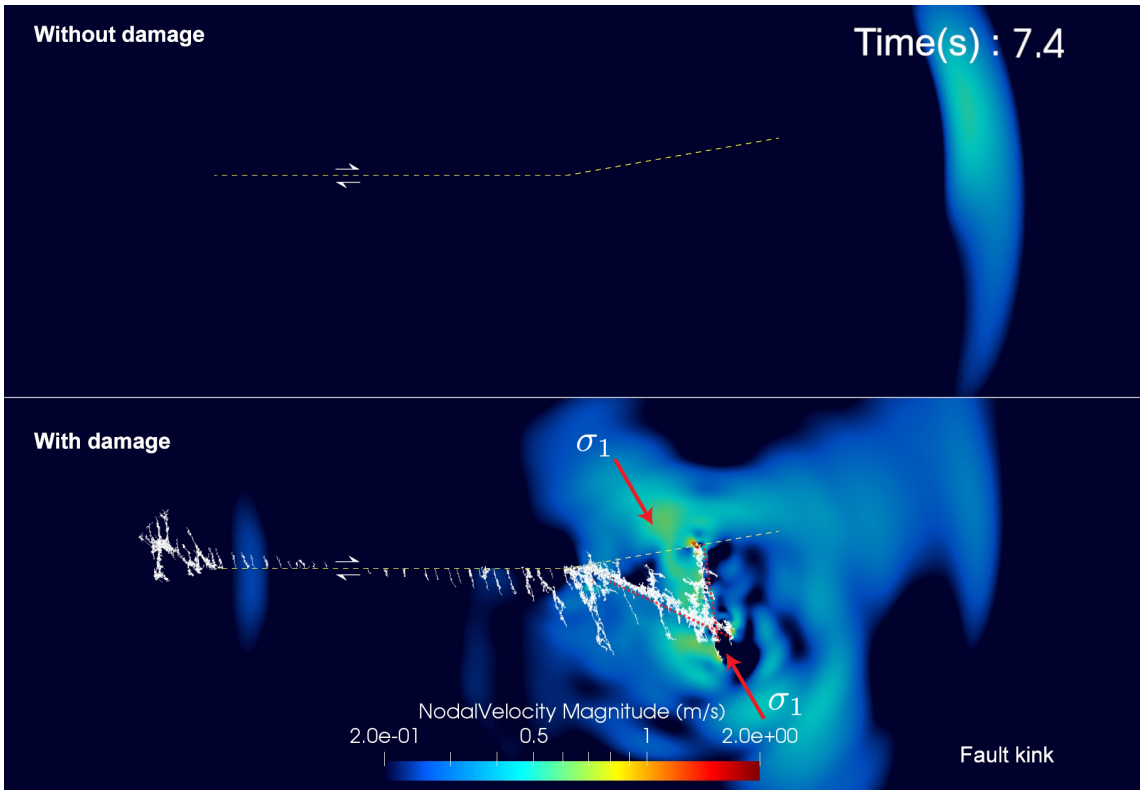

Figure 5.12: Snapshot at T = 7.4s. Eventually the rupture is arrested at the edge of the bent fault for the case without off-fault damage. In the case with off-fault damage, the branch grows as activating a lot of off-fault damage, and induces the secondary branch upward as guided by red dashed lines.

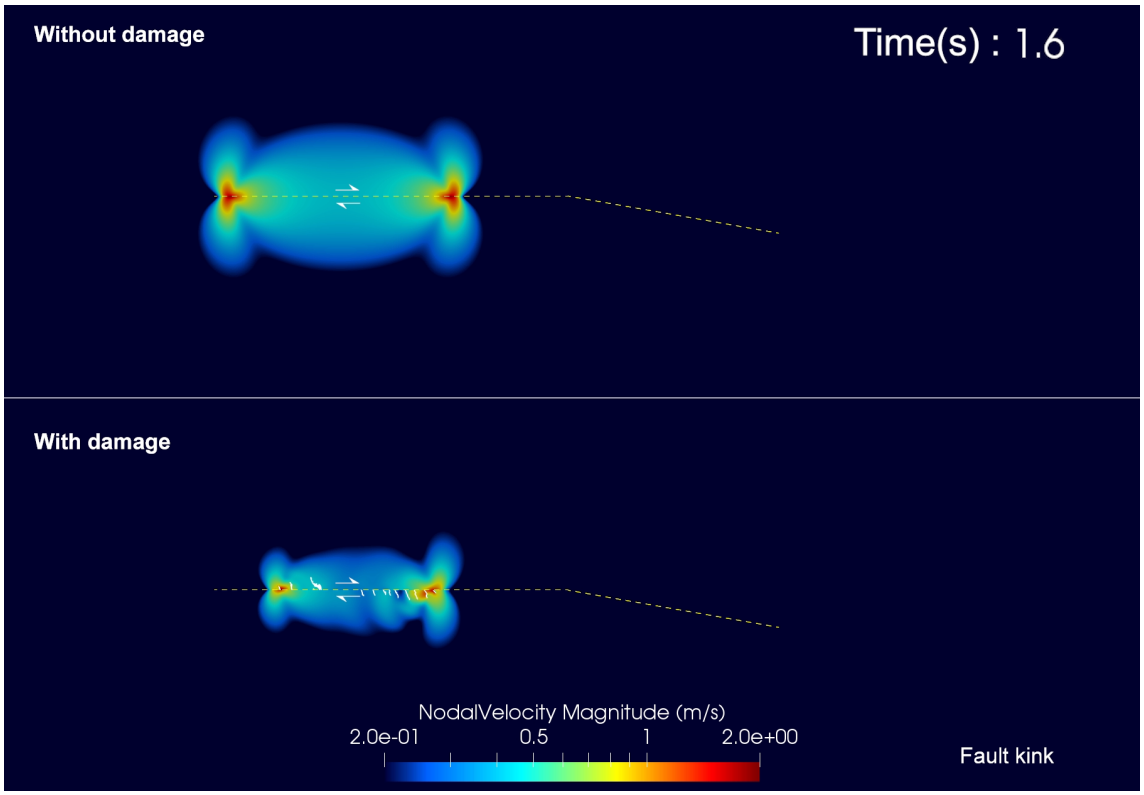

Figure 5.13: Snapshot for fault kink bent on the extensional side of the main fault. The dashed line indicates the prescribed main fault and bent fault. Top window show the result without coseismic off-fault damage, while the bottom window show the result with off-fault damage. The arrows indicate the sense of slip on the main fault. The white lines indicate the secondarily activated off-fault cracks

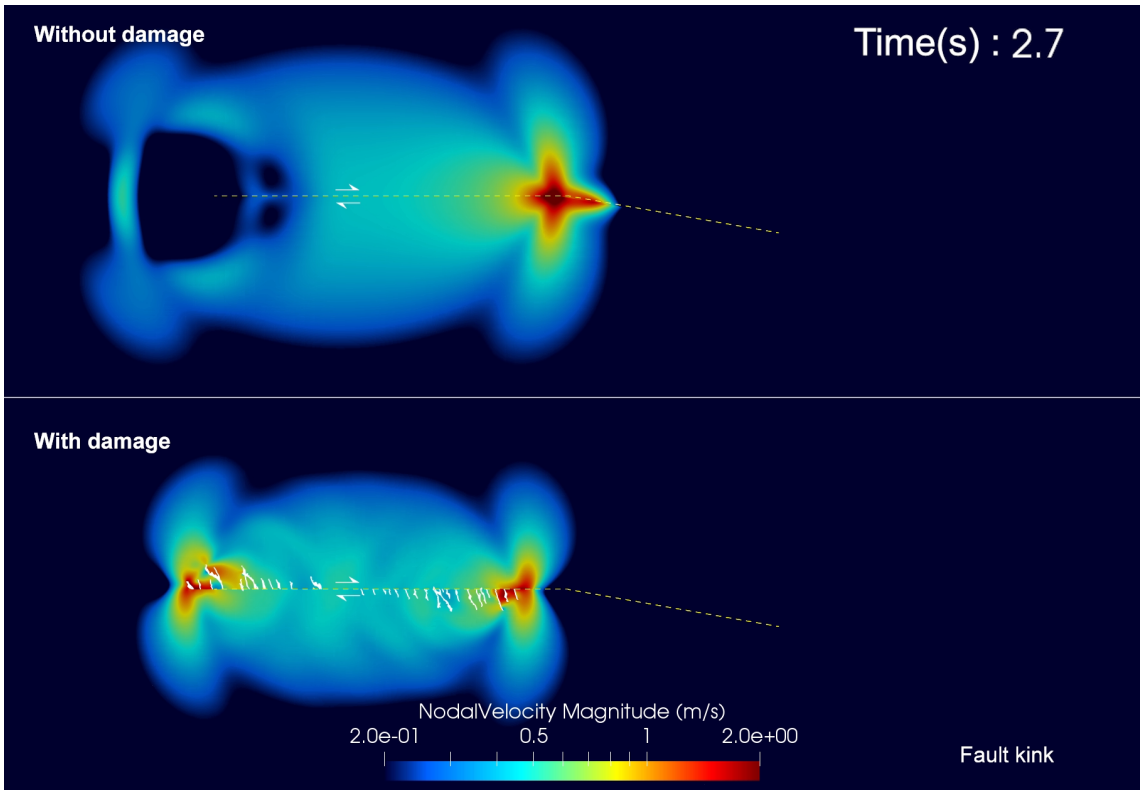

Figure 5.14: Snapshot at T = 2.7s. Supershear transition occurs for the case without off-fault damage due to the increase in τ/σ_n.

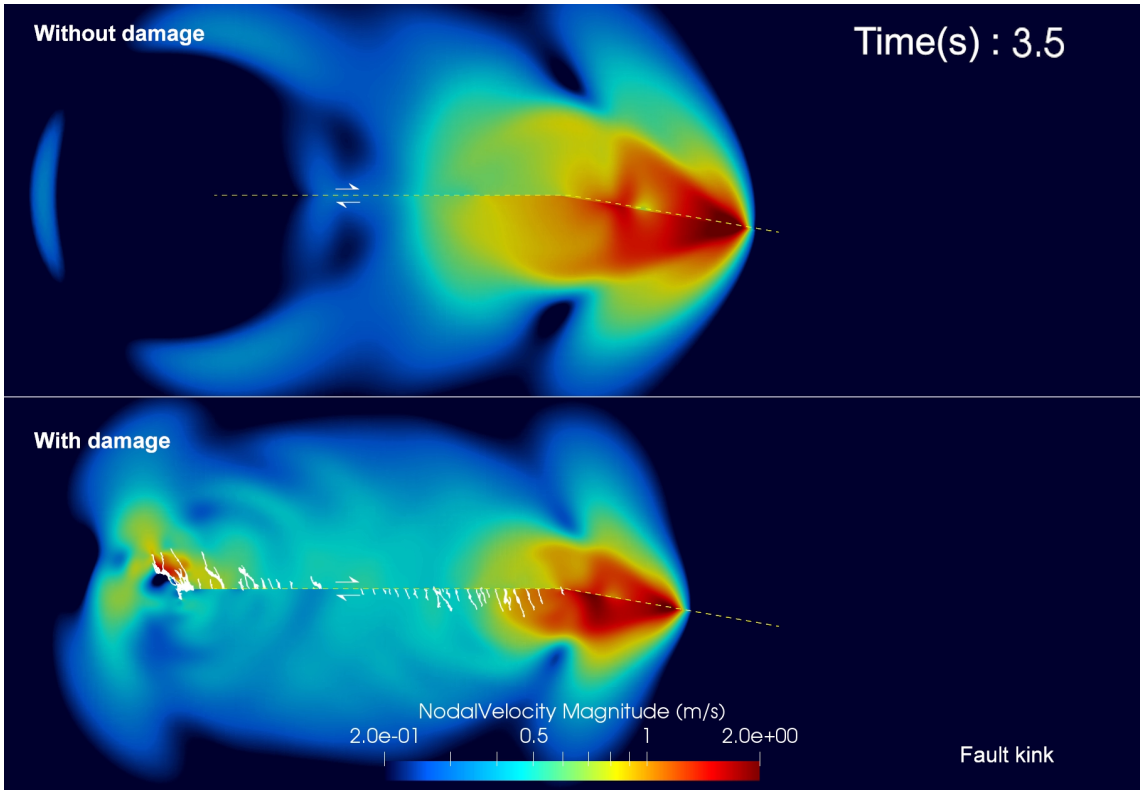

Figure 5.15: Snapshot at T = 3.5s. Supershear transitions occur for the both cases. In this case, there is little damage around the kink.

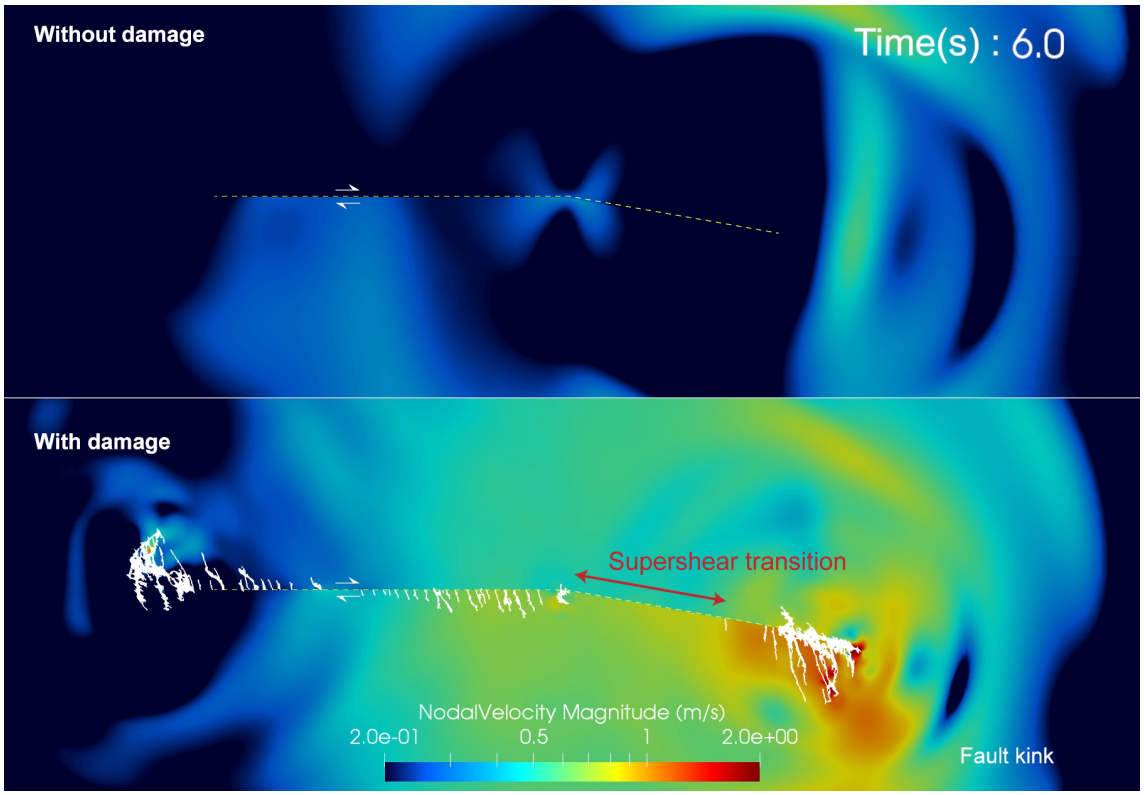

Figure 5.16: Snapshot at T = 6.0s. In both cases, the rupture propagates on the prescribed bent fault. There is a gap of coseismic off-fault damage for the case with off-fault damage, where the supershear transition occurs (see also 3.1.3).

5.2.3 Rough faults

Roughness of fault plays a crucial role in the rupture dynamics, radiations and coseismic off-fault damage (*Dunham et al.*, 2011b). In this section, we demonstrate a preliminary result with a self-similar fault to investigate the rupture processes on the rough fault with coseismic off-fault damage. The self-similar fault geometry is reproduced based on *Dunham et al.* (2011b). The self-similar fault profile has a spectral density, $P_m(k)$, as follows

$$P_m(k) = (2\pi)^3 \alpha^2 |k|^{-1}, \tag{5.1}$$

where k is the wave number and α is a parameter to determine the magnitude of fluctuation of the fault.

Figure 5.17 shows the self-similar fault geometry and the shear traction on the fault. α is to 3.2 X 10^{-3}. We chose the fault geometry so that the initial ratio of τ_0 to σ_n, f_0, is globally less than the static friction coefficient, f_s to avoid unexpected rupture nucleation during the loading phase.

Figures 5.18 to 5.21 show snapshots for the cases with and without off-fault damage. In the case without off-fault damage, the rupture is nucleated and propagates bilaterally. However, in the case with off-fault damage, the rupture is not successfully nucleated on the right side of the nucleation patch (Figure 5.19) due to prominent cracking at the edges of nucleation patch. One of the reasons for the nucleation failure is the artificial manipulation of nucleation process, where low f_s is assigned within the nucleation patch, which causes abrupt change of f_s at the edges of nucleation patch and consequent stress concentrations. Thus the nucleation process needs to be reconsidered to nucleate rupture on the rough fault.

In addition, the rupture on the left side is also arrested by the coseismic off-fault cracks (Figure 5.20). Thus the main fault is not fully ruptured for the case with coseismic off-fault damage. Therefore, we conclude that the roughness tends to arrest the earthquake ruptures due to the coseismic off-fault damage. Further parametric studies are needed to investigate the conditions of the arrest of ruptures and the associated off-fault damage patterns on the rough fault.

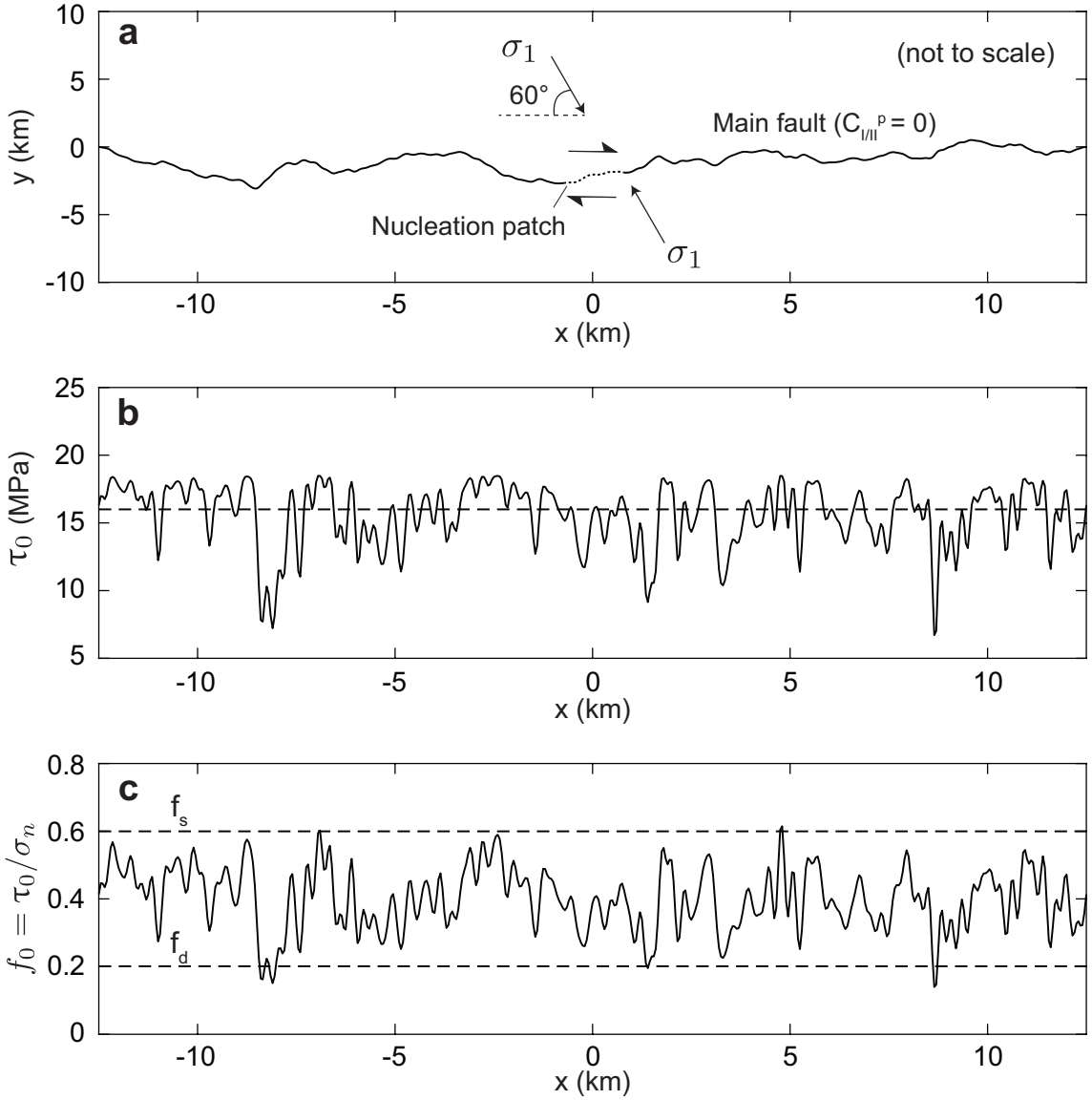

Figure 5.17: Self-similar fault geometry, initial shear traction and initial f_0 on the main fault. (a) Fault geometry. The nucleation patch is set in the middle of the fault, which is much larger than L_c to nucleate the rupture on the rough fault. Model parameters are same with the finite fault modeling (Table 5.1 and 5.2). The fault length is finite, set as 25km, and the entire fault is encompassed by the low cohesion zone. (b) Initial shear traction on the main fault. The dashed line indicates the reference shear traction with a planar fault (16MPa). (c) Initial ratio of τ_0 to σ_n. The dashed lines indicate the static and dynamic friction coefficients on the main fault.

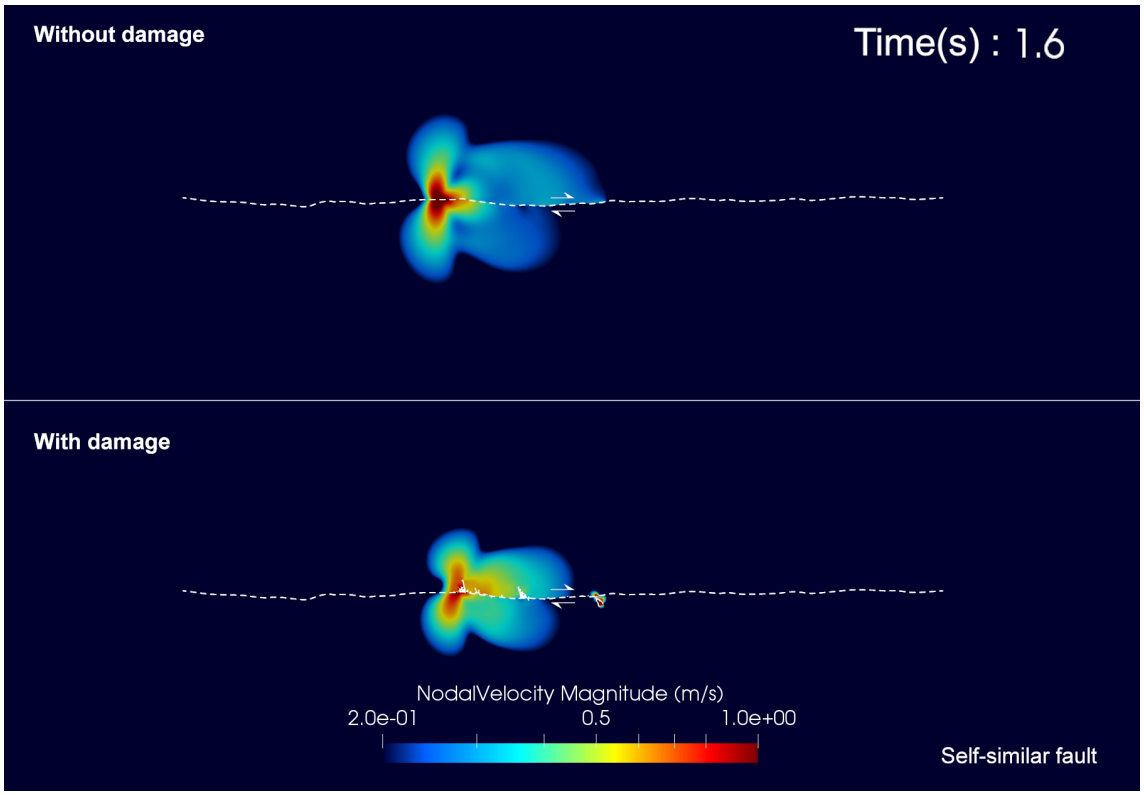

Figure 5.18: Initial snapshot for self-similar fault. The dashed line indicates the prescribed main fault. Top window show the result without coseismic off-fault damage, while the bottom window show the result with off-fault damage. The arrows indicate the sense of slip on the main fault. The white lines indicate the secondarily activated off-fault cracks

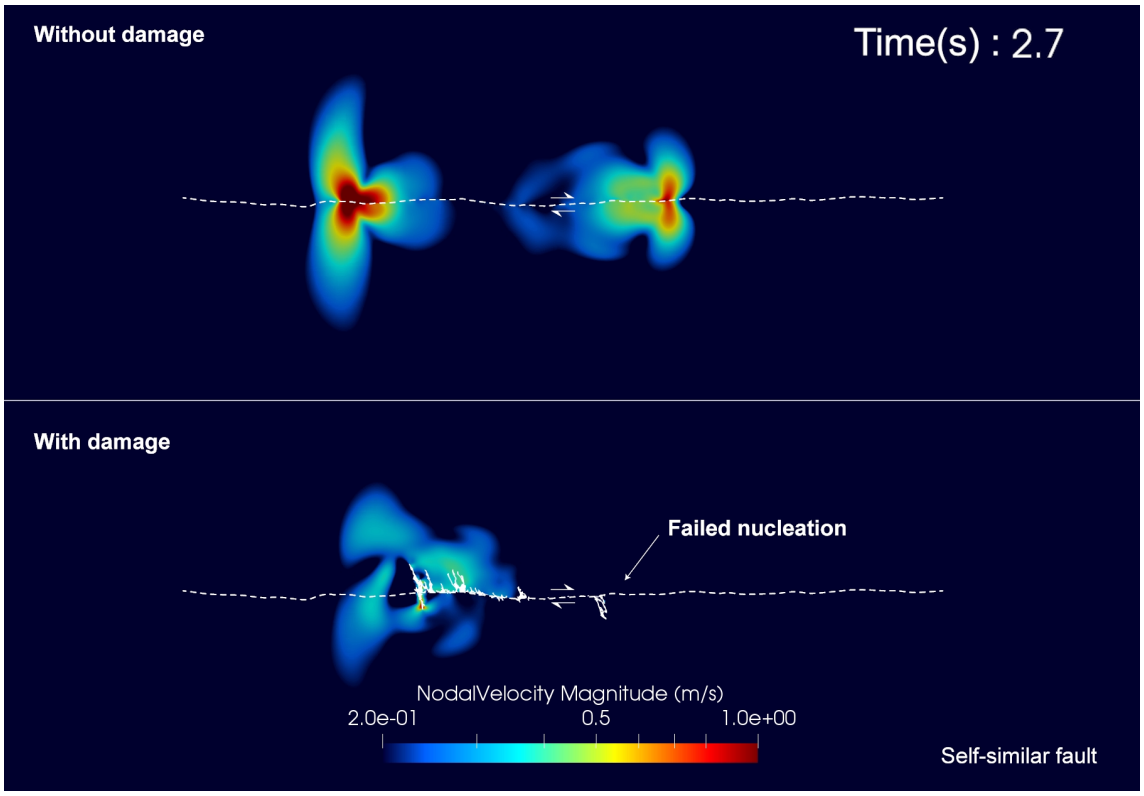

Figure 5.19: Snapshot at T = 2.7s. Nucleation is failed on the right side of nucleation patch for the case with off-fault damage.

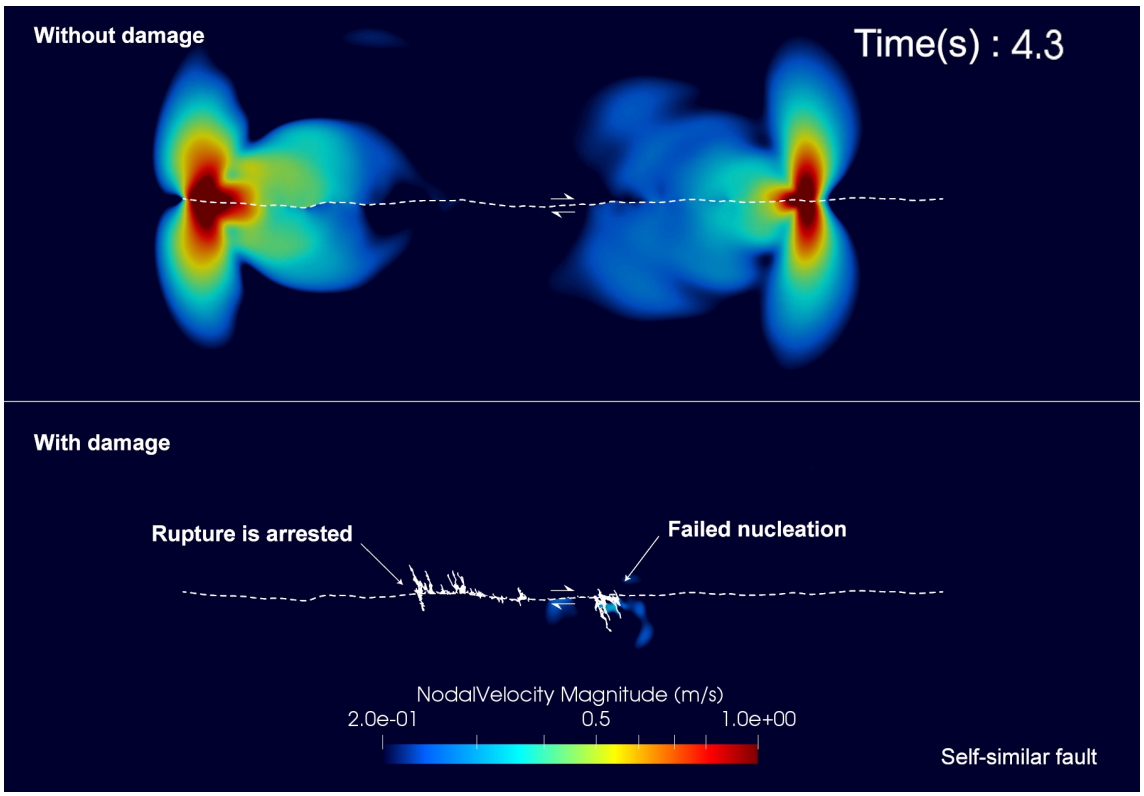

Figure 5.20: Snapshot at T = 4.3s. The rupture on the left side for the case with off-fault damage is also arrested due to the off-fault damage.

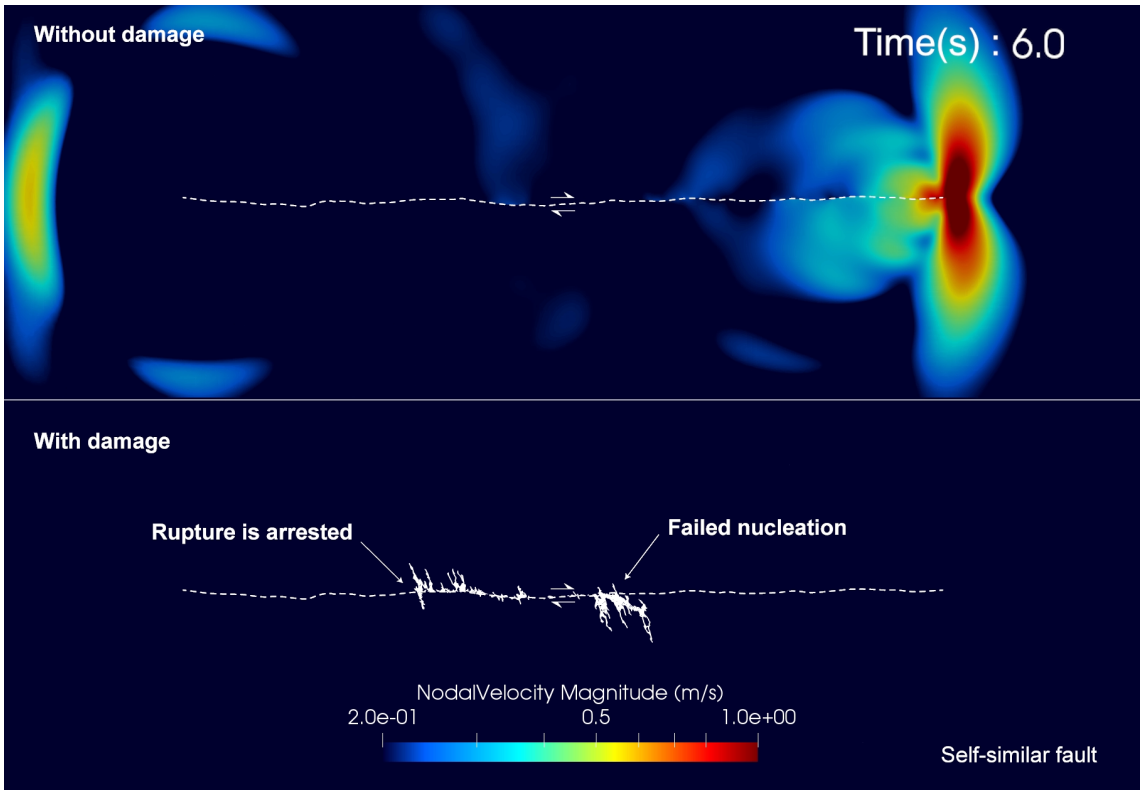

Figure 5.21: Snapshot at T = 6.0s. There is a major branch from the right edge of the nucleation patch. However, no significant radiation is observed for the case with off-fault damage.

5.2.4 Stepover faults

The stepover faults are an another important component of the natural fault network. What is of interest here is whether the rupture jumps from the main fault to the stepover fault near the main fault. Systematic numerical experiments of stepover faults are pioneered by *Harris et al*. (1991), demonstrated the geometrical conditions to nucleate the secondary rupture on the stepover fault. Parallel strike-slip faults are widely used as an example of simple stepover faults (Figure 5.22). The relative position of stepover fault is controlled by the two parameters, stepover width and overlap. The capability of rupture jumps depends on whether the stepover fault is located on the compressional side (compressional step) or the extensional side (dilational step) of the main fault. *Harris et al*. (1991) shows that the dilational step is more likely to induce the second rupture on the stepover fault. Thus in this section, we demonstrate the dilation step, and compare the cases with and without off-fault damage to investigate the effect of coseismic off-fault damage on the rupture dynamics for the stepover faults.

Figures 5.23 to 5.27 show the snapshots of the result for dilational step with and without coseismic off-fault damage. The rupture is nucleated in the middle of the main fault and propagates bilaterally. The stepover is set as 600m ($\sim 0.5L_c$), and the overlap is 2.5km ($\sim 2.1L_c$). When the rupture reaches the edges of the main fault, the rupture is arrested for the case without coseismic off-fault damage, and does not induce the second rupture on the stepover fault (Figure 5.24). However, as observed in the finite fault results (Figure 5.7), major off-fault crack path evolves from the right edge of the main fault, which reaches the stepover fault (Figure 5.24). Then as the coseismic off-fault damage evolves around the edge of the main fault, the secondary rupture is nucleated close the the major damage zone on the stepover fault (Figure 5.25). Since the secondary rupture is not nucleated for the case without coseismic off-fault damage, implying this combination of the fault geometry and the initial stress condition is not capable of rupture jumping, the modification of the elastic properties around the stepover fault due to the coseismic off-fault damage plays an important role in the nucleation of secondary rupture. The rupture then propagates on the stepover fault, and eventually transitions to supershear (Figures 5.26 and 5.27). These preliminary results for the stepover faults demonstrate the need of parametric studies to rectify the conditions of rupture jumps with coseismic off-fault damage.

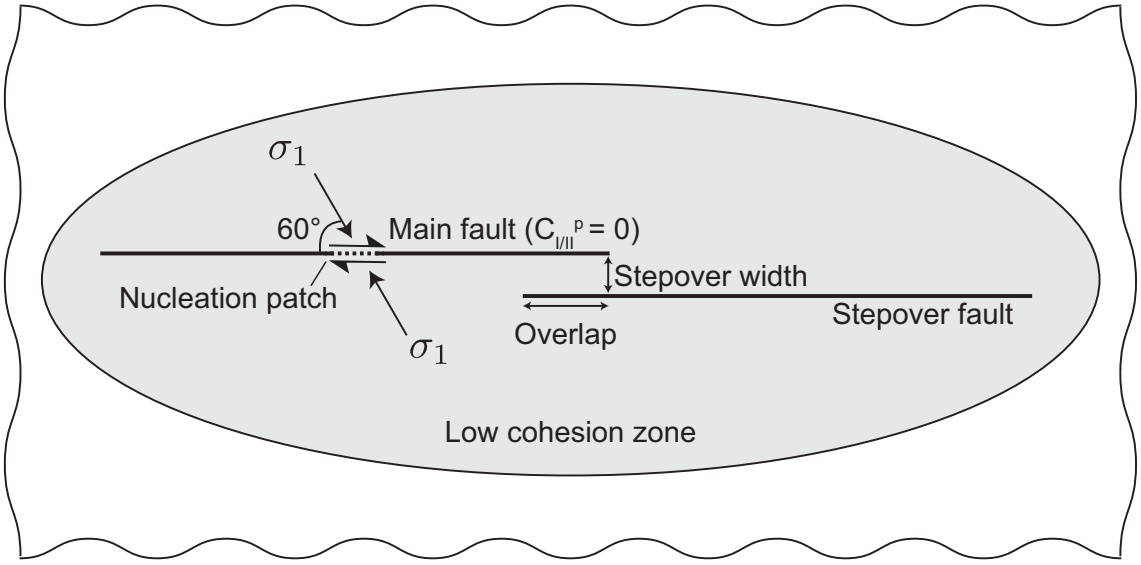

Figure 5.22: Model setup for modeling stepover faults. The material constants and relevant model parameters are same with the finite fault modeling (Table 5.1 and 5.2). The fault length is 15km, the stepover width is 600m ($\sim 0.5L_c$) and the overlap is 2.5km ($\sim 2.1L_c$).

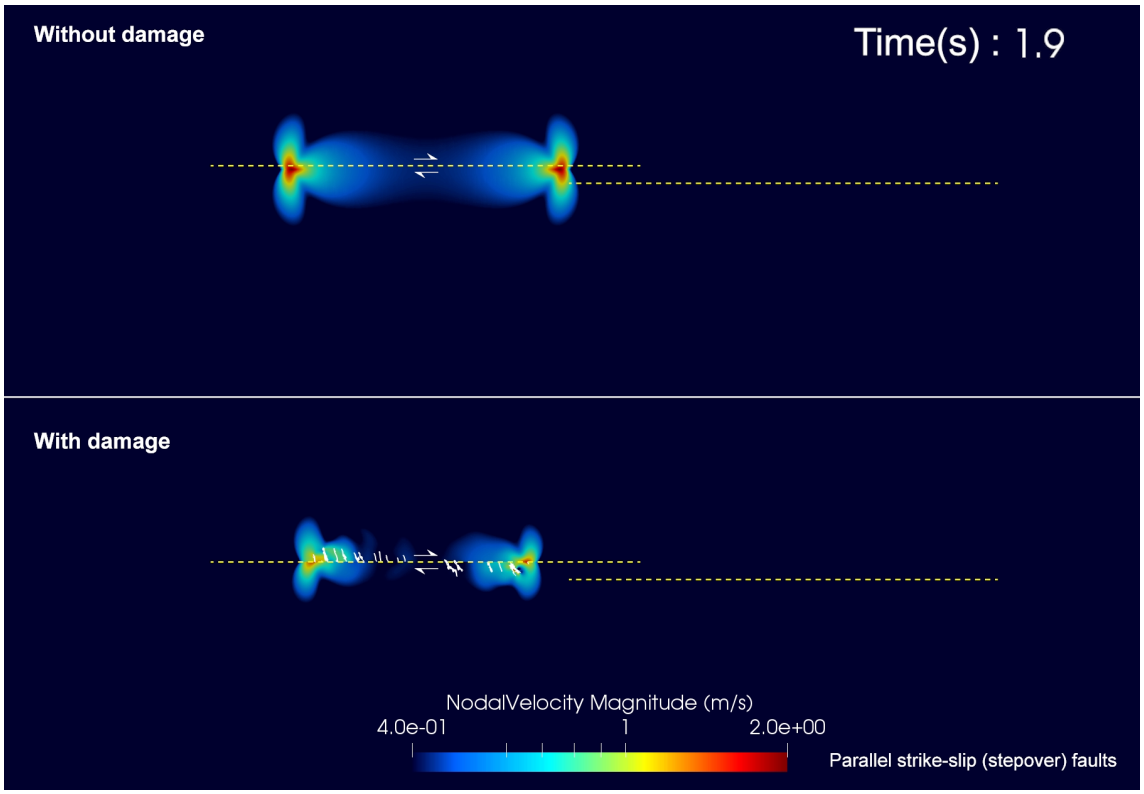

Figure 5.23: Snapshot for stepover faults. The dashed line indicates the prescribed faults. Since the main fault is right-lateral, the stepover fault is a dilational step. Top window shows the result without coseismic off-fault damage, while the bottom window shows the result with off-fault damage. The arrows indicate the sense of slip on the main fault. White lines indicate the secondarily activated off-fault cracks

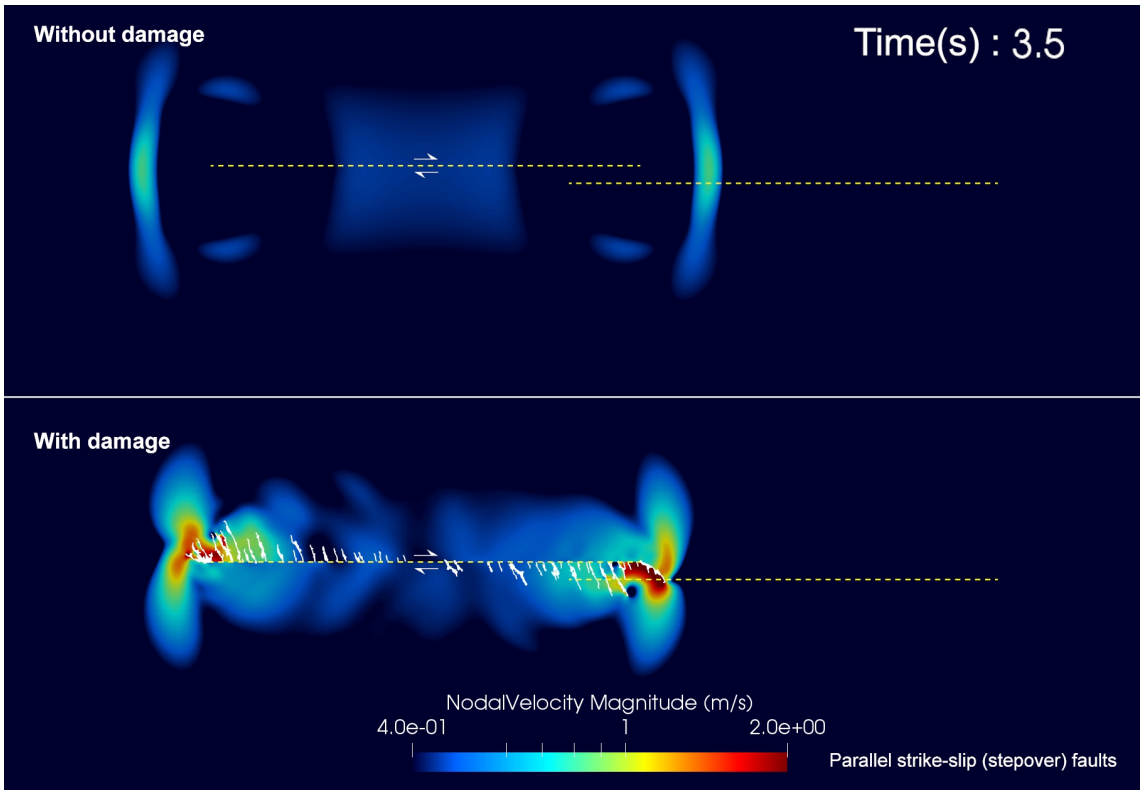

Figure 5.24: Snapshot at T = 3.5s. The rupture reaches the edges of the main fault, and is arrested for the case without off-fault damage, whereas the coseismic off-fault damage grows toward the stepover fault.

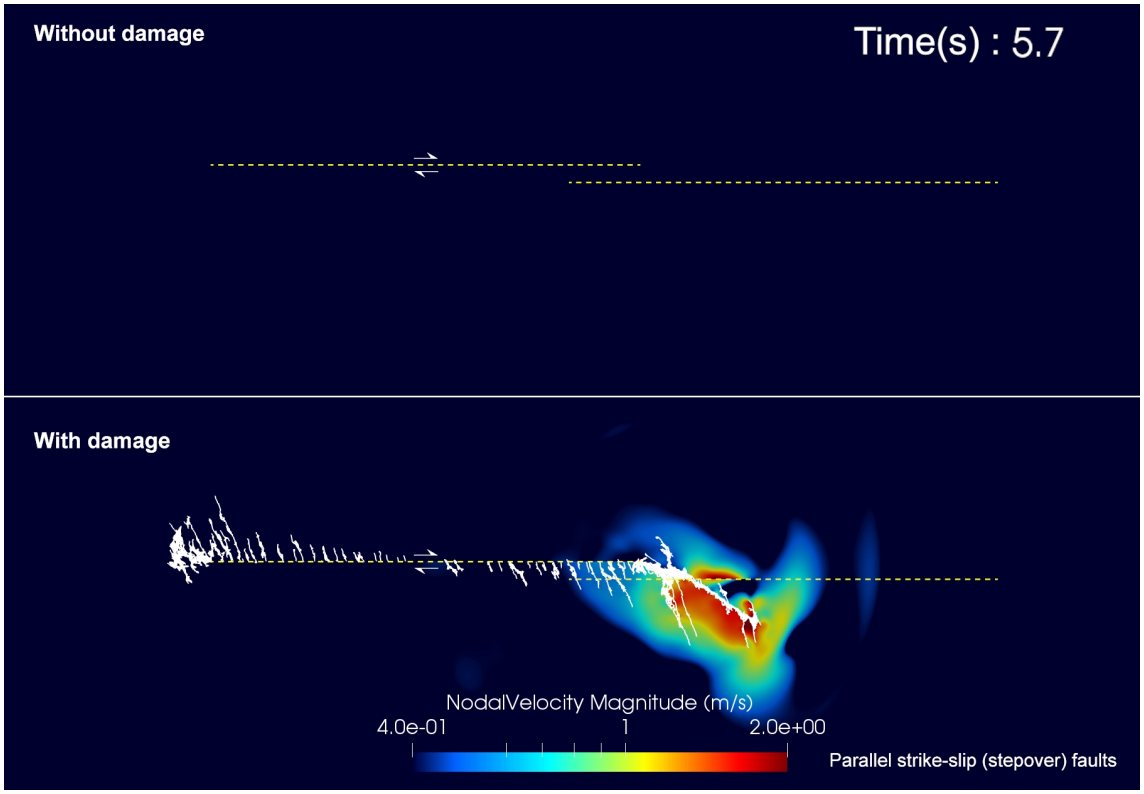

Figure 5.25: Snapshot at T = 5.7s. The coseismic off-fault damage modifies the elastic properties around the stepover fault, and the secondary rupture is eventually nucleated by the stress perturbation due to the rupture on the main fault and the change of elastic properties.

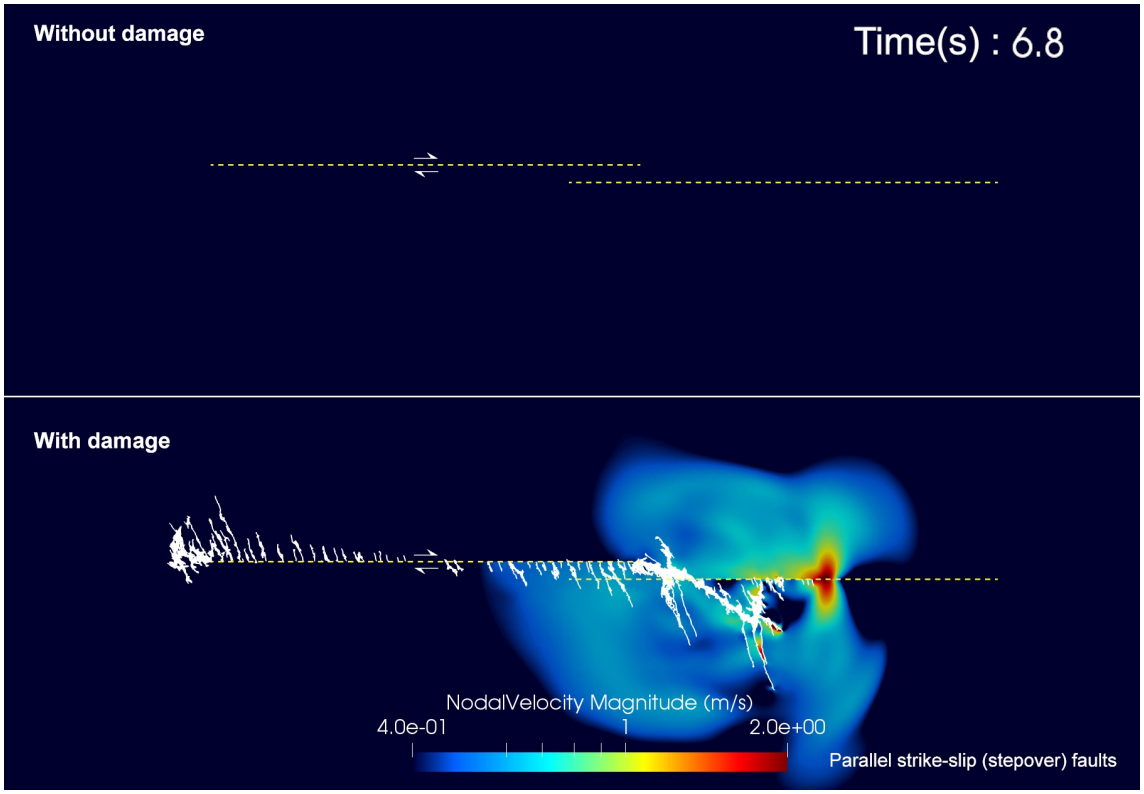

Figure 5.26: Snapshot at T = 6.8s. The secondary rupture is successfully nucleated.

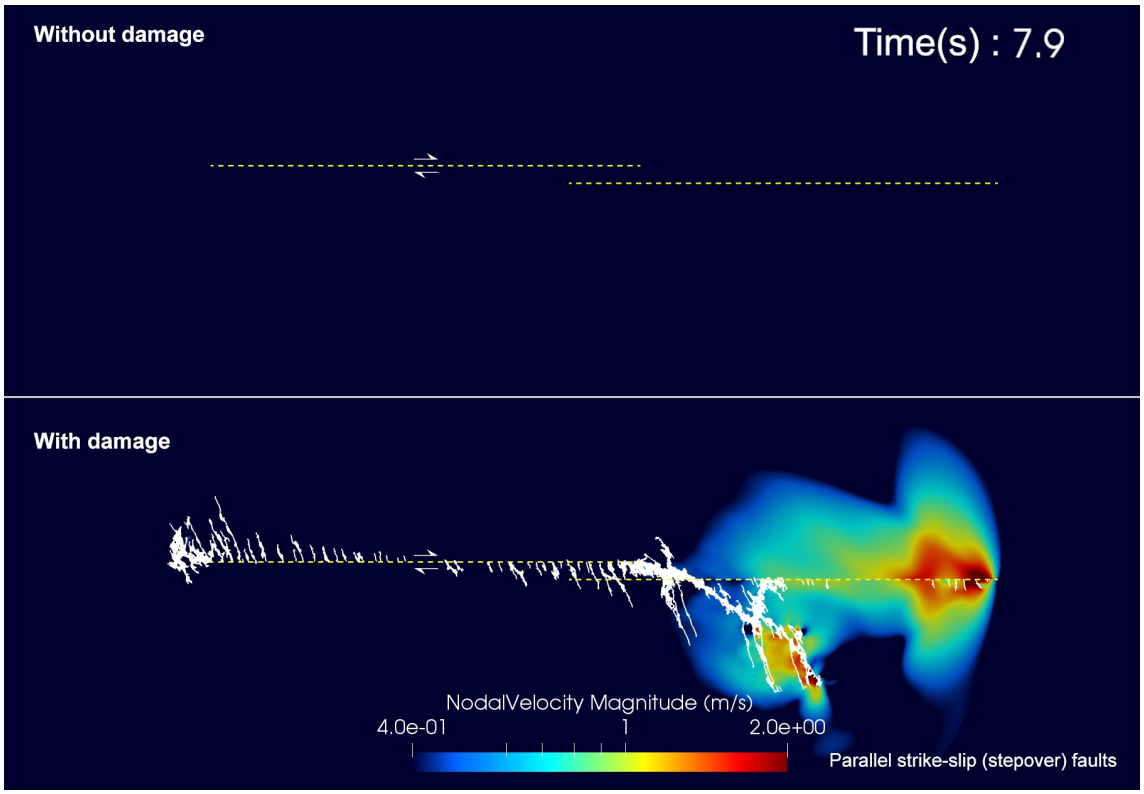

Figure 5.27: Snapshot at T = 7.9s. The rupture finally transitions to supershear on the stepover fault, which implies the supershear transition length decreases due to the feedback from the coseismic off-fault damage.

5.3 Modeling thrust earthquakes with coseismic off-fault damage

Large earthquakes are mostly observed on thrust faults, which cause a serious disaster due to ground shaking and destructive tsunamis. Thus the study of the earthquake ruptures on the thrust faults has a great impact on disaster prevention. Figure 5.28 shows a cross section of Nankai subduction zone, off southwest Japan. The multichannel seismic (MCS) reflection profiles elucidate the structure of the plate boundary and splay faults, which reaches the ocean bottom. Although the shallow part of the thrust faults is considered to be frictionally stable , and thus be aseismic (e.g. *Moore and Saffer*, 2001), coseismic slip sometimes occurs even near the trench as demonstrated by Tohoku. *Gabuchian et al*. (2017) demonstrated the release of the counterclockwise torque caused by the dynamic rupture on the thrust fault can break the free surface, which results in a large deformation of the hanging-wall wedge. *Ma and Hirakawa* (2013) conducted the dynamic rupture modeling on the thrust fault with inelastic constitutive formulations, which shows a significant plastic deformation on the hanging-wall wedge. They also showed that the plastic deformation smooths out the source time function and decreases the radiated energy.

The previous studies highlight the importance of the deformation on the hanging-wall wedge for the thrust earthquakes. However, the mechanism of secondary fracturing on the thrust fault remains to be fully understood because of limitations of computation and model formulation; the release of the counterclockwise torque will dynamically activate the secondary tensile cracks on the hanging-wall wedge, and the feedback of the coseismic off-fault damage will modify the rupture dynamics, damage pattern and radiations on the thrust faults. Therefore, we conducted dynamic earthquake rupture modeling with thrust fault model to investigate the mechanism of activations of coseismic off-fault damage on the wedge and its effect on the rupture process and radiation.

Figure 5.29 illustrates the model setup of the thrust earthquake modeling. Firstly, we conduct the rupture modelings with a simple planar thrust fault, where the rupture is nucleated in the middle of the fault, and propagates bilaterally. We examined 30° and 60° cases for the angles of the thrust fault to the free surface. The size of computational domain is set large enough to avoid the feedback from the rupture propagating downward. The prescribed thrust fault penetrates the free surface.The bottom and right edges of the computational domain are fixed, while the horizontal vertical stresses, σ_1 and σ_2, are applied on the left and top edges. It is noteworthy that the σ_2 cannot be zero for the case of 30 °; otherwise, the rupture on the thrust fault is unexpectedly nucleated from the free surface before the nucleation phase due to the local decrease in normal stress around the free surface. To avoid the unexpected nucleation of the rupture, we need to take into account the topology of the free surface, or initial cohesions on the thrust fault.

Figure 5.30 shows the snapshots of thrust earthquake modeling with the dip angle of 30°. In this case, the coseismic off-fault damage is not activated due to the low angle of the maximum principal stress to the thrust fault (*Poliakov et al*., 2002; *Ngo et al*., 2012). The feedback from the hanging-wall wedge is observed, whereas there is no interesting damage on the wedge because of the coarse mesh size and model parametrization. Figure 5.31

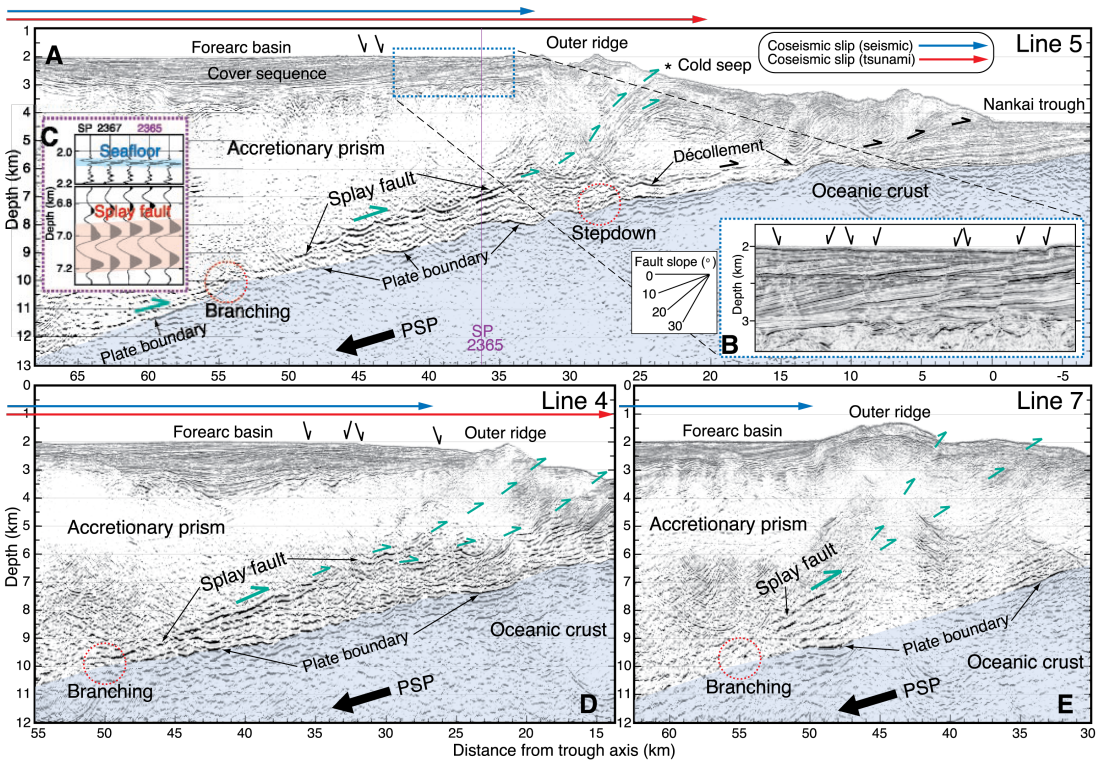

Figure 5.28: Cross section of Nankai subduction zone, off southwest Japan. The subducting oceanic crust is shaded light blue. The seaward distribution of the 1944 Tonankai coseismic slips estimated from tsunami (red lines) and seismic (blue lines) inversions is projected in the profiles. Locations of both the splay faults initial branching and the décollement stepdown to the top of the oceanic basement are marked in orange dotted circles. Green and black arrows indicate motions of the splay fault slip, and the décollement or normal fault, respectively. Vertical exaggeration is 2X. (A) The Philippine Sea Plate (PSP) subducting beneath the upper plate produces a huge accretionary prism. The location of the cold seep is marked by an asterisk. Note active normal faults [(B), inset] cutting the well-stratified, landward-tilting cover sequence and reverse polarity reflection [(C), inset] of the splay fault at 7 km depth around the shot point (SP) 2365 indicated by purple line. (D, E) Cross sections on the different survey lines close to (A). Reprinted from *Park et al*. (2002).

show the snapshots with the dip angle of 60°, where the usual coseismic off-fault damage is observed, whereas no damage on the wedge. We cannot conclude anything with these results because of coarse mesh discretization and non-realistic parametrization, such as uniform initial stress state regardless of lithostatic pressure. However, these results clearly demonstrate the potential of FDEM to conduct the further modeling of thrust earthquakes with the coseismic off-fault damage.

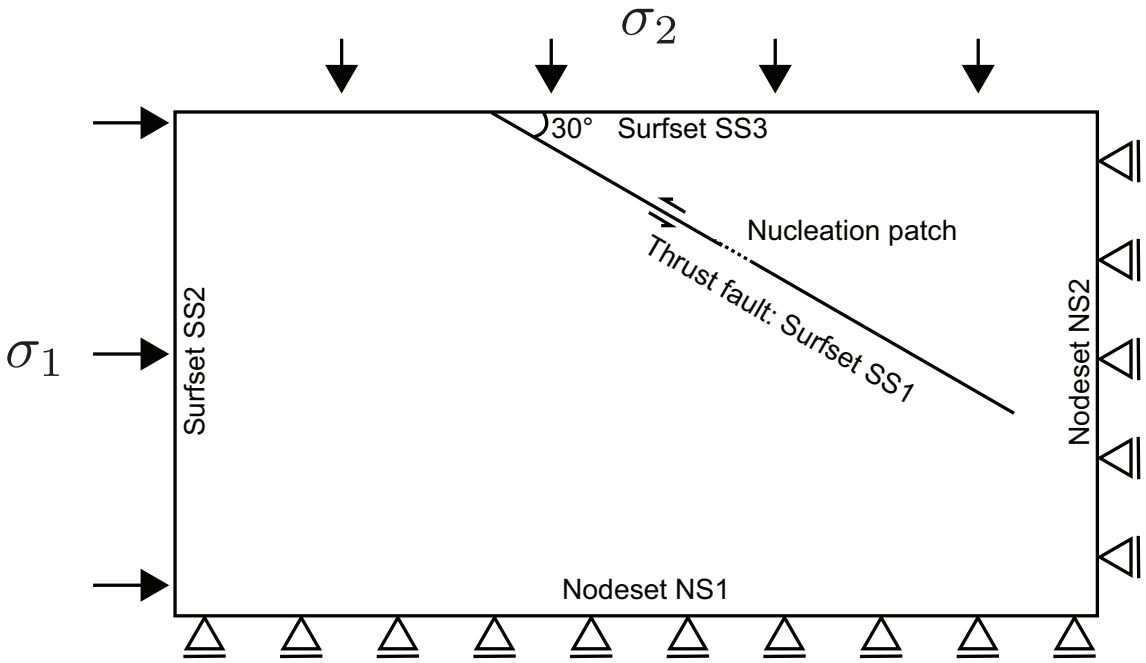

Figure 5.29: Model description of thrust earthquake rupture modeling. σ_1 and σ_2 are assumed as external loading. NS1-2 and SS1-3 indicate the node and edge groups, respectively, for boundary conditions.

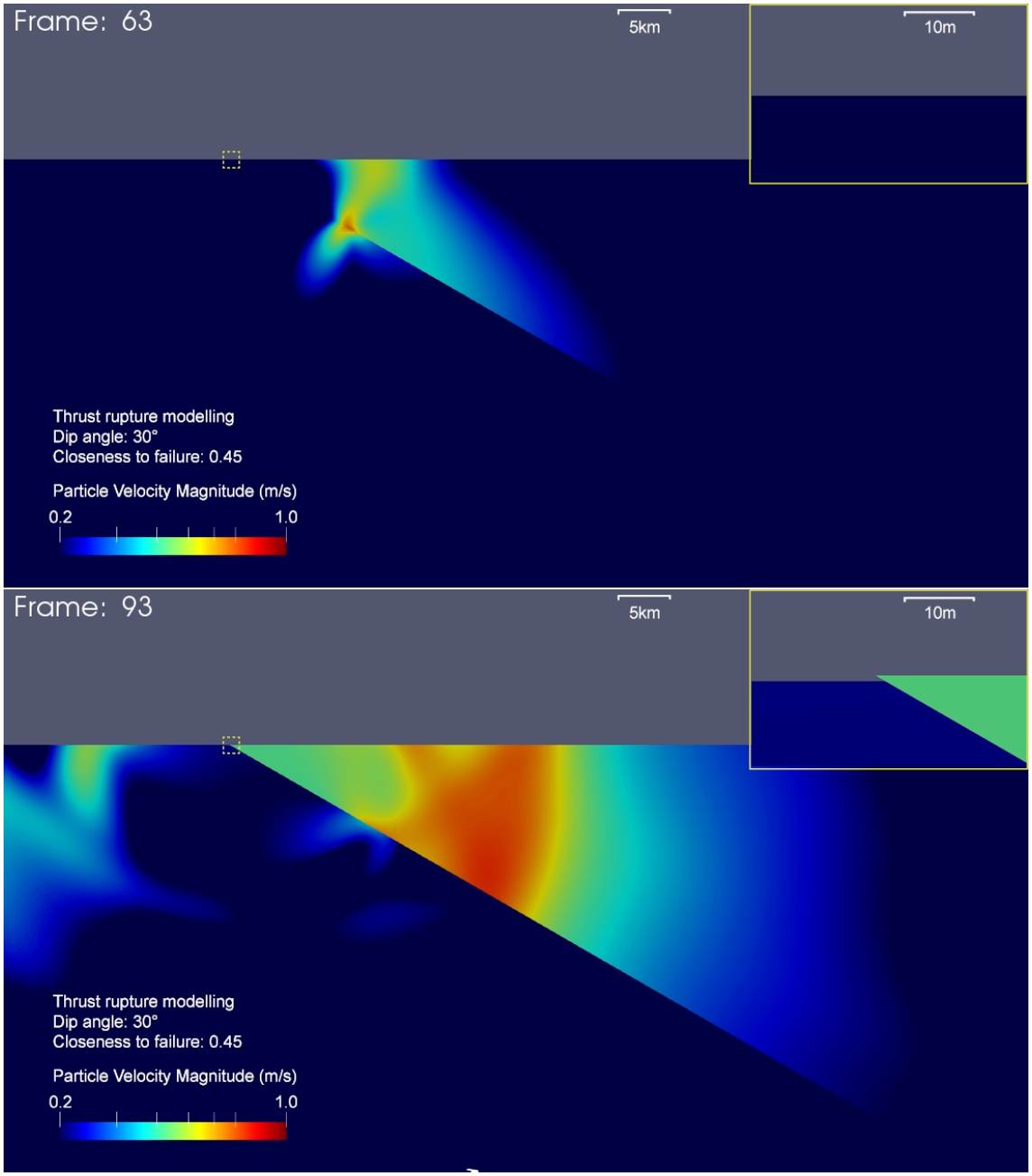

Figure 5.30: Snapshots of thrust earthquake modeling with the dip angle of 30°. Color contour shows the particle velocity magnitude. The coseismic off-fault damage is not observed in this case due to the low angle of the maximum principal stress to the thrust fault. The inset shows the focused window around the edge of thrust fault.

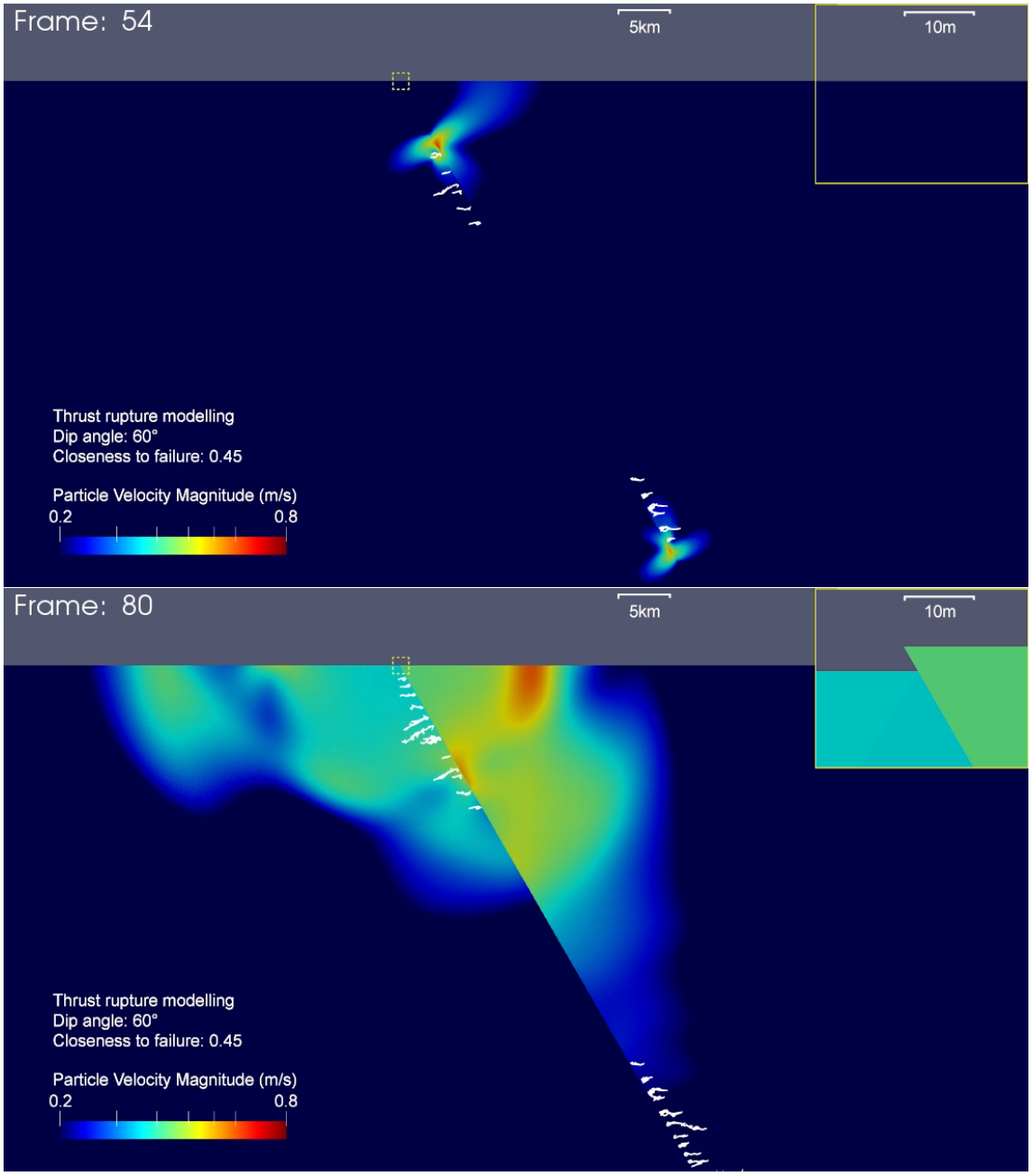

Figure 5.31: Snapshots of thrust earthquake modeling with the dip angle of 60°. White lines indicate the secondarily off-fault cracks.

5.4 Discussion and summary

In this chapter, we demonstrated the perspective works on the interaction between coseismic damage and first-order geometrical complexities (including free surface). These preliminary results already reveal some effects of the coseismic off-fault damage on the rupture process and damage patterns, and can be applied for the analysis of natural earthquakes. For example, the results of fault kinks suggest that instead of propagating along pre-existing fault, the secondary major cracks are activated from the kink of the fault bended on the compressional side of the main fault, which explains the large damage zone in the northwestern part of the Papatea fault (Figure 4.29). The arrest of the rupture on the northern part of Papatea fault in the second scenario (Figure 4.23) is also observed in the results of rough faults, where the rupture is trapped by the secondary off-fault cracks. Hence, the analysis of the first-order geometrical complexities helps the explanation of rupture processes on the natural fault network as it can be decomposed into such simple geometrical complexities.

The preliminary results of thrust earthquakes show the capability of FDEM for the modeling with free surfaces. We need to firstly reconsider 1) nonuniform initial stress state corresponding to lithostatic pressure 2) topology of free surface 3) low cohesion zone on the wedge in order to evaluate the coseismic off-fault damage associated with thrust earthquakes.

Finally, we list the other perspectives as follows:

- **Parametric studies on the initial stress state for the fundamental analysis**

  Since the fundamental analysis of coseismic off-fault damage, as discussed in Chapter 3, has been done with a limited conditions, such as a fixed φ and d_{MC}, and initially intact rock, we need to investigate the effect of these parameters on the damage pattern. *Poliakov et al*. (2002) and *Rice et al*. (2005) theoretically demonstrate that the small φ causes less damage than the large φ, whereas the secondary fracture network can be activated on the compressional side of the fault. In natural fault networks, the off-fault damage is often observed in the both sides of the fault. We now assume that the pre-damage of the off-fault medium, initial cohesion on the main fault, which is assumed to be zero in this study, and the φ play a role in the symmetric pattern of the off-fault damage across the fault.

- **Evolution of the coseismic off-fault damage during earthquake cycles**

  Due to limitations of model formulations, the earthquake cycles on the same fault with coseismic off-fault damage remain to be done. However, the process of evolution and saturation of the off-fault damage caused by the earthquake cycles is of great interest, which may help to understand the morphosis of natural fault networks. We need to patch the healing process of the off-fault cracking during interseismic period, and reload the system to nucleate the second rupture on the same fault.

- **Consistency and discrepancy between kinematic models and rupture dynamics**

  The characterization of earthquake rupture dynamics from kinematic source representation has been conducted to estimate the hypocenter, focal mechanism, seismic

radiation and eventually ground motion which is used for the earthquake disaster prevention and early warning system. The seismic moment rate function, also called Source Time Function (STF), describes the temporal evolution of the earthquake rupture. Furthermore, the spectrogram of the STF gives a reasonable approximation of the evolution of radiated energy with time, or the radiated energy rate. The radiated energy rate, estimated using the far-field P and S waves, is proportional to the squared seismic moment acceleration (e.g *Ide et al.*, 2008; *Yabe and Ide*, 2014; *Denolle et al.*, 2015). Thus it also contains the information of rupture dynamics as well as the overall energy flux of the earthquake rupture event. Hence, the first-order analysis on the source kinematic model plays an important role in understanding the details of source physics and its associated radiation.

Even though the broadband seismic observation network has been built all over the world, so that the real-time and high-quality seismic data can be acquired, the details of rupture dynamics remain obscure due to the methodological limitations of the kinematic inversion models, where the fault geometry is often imposed to be a planar, surrounded by a purely elastic medium. In addition, the complex rupture process such as fault branching, rupture jumps and co-seismic off-fault damage around faults might be masked in the canonical analysis with far-field seismic waves, as they carry the averaged information of the earthquake rupture.

Therefore, the purpose of this perspective is to reveal the discrepancy, and consistency, between kinematic models and detailed rupture dynamics (Figure 5.32). Our physics-based dynamic earthquake rupture modeling directly evaluates the detailed rupture process and its associated radiation with coseismic off-fault damage. We firstly apply kinematic inversion techniques to the model outputs. We then compare the inferred rupture dynamics from the kinematic inversion models with the true model obtained from the dynamic earthquake rupture modeling, which will clarify and quantify the discrepancy, and consistency, between the kinematic inversions and the actual rupture dynamics including coseismic off-fault damage. This study will go a long way towards the better understanding of rupture dynamics estimated with kinematic model and could provide guidelines to improve the latter.

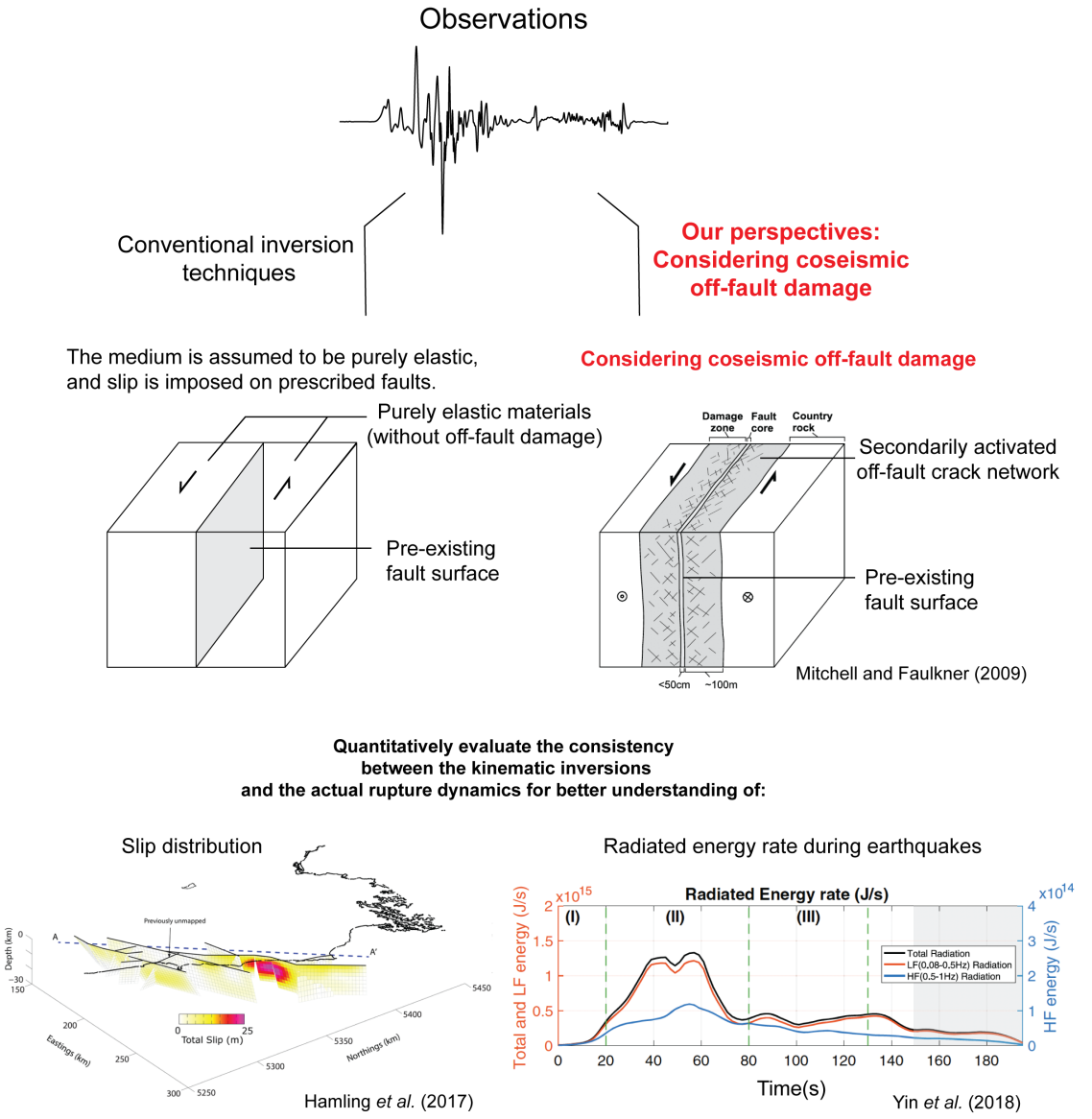

Figure 5.32: Schematic of the quantitative analysis of consistency between kinematic models and rupture dynamics.

6. Conclusions

The full mechanism of earthquake ruptures is always difficult to explain because of the multiscale geometrical complexity, fluid-structure interaction, mineral transformation and other thermodynamical processes. On top of that, the Earth's crust is massively heterogeneous. Even if we figure out a set of coupled physical mechanisms to reasonably model earthquakes, we can never completely deduce the behavior of natural faults because of limitations of measurements in depth and the chaotic aspect of the system.

Then a question arises: *What is the aim of modeling earthquake ruptures even if we can never reproduce them completely?* Our work during this thesis tackled this question in a sense that we investigate whether the numerical modeling can capture the broad effect (in a statistical sense) of coseismic off-fault damage inferred from observations. Our physics-based numerical modeling reveals the effect of off-fault damage on rupture dynamics, associated seismic radiation and the overall energy budget. This work also narrows down the subset of rupture scenarios based on coseismic damage pattern with careful cross-validation between observations and models. These results are universal as long as the dominant physical mechanism is correctly captured. Therefore, the aim and the significance of modeling in this thesis was to estimate the dynamic fracturing mechanisms, based on well-established physics of fractures, and thus can be universally accepted to explain natural phenomena even if with limited conditions and at a semi-qualitative level.

The effect of coseismic off-fault damage has been pointed out for a long time, but not fully understood, especially the activation of secondary off-fault fracture network, due to limitations of model formulations. The numerical techniques of the earthquake rupture modeling have constantly advanced since *Andrews* (1976). With the flow of time, we presented in this thesis an application of FDEM, which takes into account the spontaneous activation of secondary cracks caused by dynamic earthquake ruptures, and thereby allows us to evaluate the damage pattern, the radiation and overall energy budget associated with the earthquake ruptures. We also demonstrated the potential of FDEM for the modeling of natural earthquakes with the 2016 Kaikōura earthquake as an example.

We firstly presented the fundamental analysis of the coseismic off-fault damage on the rupture dynamics in Chapter 3, which includes

1. Description of a continuum-discontinuum approach framework for the dynamic earthquake rupture modeling

2. Cross-validation of FDEM for earthquake rupture modeling

3. The effect of coseismic damage on rupture velocity and supershear transition

4. Fracturing mechanisms, fracture density and enhanced high-frequency radiation
5. Evolution of damage zone with depth
6. Overall energy budget associated with earthquake ruptures

We also described a systematic procedure of dynamic earthquake rupture modeling with FDEM framework for future collaborations. This fundamental analysis highlights the capability of the FDEM for the continuum-discontinuum analysis and the role of coseismic off-fault damage.

We then demonstrated the application for the 2016 Mw 7.8 Kaikōura earthquake in New Zealand in Chapter 4, which includes

1. Examination of the hypothetical rupture scenarios on the Jordan - Kekerengu - Papatea fault system
2. Comparison of the deformation profiles to the observations
3. The evolution of stress states on the prescribed faults
4. Near-field ground motions

This is the first-of-its-kind application for the 2-D natural faults with coseismic off-fault damage, which elucidates the most likely rupture scenario by the comparison to the observations. This result shows that the FDEM can be effectively used to model dynamic ruptures on the complex fault geometry because of the simplicity of its algorithmic framework. Therefore, further applications of the rupture modeling on the natural faults by the continuum-discontinuum approach with FDEM are expected.

Finally, we listed the preliminary results for the perspectives, which includes

1. First-order geometrical complexities (finite fault, kinks, roughness, stepovers)
2. Thrust fault with free surface
3. List of future works which remain to be initiated

The preliminary results already show the characteristic rupture processes, which are also observed in the modeling of the Kaikōura earthquake. The results for modeling thrust earthquakes demonstrate the capability of the rupture modeling with free surface, which causes significant deformation on the wedge near the surface. Although these topics need additional discussion, we are motivated to extend these studies to understand the role of coseismic off-fault damage on such first-order complex fault geometry and the thrust earthquakes.

Overall, the work presented in this thesis has opened an avenue to model dynamic earthquake ruptures with the continuum-discontinuum approach framework, which allows for the dynamic earthquake ruptures on natural fault networks with coseismic off-fault damage. Although most of the present results are with simplified model, the results clearly show the significant effect of the coseismic off-fault damage on rupture dynamics. Therefore, further studies on coseismic off-fault damage are necessary to better understand faulting mechanisms in natural earthquakes.

Appendices

Appendix A. Computational Efficiency

The FDEM is suitable for MPI parallelization by domain decomposition approach, in which the physical space is discretized by prescribed MPI domain grids (*Munjiza et al.*, 2011). Since a processor is assigned to a MPI domain, the total number of element is desired to be well averaged by the number of processors to enhance the computational efficiency. We examined a rupture modeling with different number of processors to evaluate the efficiency of MPI parallelization for this problem. We used the constant G_{IIC} case at 2 km depth with off-fault damage for this comparison. We used dual 8-core Intel Xeon (Sandy Bridge) processors in LANL. Figure A1 shows the computational time and the desired mean element number par MPI domain. Computational time decreases linearly in log-log space with the number of processors, implying the MPI parallelization is efficient in our problem. The approximate curve is obtained as

$$T = 10^{2.3575} N^{-0.7656}. \tag{6.1}$$

Ideally, the rate of decrease of computational time converges to be in inverse proportion to the number of processors, which means the computational time is proportional to the N^{-1}, without consideration of time consumed for communication between processors. Thus the grid of MPI domain used in this study can still be improved by adjusting it to the adaptive mesh and averaging the number of element per MPI domain.

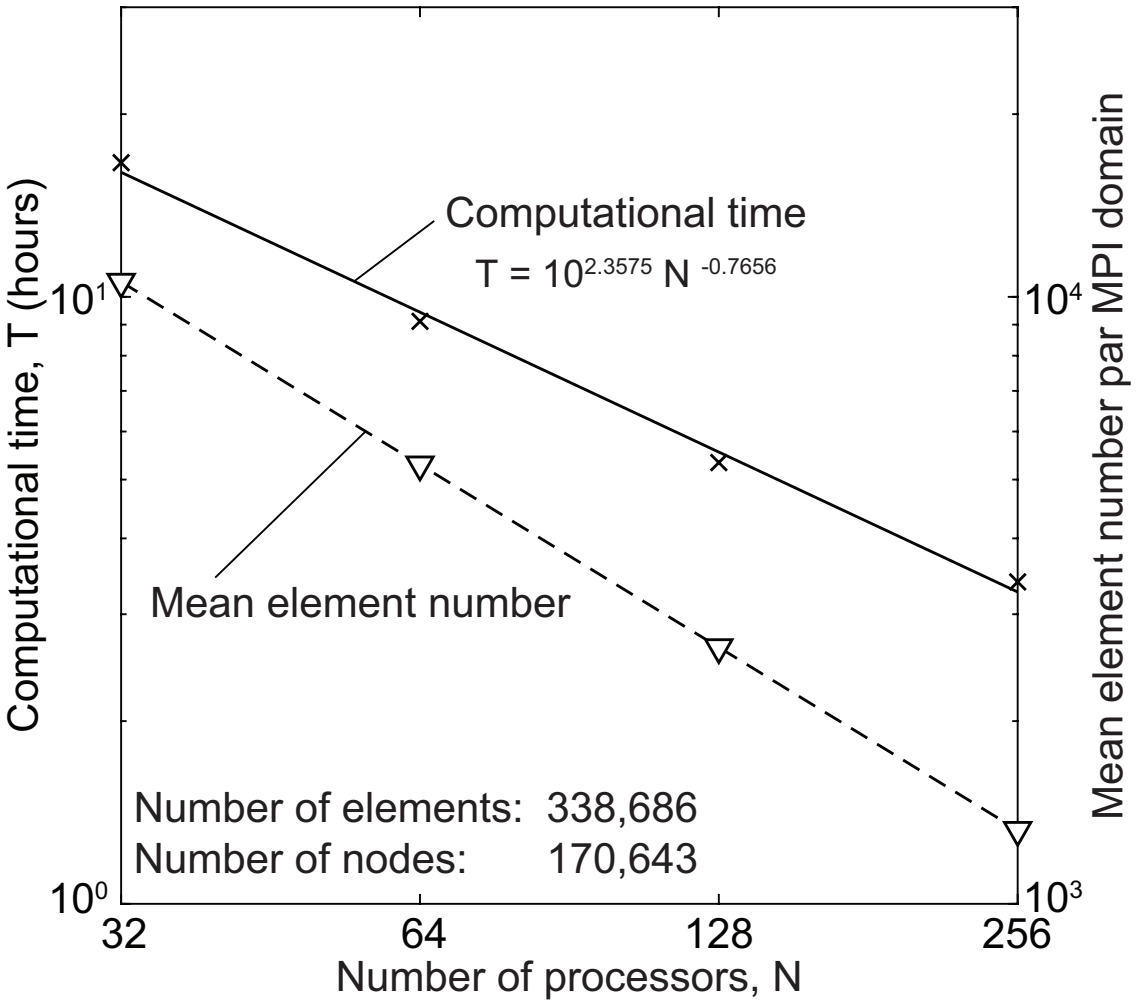

Figure A.1 – Computational time as a function of number of processors. Markers indicate examined cases. Solid line indicates the approximate curve of computational time, while dotted line indicates the ideal mean element number.

Appendix B. A recipe for the dynamic earthquake rupture modeling with FDEM

The procedure of rupture modeling, such as applying initial stress and nucleation processes, depends on the numerical schemes. Here, we describe a flowchart of dynamic earthquake rupture modeling with FDEM, which has some specific processes for mesh discretization, pre-loading and rupture nucleation phases.

B.1 Mesh discretization and grouping by blocks

The computational domain is discretized by finite elements as canonical FEM. We usually discretize by unstructured meshes, which are adaptive for non-planar faults. The size of elements are adjusted as fine near the faults to improve the numerical accuracy, and as coarse, as a function of distance from the faults to reduce the computational cost. Then we need to group the meshes to prescribe faults, nucleation zone and low cohesion zone. The numerical domain is also discretized into rectangular MPI domains. Note that the grid of MPI domains can be independent of mesh topology, and the elements are assigned into each grid and are computed by a processor (*Munjiza et al.*, 2011). Thus the number of processors for the computation is equal to the MPI domains.

Figure B1 show a schematic of mesh discretization and grouping by blocks for a natural fault network. We demonstrate a mesh associated with the 2016 Kaikōura earthquake (discussed in Chapter 4) as an example. Firstly, the fault geometry is taken from the observations. We then discretize the computational domain along the faults, and group the meshes corresponding to blocks as shown in Figure B1. the elements attached with the faults are grouped on both sides of the faults. Then the elements in the nucleation zone is subtracted from the fault groups, and assigned as nucleation blocks. The low cohesion zone is also arbitrary assigned near the faults.

We then describe the parameters for contact interactions between the elements, such as friction and cohesion. We can assign parameters for the interactions between the elements in the block and the interactions between the boundary of blocks, i.e., the interactions for the prescribed faults. Note that we can increase the number of groups if we need to model more heterogeneous materials.

B.2 Relaxation and nucleation phases

To nucleate the dynamic ruptures, we firstly need to accumulate the strain energy in the medium. The initial stress, σ_0, is imposed for the canonical numerical schemes for earthquake rupture modelings, such as FEM, SEM, and BIEM, and we immediately nucleate the dynamic rupture at the first timestep, $T = 0$.

However, as is the case with the Discrete Element Method (DEM), we firstly need to pack the elements to produce the initial stress state in the medium, which we call *relaxation phases*. We need to follow a procedure in order to avoid cohesive failures or unexpected ruptures during these relaxation phases. The medium is stabilized at the end

of the relaxation phases, where the kinetic energy of the medium is well-converged to a low level.

The flowchart is described as follows:

Relax phase 1- Temporally bonding the prescribed faults with surface pressures

Firstly, the prescribed faults need to be bonded by an appropriate surface pressure to avoid unexpected slips on the faults, which causes undesired slip-weakening of the friction before the nucleation of dynamic ruptures. When we suddenly apply the initial stress in the medium before this bonding process, the frictional resistance does not work because of zero normal stress on the fault at the first step of this phase, which causes a small slip on the fault. Thus we need to initially apply the temporal normal stress on the fault to cause the friction on the faults, which resists against the unexpected slip for the later phases.

We also assign the parameters for the contact interaction, such as the friction coefficients and the peak cohesion. In this phase, we need to assign the temporal peak cohesions, which is large enough to avoid to the unexpected cohesive failure due to the numerical oscillations of the elements during relaxation phases. We usually set the peak cohesions 1000 times lager than the original cohesions.

In the beginning of simulations, we also assign the partitions of MPI domains and the location of virtual sensors. We cannot change them during the simulation.

Relax phase 2- Applying the initial stress in the medium

Next, we apply the initial stress in the medium. There are two ways to apply the stress in the FDEM framework; 1) imposing the initial stress on the elements, or 2) loading the stress on the boundary of the medium as external loading. In the former case, we need to fix the motion on the boundary of the medium, and let the elements be relaxed until the medium is stabilized. If the elements are not allowed to overlap, i.e., for the case of the infinite penalty, the medium is ideally static in this phase. However, because of the penalty functions in the FDEM framework, a small perturbation is caused by the overlapping of the elements. This perturbation is eventually suppressed to a negligible level by the artificial viscous damping. The advantage is to be able to reproduce a uniform stress state in the medium, whereas the disadvantage is that it is not capable of modeling free surfaces on the medium.

In the later case, we simply apply the tractions on the boundary of the medium as external loading. In this way, we can model the free surfaces on the medium, whereas it needs more time to apply the stress and stabilize the medium.

In this phase, the temporal bonding on the fault is kept to suppress the unexpected slip. The peak cohesions are also kept large to avoid the cohesive failure due to the abrupt perturbation of the medium caused by the application of the stresses.

Relax phase 3- Setting the original cohesions and stabilizing the medium

Finally, we reset the peak cohesions to its original values, and stabilize the medium with artificial viscous damping. We also remove the temporal bonds of the faults

in this phase because the frictional resistance fully works after applying the initial stress in the previous phase.

Figure B2 shows the history of kinetic energy of the medium,

$$E_K = \int_V \frac{1}{2}\rho \dot{u}_i \dot{u}_i dV, \tag{6.2}$$

during the relax phase 3 and the nucleation phase. E_K is useful to check if the relaxation phases are properly processed. We need to stabilize the medium until the curve of E_K converges to a low level enough to ignore the effect of initial particle motions to the following nucleation phase.

Nucleation phase - Nucleating the dynamic rupture

We can now nucleate the dynamic rupture with the proper initial stress state and the parameters for the contact interactions. The rupture is nucleated by imposing the lower static friction coefficient on the nucleation area of the fault, where the size of the nucleation area is set larger than the nucleation length, L_c. For the sake of simplicity, the timestep is usually reset to zero at the beginning of this phase.

It is noteworthy that the procedure of these relaxation phases is in analogy to the accumulation of the strain energy during the interseismic period of natural earthquakes. The slip on the fault is usually accumulated over the years caused by the external loading (e.g. *Lapusta et al*., 2000), then the rupture is spontaneously nucleated as releasing its accumulated strain energy. However, since we focus only the dynamic part of the earthquake ruptures, we "skip" the interseismic process of the accumulation of strain energy by these relaxation phases. Therefore, we need to consider reasonable interpretations of the relaxation phases when we conduct the modeling of second ruptures on the same fault to investigate the evolution and the saturation of the coseismic off-fault damage.

B.3 Outputs

The output of the simulation includes the particle velocity components, the stress field, secondary cracks with damage type and the motion and velocity of virtual sensors. We post-process these raw datasets to plot the snapshots, and to evaluate the radiations and the overall energy budget. The data is output in VTK (Visualization ToolKit) format, which allows us to process the data with Paraview [1], and the associated python module, simple [2].

[1] https://www.paraview.org

[2] https://www.paraview.org/ParaView3/Doc/Nightly/www/py-doc/paraview.simple.html

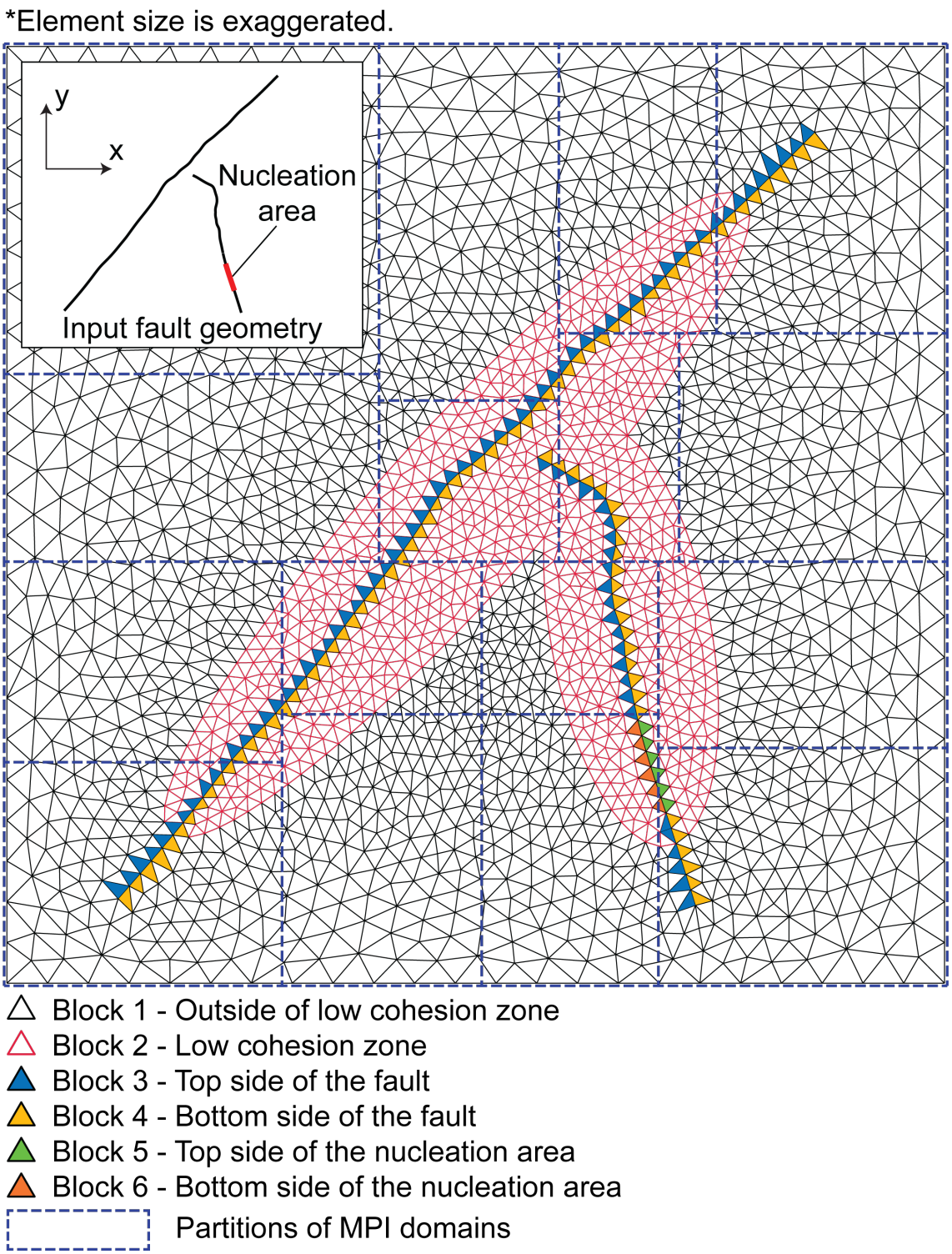

Figure B.1 — Mesh discretization and grouping by blocks. The input fault geometry is illustrated in the inset. The main figure shows the mesh discretization and the blocks. The type of blocks are indicated by colors. The dashed line shows the MPI domains. In this case, the number of required processors is 16.

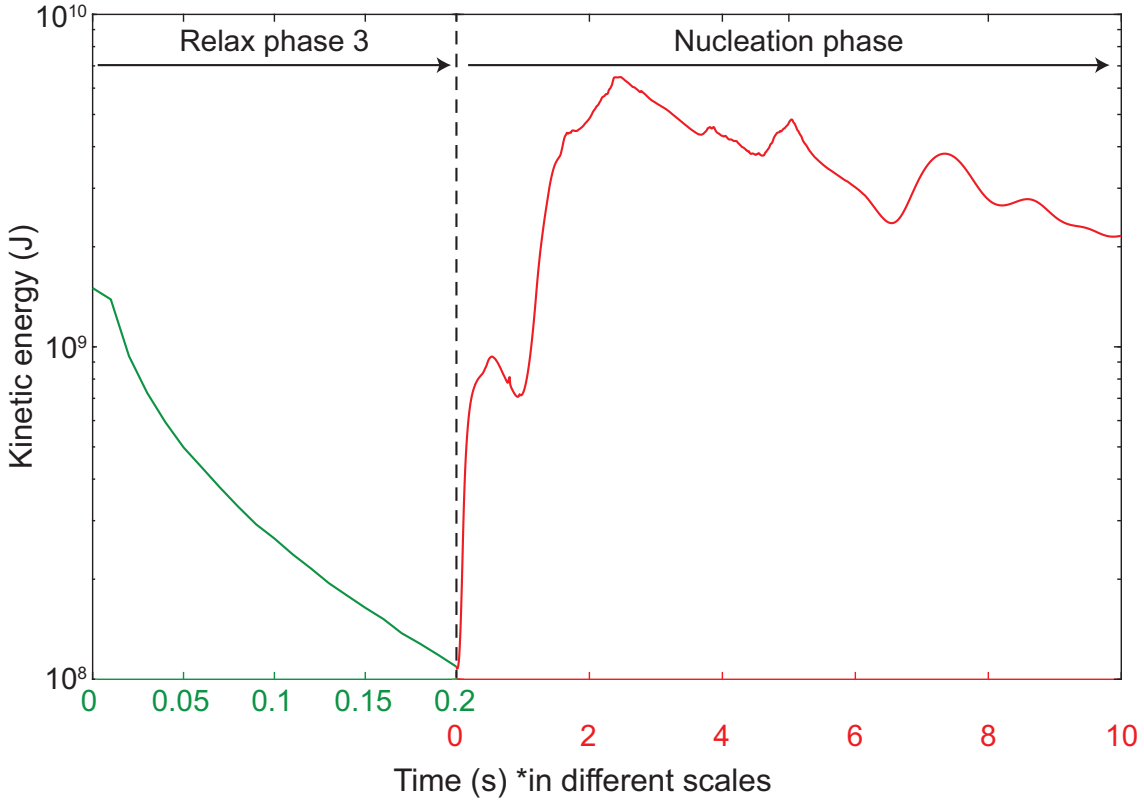

Figure B.2 – History of kinetic energy during relax phase 3 and nucleation phase. It is plotted in different time scales as the relaxation phase takes less time than the nucleation phase.

Appendix C. Mesh Dependency of FDEM

Since potential failure planes are constrained by the element boundary, where the cohesive and friction laws are prescribed, the mesh dependency for damage pattern has to be assessed. Firstly, the mesh orientation should be as random as possible in the FDEM framework, so that it introduces less constraints in the orientation of cracks. We performed two simulations with exactly same model description except for the mesh topology #1 and #2. Figure C1 shows the damage pattern, the distribution of orientation of potential failure planes and rose diagram. There is certainly a difference in the damage patterns. However, the distribution of orientation of cracks is comparable enough for the arguments we discuss in subsection 3.1.4, which implies that the mesh topology does not affect the statistical quantities, such as the high-frequency radiation and the overall energy budget, as long as the physical space is sufficiently discretized.

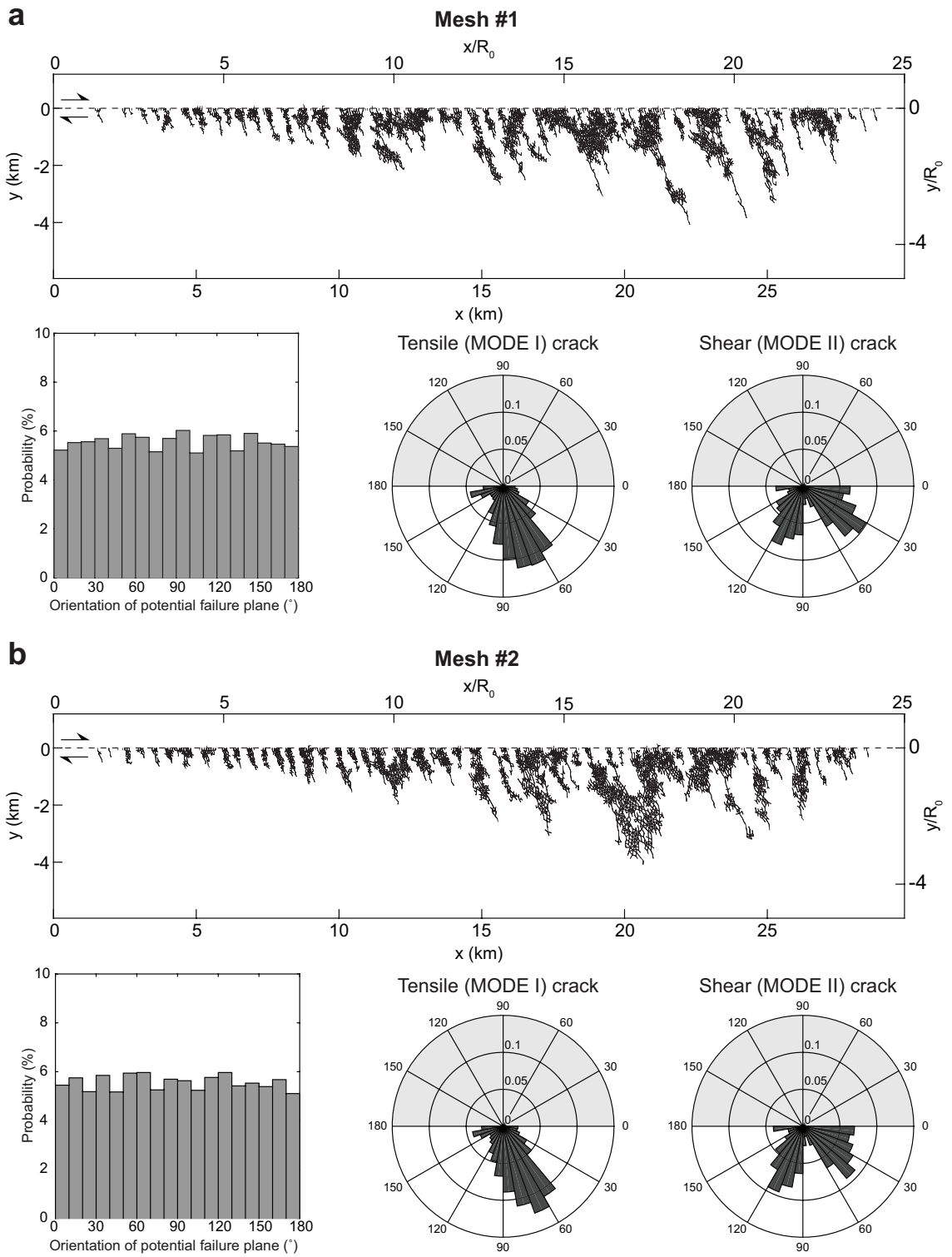

Figure C.1 – Damage pattern, orientation of potential failure planes and rose diagram with different meshes. Model description is exactly same except for the topology of mesh. In Mesh #2, the scale factor of geometric progression for adaptive mesh size is slightly larger to change the mesh topology.

Appendix D. The first and second scenarios without coseismic off-fault damage

Figures D1 to D4 show the first scenario without the coseismic off-fault damage. In this case, only prescribed faults are ruptured, whereas the off-fault medium behaves as purely elastic material. This condition is same as conventional dynamic earthquake rupture modelings with purely elastic constitutive laws. The rupture is nucleated the southern part of Papatea fault, and propagates northward. The rupture then jumps to the Jordan thrust - Kekerengu fault, and propagates bilaterally same as the case with off-fault damage. However, the rupture on the Kekerengu fault transitions to supershear without off-fault damage, while the rupture remains sub-Rayleigh for the case with off-fault damage. Therefore, the rupture dynamics can be modified by the coseismic off-fault damage on the natural fault system.

Figures D5 to D8 show the second scenario without the coseismic off-fault damage. In this case, the rupture initially propagates northward on Jordan - Kekerengu fault system, and the rupture on the Papatea fault is induced by the stress perturbation around the triple junction. In the case with the coseismic off-fault damage, this secondary rupture nucleated from the northern part of Papatea fault is arrested by the spontaneous activation of off-fault cracks. However, without coseismic off-fault damage, the entire Papatea fault is eventually ruptured because the induced rupture is not arrested by the coseismic off-fault damage. Thus, the entire Papatea fault is ruptured for both scenarios with purely elastic assumption, which causes the ambiguity in the determination of most likely rupture scenario. Therefore, the coseismic off-fault damage is an indispensable factor to narrow down the rupture scenarios as incorporated with the observations.

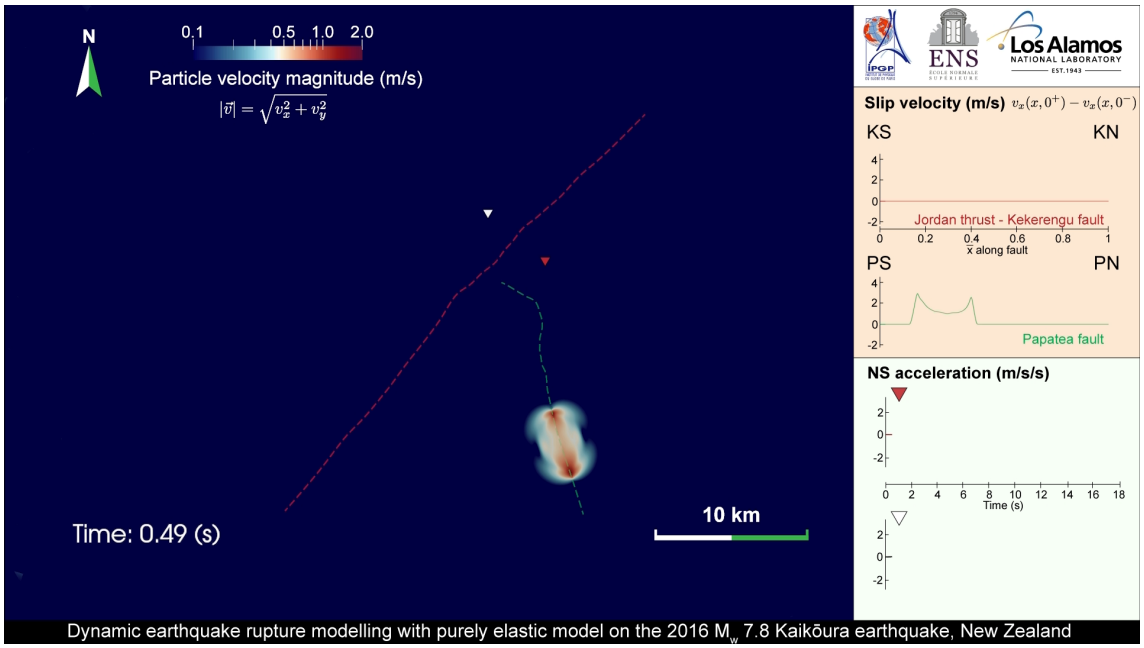

Figure D.1 – The snapshots of the first scenario without off-fault damage. The rupture is nucleated at the southern part of Papatea fault.

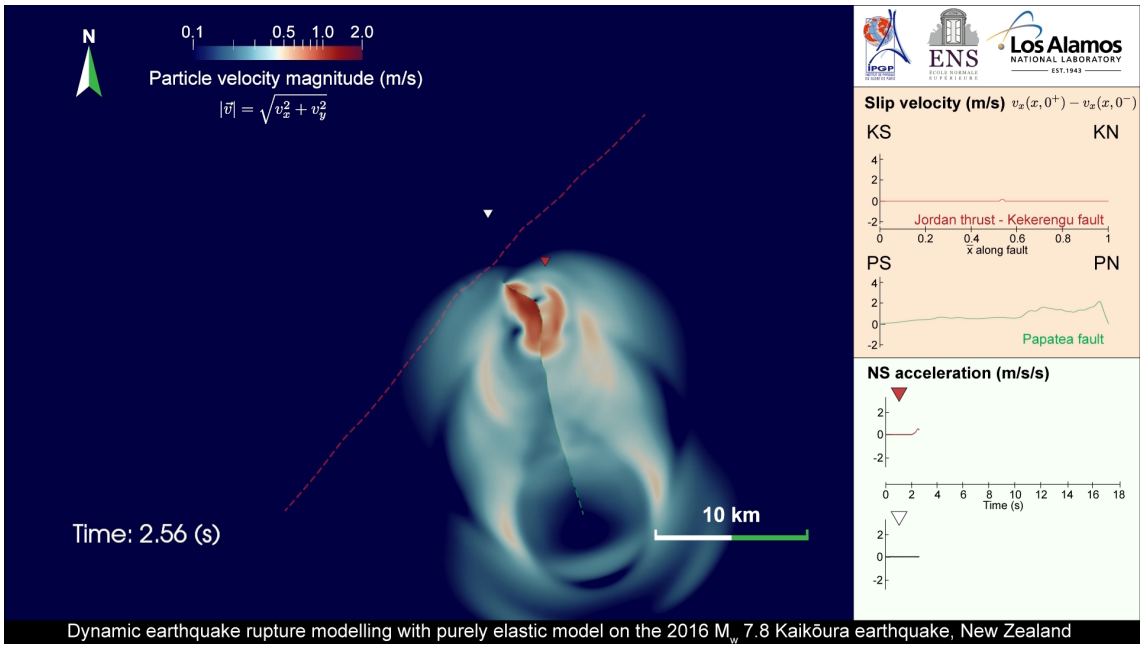

Figure D.2 – The rupture propagates northward on the Papatea fault, and triggers the next rupture on Jordan thrust - Kekerengu fault as shown in the slip velocity on the top-right window.

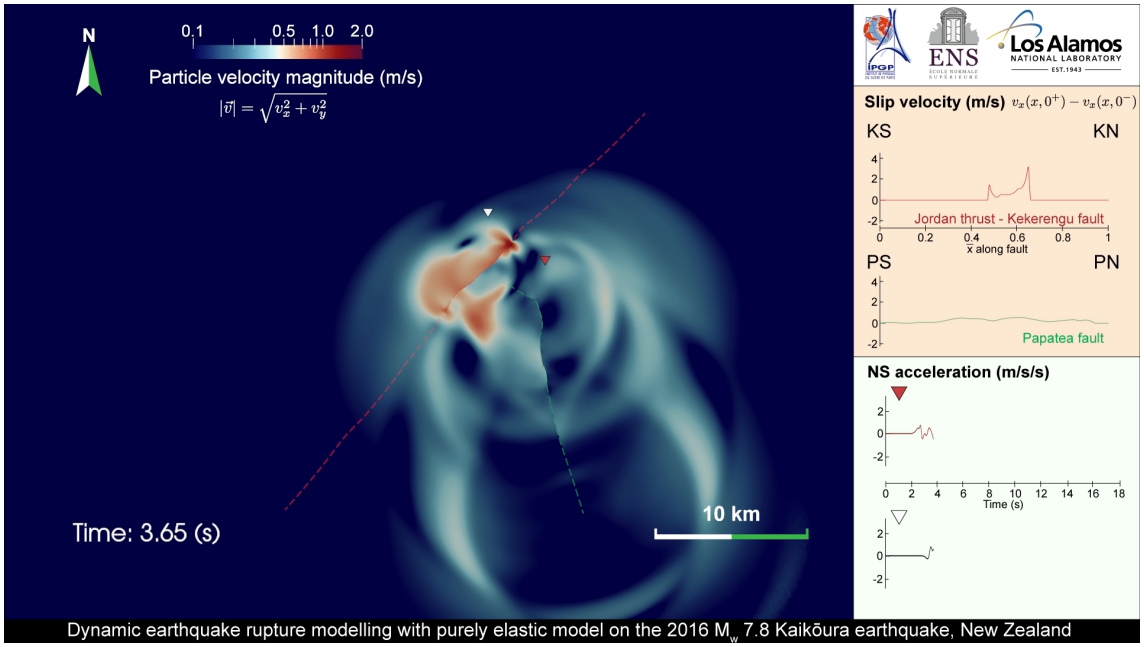

Figure D.3 – The rupture starts to propagate bilaterally on Jordan thrust - Kekerengu fault.

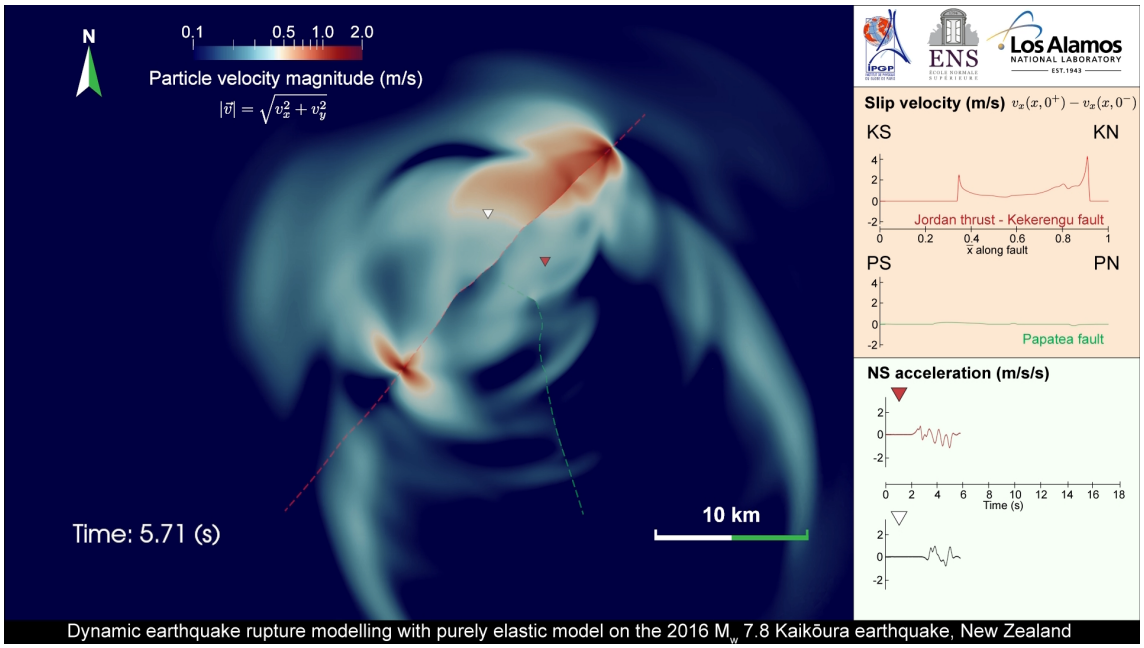

Figure D.4 – The rupture on Kekerengu fault transitions to supershear, while the rupture remains sub-Rayleigh on Jordan thrust.

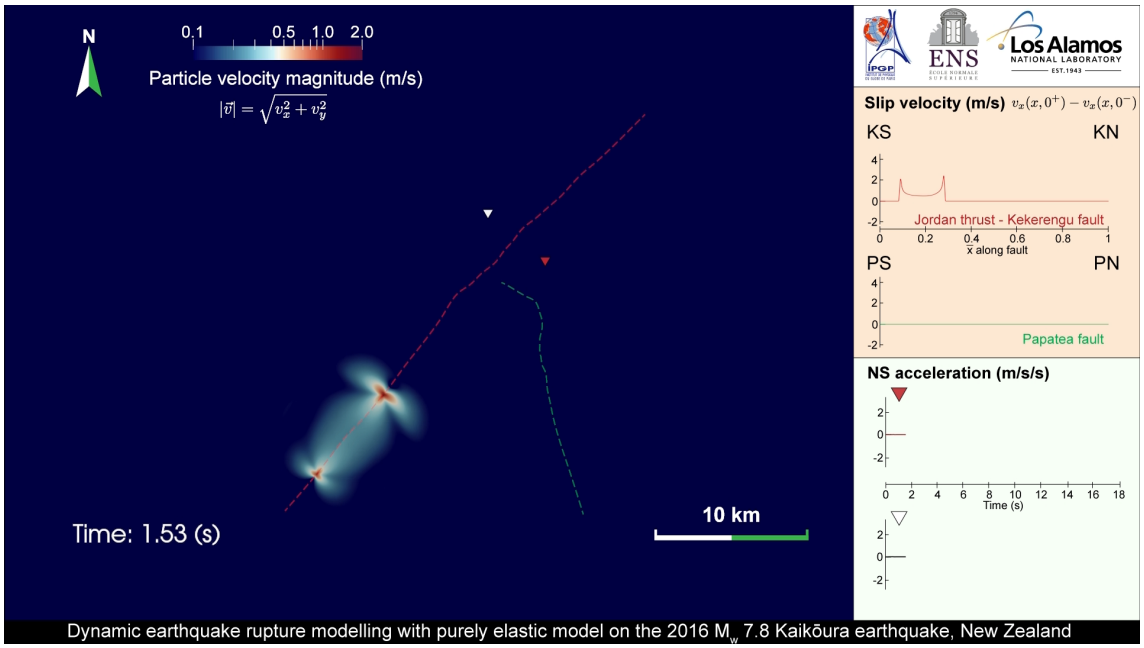

Figure D.5 – The snapshots of the second scenario without off-fault damage. The rupture is nucleated at the southern part of Jordan thrust.

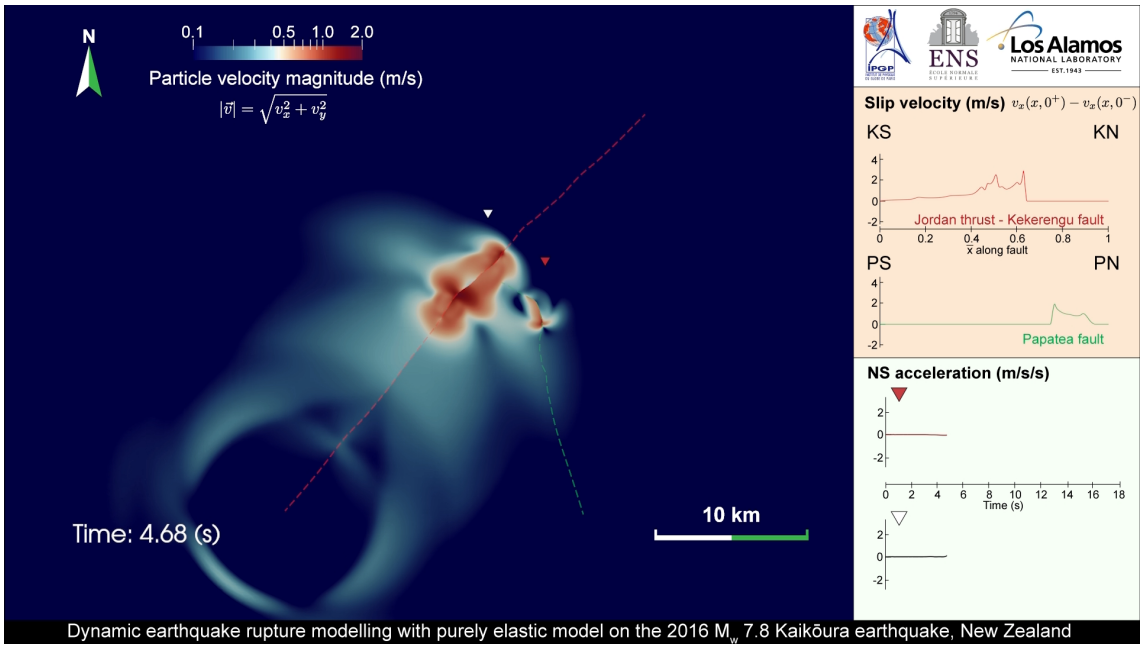

Figure D.6 – The rupture propagates northward, and triggers the rupture at the northern part of Papatea fault.

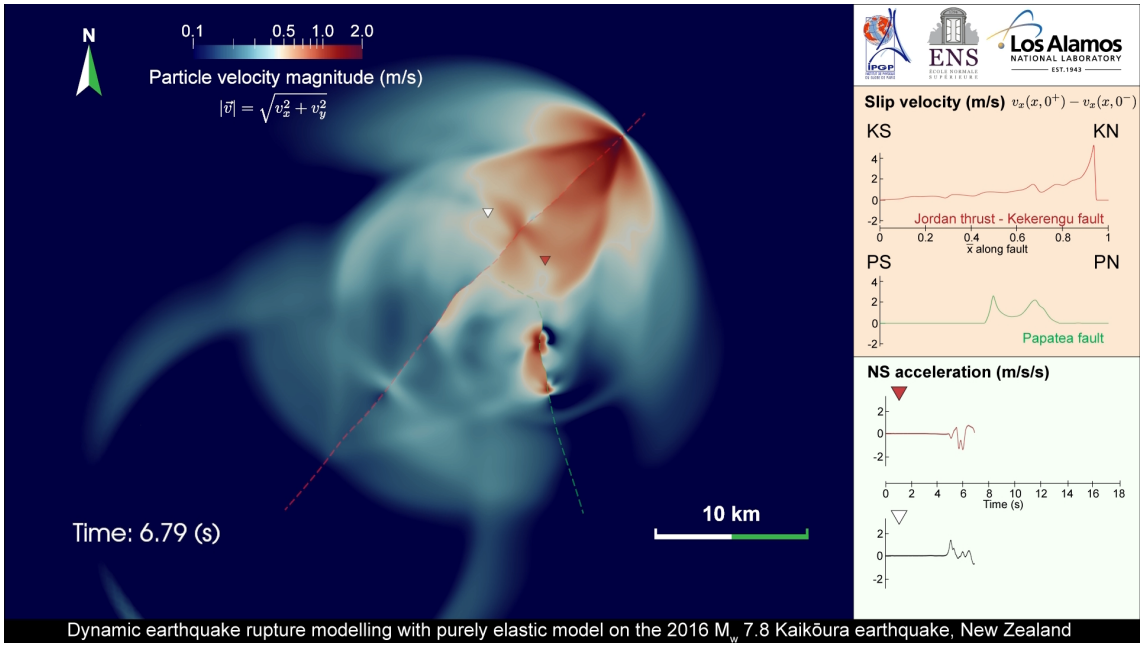

Figure D.7 – In this case, the rupture on the Papatea fault is not arrested and propagates southward.

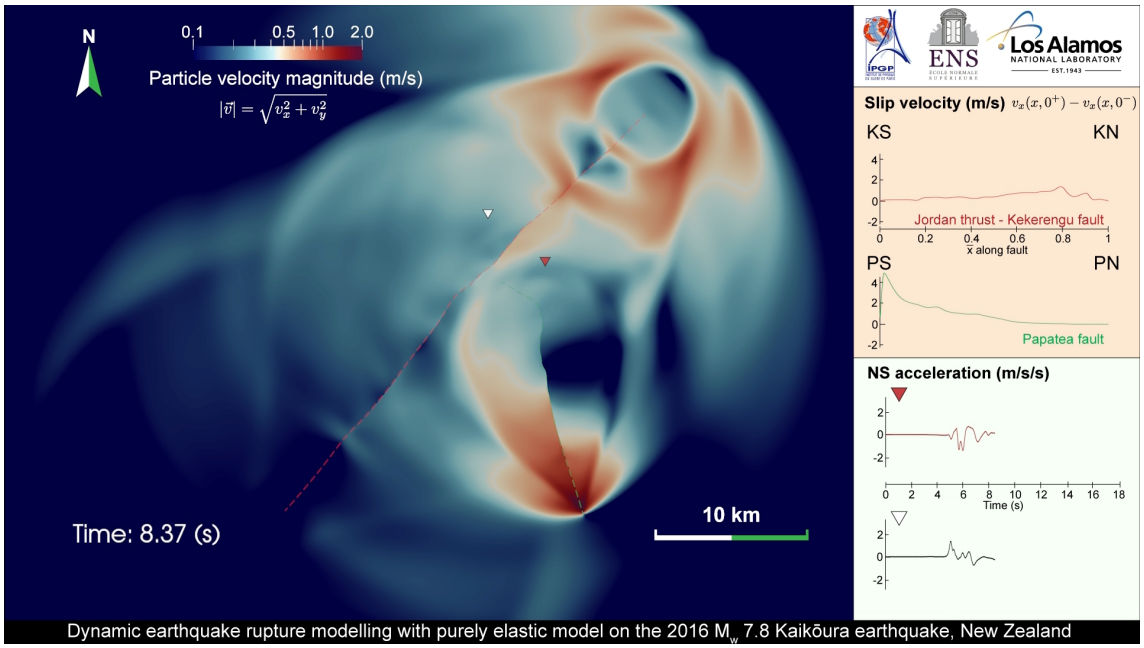

Figure D.8 – Eventually, the rupture transitions to supershear on Papatea fault, and the entire fault is ruptured.

Bibliography

Adda-Bedia, M., and R. Madariaga (2008), Seismic radiation from a kink on an antiplane fault, *Bull. Seismol. Soc. Am.*, *98*(5), 2291–2302, doi:10.1785/0120080003.

Aki, K. (1987), Magnitude-frequency relation for small earthquakes: A clue to the origin of $f$max of large earthquakes, *J. Geophys. Res.*, *92*(B2), 1349–1355, doi:10.1029/JB092iB02p01349.

Aki, K., and P. G. Richards (2002), *Quantitative Seismology*, University Science Books.

Ando, R., and T. Yamashita (2007), Effects of mesoscopic-scale fault structure on dynamic earthquake ruptures: Dynamic formation of geometrical complexity of earthquake faults, *J. Geophys. Res.*, *112*(B9), doi:10.1029/2006JB004612.

Andrews, D. (1999), Test of two methods for faulting in finite-difference calculations, *B. Seismol. Soc. Am.*, *89*(4), 931–937.

Andrews, D. J. (1976), Rupture velocity of plane strain shear cracks, *J. Geophys. Res.*, *81*(B32), 5679–5689, doi:10.1029/JB081i032p05679.

Andrews, D. J. (1985), Dynamic plane-strain shear rupture with a slip-weakening friction law calculated by a boundary integral method, *Bull. Seism. Soc. Am.*, *75*, 1–21.

Andrews, D. J. (2005), Rupture dynamics with energy loss outside the slip zone, *J. Geophys. Res.*, *110*, 1307, doi:10.1029/2004JB003191.

Aochi, H., and E. Fukuyama (2002), Three-dimensional nonplanar simulation of the 1992 landers earthquake, *J. Geophys. Res.*, *107*(B2), doi:10.1029/2000JB000061.

Aochi, H., E. Fukuyama, and M. Matsu'ura (2000), Selectivity of spontaneous rupture propagation on a branched fault, *Geophys. Res. Lett.*, *27*, 3635–3638, doi:10.1029/2000GL011560.

Backus, G., and M. Mulcahy (1976a), Moment tensors and other phenomenological descriptions of seismic sources—i. continuous displacements, *Geophys. J. Int.*, *46*(2), 341–361.

Backus, G., and M. Mulcahy (1976b), Moment tensors and other phenomenological descriptions of seismic sources—ii. discontinuous displacements, *Geophys. J. Int.*, *47*(2), 301–329.

Beeler, N., R. Simpson, S. Hickman, and D. Lockner (2000), Pore fluid pressure, apparent friction, and coulomb failure, *J. Geophys. Res.*, *105*(B11), 25,533–25,542, doi:10.1029/2000JB900119.

Ben-Zion, Y., and Z. Shi (2005), Dynamic rupture on a material interface with spontaneous generation of plastic strain in the bulk, *Earth Planet. Sc. Lett.*, *236*(1-2), 486–496, doi:10.1016/j.epsl.2005.03.025.

Ben-Zion, Y., Z. Peng, D. Okaya, L. Seeber, J. G. Armbruster, N. Ozer, A. J. Michael, S. Baris, and M. Aktar (2003), A shallow fault-zone structure illuminated by trapped waves in the Karadere–Duzce branch of the North Anatolian Fault, western Turkey, *Geophys. J. Int.*, *152*(3), 699–717, doi:10.1046/j.1365-246X.2003.01870.x.

Bhat, H. S. (2007), Role of geometric complexities and off-fault damage in dynamic rupture propagation, Ph.D. thesis, Harvard University.

Bhat, H. S., R. Dmowska, J. R. Rice, and N. Kame (2004), Dynamic slip transfer from the denali to totschunda faults, alaska: Testing theory for fault branching, *Bull. Seism. Soc. Am.*, *94*, S202–S213, doi:10.1785/0120040601.

Bhat, H. S., M. Olives, R. Dmowska, and J. R. Rice (2007), Role of fault branches in earthquake rupture dynamics, *J. Geophys. Res.*, *B11309*, doi:10.1029/2007JB005027.

Bhat, H. S., A. J. Rosakis, and C. G. Sammis (2012), A micromechanics based constitutive model for brittle failure at high strain rates, *J. Appl. Mech.*, *79*(3), doi:10.1115/1.4005897.

Brace, W. F., and J. D. Byerlee (1966), Stick-slip as a mechanism for earthquakes, *Science*, *153*(3739), 990–992, doi:10.1126/science.153.3739.990.

Burridge, R., and L. Knopoff (1964), Body force equivalents for seismic dislocations, *Bulletin of the Seismological Society of America*, *54*(6A), 1875, doi:10.1785/gssrl.74.2.154.

Cappa, F., C. Perrin, I. Manighetti, and E. Delor (2014), Off-fault long-term damage: A condition to account for generic, triangular earthquake slip profiles, *Geochem. Geophys. Geosyst.*, *15*(4), 1476–1493, doi:10.1002/2013GC005182.

Castro, R. R., and Y. Ben-Zion (2013), Potential signatures of damage-related radiation from aftershocks of the 4 April 2010 (Mw 7.2) El Mayor–Cucapah Earthquake, Baja California, México, *Bull. Seism. Soc. Am.*, *103*(2A), 1130–1140, doi:10.1785/0120120163.

Chester, F. M., J. P. Evans, and R. L. Biegel (1993), Internal structure and weakening mechanisms of the san andreas fault, *J. Geophys. Res.*, *98*, 771–786, doi:10.1029/92JB01866.

Cho, S. H., Y. Ogata, and K. Kaneko (2003), Strain-rate dependency of the dynamic tensile strength of rock, *Int. J. Rock Mech. Min. Sci.*, *40*(5), 763–777, doi:10.1016/S1365-1609(03)00072-8.

Choi, J.-H., Y. Klinger, M. Ferry, J.-F. Ritz, R. Kurtz, M. Rizza, L. Bollinger, B. Davaasambuu, N. Tsend-Ayush, and S. Demberel (2018), Geologic inheritance and earthquake rupture processes: The 1905 M≥ 8 Tsetserleg-Bulnay strike-slip earthquake sequence, Mongolia, *J. Geophys. Res.*, *123*(2), 1925–1953, doi:10.1002/2017JB013962.

Clark, K., E. Nissen, J. Howarth, I. Hamling, J. Mountjoy, W. Ries, K. Jones, S. Goldstien, U. Cochran, P. Villamor, et al. (2017), Highly variable coastal deformation in the 2016 Mw7. 8 Kaikōura earthquake reflects rupture complexity along a transpressional plate boundary, *Earth Planet. Sc. Lett.*, *474*, 334–344, doi:10.1016/j.epsl.2017.06.048.

Cocco, M., and J. R. Rice (2002), Pore pressure and poroelasticity effects in coulomb stress analysis of earthquake interactions, *J. Geophys. Res.*, *107*(B2), ESE–2, doi:10.1029/2000JB000138.

Coulomb, C. A. (1773), Essai sur une application des règles de maximis et minimis à quelques problèmes de statique relatifs à l'architecture, *Mémoires De Mathématique Et Physique Presenté A L'Acádemie Des Sciences Par Savantes Etrangères*, pp. 343–382.

Dalguer, L. A., K. Irikura, and J. D. Riera (2003), Simulation of tensile crack generation by three-dimensional dynamic shear rupture propagation during an earthquake, *J. Geophys. Res.*, *108*(B3), doi:10.1029/2001JB001738.

Day, S. M. (1982), Three-dimensional finite difference simulation of fault dynamics: rectangular faults with fixed rupture velocity, *Bull. Seism. Soc. Am.*, *72*(3), 705–727.

Day, S. M., L. A. Dalguer, N. Lapusta, and Y. Liu (2005), Comparison of finite difference and boundary integral solutions to three-dimensional spontaneous rupture, *J. Geophys. Res.*, *110*(B12307), doi:10.1029/2005JB003813.

De La Puente, J., J.-P. Ampuero, and M. Käser (2009), Dynamic rupture modeling on unstructured meshes using a discontinuous Galerkin method, *J. Geophys. Res.*, *114*(B10), B10,302, doi:10.1029/2008JB006271.

Denolle, M. A., W. Fan, and P. M. Shearer (2015), Dynamics of the 2015 M7.8 Nepal earthquake, *Geophys. Res. Lett.*, *42*(18), 7467–7475, doi:10.1002/2015GL065336.

Di Toro, G., S. Nielsen, and G. Pennacchioni (2005), Earthquake rupture dynamics frozen in exhumed ancient faults, *Nature*, *436*(7053), 1009, doi:10.1038/nature03910.

Dieterich, J. H. (1978), Time-dependent friction and the mechanics of stick-slip, *Pure Appl. Geophys.*, *116*(4-5), 790–806, doi:10.1007/BF00876539.

Dieterich, J. H. (1979a), Modeling of rock friction: 1. experimental results and constitutive equations, *J. Geophys. Res.*, *84*(B5), 2161–2168, doi:10.1029/JB084iB05p02161.

Dieterich, J. H. (1979b), Modeling of rock friction: 2. simulation of preseismic slip, *J. Geophys. Res.*, *84*(B5), 2169–2175, doi:10.1029/JB084iB05p02169.

Duan, B., and S. M. Day (2008), Inelastic strain distribution and seismic radiation from rupture of a fault kink, *J. Geophys. Res.*, *113*(B12), doi:10.1029/2008JB005847.

Dunham, E. M., D. Belanger, L. Cong, and J. E. Kozdon (2011a), Earthquake ruptures with strongly rate-weakening friction and off-fault plasticity, part 1: Planar faults, *Bull. Seism. Soc. Am.*, *101*(5), 2296–2307, doi:10.1785/0120100075.

Dunham, E. M., D. Belanger, L. Cong, and J. E. Kozdon (2011b), Earthquake ruptures with strongly rate-weakening friction and off-fault plasticity, part 2: Nonplanar faults, *Bull. Seism. Soc. Am.*, *101*(5), 2308–2322, doi:10.1785/0120100076.

Duputel, Z., and L. Rivera (2017), Long-period analysis of the 2016 Kaikoura earthquake, *Phys. Earth Planet. In.*, *265*, 62–66, doi:0.1016/j.pepi.2017.02.004.

Faulkner, D. R., T. M. Mitchell, D. Healy, and M. J. Heap (2006), Slip on'weak'faults by the rotation of regional stress in the fracture damage zone, *Nature*, *444*(7121), 922–925, doi:10.1038/nature05353.

Faulkner, D. R., T. M. Mitchell, E. Jensen, and J. Cembrano (2011), Scaling of fault damage zones with displacement and the implications for fault growth processes, *J. Geophys. Res.*, *116*(B05403), doi:10.1029/2010JB007788.

Field, E. H., T. H. Jordan, M. T. Page, K. R. Milner, B. E. Shaw, T. E. Dawson, G. P. Biasi, T. Parsons, J. L. Hardebeck, A. J. Michael, et al. (2017), A synoptic view of the third uniform california earthquake rupture forecast (ucerf3), *Seismol. Res. Lett.*, *88*(5), 1259–1267, doi:10.1785/0220170045.

Fletcher, J. M., O. J. Teran, T. K. Rockwell, M. E. Oskin, K. W. Hudnut, K. J. Mueller, R. M. Spelz, S. O. Akciz, E. Masana, G. Faneros, et al. (2014), Assembly of a large earthquake from a complex fault system: Surface rupture kinematics of the 4 April 2010 El Mayor–Cucapah (Mexico) Mw 7.2 earthquake, *Geosphere*, *10*(4), 797–827, doi:10.1130/GES00933.1.

Fliss, S., H. S. Bhat, R. Dmowska, and J. R. Rice (2005), Fault branching and rupture directivity, *J. Geophys. Res.*, *B06312*, doi:10.1029/2004JB003368.

Freund, L. B. (1990), *Dynamic Fracture Mechanics*, Cambridge University Press, Cambridge.

Fukuyama, E. (2005), Radiation energy measured at earthquake source, *Geophysical research letters*, *32*(13), doi:10.1029/2005GL022698.

Gabriel, A.-A., J.-P. Ampuero, L. Dalguer, and P. M. Mai (2013), Source properties of dynamic rupture pulses with off-fault plasticity, *J. Geophys. Res.*, *118*(8), 4117–4126, doi:10.1002/jgrb.50213.

Gabuchian, V., A. J. Rosakis, H. S. Bhat, R. Madariaga, and H. Kanamori (2017), Experimental evidence that thrust earthquake ruptures might open faults, *Nature*, *545*(336–339), doi:10.1038/nature22045.

Hamling, I. J., S. Hreinsdóttir, K. Clark, J. Elliott, C. Liang, E. Fielding, N. Litchfield, P. Villamor, L. Wallace, T. J. Wright, E. D'Anastasio, S. Bannister, D. Burbidge, P. Denys, P. Gentle, J. Howarth, C. Mueller, N. Palmer, C. Pearson, W. Power, P. Barnes, D. J. A. Barrell, R. Van Dissen, R. Langridge, T. Little, A. Nicol, J. Pettinga, J. Rowland, and M. Stirling (2017), Complex multifault rupture during the 2016 Mw 7.8 Kaikōura earthquake, New Zealand, *Science*, doi:10.1126/science.aam7194.

Hanks, T. C. (1982), f max, *Bull. Seismol. Soc. Am.*, *72*(6A), 1867–1879.

Hanks, T. C., and R. K. McGuire (1981), The character of high-frequency strong ground motion, *Bull. Seismol. Soc. Am.*, *71*(6), 2071–2095.

Harris, R. A., and S. M. Day (1993), Dynamics of fault interaction-parallel strike-slip faults, *J. Geophys. Res.*, *98*(B3), 4461–4472, doi:10.1029/92JB02272.

Harris, R. A., R. J. Archuleta, and S. M. Day (1991), Fault steps and the dynamic rupture process: 2-D numerical simulations of a spontaneously propagating shear fracture, *Geophys. Res. Lett.*, *18*(5), 893–896, doi:10.1029/91GL01061.

Harris, R. A., M. Barall, R. J. Archuleta, E. M. Dunham, B. Aagaard, J.-P. Ampuero, H. S. Bhat, V. Cruz-Atienza, L. Dalguer, P. Dawson, S. M. Day, B. Duan, G. Ely, Y. Kaneko, Y. Kase, N. Lapusta, Y. Liu, S. Ma, D. D. Oglesby, K. B. Olsen, A. Pitarka, S. Song, and E. L. Templeton (2009), The SCEC/USGS dynamic earthquake rupture code verification exercise, *Seismol. Res. Lett.*, *80*(1), doi:10.1785/gssrl.80.1.119.

Heidbach, O., M. Rajabi, K. Reiter, and M. Ziegler (2016), World stress map database release 2016, *GFZ Data Services*, doi:10.5880/WSM.2016.001.

Holden, C., Y. Kaneko, E. D'Anastasio, R. Benites, B. Fry, and I. J. Hamling (2017), The 2016 Kaikōōura earthquake revealed by kinematic source inversion and seismic wavefield simulations: Slow rupture propagation on a geometrically complex crustal fault network, *Geophys. Res. Lett.*, doi:10.1002/2017GL075301.

Hollingsworth, J., L. Ye, and J.-P. Avouac (2017), Dynamically triggered slip on a splay fault in the Mw 7.8, 2016 Kaikoura (New Zealand) earthquake, *Geophys. Res. Lett.*, *44*(8), 3517–3525, doi:10.1002/2016GL072228.

Ida, Y. (1972), Cohesive force across tip of a longitudinal-shear crack and griffiths specific surface-energy, *J. Geophys. Res.*, *77*, 3796–3805, doi:JB077i020p03796.

Ide, S., G. C. Beroza, D. R. Shelly, and T. Uchide (2007), A scaling law for slow earthquakes, *Nature*, *447*(7140), 76–79, doi:10.1038/nature05780.

Ide, S., K. Imanishi, Y. Yoshida, G. C. Beroza, and D. R. Shelly (2008), Bridging the gap between seismically and geodetically detected slow earthquakes, *Geophys. Res. Lett.*, *35*(10), L10,305, doi:10.1029/2008GL034014.

Ikeda, Y., N. Chida, T. Nakata, H. Kaneda, M. Tajikara, and S. Takazawa (2001), 1: 25,000-scale active fault map in urban area "Kumamoto", *Tech. rep.*, Tech. Rep. of the GSI.

Ishimoto, M. (1932), Existence d'une source quadruple au foyer sismique d'apres l'etude de la distribution des mouvements initiaux des secousses sismiques, *Bulletin of the Earthquake Research Institute, Tokyo Imperial University*, *10*(2), 449–471.

Kääb, A., B. Altena, and J. Mascaro (2017), Coseismic displacements of the 14 November 2016 Mw 7.8 Kaikoura, New Zealand, earthquake using the planet optical cubesat constellation, *Nat. Hazard. Earth. Sys.*, *17*(5), 627–639, doi:10.5194/nhess-17-627-2017.

Kame, N., J. R. Rice, and R. Dmowska (2003), Effects of prestress state and rupture velocity on dynamic fault branching, *J. Geophys. Res.*, *108*(B5), doi:10.1029/2002JB002189.

Kanamori, H., and E. E. Brodsky (2004), The physics of earthquakes, *Rep. Prog. Phys.*, *67*(8), 1429, doi:10.1063/1.1387590.

Kaneko, Y., N. Lapusta, and J. P. Ampuero (2008), Spectral element modeling of spontaneous earthquake rupture on rate and state faults: Effect of velocity-strengthening friction at shallow depths, *J. Geophys. Res.*, *113*(B09317), doi:10.1029/2007JB005553.

Kaneko, Y., J.-P. Ampuero, and N. Lapusta (2011), Spectral-element simulations of long-term fault slip: Effect of low-rigidity layers on earthquake-cycle dynamics, *J. Geophys. Res.*, *116*(B10313), doi:10.1029/2011JB008395.

Kaneko, Y., E. Fukuyama, and I. J. Hamling (2017), Slip-weakening distance and energy budget inferred from near-fault ground deformation during the 2016 Mw7. 8 Kaikōura earthquake, *Geophys. Res. Lett.*, *44*(10), 4765–4773, doi:10.1002/2017GL073681.

Kearse, J., T. A. Little, R. J. Van Dissen, P. M. Barnes, R. Langridge, J. Mountjoy, W. Ries, P. Villamor, K. J. Clark, A. Benson, et al. (2018), Onshore to offshore ground-surface and seabed rupture of the Jordan–Kekerengu–Needles fault network during the 2016 M w 7.8 Kaikōura earthquake, New Zealand, *Bull. Seismol. Soc. Am.*, doi:10.1785/0120170304.

King, G., and J. Nábělek (1985), Role of fault bends in the initiation and termination of earthquake rupture, *Science*, *228*(4702), 984–987, doi:10.1126/science.228.4702.984.

King, G. C. P., R. S. Stein, and J. Lin (1994), Static stress changes and the triggering of earthquakes, *Bull. Seism. Soc. Am.*, *84*(3), 935–953.

Klinger, Y., K. Okubo, A. Vallage, J. Champenois, A. Delorme, E. Rougier, Z. Lei, E. E. Knight, A. Munjiza, C. Satriano, S. Baize, R. Langridge, and H. S. Bhat (2018), Earthquake damage patterns resolve complex rupture processes, *subm. Geophys. Res. Lett.*

Knight, E. E., E. Rougier, and Z. Lei (2015), Hybrid optimization software suite (HOSS) – educational version LA-UR-15-27013, *Tech. rep.*, Los Alamos National Laboratory.

Kobayashi, H., K. Koketsu, and H. Miyake (2017), Rupture processes of the 2016 Kumamoto earthquake sequence: causes for extreme ground motions, *Geophys. Res. Lett.*, *44*(12), 6002–6010, doi:10.1002/2017GL073857.

Koller, M. G., M. Bonnet, and R. Madariaga (1992), Modelling of dynamical crack propagation using time-domain boundary integral equations, *Wave Motion*, *16*(4), 339–366, doi:10.1016/0165-2125(92)90022-T.

Kostrov, B. V. (1974), Seismic moment and energy of earthquakes, and seismic flow of rock, *Izv. Acad. Sci. USSR Phys. Solid Earth*, *1*, 23–44.

Lachenbruch, A. H. (1980), Frictional heating, fluid pressure, and the resistance to fault motion, *J. Geophys. Res.*, *85*(B11), 6097–6112, doi:10.1029/JB085iB11p06097.

Langridge, R., W. Ries, N. Litchfield, P. Villamor, R. Van Dissen, D. Barrell, M. Rattenbury, D. Heron, S. Haubrock, D. Townsend, et al. (2016), The New Zealand active faults database, *New Zealand Journal of Geology and Geophysics*, *59*(1), 86–96, doi:10.1080/00288306.2015.1112818.

Langridge, R. M., J. Rowland, P. Villamor, J. Mountjoy, D. B. Townsend, E. Nissen, C. Madugo, W. F. Ries, C. Gasston, A. Canva, et al. (2018), Coseismic rupture and preliminary slip estimates for the papatea fault and its role in the 2016 Mw 7.8 Kaikōura, New Zealand, Earthquake, *Bull. Seismol. Soc. Am.*, doi:10.1785/0120170336.

Lapusta, N., and J. R. Rice (2003), Nucleation and early seismic propagation of small and large events in a crustal earthquake model, *J. Geophys. Res.*, *108*(B4), doi:10.1029/2001JB000793.

Lapusta, N., J. R. Rice, Y. Ben-Zion, and G. Zheng (2000), Elastodynamic analysis for slow tectonic loading with spontaneous rupture episodes on faults with rate-and-state-dependent friction, *J. Geophys. Res.*, *105*(B10), 23,675–23,789, doi:10.1029/2000JB900250.

Lei, Q., and G. Ke (2018), Correlation between fracture network properties and stress variability in geological media, *Geophys. Res. Lett.*, *45*(9), 3994–4006, doi:10.1002/2018GL077548.

Lei, Z., E. Rougier, E. Knight, and A. Munjiza (2014), A framework for grand scale parallelization of the combined finite discrete element method in 2d, *Comp. Part. Mech.*, *1*(3), 307–319, doi:10.1007/s40571-014-0026-3.

Lisjak, A., Q. Liu, Q. Zhao, O. K. Mahabadi, and G. Grasselli (2013), Numerical simulation of acoustic emission in brittle rocks by two-dimensional finite-discrete element analysis, *Geophys. J. Int.*, *195*(1), 423–443, doi:10.1093/gji/ggt221.

Lisjak, A., G. Grasselli, and T. Vietor (2014), Continuum–discontinuum analysis of failure mechanisms around unsupported circular excavations in anisotropic clay shales, *Int. J. Rock Mech. Min. Sci.*, *65*, 96–115, doi:10.1016/j.ijrmms.2013.10.006.

Litchfield, N. J., P. Villamor, R. J. V. Dissen, A. Nicol, P. M. Barnes, D. J. A. Barrell, J. R. Pettinga, R. M. Langridge, T. A. Little, J. J. Mountjoy, et al. (2018), Surface rupture of multiple crustal faults in the 2016 Mw 7.8 Kaikōura, New Zealand, Earthquake, *Bull. Seismol. Soc. Am.*, doi:10.1785/0120170300.

Ma, S., and D. Andrews (2010), Inelastic off-fault response and three-dimensional dynamics of earthquake rupture on a strike-slip fault, *J. Geophys. Res.*, *115*(B4), doi:10.1029/2009JB006382.

Ma, S., and E. T. Hirakawa (2013), Dynamic wedge failure reveals anomalous energy radiation of shallow subduction earthquakes, *Earth and Planetary Science Letters*, *375*, 113–122, doi:10.1016/j.epsl.2013.05.016.

Madariaga, R. (1976), Dynamics of an expanding circular fault, *Bull. Seism. Soc. Am.*, *66*(3), 639–666.

Madariaga, R. (1977), High-frequency radiation from crack (stress drop) models of earthquake faulting, *Geophys. J. Roy. Astr. S.*, *51*, 625–651, doi:10.1111/j.1365-246X.1977.tb04211.x.

Madariaga, R., J. P. Ampuero, and M. Adda-Bedia (2006), *Seismic Radiation from Simple Models of Earthquakes*, pp. 223–236, American Geophysical Union (AGU), doi:10.1029/170GM23.

Mahabadi, O., B. Tatone, and G. Grasselli (2014), Influence of microscale heterogeneity and microstructure on the tensile behavior of crystalline rocks, *J. Geophys. Res.*, *119*(7), 5324–5341, doi:10.1002/2014JB011064.

Manighetti, I., G. C. P. King, Y. Gaudemer, C. H. Scholz, and C. Doubre (2001), Slip accumulation and lateral propagation of active normal faults in Afar, *J. Geophys. Res.*, *106*(B7), 13,667–13,696, doi:10.1029/2000JB900471.

Manighetti, I., G. King, and C. G. Sammis (2004), The role of off-fault damage in the evolution of normal faults, *Earth Planet. Sc. Lett.*, *217*(3), 399–408, doi:10.1016/S0012-821X(03)00601-0.

Marty, S., F. X. Passelègue, J. Aubry, A. Schubnel, H. S. Bhat, and R. Madariaga (2018), Acoustic study of high-frequency radiation release during experimental earthquakes, *to be subm. Geophys. Res. Lett.*

Maruyama, T. (1963), On the force equivalent of dynamic elastic elastic dislocation with reference to the earthquake mechanism, *Bull. Earthq. Res. Inst.*, *41*, 467–488.

Mitchell, T. M., and D. R. Faulkner (2009), The nature and origin of off-fault damage surrounding strike-slip fault zones with a wide range of displacements: a field study from the Atacama fault system, northern Chile, *J. Struct. Geol.*, *31*(8), 802–816, doi: 10.1016/j.jsg.2009.05.002.

Mitchell, T. M., and D. R. Faulkner (2012), Towards quantifying the matrix permeability of fault damage zones in low porosity rocks, *Earth Planet. Sc. Lett.*, *339–340*, 24–31, doi:10.1016/j.epsl.2012.05.014.

Moore, J. C., and D. Saffer (2001), Updip limit of the seismogenic zone beneath the accretionary prism of southwest Japan: An effect of diagenetic to low-grade metamorphic processes and increasing effective stress, *Geology*, *29*(2), 183–186, doi: 10.1130/0091-7613(2001)029<0183:ULOTSZ>2.0.CO;2.

Morishita, Y., T. Kobayashi, S. Fujiwara, and H. Yarai (2017), Complex crustal deformation of the 2016 Kaikoura, New Zealand, earthquake revealed by ALOS-2, *Bull. Seismol. Soc. Am.*, *107*(6), 2676–2686, doi:10.1785/0120170143.

Munjiza, A., D. Owen, and N. Bicanic (1995), A combined finite-discrete element method in transient dynamics of fracturing solids, *Eng. Computation*, *12*(2), 145–174, doi:10.1108/02644409510799532.

Munjiza, A., K. R. F. Andrews, and J. K. White (1999), Combined single and smeared crack model in combined finite-discrete element analysis, *Int. J. Numer. Meth. Eng.*, *44*(1), 41–57, doi:10.1002/(SICI)1097-0207(19990110)44:1<41::AID-NME487>3.0.CO;2-A.

Munjiza, A., E. E. Knight, and E. Rougier (2015), *Large strain finite element method: a practical course*, John Wiley & Sons.

Munjiza, A. A. (2004), *The combined finite-discrete element method*, John Wiley & Sons, doi:10.1002/0470020180.

Munjiza, A. A., E. E. Knight, and E. Rougier (2011), *Computational mechanics of discontinua*, John Wiley & Sons, doi:10.1002/9781119971160.

Nakata, T., A. Tokada, H. Chida, H. Kaneda, M. Tajikara, and S. Takazawa (2001), 1: 25,000-scale active fault map in urban area "Yatsushiro", *Tech. rep.*, Tech. Rep. of the GSI, D1-No.388.

Ngo, D., Y. Huang, A. J. Rosakis, W. A. Griffith, and D. D. Pollard (2012), Off-fault tensile cracks: A link between geological fault observations, lab experiments, and dynamic rupture models, *J. Geophys. Res.*, *117*, B01,307, doi:10.1029/2011JB008577.

Nur, A., and G. Simmons (1969), The effect of saturation on velocity in low porosity rocks, *Earth Planet. Sc. Lett.*, *7*(2), 183–193, doi:10.1016/0012-821X(69)90035-1.

Obara, K. (2002), Nonvolcanic deep tremor associated with subduction in southwest Japan, *Science*, *296*(5573), 1679–1681, doi:10.1126/science.1070378.

Ohnaka, M. (2003), A constitutive scaling law and a unified comprehension for frictional a constitutive scaling law and a unified comprehension for frictional slip failure, shear fracture of intact rock, and earthquake rupture, *J. Geophys. Res.*, *108*(B2), 2080, doi: 10.1029/2000JB000123.

Okada, Y. (1985), Surface deformation due to shear and tensile faults in a half-space, *Bull. Seismol. Soc. Am.*, *75*(4), 1135–1154.

Okada, Y. (1992), Internal deformation due to shear and tensile faults in a half-space, *Bull. Seismol. Soc. Am.*, *82*(2), 1018.

Okubo, P. G. (1989), Dynamic rupture modeling with laboratory-derived constitutive relations, *J. Geophys. Res.*, *94*(B9), 12,321–12,335, doi:10.1029/JB094iB09p12321.

Omori, F. (1912), Chapter I. general considerations (the eruptions and earthquakes of the asama-yama), *Bull. Earthq. Int. Comm.*, *6*(1), 1–16.

Palmer, A. C., and J. R. Rice (1973), Growth of slip surfaces in progressive failure of over-consolidated clay, *Proc. R. Soc. Lond. Ser-A*, *332*, 527–548, doi:10.1098/rspa.1973.0040.

Park, J. O., T. Tsuru, S. Kodaira, P. R. Cummins, and Y. Kaneda (2002), Splay fault branching along the Nankai subduction zone, *Science*, *297*(5584), 1157–1160, doi: 10.1126/science.1074111.

Passelègue, F. X., A. Schubnel, S. Nielsen, H. S. Bhat, D. Deldicque, and R. Madariaga (2016), Dynamic rupture processes inferred from laboratory microearthquakes, *J. Geophys. Res.*, *121*, doi:10.1002/2015JB012694.

Perrin, C., I. Manighetti, and Y. Gaudemer (2016a), Off-fault tip splay networks: A genetic and generic property of faults indicative of their long-term propagation, *C. R. Geosci.*, *348*(1), 52–60, doi:10.1016/j.crte.2015.05.002.

Perrin, C., I. Manighetti, J.-P. Ampuero, F. Cappa, and Y. Gaudemer (2016b), Location of largest earthquake slip and fast rupture controlled by along-strike change in fault structural maturity due to fault growth, *J. Geophys. Res.*, *121*(5), 3666–3685, doi:10.1002/2015JB012671.

Poliakov, A. N. B., R. Dmowska, and J. R. Rice (2002), Dynamic shear rupture interactions with fault bends and off-axis secondary faulting, *J. Geophys. Res.*, *107*(B11), doi:10.1029/2001JB000572.

Rao, Q., Z. Sun, O. Stephansson, C. Li, and B. Stillborg (2003), Shear fracture (Mode II) of brittle rock, *Int. J. Rock Mech. Min. Sci.*, *40*(3), 355–375, doi:10.1016/S1365-1609(03)00003-0.

Rattez, H., I. Stefanou, J. Sulem, M. Veveakis, and T. Poulet (2018), Numerical analysis of strain localization in rocks with thermo-hydro-mechanical couplings using Cosserat continuum, *Rock Mech. Rock. Eng.*, doi:10.1007/s00603-018-1529-7.

Rempe, M., T. Mitchell, J. Renner, S. Nippress, Y. Ben-Zion, and T. Rockwell (2013), Damage and seismic velocity structure of pulverized rocks near the san andreas fault, *J. Geophys. Res.*, *118*(6), 2813–2831, doi:10.1002/jgrb.50184.

Rice, J., and A. Ruina (1983), Stability of steady frictional slipping, *J. Appl. Mech.*, *50*, 343–349, doi:10.1115/1.3167042.

Rice, J. R. (1980), The mechanics of earthquake rupture, in *Physics of the earth's interior (Proc. Intn'l. School of Physics 'Enrico Fermi', Course 78, 1979)*, edited by A. M. Dziewonski and E. Boschi, pp. 555–649, Italian Physical Society and North-Holland Publishing Co., Amsterdam.

Rice, J. R. (1993), Spatio-temporal complexity of slip on a fault, *J. Geophys. Res.*, *98*(B6), 9885–9907, doi:10.1029/93JB00191.

Rice, J. R., and Y. Ben-Zion (1996), Slip complexity in earthquake fault models, *Proc. Natl. Acad. Sci. USA*, *93*(9), 3811–3818.

Rice, J. R., C. G. Sammis, and R. Parsons (2005), Off-fault secondary failure induced by a dynamic slip pulse, *Bull. Seism. Soc. Am.*, *95*(1), 109–134, doi:10.1785/0120030166.

Rivera, L., and H. Kanamori (2005), Representations of the radiated energy in earthquakes, *Geophys. J. Int.*, *162*(1), 148–155, doi:10.1111/j.1365-246X.2005.02648.x.

Rogers, T. H., and R. D. Nason (1971), Active displacement on the calaveras fault zone at Hollister, California, *Bull. Seismol. Soc. Am.*, *61*(2), 399–416.

Rojas, O., S. Day, J. Castillo, and L. A. Dalguer (2008), Modelling of rupture propagation using high-order mimetic finite differences, *Geophys. J. Int.*, *172*(2), 631–650, doi:10.1111/j.1365-246X.2007.03651.x.

Romanet, P., H. S. Bhat, R. Jolivet, and R. Madariaga (2018), Fast and slow earthquakes emerge due to fault geometrical complexity, *Geophys. Res. Lett.*, doi:10.1029/2018GL077579.

Rosakis, A. J., O. Samudrala, and D. Coker (1999), Cracks faster than the shear wave speed, *Science*, *284*, 1337–1340, doi:10.1126/science.284.5418.1337.

Rosakis, A. J., H. Kanamori, and K. W. Xia (2006), Laboratory earthquakes, *Int. J. Fract.*, *138*, 211–218, doi:10.1007/s10704-006-0030-6.

Rosu, A.-M., M. Pierrot-Deseilligny, A. Delorme, R. Binet, and Y. Klinger (2015), Measurement of ground displacement from optical satellite image correlation using the free open-source software micmac, *ISPRS Journal of Photogrammetry and Remote Sensing*, *100*, 48–59, doi:10.1016/j.isprsjprs.2014.03.002.

Rougier, E., E. E. Knight, A. Munjiza, A. J. Sussman, S. T. Broome, R. P. Swift, and C. R. Bradley (2011), The combined finite-discrete element method applied to the study of rock fracturing behavior in 3D, in *45th US Rock Mechanics/Geomechanics Symposium*, American Rock Mechanics Association.

Ruina, A. (1983), Slip instability and state variable friction laws, *J. Geophys. Res.*, *88*(10), 359–370, doi:10.1029/JB088iB12p10359.

Savage, H. M., and E. E. Brodsky (2011), Collateral damage: Evolution with displacement of fracture distribution and secondary fault strands in fault damage zones, *J. Geophys. Res.*, *116*(B03405), doi:10.1029/2010JB007665.

Scholz, C. H. (1998), Earthquakes and friction laws, *Nature*, *391*(6662), 37–42, doi:10.1038/34097.

Segall, P., and D. D. Pollard (1980), Mechanics of discontinuous faults, *J. Geophys. Res.*, *85*(B8), 4337–4350, doi:10.1029/JB085iB08p04337.

Shi, Z., Y. Ben-Zion, and A. Needleman (2008), Properties of dynamic rupture and energy partition in a solid with a frictional interface, *J. Mech. Phys. Solids*, *56*(1), 5–24, doi:10.1016/j.jmps.2007.04.006.

Shipton, Z. K., and P. A. Cowie (2001), Damage zone and slip-surface evolution over μm to km scales in high-porosity navajo sandstone, utah, *J. Struct. Geol.*, *23*(12), 1825–1844, doi:10.1016/S0191-8141(01)00035-9.

Sibson, R. H. (1977), Fault rocks and fault mechanisms, *J. Geol. Soc. (London, U.K.)*, *133*(3), 191–213, doi:10.1144/gsjgs.133.3.0191.

Sibson, R. H. (1985), Stopping of earthquake ruptures at dilational fault jogs, *Nature*, *316*(6025), 248–251, doi:10.1038/316248a0.

Sowers, J. M., J. R. Unruh, W. R. Lettis, and T. D. Rubin (1994), Relationship of the Kickapoo fault to the Johnson Valley and Homestead Valley faults, San Bernardino county, California, *Bull. Seism. Soc. Am.*, *84*(3), 528–536.

Stein, R. S. (1999), The role of stress transfer in earthquake occurrence, *Nature*, *402*(6762), 605, doi:10.1038/45144.

Steketee, J. A. (1958), Some geophysical applications of the elasticity theory of dislocations, *Can. J. Phys.*, *36*(9), 1168–1198.

Stirling, M. W., N. Litchfield, P. Villamor, R. Van Dissen, A. Nicol, J. Pettinga, P. Barnes, R. Langridge, T. Little, D. Barrell, et al. (2017), The Mw 7.8 2016 Kaikōura earthquake: Surface fault rupture and seismic hazard context, *Bulletin of the New Zealand Society for Earthquake Engineering*, *50*(2), 73–84.

Templeton, E. L., and J. R. Rice (2008), Off-fault plasticity and earthquake rupture dynamics: 1. dry materials or neglect of fluid pressure changes, *J. Geophys. Res.*, *113*(B09306), doi:10.1029/2007JB005529.

Templeton, E. L., A. Baudet, H. S. Bhat, R. Dmowska, J. R. Rice, A. J. Rosakis, and C. E. Rousseau (2009), Finite element simulations of dynamic shear rupture experiments and dynamic path selection along kinked and branched faults, *J. Geophys. Res.*, *B08304*, doi:10.1029/2008JB006174.

Thomas, M. Y., and H. S. Bhat (2018), Dynamic evolution of off-fault medium during an earthquake: a micromechanics based model, *Geophys. J. Int.*, *214*(2), 1267–1280, doi:10.1093/gji/ggy129.

Thomas, M. Y., N. Lapusta, H. Noda, and J.-P. Avouac (2014), Quasi-dynamic versus fully dynamic simulations of earthquakes and aseismic slip with and without enhanced coseismic weakening, *J. Geophys. Res.*, *119*(3), 1986–2004, doi:10.1002/2013JB010615.

Thomas, M. Y., H. S. Bhat, and Y. Klinger (2017), Effect of brittle off-fault damage on earthquake rupture dynamics, in *Fault Zone Dynamic Processes : Evolution of Fault Properties During Seismic Rupture, Geophysical Monograph 227*, edited by M. Y. Thomas, H. S. Bhat, and T. M. Mitchell, pp. 255–280, American Geophysical Union (AGU), doi:10.1002/9781119156895.ch14.

Townend, J., S. Sherburn, R. Arnold, C. Boese, and L. Woods (2012), Three-dimensional variations in present-day tectonic stress along the Australia–Pacific plate boundary in New Zealand, *Earth Planet. Sc. Lett.*, *353*, 47–59, doi:10.1016/j.epsl.2012.08.003.

Tse, S. T., and J. R. Rice (1986), Crustal earthquake instability in relation to the depth variation of frictional slip properties, *J. Geophys. Res.*, *91*(B9), 9452–9472, doi:10.1029/JB091iB09p09452.

Ulrich, T., A.-A. Gabriel, J.-P. Ampuero, and W. Xu (2018), Dynamic viability of the 2016 Mw 7.8 Kaikōura earthquake cascade on weak crustal faults, *EarthArXiv*, doi:10.31223/osf.io/aed4b.

Vallage, A., Y. Klinger, R. Grandin, H. S. Bhat, and M. Pierrot-Deseilligny (2015), Inelastic surface deformation during the 2013 Mw 7.7 Balochistan, Pakistan, earthquake, *Geology*, *43*(12), 1079–1082, doi:10.1130/G37290.1.

Venkataraman, A., and H. Kanamori (2004), Observational constraints on the fracture energy of subduction zone earthquakes, *J. Geophys. Res.*, *109*(B5), doi:10.1029/2003JB002549.

Viesca, R., J. Rice, and E. M. Dunham (2009), Plastic deformation at a propagating rupture front: Its coupling to fault pore pressure and influence on the seismic moment tensor, *Paper presented at Southern California Earthquake Center Annual Meeting, Palm Springs, CA*.

Viesca, R. C., and D. I. Garagash (2015), Ubiquitous weakening of faults due to thermal pressurization, *Nature Geosci.*, *8*(11), 875–879, doi:10.1038/ngeo2554.

Viesca, R. C., E. L. Templeton, and J. R. Rice (2008), Off-fault plasticity and earthquake rupture dynamics: 2. case of saturated off-fault materials, *J. Geophys. Res.*, *113*(B09307), doi:10.1029/2007JB005530.

Wallace, R. E., and H. T. Morris (1986), Characteristics of faults and shear zones in deep mines, *Pure Appl. Geophys.*, *124*(1), 107–125, doi:10.1007/BF00875721.

Walsh, J. B. (1965a), The effect of cracks on the compressibility of rock, *J. Geophys. Res.*, *70*(2), 381–389.

Walsh, J. B. (1965b), The effect of cracks on the uniaxial elastic compression of rocks, *J. Geophys. Res.*, *70*(2), 399–411.

Wang, T., S. Wei, X. Shi, Q. Qiu, L. Li, D. Peng, R. J. Weldon, and S. Barbot (2018), The 2016 Kaikōura earthquake: Simultaneous rupture of the subduction interface and overlying faults, *Earth Planet. Sc. Lett.*, *482*, 44–51, doi:10.1016/j.epsl.2017.10.056.

Wei, S., E. Fielding, S. Leprince, A. Sladen, J.-P. Avouac, D. Helmberger, E. Hauksson, R. Chu, M. Simons, K. Hudnut, T. Herring, and R. Briggs (2011), Superficial simplicity of the 2010 El Mayor-Cucapah earthquake of Baja California in Mexico, *Nature Geosci.*, *4*(9), 615–618, doi:10.1038/NGEO1213.

Wilson, B., T. Dewers, Z. Reches, and J. Brune (2005), Particle size and energetics of gouge from earthquake rupture zones, *Nature*, *434*(7034), 749, doi:10.1038/nature03433.

Xu, S., Y. Ben-Zion, and J.-P. Ampuero (2012a), Properties of inelastic yielding zones generated by in-plane dynamic ruptures—I. Model description and basic results, *Geophys. J. Int.*, *191*(3), 1325–1342, doi:10.1111/j.1365-246X.2012.05679.x.

Xu, S., Y. Ben-Zion, and J.-P. Ampuero (2012b), Properties of inelastic yielding zones generated by in-plane dynamic ruptures—II. Detailed parameter-space study, *Geophys. J. Int.*, *191*(3), 1343–1360, doi:10.1111/j.1365-246X.2012.05685.x.

Xu, S., Y. Ben-Zion, J.-P. Ampuero, and V. Lyakhovsky (2015), Dynamic ruptures on a frictional interface with off-fault brittle damage: feedback mechanisms and effects on slip and near-fault motion, *Pure Appl. Geophys.*, *172*(5), 1243–1267, doi:10.1007/s00024-014-0923-7.

Xu, W., G. Feng, L. Meng, A. Zhang, J. P. Ampuero, R. Bürgmann, and L. Fang (2018), Transpressional Rupture Cascade of the 2016 Mw 7.8 Kaikoura Earthquake, New Zealand, *J. Geophys. Res.*, *123*, doi:10.1002/2017JB015168.

Yabe, S., and S. Ide (2014), Spatial distribution of seismic energy rate of tectonic tremors in subduction zones, *Journal of Geophysical Research: Solid Earth*, *119*(11), 8171–8185, doi:10.1002/2014JB011383.

Yamashita, T. (2000), Generation of microcracks by dynamic shear rupture and its effects on rupture growth and elastic wave radiation, *Geophys. J. Int.*, *143*(2), 395–406, doi:10.1046/j.1365-246X.2000.01238.x.

Yue, H., T. Lay, and K. Koper (2012), En échelon and orthogonal fault ruptures of the 11 April 2012 great intraplate earthquakes, *Nature*, *490*, 245–249, doi:10.1038/nature11492.

Zhang, H., K. D. Koper, K. Pankow, and Z. Ge (2017), Imaging the 2016 Mw 7.8 Kaikoura, New Zealand, earthquake with teleseismic P waves: A cascading rupture across multiple faults, *Geophys. Res. Lett.*, *44*(10), 4790–4798, doi:10.1002/2017GL073461.

Zhao, Q., A. Lisjak, O. Mahabadi, Q. Liu, and G. Grasselli (2014), Numerical simulation of hydraulic fracturing and associated microseismicity using finite-discrete element method, *J. Rock. Mech. Geotech. Eng.*, *6*(6), 574–581, doi:10.1016/j.jrmge.2014.10.003.

Zoback, M. D., and J. H. Healy (1992), In situ stress measurements to 3.5 km depth in the Cajon Pass scientific research borehole: Implications for the mechanics of crustal faulting, *J. Geophys. Res.*, *97*(B4), 5039–5057, doi:10.1029/91JB02175.

UNIVERSITÉ SORBONNE PARIS CITÉ

Dynamic earthquake ruptures on multiscale fault and fracture networks

par

Kurama OKUBO

Résumé

Les zones de faille naturelles présentent une complexité structurelle à différentes échelles. Elles sont composées d'un réseau de failles majeures où le glissement principal s'effectue, lui-même entouré d'un réseau méso- et microscopique de fractures. Cette complexité géométrique impacte la dynamique de la rupture, la propagation des ondes sismiques ainsi que le bilan énergétique lors des tremblements de terre. Les observations géologiques et géophysiques des systèmes de faille montrent une corrélation entre la distribution spatiale de la densité de microfractures et la distance au plan principal de rupture. De leur étude de terrain, *Faulkner et al.* (2011) ont déduit que cette structure particulière des zones de failles s'explique par les irrégularitiés géométriques et l'endommagement cosismique. Les expériences en laboratoire sur la rupture dynamique montrent également un contenu haute-fréquence enrichi, comme il est observé pour les séismes naturels. Ceci est considéré comme la contribution de l'endommagement cosismique. Les outils de modélisation numérique, qui prennent en compte l'endommagement cosismique, ont permis d'explorer l'évolution des microfractures dans les zones de failles durant les séismes, et leur impact en retour sur la rupture dynamique. En revanche, les modèles existants ne permettaient pas la génération, dynamique, de fractures secondaires dans le milieu qui entourent les failles majeures. Dans cette étude, afin de pouvoir modéliser des ruptures sismiques le long de failles à géométrie réaliste, associées à la création de fractures secondaires, nous proposons une approche qui allie la modélisation des milieux continus et discontinus, en utilisant la méthode combinée des éléments finis et discrets (FDEM). Nous présentons d'abord les résultats des modélisations de rupture dynamique avec génération de fractures secondaires. Ces simulations illustrent les mécanismes de l'endommagement, une diminution de la vitesse de rupture, et les radiations hautes fréquences en champ proche. Le budget énergétique est également modifié en raison des radiations et de la dissipation de l'énergie de fracture lié à l'endommagement. Nous avons par la suite réalisé des expériences numériques afin de reproduire la rupture dynamique lors du séisme de Kaikōura (magnitude 7.8), qui s'est produit en 2016, sur le système de failles de l'île sud de la Nouvelle-Zélande. Nous avons pu démontrer qu'en comparant les observations de terrain avec la nature de l'endommagement et les profils de déplacement générés par nos modèles, il est possible de discriminer parmi les différents scénarios potentiels de rupture cosismique. En conclusion, les travaux réalisés au cours de cette thèse proposent une nouvelle génération de modèles qui, grâce à l'approche combinée des milieux continus et des milieux discrets, permet l'activation et la génération de systèmes de fractures secondaires en lien avec les séismes sur les failles majeures. Ils démontrent les effets significatifs que peut jouer l'endommagement généré lors des séismes.

Modélisation de rupture dynamique; endommagement cosismique; structure de faille complexe; méthode combinée des éléments finis et discrets; radiations hautes fréquences; le séisme de Kaikōura

Abstract

Multiscale fault structures consist of macroscopic major fault networks surrounded by mesoscopic and microscopic fracture networks, considered as off-fault damage. Such geometrical complexity of natural fault structure modifies the rupture dynamics, the seismic wave radiation and the overall energy budget associated with earthquakes. Field observations have recorded a correlation of fracture density to the distance from the fault cores, and also a strong link with the quantity of fault slip. In their geological study, *Faulkner et al.* (2011) concluded that the observed scaling inside the fault zone is better explained by the geometric irregularities and/or the coseismic damage. An enhanced high-frequency content, expected to be caused by the coseismic damage, is also observed during laboratory experiments of dynamic ruptures. Past work has explored the evolution of secondary coseismic off-fault damage caused by the dynamic earthquake ruptures within the context of effective constitutive laws. However, the current existing models cannot allow for the activation of individual secondary off-fault cracks due to limitations of model formulations. Here we propose a continuum-discontinuum approach framework with combined finite-discrete element method (FDEM) to model dynamic earthquake rupture with the coseismic off-fault damage along natural fault networks. We firstly modeled the dynamic earthquake rupture with the coseismic off-fault damage on a single planar fault. We showed the mechanism of dynamically generated off-fault crack network, the decrease in rupture velocity and the enhancement of high-frequency radiation in near-field ground motion. The overall energy budget is modified due to the additional radiation, and dissipation of the energy, associated with the secondary off-fault cracks. We then conducted a dynamic earthquake rupture modeling on the 2016 Kaikōura earthquake, which shows a great potential to narrow down a subset of hypothetical rupture scenarios by comparing the displacement field perturbed by the coseismic off-fault damage with the observations. Overall, this work has opened an avenue to model the dynamic earthquake ruptures with the continuum-discontinuum approach framework, which elucidates the effect of coseismic off-fault damage on the earthquake rupture dynamics and has shown the potential of further applications to natural fault systems.

Modeling dynamic earthquake ruptures; coseismic off-fault damage; complex fault structure; combined finite-discrete element method; high-frequency radiation; Kaikōura earthquake